

**LAMINATED CHEMICAL AND PHYSICAL MICRO-JET
ACTUATORS BASED ON CONDUCTIVE MEDIA**

A Thesis
Presented to
The Academic Faculty

by

Priya D. Gadiraju

In Partial Fulfillment
of the Requirements for the Degree
Doctor of Philosophy in the
School of Chemical & Biomolecular Engineering

Georgia Institute of Technology
December 2008

**LAMINATED CHEMICAL AND PHYSICAL MICRO-JET
ACTUATORS BASED ON CONDUCTIVE MEDIA**

Approved by:

Dr. Mark G Allen, Advisor
School of Chemical & Biomolecular
Engineering
Georgia Institute of Technology

Dr. Mark Prausnitz
School of Chemical & Biomolecular
Engineering
Georgia Institute of Technology

Dr. Ari Glezer
Woodruff School of Mechanical
Engineering
Georgia Institute of Technology

Dr. William Koros
School of Chemical & Biomolecular
Engineering
Georgia Institute of Technology

Dr. Sue Ann Bidstrup Allen
School of Chemical & Biomolecular
Engineering
Georgia Institute of Technology

Date Approved: November 7, 2008

In memory of my kid brother Venkat Raju Namburi ...

ACKNOWLEDGEMENTS

I would like to take this opportunity to thank everyone who deserves recognition for helping me throughout the course of my PhD. First of all, I would like to express gratitude to my thesis advisor, Mark Allen, for his patience and invaluable guidance throughout my research. He has always been there for me whenever I needed support, but at the same time allowed me to explore and learn on my own. I would like to thank him for involving me in several challenging projects that helped me expand my scope of knowledge and gain a practical edge. I would also like to thank Dr. Ari Glezer, Dr. Mark Prausnitz and Dr. William Koros for offering similar support and encouragement. Though not my academic advisors, they were always available to provide technical discussions. I appreciate their advice and support, which were invaluable for my degree completion.

I met some great people during my stay at Georgia Tech, especially in MSMA group. I would like to thank all of them and other colleagues who worked directly on the projects mentioned in this thesis. First and foremost of all, I would like to thank Brian English for his constant guidance throughout my PhD, especially in the early years when he guided me at each and every step of the research. I owe him for teaching me how to make circuitry. I also thank Richard Shafer for taking time everyday to ask me how my work was going or for suggesting better ways to do certain things. I also thank Jeong Woo Lee for helping me with skin testing experiments and I truly enjoyed all the time that we spent doing experiments together. I would like to thank some of the previous MSMA group members Yong Kyu Yoon, Jin Woo Park and Jung Hwan Park for guiding

me during the beginning of my PhD. I would also like to thank Suchitra Konduri for making my stay at Tech more enjoyable.

Finally, this thesis would not have been possible without the unconditional love and support from my parents, Mr. Suryanarayana Raju Gadiraju and Mrs. Rukmini Vetukuri. I thank them from the bottom of my heart for raising me to be the person that I am and for teaching me the difference between good and bad. I am extremely grateful to my sister, Rama Padmini Gadiraju for always being there for me and for providing me the emotional support that I so badly needed during my stay away from home. She has been my best friend and my pillar of strength throughout my life. I would also like to thank my husband, Mr. Nikhil Penmetsa for putting up with me when I went on tirades regarding my work. His love and support continue to brighten my life. Finally, I would like to thank my in-laws, aunts and uncles for always being there for me and treating me as their own daughter.

TABLE OF CONTENTS

	Page
ACKNOWLEDGEMENTS	iv
LIST OF TABLES	x
LIST OF FIGURES	xi
LIST OF SYMBOLS AND ABBREVIATIONS	xvii
SUMMARY	xxi

CHAPTER

1 INTRODUCTION	1
1.1 Problem Statement	3
1.2 Objectives and Overview	9
2 LITERATURE REVIEW	11
2.1 Chemical based Microactuators	11
2.1.1 Solid Propellant	13
2.1.1.1 Double Base Propellants	16
2.1.1.2 Composite Propellants	17
2.1.2 Powder Processing	26
2.1.3 Propellant Ignition Sources	30
2.1.4 Solid Propellant Microactuators	32
2.1.4.1 Digital Micropropulsion	33
2.1.4.2 Micropyros	36
2.1.4.3 Gas Generation Actuators	41
2.2 Physical based Microactuators	44
2.2.1 Transdermal Drug Delivery	45

2.2.1.1	Skin Anatomy	46
2.2.1.2	Mechanical Properties of Skin	48
2.2.2	Skin Permeability Enhancement Techniques	50
2.2.2.1	Chemical Approaches	51
2.2.2.2	Physical Approaches	52
2.2.2.2.1	Electrical based Approaches	52
2.2.2.2.2	Thermal based Approaches	55
2.2.2.2.3	Mechanical based Approaches	56
3	FABRICATION PROCESS DEVELOPMENT	59
3.1	Lamination	62
3.1.1	Adhesive Lamination	62
3.1.1.1	Adhesive Selection	65
3.2	Laser Micromachining	70
3.2.1	Common Lasers Used in Industry	73
3.3	Fabrication Sequence	75
3.3.1	Two-Dimensional Electrode based Radial Array Structures	76
3.3.1.1	Chemical based Microactuators	77
3.3.1.2	Physical based Microactuators	81
3.3.2	Three-Dimensional Electrode based Radial Array Structures	83
4	TEST METHODS	86
4.1	Chemical based Microactuators	86
4.1.1	Propellant Processing	86
4.1.2	Fuel Conductivity Measuring Setup	96
4.1.3	Gas Generation Measuring Setup	97
4.1.3.1	Pressure Sensor Calibration	100

4.1.4	Force and Burn Time Measuring Setup	101
4.1.4.1	Force Sensor Calibration	106
4.1.5	Impulse Measuring Setup	108
4.1.5.1	Impulse Calculations	113
4.1.6	Ignition Electronics Setup	114
4.1.6.1	Equipment and Setup	117
4.1.6.2	Actuator Electrical Packaging Issues	122
4.2	Physical based Microactuators	124
4.2.1	Force and Burn Time Measuring Setup	124
4.2.2	Ignition Electronics Setup	125
4.2.3	Permeability Testing Setup	126
4.2.3.1	Quantitative Drug Permeability Measuring Setup	127
4.2.4	Histological Skin Examination	129
5	RESULTS	131
5.1	Chemical based Microactuators	131
5.1.1	Fuel Conductivity Results	132
5.1.2	Actuator Modeling and Design	139
5.1.2.1	Ignition Delay Time Simulations	139
5.1.2.2	Impulse and Discharge Time Simulations	149
5.1.2.2.1	Nozzle Design	162
5.1.2.2.2	Combustion Chamber Design	163
5.1.3	Ignition Power Supply Characterization	165
5.1.4	Actuator Performance	174
5.1.4.1	Propellant Geometry and Composition Effects	174
5.1.4.2	Nozzle Geometry Effects	185

5.1.4.3 Solid Propellant Gas Generation	188
5.1.6 Microactuator Feasibility for Projectile Maneuvering	194
5.1.6.1 Application Requirements	195
5.1.6.2 Actuator Performance	197
5.2 Physical based Microactuators	201
5.2.1 Actuator Characterization	201
5.2.1.1 Mechanical Characterization	203
5.2.1.2 Thermal Characterization	207
5.2.2 Skin Characterization	208
5.2.2.1 Thermo-Mechanical Exposure of Skin	208
5.2.2.2 Thermal Exposure of Skin	216
5.2.2.2.1 Temperature Profile of Skin	217
6 CONCLUSIONS	225
6.1 Chemical based Microactuators	226
6.2 Physical based Microactuators	229
APPENDIX A: THREE DIMENSIONAL MICROACTUATORS BASED ON LITHOGRAPHY AND LASER MICROMACHINING	232
APPENDIX B: POWER CIRCUIT FOR PORTABLE APPLICATIONS	234
APPENDIX C: NUMERICAL SIMULATIONS BASED ON NOZZLE THEORY.	236
REFERENCES	239
VITA	247

LIST OF TABLES

	Page
Table 1: Properties of solid propellant components	20
Table 2: Survey of health and detonation risks of solid propellant formulations	20
Table 3: Considerations to be made while choosing appropriate adhesive	68
Table 4: Lamination adhesives tested	69
Table 5: Adhesive overflow testing	69
Table 6: Laser machining equipment	72
Table 7: List of ingredients for composite conductive propellants	88
Table 8: Propellant mixtures prepared in lab and tested for fuel conductivity	94
Table 9: Sample weight ratios for the finalized solid propellant formulations	94
Table 10: Conductivity data for several composite propellant mixtures tested in lab...	137
Table 11: predicted ignition delay times for three fuel compositions prepared in lab..	149
Table 12: Specific impulse delivered by several propellant formulations... ..	177
Table 13: Amount of gas generated for perchlorate and GAP based fuels	193
Table 14: Amount of forces generated by several propellants	205
Table 15: Properties of skin used in thermal simulations.....	219

LIST OF FIGURES

	Page
Figure 1: Exposure of skin to a physical microjet	8
Figure 2: Industrial solid propellant processing flow chart	28
Figure 3: Features of adhesive lamination process	64
Figure 4: New Hermes 60 W CO ₂ laser	74
Figure 5: Resonetics 15 W Nd:YLF laser	75
Figure 6: Fabrication concept of the microactuators.....	77
Figure 7: Fabrication sequence of two-dimensional electrode based radial array microactuators	80
Figure 8: Array of chemical microactuators	81
Figure 9: Array of physical microactuators	83
Figure 10: Fabrication sequence of three-dimensional electrode based radial array microactuators	85
Figure 11: Propellant powder process flowchart	93
Figure 12: Microchamber used for conductivity measurements	97
Figure 13: Pressure bomb used for measuring amount of gas released	99
Figure 14: Pressure bomb calibration	100
Figure 15: Force sensor setup	104
Figure 16: Force sensor data acquisition	105
Figure 17: Force sensor output result	105
Figure 18: Force sensor impulse calibration	107
Figure 19: A typical ballistic pendulum setup	109
Figure 20: Pendulum experimental apparatus	110
Figure 21: Pendulum measurement flowchart	112

Figure 22: Vibrometer output from pendulum setup	112
Figure 23: Ignition source schematic	115
Figure 24: Ideal ignition characteristics expected for conductive fuel actuator	115
Figure 25 Typical voltage and current data obtained with a capacitor as ignition source.....	116
Figure 26: Power supply schematic used for testing	119
Figure 27: Power supply used during testing	119
Figure 28: Typical electrical power and energy data obtained	121
Figure 29: Microactuator array with connection wires attached using soldering technique.....	123
Figure 30: Force and Impulse obtained from physical microjet actuators	125
Figure 31: Quantitative skin permeability measuring equipment	129
Figure 32: Variation of potassium perchlorate based fuel conductivity with the amount of conductive material	136
Figure 33: Variation of potassium chlorate based fuel conductivity with the amount of conductive material	137
Figure 34: Variation of fuel resistance with conductive dopant and area of the fuel mixture	138
Figure 35: Variation of fuel resistance with gap between electrodes and area of the combustion chamber for Fuel 2.....	138
Figure 36: Estimation of temperature variation with time across the gap between electrodes	146
Figure 37: Voltage distribution across the conductive propellant placed between electrodes.....	147
Figure 38: Predicted variation of ignition delay time with chamber volume and gap between electrodes	147
Figure 39: Predicted variation of ignition delay time with voltage applied across the electrodes	148
Figure 40: Simple electrical circuit with Thevenin resistance.....	148

Figure 41: Schematic of flow of gases from a combustion chamber and a diverging nozzle.....	150
Figure 42: Predicted effect of nozzle length and divergence angle on released thrust..	156
Figure 43: Predicted effect of nozzle length and divergence angle on pressure ratio ...	156
Figure 44: Predicted effect of nozzle entrance and exit dimensions on released thrust.....	157
Figure 45: Predicted effect of nozzle throat area and length on released thrust	157
Figure 46: Predicted effect of nozzle throat area and length on pressure ratio	158
Figure 47: Predicted effect of nozzle throat area on discharge time	159
Figure 48: Predicted effect of chamber volume on discharge time	160
Figure 49: Predicted variation of impulse delivered with chamber volume	161
Figure 50: Predicted variation of impulse delivered with chamber pressure	161
Figure 51: Voltage and current data obtained during ignition process	167
Figure 52: Energy consumed from the electrical setup during ignition process	167
Figure 53: Dependency of energy consumed and fuel conductivity on the amount of conductive material for potassium chlorate based fuel	168
Figure 54: Dependency of energy consumed and fuel conductivity on the amount of conductive material for potassium perchlorate based fuel	169
Figure 55: Variation of ignition delay time with input electrical energy for Fuel 5 and Fuel 7.....	171
Figure 56: Dependency of ignition delay times for Fuel 5 on chamber volume and gap between electrodes	172
Figure 57: Dependency of ignition delay time on chamber volume for Fuel 5 when the distance between electrodes is 1.5 mm	172
Figure 58: Dependency of ignition delay time on chamber volume for Fuel 5 when the distance between electrodes is 2 mm	173
Figure 59: Dependency of ignition delay time on chamber volume for Fuel 5 when the distance between electrodes is 2.5 mm	173
Figure 60: Dependency of ignition delay time on chamber volume for Fuel 8 when the distance between electrodes is 1.5 mm	174

Figure 61: Comparison of specific impulse delivered by conductive and nonconductive potassium perchlorate based fuels	178
Figure 62: Comparison of experimentally obtained specific impulse values with theoretically obtained values for several combustion chamber volumes	178
Figure 63: Variation of total impulse delivered with the amount of conductive material present in potassium perchlorate based fuel	180
Figure 64: Experimental dependency of total impulse delivered with binder concentration for potassium perchlorate based fuels	181
Figure 65: Experimental dependency of total impulse delivered with chamber volume for potassium perchlorate based fuels	182
Figure 66: Comparison of experimental and theoretically obtained total impulse for potassium perchlorate based fuels	183
Figure 67: Variation of total impulse delivered with fuel composition for potassium chlorate based fuels	184
Figure 68: Experimental dependency of total impulse delivered with chamber volume for potassium chlorate based fuels	184
Figure 69: Effect of nozzle throat area on discharge times for perchlorate based fuels.....	186
Figure 70: Effect of gap between electrodes on discharge times of the jet	187
Figure 71: High speed video capture of perchlorate – aluminum fuel jet	188
Figure 72: High speed video capture of GAP – carbon black jet	188
Figure 73: Pressure signal received from pressure transducer	191
Figure 74: Amount of gas released for Fuel 5 as a function of fuel volume	191
Figure 75: Amount of gas released for Fuel 3 as a function of fuel volume	192
Figure 76: Comparison of gas generation results for GAP based propellant (Fuel 3) and potassium perchlorate based propellant (Fuel 5).....	192
Figure 77: Impulse based displacement of 150 g projectile with x-velocity of 70 m/s and 32 actuator impulse bits in the y-direction	197
Figure 78: Actuator performance: 15 mm ³ combustion chamber with perchlorate based fuel with 0.25 x by weight of binder composition and varying conductive material composition	199

Figure 79: Actuator performance: 15 mm ³ combustion chamber with perchlorate based fuel with 0.75 x by weight of binder composition and varying conductive material composition	199
Figure 80: Actuator performance: 15 mm ³ combustion chamber with chlorate based fuels with varying compositions	201
Figure 81: Power characteristics consumed from the power supply during the arc generation process	203
Figure 82: Force data obtained for several propellants occupying a chamber volume of 1 mm ³	205
Figure 83: High speed imaging of released jet from physical microactuator	206
Figure 84: Microscopic image of skin surface exposed to an ethanol microjet	208
Figure 85: Microscopic image of trypan blue stained skin surface exposed to the jet..	209
Figure 86: Histologically examined skin surface exposed to an ethanol jet	210
Figure 87: Histologically examined skin surface exposed to an ethanol jet containing gold nano particles	210
Figure 88: Patterned mask used for localizing the effects of thermo-mechanical jet exposure on skin	211
Figure 89: Histological examination of locally exposed porcine skin	212
Figure 90: Permeability results obtained in jet exposed human cadaver skin for several propellants	214
Figure 91: Permeability results obtained in jet exposed human cadaver skin for several propellants containing solid microparticles	215
Figure 92: Dependency of permeability obtained with reaction force obtained from the jet.....	215
Figure 93: Temperature profile obtained in skin from simulations for a direct exposure to a thermo-mechanical jet	219
Figure 94: Temperature profile obtained in skin from simulations for an indirect exposure to a thermo-mechanical jet using a 25 µm thick titanium mask.....	220
Figure 95: Temperature profile obtained in skin from simulations for an indirect exposure to a thermo-mechanical jet using a 25 µm thick tungsten mask.....	220
Figure 96: Picture of skin before and after exposure to thermal jet	221

Figure 97: Skin shown in Figure 96 after treating with sulforhodamine drug to study its permeability	222
Figure 98: Histological examination of skin shown in Figure 97... ..	222
Figure 99: Locally ablated skin surface exposed to a thermal jet	224
Figure 100: Multi pillared microactuator fabrication schematic	233
Figure 101: Multi pillared three dimensional structure	233
Figure 102: Portable power circuit schematic for use in a small scale projectile	234

LIST OF SYMBOLS AND ABBREVIATIONS

Symbols

a	Linear Burn Rate Proportional Constant
a^*	Speed of Sound
A	Area
A^*	Nozzle Throat Area
c^*	Characteristic Velocity
c_p	Specific Heat at Constant Pressure
d	Thickness
E	Total Energy
E_a	Activation Energy
F	Force
g	Gravitational Constant
G_p	Puncture Toughness
ΔH_f	Heat of Formation
ΔH_v	Heat of Vaporization
I	Impulse
I_{sp}	Specific Impulse
J	Electric Current Density
k	Thermal Conductivity
L	Length
L^*	Characteristic Length
m	Mass
M	Molecular Weight

n	Linear Burn Rate Exponential Constant
N	Moles
P	Pressure
Q	Resistive Heat
r	Linear Burn Rate
R_u	Universal Gas Constant
R	Gas Constant (R_u/M)
R	Resistance
t	Time
T	Temperature
u	Flow in Streamwise Direction
v	Velocity
V	Volume
V	Voltage
w	Width
W	Electric Power
x	Streamwise Coordinate or Linear Position
z	Vertical Displacement with Respect to Gravity
α	Thermal Diffusivity
δ	Diffusivity
θ	Nozzle Divergence Half-angle
γ	Specific Heat Ratio
i	Current
ϕ	Angular Displacement of Pendulum
ρ	Density

ρ	Electrical Resistivity
σ	Electrical Conductivity
σ_p	Temperature Sensitivity of Linear Burn Rate
Ψ	Lamination Peel Strength

Abbreviations

<i>AP</i>	Ammonium Perchlorate
<i>AN</i>	Ammonium Nitrate
<i>CTPB</i>	Carboxyl-Terminated Poly-Butadiene
<i>DB</i>	Double Base Propellant
<i>DEP</i>	Diethyl Phthalate
<i>GAP</i>	Glycidyl Azide Polymer
<i>GGA</i>	Gas Generation Actuators
<i>HTPB</i>	Hydroxyl-Terminated Poly-Butadiene
<i>KC</i>	Potassium Chlorate
<i>KN</i>	Potassium Nitrate
<i>KP</i>	Potassium Perchlorate
<i>LPCVD</i>	Low Pressure Chemical Vapor Deposition
<i>MEMS</i>	Micro Electro Mechanical Systems
<i>MW</i>	Molecular Weight
<i>NG</i>	Nitroglycerine
<i>NC</i>	Nitrocellulose
<i>PU</i>	Poly Urethane
<i>PVC</i>	Poly Vinyl Chloride
<i>PBAN</i>	Polybutadiene Acrylonitrile

<i>TCR</i>	Thermal Coefficient of Resistivity
<i>μTAS</i>	Micro Total Analysis System

Subscripts

<i>a</i>	Atmospheric
<i>c</i>	Combustion Chamber
<i>e</i>	Exit
<i>el</i>	Electric
<i>g</i>	Gas Phase
<i>h</i>	Lamination Press Platen
<i>i</i>	At Time = <i>i</i>
<i>ign</i>	Ignition
<i>loss</i>	Heat Loss
<i>noz</i>	Nozzle
<i>0</i>	At Time = 0
<i>t</i>	At Time = <i>t</i>
<i>p</i>	Solid Propellant
<i>ps</i>	Power Supply
<i>pen</i>	Pendulum
<i>sit</i>	Self Propagation Temperature
<i>u</i>	Decomposition

SUMMARY

This dissertation presents the development of electrically-powered, lamination-based microactuators for the realization of large arrays of high impulse and short duration micro-jets with potential applications in the field of micro-electro-mechanical systems (MEMS). Microactuators offer unique control opportunities by converting the input electrical or chemical energy stored in a propellant into useful mechanical energy. This small and precise control obtained can potentially be applied towards aerodynamic control and transdermal drug delivery applications. This thesis work discusses the feasibility of using microactuators for two such applications: Control of the motion of a spinning projectile by utilizing the chemically-driven microjets ejected from the actuators, and enhancement of the permeability properties of skin by selectively ablating the stratum corneum layer of skin using the physical microjets ejected from the actuators. This enhanced permeability of skin can later be used for the delivery of high molecular weight drugs for transdermal drug delivery.

The development of electrically powered microactuators starts by fabricating an array of radially firing microactuators using lamination-based microfabrication techniques that potentially enable batch fabrication at low cost. The microactuators of this thesis consist of three main parts: a micro chamber in which the propellant is stored; two electrode structures through which electrical energy is supplied to the propellant; and a micro nozzle through which the propellant or released gases from the propellant are expanded as a jet. Once the actuators are fabricated, they are integrated with MEMS-process-compatible propellants and optimized so as to produce instantaneous ignition of

the propellant. This instantaneous ignition is achieved either by making the propellant itself conductive, thus, passing an electric current directly through the propellant; or by discharging an arc across the propellant by placing it between two closely spaced electrodes. The first concept is demonstrated for the application of projectile maneuvering where energetic solid propellant is used in generating a high velocity gaseous jet and the second concept is demonstrated for transdermal drug delivery application where a rapid physical jet of a non-energetic propellant is generated.

In the case of chemical-based microactuators, the feasibility of using conductive solid propellant based actuators for maneuvering a 25 mm bluff body projectile spinning at 600 Hz is presented. Several conductive solid propellants are developed and characterized for their electrical conductivity and required ignition energy. Finally, the propellant integrated microactuators are characterized for performance in terms of impulse delivered, thrust generated and duration of the jet. These experimental results are then compared to predicted results from simulations.

In the case of physical based microactuators, the feasibility of using released physical jets from the microactuator array for transdermal drug delivery application is presented. Several bio-compatible and FDA-approved liquids are used as propellants and are characterized in terms of thrusts delivered and duration of the released jets. These thermo-mechanical jets are then used to expose skin locally so as to create micro conduits in the stratum corneum layer of skin. Both thermal effects and thermo-mechanical effects of the jet on exposed skin are studied. For both cases, histology of exposed skin is presented and its permeability to drug analog molecules is studied.

CHAPTER 1

INTRODUCTION

A micro-electro-mechanical system (MEMS) is a small scale system consisting of both electrical and mechanical components integrated into a single device to help control motion of a system or to sense and obtain information from the system. Advances over the last decade in the areas of microelectronics and MEMS have enabled many possibilities in the areas of research and industry. Because of these possibilities, attention to developing microsystems using MEMS techniques continues to increase worldwide. MEMS technology and micro-engineering in general became much broader in scope, evolving as a multi-disciplinary field that investigates the physics and science of the sub-millimeter scale world and the application of this understanding to develop mass producible devices and systems for many applications.

Micro-engineering includes research with respect to technologies of materials and processes required to make MEMS components, integration of these components into micro devices, and applications. Potential advances in the area of MEMS could be in multiple areas including materials, fabrication techniques, and new applications. Several applications were demonstrated for MEMS devices including but not limited to the fields of biomedical, aerospace and chemical engineering. In aerospace engineering, MEMS enables accurate control of fluidics using micro sensors and actuators. Use of MEMS devices have successfully been demonstrated in this area for communications, satellite control, automotive control and safety systems [1]. In the biomedical field, MEMS enables the development of medical sensors such as portable gas sensors that detect

airborne toxins, medical devices such as micro needles for drug delivery applications, and wireless pressure sensors for health monitoring. These systems benefit from the advantages offered by microengineering technology such as reduction in size, mass and input power requirements. Hence, MEMS devices offer portability, batch fabrication and cost effectiveness. Commercialization of such devices would not only require the development of the device but also integration of the device with electronics. Several such integrated MEMS products are currently available in the commercial market. Chemical sensors, acceleration and pressure transducers, ink-jet printers are a few of these.

Microfluidic actuators potentially add unique control opportunities by generating forces in fluidic environments and using these generated forces for fluidic actuation purposes [2]. Examples of microfluidic actuators include microvalves [3], micropumps [4] and mixers [5]. These fluidic actuators were developed and demonstrated in the literature with a variety of actuation methods including piezoelectric, electrostatic, thermal, pneumatic, electromagnetic, combustion and capillary actions [6]. A thermo-pneumatic valve, for example, is made by inserting a resistive heater into an enclosed cavity behind a diaphragm. When heat is delivered to the fluid in the cavity by supplying electric current to the heater, the fluid expands, pushing the diaphragm out. The extended diaphragm can then be used to block a channel, acting as a valve.

Liquid microjets developed from fluidic actuators that utilize piezoelectric [7], pneumatic [8] and capillary actions [9] for actuation offer precise control of operation over small flow rates of liquids, and were demonstrated successfully in commercial applications such as drug delivery as sample fillers in gene chip technology, as cutting

tools for microsurgery, in miniature chemical analysis systems as in integrated multi-step micro total analysis systems (μ TAS), and as ink sprayers in inkjet printers. Fluidic actuators utilizing electro-kinetic actuation were demonstrated for boundary layer drag reduction for control of aircraft. Actuators based on combustion actuation [10] offer much larger flow rates and generate larger forces than other types of fluidic actuators and were successfully demonstrated for defense based applications, energy based applications and for chemical processing. Some major defense-based applications of combustion microactuators reported in the literature are for satisfying nano satellite propulsion needs of microspacecraft and for microscale power generation in the area of man-portable power. In the energy area, these devices offer increasingly important uses such as power packs based on combustion rather than electro-chemistry and for extending operating times of electronic devices by providing the required heating or cooling. In the area of chemical processing, miniaturized chemical reactors could provide on-site neutralization of toxic chemicals thereby eliminating the need for transport and burial [11].

1.1 Problem Statement

Microjet actuators are defined as small scale actuators that utilize the energy stored or supplied to a propellant to produce high velocity, high temperature jets. Fluidic microjets offer unique control opportunities by converting the input electrical or chemical energy stored in the propellant into useful mechanical energy. This small and precise control obtained can potentially be applied to aerodynamic and transdermal drug delivery applications. In this thesis, we are interested in two such applications: to control the motion of a spinning projectile by utilizing the chemically-driven microjets ejected from the actuators; and to enhance the permeability property of skin by selectively ablating the

stratum corneum layer of skin using the physical microjets ejected from the actuators. This enhanced permeability of skin can later be used for the delivery of high molecular weight drugs for transdermal drug delivery.

The application of projectile maneuvering requires the delivery of large, accurate thrusts and aerodynamic forces from the fluidic jet. Hence, combustion based microjet actuators are considered for this application. A typical combustion actuator consists of a combustion chamber filled with gaseous, liquid, or solid chemically reactive propellant in contact with a heater. The heater is typically a resistive heating element such as a bridge wire or a pair of electrodes to which electrical energy is supplied. The heater ignites the propellant in the chamber, thus releasing a gaseous combustion jet. The propellant stored in the chamber plays a significant role in determining the performance that can be obtained from the actuator. Liquid propellants offer larger thrusts, but solid propellants offer greater simplicity in fabrication [12]. Our work mainly concentrates on conductive solid propellant development, its integration with the microactuator and its demonstration for control of thrusts generated and the timing of the combustion event. So, the goal of this part of the thesis is to fabricate and characterize lamination based, conductive solid propellant microjet actuators and to study the possibility of integrating these actuators into an aerodynamic control research vehicle.

Conductive solid propellant helps in minimizing the duration of the released chemical jets by causing an instantaneous ignition of fuel and thus, minimizing the reaction time of the propellant. It also serves to simplify device fabrication by allowing ignition to occur by passing current directly through the fuel sample from two MEMS fabricated electrodes as opposed to relying on the transfer of heat from external or

embedded igniters [13]. In this case, the heat dissipated by the resistance of the fuel itself causes ignition. DiBiaso et al. [13, 14] have demonstrated that the addition of at least 20% by volume of conductive dopant enables conventional composite propellants to become conductive with minimal reduction in the burn rate of the fuel.

The work performed in this thesis is an extension to the above mentioned work and further efforts are made to develop more conductive propellants that are suitable to be implemented into the microactuators. In this regard, three points will be demonstrated. First, solid propellants and conductive dopants that are suitable for the application are studied and propellant processing techniques suitable for micro-scale applications are developed. Second, laser micromachining and lamination techniques are used to produce batch-fabricated fluidic actuators that withstand harsh environments. Third, testing methods are developed to study the performance of the actuator in terms of thrust delivered, duration of the jet and total impulse delivered by the jet. The actuators are designed to optimize the performance by varying the solid propellant or geometry of the microactuator. Finally, the actuator performance is validated for maneuvering the path of a 25 mm diameter projectile spinning at 600 Hz. With the demonstration of these three points, the following fundamental advances in MEMS technology are achieved:

- New MEMS processing techniques for robust actuators.
- Solid propellant selection criteria for millimeter-scale solid propellant actuators.
- New concept for ignition of solid propellants.
- Expanding the existing performance range of MEMS based solid propellant combustors.
- Demonstrate precise time control of conductive solid propellant actuators with

respect to ignition delay times and durations.

- Develop characterization techniques for MEMS based solid propellant actuators.

The second part of this thesis focuses on developing physical-based microactuators for transdermal drug delivery applications. The application of transdermal drug delivery requires the permeability of skin to be increased for the delivery of high molecular weight drugs. Several skin permeability enhancements techniques have already been reported in the literature [15]. In this work, a new physical enhancement technique is developed by means of applying the physical microjets released from the actuators onto the skin. The physical based microactuators deliver rapid jets with small and accurate thrusts and impulse levels. These rapid jets when exposed onto skin should selectively ablate the top layer of skin, stratum corneum, by thermal and mechanical means with minimal to no damage to the underlying layers. The physical microjet actuators consist of a chamber filled with liquid propellant placed between two electrodes. When sufficient electrical energy is supplied to the closely spaced electrodes, an arc is discharged between electrodes building up temperature and pressure within the system. This causes a phase change of the propellant and the high pressured propellant exits the chamber in the form of a fluidic jet, through a nozzle.

The thermo-mechanical properties of the released jet are studied and its effect on enhancing the permeability of skin is demonstrated. The treated skin surface is studied using skin histology experiments. From a conceptual point of view, three approaches to skin ablation are demonstrated using the same microactuators. First, the skin is directly exposed to the released jet from the microactuator as shown in Figure 1(a) and the effect of thermo-mechanical ablation is demonstrated. Next, isolated parts of skin are exposed

to the released jet as shown in Figure 1(b) and the localized effects of thermo-mechanical ablation are studied. Finally, the skin is indirectly exposed to the jet using a masking system that isolates the thermal and mechanical effects of the jet as shown in Figure 1(c) and the effect of thermal ablation is studied. All the above concepts are demonstrated using the same microactuators.

From the microactuator device point of view, three points will be demonstrated. First, the device concept is validated by batch fabricating fluidic microactuators using laser micromachining and lamination techniques. Second, the performance of the jet is characterized in terms of duration and thrusts delivered for various propellants. Third, the post exposure permeability and histology of the skin are studied. The actuators are designed to optimize the performance by varying the propellants used and geometry of the microactuator. With the demonstration of these points, the following fundamental advances in the area of transdermal drug delivery are achieved:

- Thermal and mechanical based permeability enhancement concepts for transdermal drug delivery are demonstrated.
- An array of devices that are batch fabricated using MEMS process compatible techniques are developed.
- Fluidic jets of several biocompatible liquids are released from the actuators and their use for permeability enhancement of skin is demonstrated.
- The possibility of achieving extremely fast ablation times using these fluidic jets allow for minimizing the pain associated with skin permeability.
- Flexibility of exposed skin's area and depth is achievable by controlling the jet's magnitude to meet the requirements for the delivery of a specific drug.

- Allows for selective ablation of skin by utilizing masking patterns.
- Can be used as a pretreatment technique which can be integrated with many other drug delivery approaches.

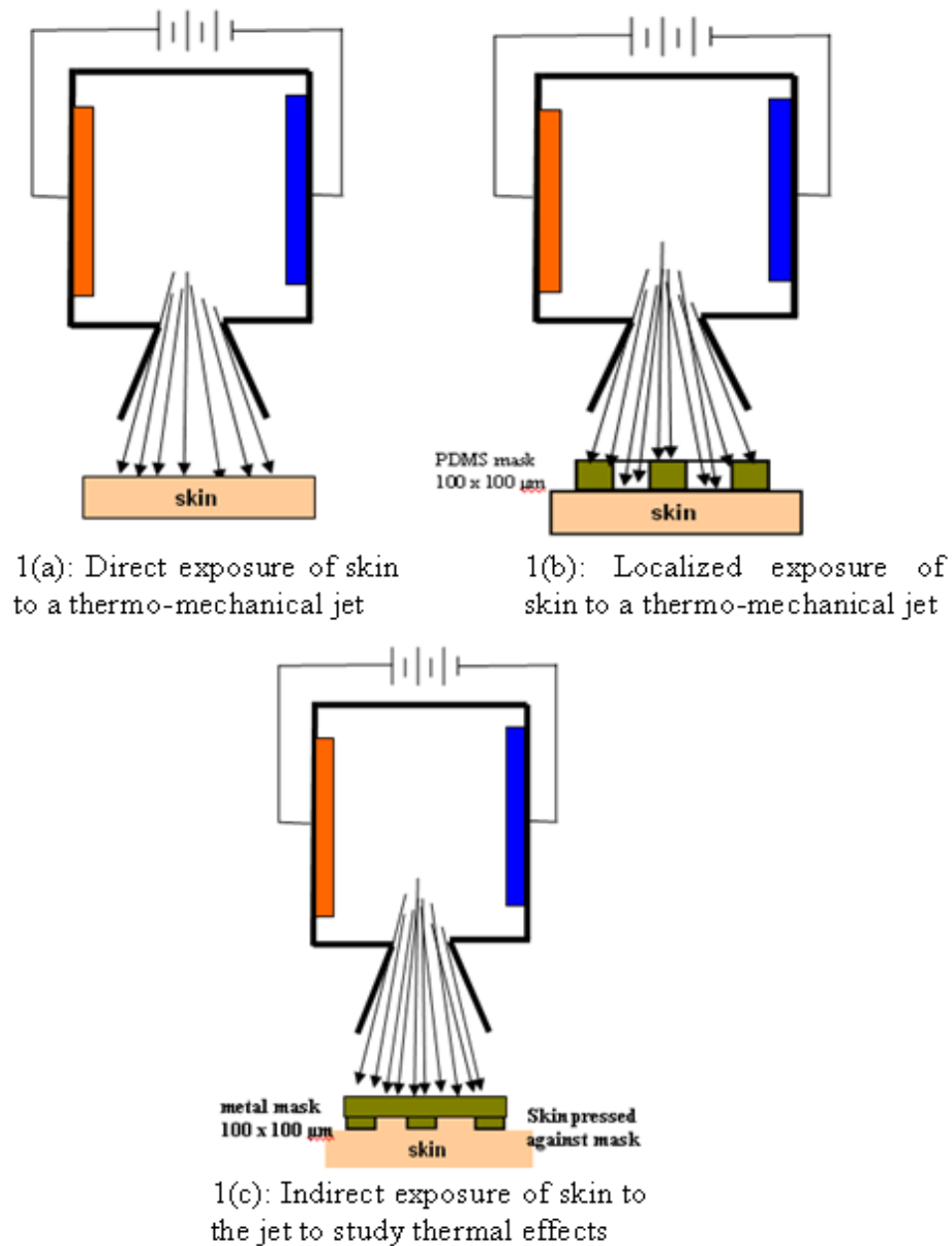


Figure 1: Exposure of skin to a physical microjet

1.2 Objectives and Overview

The body of this thesis is divided into six sections. Chapter 2 reviews existing literature for both chemical and physical based microjet actuators. For chemical based microjet actuators, solid propellants are reviewed in general and among these, the best suitable propellants for the microactuator development are short listed based on a set of selection criteria. Industry standard propellant powder processing is reviewed to establish techniques for small scale, lab based powder processing that offers reliable performance from the solid propellants. Many of the existing propellant ignition concepts are examined and the need for a new ignition concept is explained. Some of the existing solid propellant microactuators are reviewed in detail and the performance achieved by these actuators is reported. For physical based microactuators, as the main application of interest in this research is transdermal drug delivery, the anatomy of skin and its mechanical properties are reviewed. Several existing skin permeability enhancement techniques and their limitations are presented. The goal of this chapter is to highlight the advantages and limitations of the existing techniques and provide ground work for optimizing the performance of our devices according to the requirements of the application.

Chapter 3 details the actuator fabrication process. The same fabrication techniques are used in the fabrication of both chemical and physical microactuators. This chapter reviews the laser micromachining and adhesive lamination techniques used for fabrication in detail and then presents equipment and detailed fabrication sequences involved in the fabrication of the microactuators.

Chapter 4 details the methods and experimental apparatus used for the characterization of microactuators. Chapter 5 presents the results of characterization experiments for both chemical and physical microactuators. For chemical microjet actuators, the released jets are characterized for the amount of delivered thrust, impulse and duration and whether they meet the performance requirements for maneuvering a projectile is discussed. For physical microjet actuators, the released jets are characterized in a similar fashion and are applied for transdermal drug delivery application. The treated skin is characterized to study its permeability to drug analog molecules. The purpose of these chapters is to verify the operation of the microactuator arrays and their possible use towards specific applications. Finally, Chapter 6 discusses the established solutions and possible future work in these areas.

CHAPTER 2

LITERATURE REVIEW

2.1 Chemical based Microactuators

Chemical based actuators utilize the chemical energy stored in a propellant to produce thermo-mechanical forces that could be used for mechanical actuation. They operate on the principle of producing thrusts by escaping hot gases generated by propellant combustion through a nozzle. A chemical actuator consists of a combustion chamber, a nozzle and an ignition source. A gaseous, liquid or solid propellant is filled in the chamber and is ignited using an ignition source. When sufficient energy is supplied to the propellant from the ignition source, combustion takes place releasing high temperature, low molecular weight product molecules. Thrust is generated when these product gases are exhausted through a nozzle into the surrounding environment.

Advances in microsystem fabrication technology have enabled miniaturization of these chemical actuators to the point that they can be usefully deployed for micropropulsion. The motivation for miniaturizing chemical actuators is the potential for gains in performance/size ratio and the possibility of increased integration. Also, the impulse precision producible by nano and micro thrusters cannot be achieved with conventional propulsion systems. Among the propulsion systems under investigation for miniaturization of chemical actuators are cold gas thruster, subliming solid thruster, solid propellant thruster, vaporizing liquid thruster, micro ion thruster and pulsed plasma thruster [16].

Chemical based actuators are broadly classified based on the type of propellant used into solid, hybrid and liquid propellant actuators. Compared to solid propellants,

liquid propellants offer higher specific impulse [17] but they require complex fluid flow and storage systems and suffer from problems such as density, fluid flow behavior and combustion instability. Solid propellants on the other hand, require much simpler storage and handling systems with no moving parts, thus reducing fabrication times and allowing for increased fabrication yields [12]. Solid propellants can be stored for longer periods before firing and require negligible pre-firing preparations. However, solid propellant actuators are one shot devices that lack restart ability. This limitation can be overcome by utilizing MEMS techniques for fabricating an array of multiple actuators. The technology of solid propellant and MEMS based actuators has widely been developed because of the areas of spacecraft and military. Solid propellants have been used in these areas for many applications requiring high thrusts such as in rockets for space travel and for attitude control systems in satellites [12, 18].

Over the last decade, solid propellants have been the first choice for the development of combustion based microactuators for use in smaller control vehicles which require less thrust levels from the propellant [19]. The same solid propellant based technology is used in our research to generate thrusts that are required to maintain control authority of smaller projectile. By reducing the size of actuators, control electronics and power supply, a complete control system can be fit into a projectile smaller than a soda can. Since the proposed microactuators have similar chemistry, components and designs as that of a solid propellant actuator, we begin our literature review with solid propellants, their current applications in microactuator technology and finally, determine the feasibility of using solid propellant microactuators for projectile maneuvering application.

The goal of this literature review is to establish the feasibility of fabricating chemical microjet actuators that are capable of generating tens of Newtons of thrust with millisecond-scale rise and fall times. Solid propellants suitable for our application are surveyed and existing industrial based powder processing techniques are looked at to achieve repeatable performance. Finally, a review of current research in solid propellant microactuators is presented: Among these, Digital micropropulsion [20], Micropyros [21] and Gas generating actuators [19, 22] are looked at in detail to study their fabrication techniques, performance and testing of MEMS based microactuators. A review of the fabrication and processing techniques used to make solid fuel microactuators is presented in this chapter with the detailed fabrication of microactuators.

2.1.1 Solid Propellant

Solid propellant forms an integral component of the proposed microactuator. It is the main source of chemical energy that is required to increase system pressure and convert pressure to mechanical actuation. Solid propellants are mixtures of fuel and oxidizer that are cast, hardened and stored in a combustion chamber until ignition. Upon ignition, a chemical reaction takes place between the fuel and oxidizer components of the propellant producing high temperature, low molecular weight gases. When these gases are made to flow through a constriction, such as a nozzle, the velocity of exhaust gases increases producing thrust. The use of solid propellant allows for the overall simplification of device fabrication, thereby eliminating the need for complex handling and storage systems such as microvalves and micropumps [17, 23]. It requires a fairly simple actuator system to operate and to produce good performance. It can be stored for long periods before firing and requires negligible pre-firing preparation. Hence, solid

propellant selection becomes a prime and important factor while optimizing the microactuator for its performance. This selection of a solid propellant depends on several of the following factors:

- The propellant must be able to achieve desired performance for an application.
- It must be easily available.
- The hazards associated with propellant processing must be minimal.
- It must be processible for both small scale and large scale operations with minimal powder processing requirements.
- It must have the desired ballistic properties.
- It must have satisfactory mechanical and thermal properties.
- It must be capable of withstanding harsh environmental conditions.
- It must be sensitive to electrical ignition.

Safety and availability of propellant are extremely important when choosing a propellant for microactuator application because most chemicals that meet the performance requirements are potentially lethal or government regulated. The propellant must be shock insensitive and friction insensitive as the actuator must be able to operate and survive in harsh environments. Since the main focus of this research is on electrical based actuation, the propellant must be sensitive to electrical ignition. Powder processing requirements must be minimal to achieve uniform and repeatable combustion rate from a propellant.

The performance characteristics such as combustion rate and specific impulse of the propellant play a significant role in determining the mechanical performance achievable by the microactuator. The combustion temperature and the reaction rate of the

propellant affect the performance of the actuator. The solid propellant must possess a low combustion temperature to speed up the combustion process and to minimize thermal crosstalk between adjacent microactuators when one or more actuators are fabricated on the same substrate. This minimization of crosstalk is essential to avoid inadvertent ignition of nearby devices and to achieve better control over jet production. Also, a lower combustion temperature allows for reaction controllability, which is necessary to ensure that the jet of released gases from the actuator is fired in the appropriate direction at the appropriate time. The reaction rate of the propellant affects the burn time of the propellant and the thrusts delivered thus, controlling the total impulse that can be delivered by the actuator.

Propellant performance is typically measured in terms of specific impulse and linear burn rate. Specific impulse is defined as the impulse delivered per unit weight of the propellant [23]. Solid propellants, when used in large scale thrusters are reported to achieve specific impulses of about 150 to 250 s [12, 24] and when used in small scale thrusters are reported to achieve specific impulses of 10 to 15 s. The linear burn rate of a propellant is defined as the regression rate of a combustion surface. Vieille and Piobert investigated combustion rate characteristics of propellants in the early 19th century [12] and reported that the propellant burn rate is proportional to the pressure at the combustion surface to some exponent according to:

$$r = aP^n \quad (1)$$

In this equation, ' r ' is the linear burn rate of solid propellant which is proportional to pressure at the combustion surface ' P ' to some exponent ' n ' and ' a ' is the constant of proportionality. Both ' a ' and ' n ' depend on a particular propellant chemistry.

Solid propellants are broadly classified into two categories: double base propellants and composite propellants. Double base propellants typically consist of a colloidal gel of two nitric esters: nitrocellulose and nitroglycerine. Composite propellants typically consist of a mixture of separate ingredients, some of which are oxygen rich and serve as oxidants, and others are oxygen deficient and serve as fuels.

2.1.1.1 Double Base Propellants

A double base propellant consists of a homogeneous mixture of oxidizer and fuel components chemically linked together in a single mixture. The first double base propellant was developed in the form of smokeless gun powder by Vieille in 1886 [12] and has widely been used in ammunition since then. Smokeless gunpowder is made from a mixture of nitroglycerine and nitrocellulose with a typical mixture ratio of 1.24 with optional additives such as 10% diethylphthalate (DEP) added for stability [24]. This mixture has a solid density of 1.55 g/cc and achieves a maximum specific impulse of 240 s at 10 MPa pressure with an adiabatic flame temperature of 2690°K. The pressure exponent, ' n ', reported for basic double base (DB) propellants is 0.62 across a range of mixtures, and the linear burn rates reported are approximately 0.7 mm/s at 2 atm, 2.2 mm/s at 10 atm and 9 mm/s at 100 atm [24]. Double base propellants offer repeatable performance because of the possibility of controlling oxidizer and fuel compositions precisely [12]. Also, the performance of this fuel mixture can easily be varied by varying the ratio of nitrocellulose (NC) and nitroglycerine (NG) or by adding any additives to the mixture.

Nevertheless, there are certain limitations associated with using double base propellants in microactuators. They typically require very high temperatures to react. For

example, smokeless gun powder reacts at above 2500°C. Because nitrocellulose is difficult to shape, often plasticizers such as tri-methylolethane trinitrate are added to the fuel mixture to be able to cast the propellant into a desired shape. They are often obtained commercially in a preset shape with specific composition or in the form of small pellets. Double base propellants are somewhat insensitive to hot wire ignition [25] and are difficult to detonate even when confined. Hence, often, a separate explosive charge is used along with the propellant to initiate the ignition process. Though, double base (DB) propellants are safe to handle with low risk of accidental misfires, there are certain health hazards associated with them. Exposure to a double base (DB) propellant may cause irritation of nose, mouth, lungs and skin or might result in a drop in blood pressure because of the presence of nitroglycerine.

2.1.1.2 Composite Propellants

A composite propellant consists of a heterogeneous mixture of oxidizer and fuel components generally held together in a matrix using a binder [12, 24, 26]. The oxidizer component provides the necessary oxygen that is required for sustaining combustion reaction and is often the most important ingredient of the fuel mixture that controls combustion rate and performance of the fuel. In most composite propellants, oxidizer accounts for about 50-90% of weight of the whole mixture. Depending on the components and fuel composition used in the propellant mixture, composite propellants offer a wide range of performance in terms of burn rates and specific impulse. Hence, the performance, safety and availability of these fuels can easily be altered to meet the specific requirements at hand. Most composite propellants though, are less hazardous to manufacture and to handle than double base propellants, they require significant amount

of powder processing and preparation before being used. However, on microscale this can be taken to our advantage, as this provides us with an option of processing the fuel in lab allowing for finer control of propellant properties which is paramount for our application [22].

A composite propellant is typically manufactured by mixing a crystalline oxidizer with a viscous binder. The binder and oxidizer components are mechanically mixed together, cast and molded into a combustion chamber using a crosslinking agent. The mechanical mixing offers good contact between oxidizer particles and binder. The crosslinking agent helps in hardening the mixture in a desired shape. The most common oxidizers include perchlorates, chlorates and nitrates such as ammonium perchlorate and potassium nitrate and their properties are reported in Table 1. During combustion, the oxidizer component decomposes producing volatile oxidizing species which then mix with fuel component in a gas phase. The binder component in the propellant mixture is generally an organic, hydrocarbon chain that sometimes acts as a fuel source for combustion. Some of the commonly used binders in composite propellants are HTPB, CTPB, PU, PVC and PBAN. Upon ignition of the propellant, the binder pyrolyzes forming volatile fuel fragments that mix with the oxidizing species in gas phase.

The burn rate of composite propellants can often be improved by adding additives to the mixture. Most common additives reported in literature are metal fuels such as aluminum and magnesium. These metal fuels help in increasing the combustion reaction rate of composite propellant by increasing the heat generated within the fuel. A typical example of a composite propellant is a mixture of ammonium perchlorate and HTPB in a weight ratio of 86:14 [24]. For large scale combustion systems, this mixture has a specific

impulse of 250 s with an adiabatic flame temperature of 2890°K. Performance of this mixture can further be increased by altering fuel composition, by adding additive components or by changing the particle size in the mixture. Among different solid propellants, as composite propellants are more suitable for our microactuator application, we look at several common composite propellant ingredients in detail in the following section.

The choice of a composite propellant ingredient for our research is highly dictated by the performance goals required from the propellant and the ease of availability of all the individual ingredients of the propellant. As composite propellants mainly require processibility on lab scale, all the ingredients should be readily available to be purchased in bulk quantities. Hence, the choice of right propellant, development of suitable processing techniques that could be workable with small quantities of fuel mixing and understanding how the propellant chemistries would affect performance enables for obtaining accurate and maximum performance from the solid propellant.

As composite propellants may often contain as much as 90% oxidizer, the characteristics of oxidant can therefore have a considerable influence on propellant properties [27]. Oxidizers that are used in this research include potassium chlorate, potassium perchlorate and ammonium perchlorate. The properties of these oxidizers are studied to understand the feasibility of using these fuels for microactuator application. For obtaining maximum performance from the microactuator, both uses and limitations of these propellants need to be considered. The safety of using these chemicals is surveyed and reported in Table 2.

Table 1: Properties of solid propellant components [28, 29, 30]

Ingredient	Oxygen Balance %	ΔH_f [kJ/mol]	T_u [°K]	P [g/cc]
Oxidizer				
KClO ₃	40	-391	688	2.32
KClO ₄	46	-430	883	2.52
NH ₄ ClO ₄	34	-295	513	1.95
Binder				
GAP	-132	0.957	553	1.30
Nitrocellulose	-28.7	-2.61		1.67

Table 2: Survey of health and detonation risks of solid propellant formulations

Propellant Ingredient	MSDS Health	Lethal Dose	Detonation
GAP	3	N/A	Confined
KClO ₃	3	1870 mg/kg	Unconfined
KClO ₄	2	N/A	Confined
NH ₄ ClO ₄	2	N/A	Confined

Potassium Chlorate: Potassium chlorate is commonly used in pyrotechnic formulations such as safety matches, primers and flashes [27, 31]. Potassium chlorate combustions are often characterized by rapid burn rates, low ignition temperature and low temperature combustion propagation [27]. Potassium chlorate is obtained as a white powder with a density of 2.32 g/cc. It has a decomposition temperature of 673°K with a heat of formation of -91 kJ/mol and a heat of decomposition of 50.7 kJ/mol [28]. Upon decomposition, KClO₃ releases oxygen and potassium chloride according to the equation [27]:

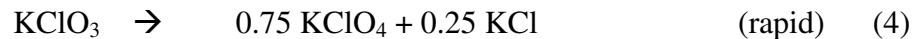


Potassium chlorate (KClO_3) is well suited for our application from a performance point of view. The rapid decomposition of KClO_3 is a benefit to be used in applications that require short impulse durations. Potassium chlorate is promising for the application of microactuators because it can be mixed into formulations that are sensitive to electrical ignition, react at low temperatures and burn very rapidly. This is useful for applications requiring faster force rise times that may be unattainable with other propellants or for use as a primary explosive with propellants that are difficult to ignite. Also, because of its low reaction temperature, it can easily be ignited with a low energy ignition source which is one of the prime factors while designing our actuators. This would require less input energy needed from the electrical circuit, thus helping in reducing the overall physical size of the circuit.

However, potassium chlorate is less safe to work with than other oxidizers because of its high thermal and mechanical sensitivity. It is often prone to accidental detonation due to shock, impact, friction and heat [27, 32]. This sensitivity increases further in presence of fuel components such as sulfur or sulfides. Specifically, potassium chlorate-sulfur chemistries and potassium chlorate-sulfide chemistries react at approximately 480°K. This property is useful for micro scale applications with large surface area to volume ratios because increased heat loss to the combustion chamber walls will reduce the temperature at the combustion surface. For comparison of the low-temperature combustion performance, the temperature required to sustain propagation, T_{sit} , of a stoichiometric KClO_3 : sulfur mixture is approximately 480°K, whereas the T_{sit} of black-powder is 1008°K according to Henkin-McGill ignition data [33].

With respect to safety, potassium chlorate is toxic when ingested, with a toxicity of rat oral 1870 mg/kg. It is a strong irritant to eyes, lungs, nose and skin possibly causing chemical burns. Precautions must be taken to mitigate the risks of personal injury in order to take advantage of the benefits of potassium chlorate. Appropriate ventilation and personal protection are required while handling potassium chlorate [32]. The safety of using potassium chlorate as an oxidizer is a liability for microactuator application. However, its sensitivity may be reduced by coating the propellant particles with viscous binders.

Potassium Perchlorate: Potassium perchlorate is a much safer oxidizer than potassium chlorate and is widely used in applications of solid propellant rockets [12] and as a primary initiator [26]. It is an extremely versatile oxidizer that can easily be modified to achieve a broader range of burn rates. Potassium perchlorate is a white powder that can be obtained in several particle size ranges as small as 100s of microns. It is hygroscopic in nature with a density of 2.53 g/cc and contains about 46% oxygen by weight. The heat of formation of KClO_4 is -430.1 kJ/mol and the decomposition temperature is 853°K. Upon decomposition, KClO_4 releases oxygen according to the following equations [34]:



Potassium perchlorate produces a dense smoke when combusted as the product, KCl, condenses. The KCl products of combustion are heavy, reducing the impulse of propellants that use potassium perchlorate. The increased decomposition temperature of potassium perchlorate compared to potassium chlorate [34], suggests that more ignition

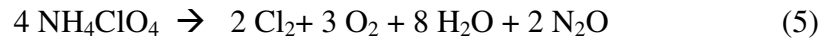
energy will be required to ignite potassium perchlorate formulations, but the increased oxygen content of potassium perchlorate will require less oxidizer, leaving room for more fuel in mixtures that use this oxidizer.

Many applications for KClO_4 are reported in the literature ranging from rocket propellants [12], airbag formulations, squibs [27], and electric matches [26]. A wide range of burn rates are reported for perchlorate based mixtures with specific impulse ranging between 165 and 210 s [34] demonstrating that these propellants could be tailored to decompose in a timely manner. The performance of perchlorate based propellants can further be improved by adding dopants and fuel components. It has been demonstrated in [34], that KClO_4 mixtures can be ignited using hot-wire ignition to obtain rapid burn rates by dissolving potassium perchlorate in aqueous solution along with cyano-metal complex fuels such as potassium ferricyanide or potassium cobaltocyanide [34, 35]. Other mixtures of potassium perchlorate have been demonstrated to be safe in everyday operation such as in automobile airbags where it is used along with sodium azide for rapid gas generation.

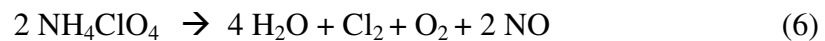
As potassium perchlorate is hygroscopic in nature, i.e., it attracts moisture, controlled powder processing required for use of potassium perchlorate increases the difficulty with producing reliable performance. Processing of perchlorate based fuels require additional steps such as grinding, sorting and drying to control the particle size and moisture content in the fuel. However, the advantages of using potassium perchlorate in a composite propellant includes safety to the user, availability of the material, demonstrated sensitivity to electrical ignition, high burn rates, and specific impulse of

optimized mixtures. Potassium perchlorate is reported as a skin, eye and lung irritant and hence, requires proper ventilation and personal protection during its handling [36].

Ammonium Perchlorate: Ammonium perchlorate (NH_4ClO_4) is one of the most widely used oxidizers in solid composite propellants. One main application of ammonium perchlorate is in solid rocket propellant formulations. Ammonium perchlorate is obtained as a white crystalline powder that is stable at room temperature. It has a density of 1.95 g/cc and contains 54.5% by weight of oxygen. The heat of formation of NH_4ClO_4 is -295 kJ/mol. The thermal decomposition of ammonium perchlorate is more complex and has been reported by Dode and by Birchumshaw and Newman [37]. The decomposition of ammonium perchlorate starts in the neighborhood of 200°C and is still slow enough to measure at 490°C. At temperatures below 300°C the major products of decomposition are indicated by the equation [38]:



At temperatures above 350°C, the following equation is more representative of the products:



Compared to potassium perchlorate, ammonium perchlorate reacts slower, reacts at a lower combustion temperature and requires significant shock to detonate making it much safer to handle than any of the previously discussed oxidizers. Though ammonium perchlorate offers the benefit of increased safety, its slow burn rate and high sensitivity to impurities makes it difficult to be used for applications requiring precise time control from the fuel mixture. Typical specific impulse of ammonium perchlorate based fuels

range from 175 to 250 s [12]. Because of its hygroscopic nature, it requires additional processing techniques like grinding, sorting and drying in order to control particle size and moisture content within the fuel.

On a small scale, ammonium perchlorate is mixed with binders such as hydroxyl-terminated poly-butadiene (HTPB) to achieve higher impulse and burn rates. HTPB not only acts as a fuel component but it also acts as a binder. Alternatively, ammonium perchlorate is mixed with glycidyl azide polymer (GAP), which is an energetic polymer to achieve higher specific impulse. Additional metal fuels such as aluminum, increases the specific impulse of the fuel mixture and additives such as ferric oxide or titanium dioxide are used to finely control the burn rate of these solid propellants. The wide use of ammonium perchlorate in large scale solid rocket motor industry demonstrates that it is safe to process on large scales, exhibits reliable performance when properly processed and can be used in formulations where maximum impulse is desired from a solid propellant.

Ammonium perchlorate based fuels offer more safety and availability when compared to other mentioned oxidizers. It has also been demonstrated as being sensitive to electrical ignition on small scales. No toxicology data is reported for ammonium perchlorate, but it is listed as a skin, eye, and lung irritant, requiring proper ventilation and personal protection during its handling [39].

Glycidyl Azide Polymer: One azide of interest for small scale gas generation applications is glycidyl azide polymer (GAP). GAP is a homogeneous polymer propellant that requires no propellant processing and could single handedly function as an oxidizer

or a fuel component. GAP ($\text{C}_3\text{H}_5\text{ON}_3$) is a liquid at room temperature, in a prepolymer form. It is polymerized to form a copolymer by reacting the terminal -OH groups with hexamethylene diisocyanate and crosslinked with tri-methylolpropane [24]. Because it is a liquid that can be hardened with the addition of a curing agent, it could readily be dispensed into combustion chambers, eliminating the need for presses and molds to form solid propellant grains. Cross-linked GAP has an adiabatic flame temperature of 1370°K at 5 MPa. The linear burn rate of GAP is 10 mm/s at 5 MPa with a reported specific impulse of 150 s [24]. It has a pressure exponent of 0.44. With respect to safety, GAP is reported to be a skin, eye and lung irritant but no lethal doses are reported [40]. GAP is a mass fire hazard when unconfined and an explosive hazard when confined or when shocked [40]. It is generally available from specialty chemical suppliers in diluted form with 60% solvent by weight.

2.1.2 Powder Processing

Composite propellant offers a good choice for obtaining wide range of performance characteristics from a propellant fuel. It can easily be processed to obtain good performance by altering the composition of each ingredient in the propellant and by using proper processing techniques. Processing of the propellant is the most important step that is required in order to achieve consistent burn rates, consistent particle sizes and consistent specific impulse from the propellant [41]. Raw material processing proves to be an important factor in not only achieving high burn rates and impulse from the propellant, but also in maintaining the consistency between batches of mixed propellant formulations. In this section, we try to survey the standard practices that are followed in industry while producing solid composite propellants. These practices help in achieving

uniform fuel compositions which result in obtaining consistent performance from the propellant.

The different unit operations used for processing industrial based solid propellant are shown in the flow chart mentioned in Figure 2 [34, 22]. These unit operations help in creating a void free propellant mixture and control the amount of moisture absorption in dry powders. The common unit operations involved in powder processing include grinding, classifying, drying, mixing, casting, curing and finishing. Following are the steps used in industrial preparation of solid propellants:

1. Grind individual ingredients separately.
2. Sort all the ingredients by size.
3. Dry all the separated ingredients.
4. Mix ingredients using a viscous binder.
5. Cast uncured propellant into combustion chambers.
6. Cure the propellant in the chamber.

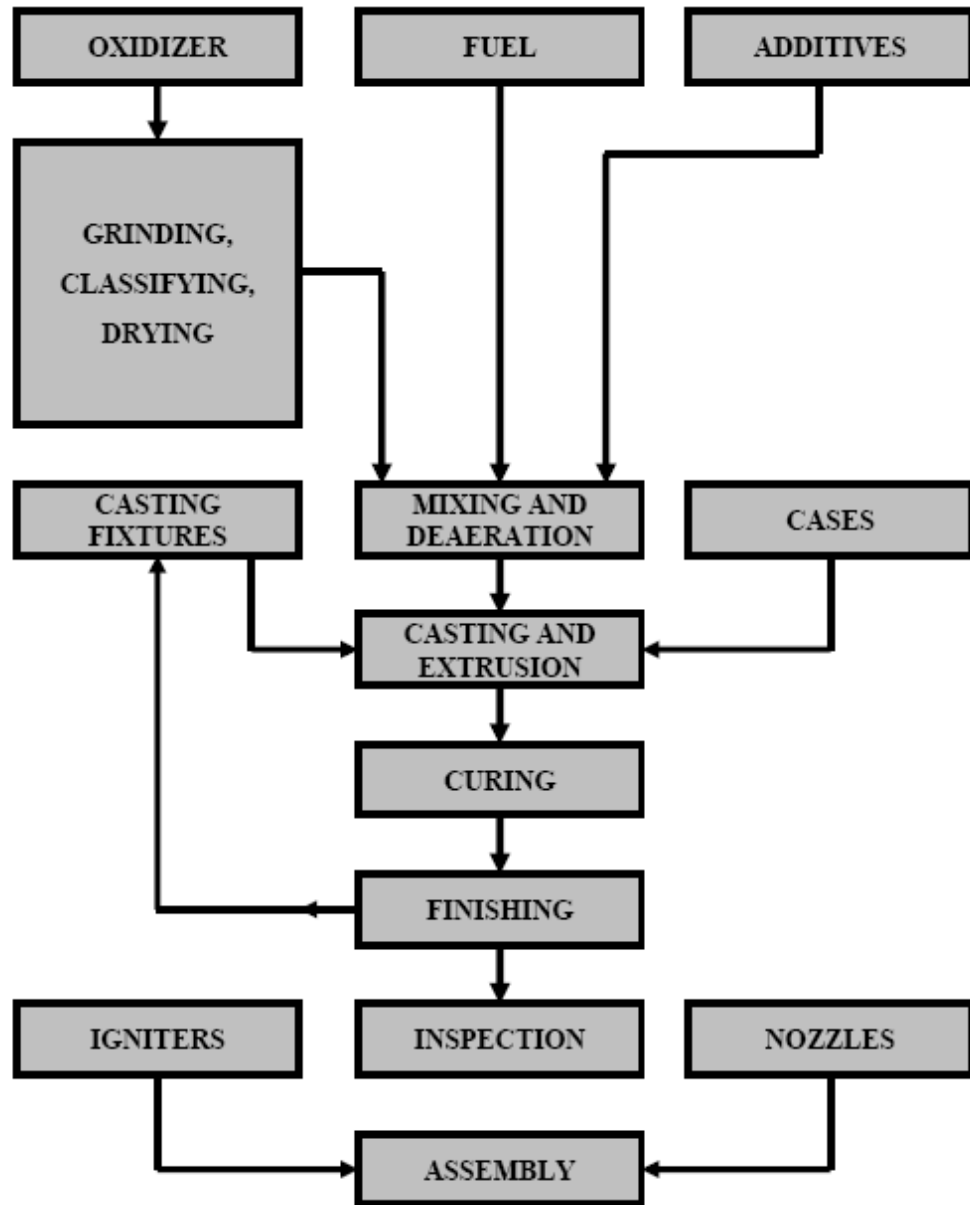


Figure 2: Industrial solid propellant processing flow chart [34, 22]

It is reported in [41] that the particle size strongly affects the burn rate of the propellant. Also, variations in propellant particle size affect the loading density of the propellant. Hence, the first two steps of processing i.e., grinding and sorting play a prime role in powder processing. They enable repeatable performance of the fuel by ensuring that the powder particle size is consistent. Grinding increases the active area of propellant grain which helps in increasing the burn rate of propellant. The reduced particle size also increases the low-pressure burn rate of solid propellant [41].

Equipments such as micro pulverizer and ball mills are generally used for grinding [27]. A micro pulverizer is an impact mill suitable for size reduction of a wide range of solids. It consists of a high speed rotor revolving inside a grinding chamber with hammers pivoted into a series of rotor disks. The particles of feed entering the grinding zone are sucked into the chamber and are subjected to a grinding force due to the high speed hammers. Based on the speed of rotation, the type of hammers and screens employed, different grades of fineness could be achieved. The rate of feed also plays an important role in determining the final mesh size of the powder. Ball mills are also used for grinding purposes, but it is considered more time consuming and dangerous than pulverizers.

After grinding and sorting, the next step in powder processing is drying of sorted ingredients. As most of the components used in composite propellants are hygroscopic in nature, they absorb moisture at room temperature. This moisture has a drastic effect on the performance of the propellant because then, more combustion energy is wasted in heating up inert materials. The standard procedure for processing inorganic oxidizers is to grind and dry no more than two days before use and then dry again [27].

The next step in propellant processing is mixing of the dried ingredients. The goal of mixing is to produce a uniform and void free solid dispersion of solid particles in a binder. Presence of voids and instabilities in mixing ratios of propellants ultimately result in instabilities in combustion. Often, a de-aeration step is performed to minimize the voids in the mixture. A screw conveyor is generally used for mixing purposes.

The filling and casting processes are used to set the propellant into its final, usable form [41]. As all the ingredients are held together during this operation, extreme care must be taken to avoid accidental misfires. Any small mechanical force such as static, friction or shock might lead to accidental ignition of the mixed propellant. Industrial standard for casting is to press the propellant and let it granulate in a desired shape.

2.1.3 Propellant Ignition Sources

Ignition of solid propellants is a series of complex processes. The production of ignition energy from an ignition source, the transfer of energy to the propellant grain, decomposition of propellant to yield gaseous intermediates and finally, exothermic reaction of these intermediates to provide feedback of energy to the propellant surface are all involved. The concept of ignition and the design of a good ignition source that can supply the required ignition energy play a significant role in the overall fabrication of the actuators [22].

In this section, we discuss the different electrical based ignition mechanisms that are currently used in the ignition of solid propellants and which could be applied for micro scale fuel ignition. Then, we propose a new electrical based ignition concept that is used in this research work. Electrical based ignition adds energy electrically to the propellant. The most common electrical based ignition of solid propellant is by resistive

ignition of fuel. An electrically conductive material such as an igniter or a bridge wire is placed in contact with the propellant. When an external electrical energy is supplied to the igniter, the temperature of the igniter element increases and heats the propellant grains in contact with it [22]. Once the decomposition temperature of the fuel is reached, it combusts. The material used for fabricating the igniter and the physical dimensions of the igniter play a significant role in this type of ignition.

The second type of electrical based ignition is electro-thermal ignition. An electro-thermal arc jet system consists of an anode and a cathode between which the propellant is placed [38]. When sufficient electrical energy is supplied to the system, an electric arc is passed through the propellant. The propellant gas is energized and is allowed to expand through an aerodynamic nozzle and generate thrust. However, this ignition concept is highly limited by the size of the system as the electrical energy required would strongly depend on the distance between the electrodes. For large scale systems, the voltage required for ignition would be several 1000s of volts which makes this highly impractical on these size scales. However, at small scales, this concept could be practical. The very high temperatures in the arc chamber plus electrode erosion are concerns that need to be addressed with this type of ignition.

Another type of electro-thermal device is a “resisto jet” which operates by passing a gas through a resistively heated coil. Electrostatic ignition is another type of ignition which uses a heated cathode filament to generate a copious supply of electrons. A voltage is applied between the engine chamber walls (the anode) and the cathode. A propellant vapor such as mercury or cesium is introduced into the chamber, whereupon the gas molecules are bombarded by the electrons which are trying to reach the walls. The ions

produced by the bombardment of atoms by electrons, are then extracted from the plasma by an electric field set up between a set of parallel electrodes downstream from the gas. Electrons are then added to the accelerated beam to keep the gas electrically neutral [38].

In our research, we propose a new concept of electro-thermal ignition where electrical current is directly passed through an energetic propellant by making the propellant itself conductive. This is achieved by adding conductive dopants to the propellant [42, 13, 14]. The conductive propellant is then placed between two electrodes and a direct current is supplied to the propellant. When sufficient electrical energy is supplied to the conductive fuel, the temperature of the fuel increases until the fuel reaches its decomposition temperature. The heat dissipated by the resistance of the fuel itself causes ignition and the released gases are then expanded through a nozzle to generate thrust. With this concept, as the entire fuel residing between the electrodes is conductive, heat transfer from one propellant grain to another is almost instantaneous, thus making the ignition process of the fuel rapid. However, with this concept, propellant ignition becomes strongly dependant on the resistance of the fuel and the energy supplied from the electrical energy source [42].

2.1.4 Solid Propellant Microactuators

The previous sections covered the types of propellants and types of ignition mechanisms that are compatible for developing chemical based microactuators. With the advances in MEMS based fabrication techniques, several solid propellant based microactuators are developed and reported in the literature [20, 21, 22, 42, 43, 44]. These microactuators are developed for specific applications such as attitude control of small scale spacecrafts and as one time flight, millimeter scale rockets in order to maximize

thrust capabilities.

This section looks in detail at some of the solid propellant based microactuators reported in the literature, their basic concept of ignition, fabrication techniques used, the obtained performance and the specific applications for which they are developed. Some of the microactuators that are investigated in detail in this literature review are the solid propellant microactuators developed by a group in Caltech [20] for kilogram-scale satellite station keeping applications, microthrusters developed under the name of Micropyros at LAAS CNRS in Toulouse [21] and finally, Gas generating actuators developed in our group (MSMA) for projectile steering applications [22].

All the microactuators mentioned in the literature have a common basic configuration, i.e., they are generally made as a three-layer configuration: a micro machined combustion chamber in which the solid propellant is stored, an ignition means such as a hot wire or an igniter and a nozzle attached to the chamber. Ignition occurs when sufficient electrical energy is supplied to the propellant using an igniter by means of resistive heating. The solid propellant combusts and the gases released during combustion then travel through the length of the nozzle to deliver desired thrusts and impulse. These microactuators form the basis for our research work as they validate the feasibility of using solid propellants to generate forces on microscale. Both advantages and limitations of these microactuators are discussed in this section and the need for a new ignition concept is mentioned.

2.1.4.1 Digital Micropropulsion

Digital micropropulsion actuators [20, 45] are developed in a collaboration between the California Institute of Technology, TRW space and technology group, and

Aerospace Corporation. These actuators are developed for applications of micro spacecraft such as high accuracy station keeping and attitude control of small satellites. This research work focused at developing propulsion systems that deliver extremely small and accurate impulse bits, on the order of 10^{-4} to 10^{-6} N-s.

These actuators are made using MEMS technologies as a three-layer sandwich configuration consisting of a top silicon wafer containing burstable diaphragms, a middle glass layer containing propellant chambers, and a bottom silicon wafer containing initiators. The chamber is filled with a combustible propellant that can be ignited to form high pressure, high temperature fluid. Once the pressure inside the chamber exceeds the burst pressure of the diaphragm, the diaphragm ruptures, and an impulse is delivered as a fluidic jet is expelled from the plenum. The top layer consisting of an array of thin square diaphragms is patterned using a <100> silicon wafer which is anisotropically etched using KOH solution to a certain thickness followed by the deposition of 0.5 μm thick silicon nitride. The middle layer consists of an array of through-holes in 1.5 mm thick glass with varying diameter holes. The bottom layer contains a matching array of poly silicon micro-resistors fabricated on top of a 3 μm SiO_2 insulating layer. The fabrication assembly process starts by bonding the bottom two layers using cyano-acrylate, then the chambers are filled with lead styphnate propellant and the top layer is then bonded again using cyano-acrylate to complete the process. As the bottom layer of these actuators is fabricated using standard CMOS processes, control electronics are incorporated into this layer. Using this fabrication process, a completed chip with an array of microactuators is demonstrated.

The performance of these actuators is measured in terms of impulse, time of

propulsion and average forces delivered. The test stand used for this purpose consists of a pendulum stand, a laser interferometer to measure the displacement history of the ballistic pendulum, an eddy current damper to rapidly restore the pendulum to quiescence after each test, and a wireless infra-red data link to communicate with the thrust-initiation electronics. A high speed camera records the combustion event at 40,500 frames per second and a video records the combustion time of the event. When the resistance of the polysilicon igniter is $210\ \Omega$ and when a voltage of 100 V is applied for 50 μs , the lead styphnate propellant occupying a volume of $0.29\ \text{mm}^3$ delivered 10^{-4} Ns of impulse and 100 watts of power. The duration of the thrust is measured to be 1 ms. However, by performing some thermo-chemistry calculations, they observed that not all the propellant was consumed during combustion, and in fact, only 10% of the propellant residing in the chamber was used to produce thrust.

These actuators successfully demonstrate the use of solid propellant microactuators for generating chemical jets that deliver impulse with millisecond duration times. However, several issues need to be addressed before these actuators could be used for the projectile maneuvering application mentioned in Section 5.1.6. First of all, the combustion durations of these actuators are well over the 0.4 ms control time allotted to control a projectile spinning at 600 Hz. In the time scales mentioned, the ignition delay times are not accounted for and these times must be addressed with the ignition electronics. The impulse delivered by these actuators is much smaller than required, but this can easily be addressed by increasing the volume of the propellant used. The microactuators mentioned in this research are made out of silicon. Though the fabrication techniques used allow for easy integration with electronics, silicon is brittle

and highly susceptible to fracture under high loads. It might not survive under the high-g launch that is common during projectile maneuvering, as discussed in Section 5.1.6. For the application of a high-g load launch of a projectile, more robust materials and solid propellants that could withstand high shock are needed.

2.1.4.2 Micropyros

The solid propellant microactuators developed under the name “Micropyros” by the group LAAS-CNRS in collaboration with CNES offered highly accurate impulses for space applications such as station keeping, orbital control and other mechanical operations like panel deployment and spacecraft separation [21]. This group published many papers in this area and is one of the major contributors for the developments taking place in the solid propellant microspacecraft area. They developed a design concept, several fabrication techniques for making the microactuators and tested the actuators for their performance. They also developed modeling techniques to predict the behavior of the actuators and to optimize the devices to satisfy specific application needs. This literature offers a complete study for the microactuator design and presents a predictive model for unsteady state gas flow inside the microthruster and subsonic flow of released jet through a nozzle.

Literature on micropyros is first presented in 1998 [46, 47] and future work is updated in [16, 49, 50]. Like digital micropropulsion actuators, MEMS-based fabrication techniques are used for fabricating micropyros. They have the same concept of ignition as digital actuators, where a polysilicon igniter is used as a resistive heating element to ignite fuel. The microthrusters are made as a configuration of three parts: the first part consists of an array of silicon micromachined igniters where a polysilicon resistor is

deposited onto a very thin dielectric membrane. This igniter section consists of patterned heaters and also functions as exhaust holes for combustion gases. Igniters are fabricated by depositing polysilicon using LPCVD on a (100) silicon wafer, and patterned using RIE plasma. The electrical pads and supply lines are patterned in gold using a liftoff technique followed by anisotropic etching of silicon. The second part consists of an array of propulsion tanks that are fabricated in materials like quartz, ceramic, alumina or a thick silicon substrate. The use of ceramic or quartz is advantageous when compared to silicon because they allow for minimization of thermal losses through the walls because of their relatively low thermal conductivity. The third layer consists of an array of nozzles added on top of the structure. Glycidyl azide polymer (GAP) is used as the choice of propellant in these actuators. In their early devices, GAP mixture is procured as a thick film before deposition. However, in their advanced research, more efficient propellant handling and filling processes are developed. The viscous propellant is injected into the chamber using vacuum injection to obtain cavity-free propellant. A masking layer on top of the substrate is used to control the areas affected by the propellant flow. Once the chambers are filled with propellant, it is allowed to cure at temperatures that make the propellant solid. Once the propellant is cured, epoxy is used to seal the bases of the combustion chambers. One significant difference between the digital propulsion actuators and micropropulsors is the diverging nozzles used in the latter to exhaust the combustion products. Also, the igniter position is altered to study its effect on ignition. So, these actuators have more control variables in terms of device parameters than the digital propulsion devices. Efforts are also made in this research work to use ammonium perchlorate (AP) based composite solid propellants that are more insensitive to shock.

The initial results of testing showed the electrical parameters required for ignition, times associated with ignition, temperature profile and energy requirements of the microactuator. When a polysilicon igniter is used, power inputs of 52 mW are measured for a 290°C igniter [47]. This showed a major improvement with respect to input power when compared to the input power required by digital micropropulsion actuators. For polysilicon igniters with dimensions of 2 mm x 0.1 mm, ignition occurred when an input power of 0.5 to 7.5 mW/m², which corresponds to 0.1 to 1.5 W, is supplied. This variation is because of the location of the igniter and how well the igniter is placed in contact with the propellant. They have also studied the effect of conduction and convection losses when the initiator comes in contact with a dielectric membrane, air and with fuel. The heat losses from the microheater are accounted at 75% at 400°C when it comes in contact with air. When air is replaced with GAP fuel mixture and the igniter is completely submerged in the fuel, the heat transfer from the igniter is limited to the fuel and any losses in input energy are minimized as all the input energy is used to heat the propellant. The delay times associated with ignition are measured to be dependent on the input power. For example, for the same igniter properties, an ignition delay of about 1 s is observed when the input power is 100 mW and is reduced to 11 ms when the input power is increased to 1.5 W. Though these ignition delays are much larger than the ones proposed by digital micropropulsion devices, they would be allowable for our application as long as they can be addressed and programmed using the control electronics and the jitter associated with the delay times from device to device is less than the 0.4 ms actuation time that is required for controlling the maneuvering of a 25 mm projectile. The effect of varying the igniter area on the ignition process is also studied. As the ratio of

igniter to substrate area is increased, the steady state temperature decreased for a constant input power. This decrease is explained by increased convection effects from larger area igniters. These experiments highlighted the tradeoffs necessary with respect to the igniter design.

The effect of chamber geometry, nozzle geometry and solid propellant composition is studied using a transient heat transfer model [48, 49]. Initial studies computed the time and one-dimensional spatial evolution of gas flow through a nozzle [48]. The flow of gases is simulated in three separate regions: chamber, throat and nozzle and as two time periods: steady and unsteady. Several valid assumptions are made during modeling. Combustion products are assumed to be single phase, ideal gases with uniform temperature, pressure and density. Chamber walls are assumed to be adiabatic so that the heat losses from the system are minimal. Finally, the flow of gases through the nozzle is assumed to be subsonic and inviscid. The unsteady state time period increased with an increase in the diverging length of the nozzle. The unsteady state chamber pressures and mass flow through the nozzle values are twice that of steady state values. It is observed that chamber to throat area ratios in excess of 10 produced supersonic exhaust velocities in the diverging section of the nozzle and with an increase in chamber to throat area ratios the thrusts delivered increases. The expansion behavior of released gases is studied for GAP propellants for various divergence angles and lengths of the nozzle. Using these simulations, steady state thrusts delivered are measured to be between 5 mN and 75 mN.

The next modeling done [49] is focused at developing a simple and predictive compact model that could be adapted to several microthruster conditions. This is based on a one-dimensional, lumped parameter approach that adapted similar assumptions as

the previous model, except this model allowed for isentropic and supersonic nozzle flow of released gases and accounted for heat losses from the chamber walls. The model studies the unsteady state behavior of pressure, temperature, gas density, exhaust velocity and mass flow and predicts the effect of heat losses, thrusts generated and impulse delivered from these devices. In the absence of any heat losses from the combustion chamber, the adiabatic combustion temperature is calculated to be 2000°K at 0.15 s, chamber pressure remained constant at 5 bar and a thrust of 3 mN is delivered. In the presence of heat losses, the adiabatic combustion temperature is slightly less than 2000°K at 0.15 s which eventually dropped to about 1650°K . The chamber pressure also decreased by about 7% and the thrust delivered is measured to be 2.6 mN. The optimum impulse is measured to be 1.39 mNs at a nozzle exit to throat area ratio of 1.3. Then, efforts are made to study the effect of nozzle length on performance and it is reported that the nozzle diverging length is not significant at these microcombustor scales when the released jet is exhausted into atmosphere. The model is then applied to the microcombustor geometry developed by Rossi et al., [12] and the predicted performance values are obtained. For a chamber to throat area of 60, the chamber pressure reached 5 bar and thrust of 4.8 mN is delivered in a time scale of 180 ms and remained constant for 250 ms. Impulse delivered at these ratios is measured to be 1.2 mNs. When the chamber to throat area is reduced to 16, the chamber pressures reached 1.6 bars in 200 ms. The thrust achieved is 1.7 mN at 200 ms and remained constant for 350 ms. The steady state portion of combustion delivered an impulse of 0.6 mNs. Next, efforts are made to experimentally measure the performance of the devices and validate the results obtained from the previous predictive model. A thrust stand is put together for measuring the

thrusts delivered in 0.3 to 30 mN range [50]. A thruster chamber with 4 mm in diameter is filled with propellant and the thrust delivered is measured to be 0.5 mN for 7 s [48].

The micropyros discussed so far demonstrated that solid propellant microactuators can successfully be fabricated to operate at much lower power inputs and may be feasible to be used for projectile maneuvering applications. However, the delay times associated with ignition by means of an igniter still needs to be addressed. These actuators also demonstrated the use of less sensitive composite solid propellants that withstand shock detonation than lead styphnate used by digital micropropulsion devices and this proves to be valuable information while choosing the propellant for our high-g-launch applications. However, like digital micropropulsion actuators these thrusters use silicon based materials and fabrication techniques for device manufacturing. This does not lend itself to high-g load environments such as munitions launch and needs to be addressed in our research.

2.1.4.3 Gas Generation Actuators

The above mentioned actuators formed the basis for the research performed in our group, Micro Sensors and Micro Actuators (MSMA) at Georgia Tech. Previous work of our group focused on developing solid propellant microactuators for the specific applications of gas generation and projectile maneuvering [13, 14, 19, 22, 42]. For this work, the research done by above mentioned groups proved as a stepping stone in designing the research goals and further attempts are made to address several of the issues mentioned in the last two sections. English [22] worked towards developing gas generation microactuators using fabrication techniques other than conventional MEMS fabrication techniques and materials that are more thermally and mechanically stable than

silicon. The preliminary research done in this direction is presented in [19] where large arrays of high power, short duration microactuators are realized and implemented for the flight control and course correction of a 40 mm diameter gun-launched projectile.

Gas generation actuators are conceptually similar to previously mentioned micropyros in that solid fuel is ignited using a resistive heating element as an ignition source, combusted within a combustion chamber and the released gases are then exhausted through a nozzle. However, unlike the previously developed microactuators, GGAs are designed to operate in atmospheric conditions and can take advantage of flow-control techniques in which the generated gas can interact with embedded flow surrounding the moving projectile to produce larger forces [22]. The GGAs are tested on a gun launched projectile platform with a spin rate of 60 Hz. Robust materials and new fabrication techniques are used in the fabrication of GGAs. Design of the igniters is optimized so as to create a larger combustion front, thereby generating larger forces in shorter times. This research work focused towards developing combustors with simpler fabrication techniques, using robust materials that can withstand 10g-launching loads, ability to fabricate an array of single shot disposable actuators that operate at low input ignition power and that generate rapid rise and fall force times with less than 4 ms total burn time. They demonstrated the fabrication of an array of 16 combustors aligned radially in a 30 mm inner diameter disk using laser micromachining and laser fabrication techniques each with a volume of 3.3 mm^3 . Testing has shown that a combustor chamber with a volume of 3.3 mm^3 filled with polymeric GAP fuel produced impulses of $1 \pm 0.22 \text{ N-ms}$ and a peak force of 250 mN. The ignition delay times are measured to be $4.3 \pm 0.3 \text{ ms}$ and the combustion duration is measured to be $3.7 \pm 1 \text{ ms}$. Even though the

impulse delivered from these devices is much less than the required impulse for steering a smaller projectile, in further testing, it is shown that the impulse can easily be amplified by increasing the chamber volume and changing the propellant [22]. The ignition delay times are successfully accounted for with the control electronics so that the only times associated with the actuators are the combustion times and duration of the jets. A portable electrical setup is successfully demonstrated so as to deliver 250 mJ required for ignition. These actuators are reported to successfully meet the requirements for a 50 mm projectile in terms of the impulse delivered, thrusts generated and the duration of the jets. Even though there is a large improvement with respect to decreasing the burn times when compared to the microactuators discussed in the previous sections, the times obtained are not yet sufficient to be used for the application of spinning a smaller projectile at 600 Hz.

The work reported in this thesis is an extension to the GGA work performed in our lab previously. All the above mentioned microactuators helped us in identifying the probable limitations or issues that we might face while developing chemical based microactuators and utilizing them for a specific application. Hence, efforts are made to improvise on the solid propellant microactuators so that they can successfully be used for spinning a smaller projectile at 600 Hz. As mentioned in Section 5.1.6, for this case, the overall burn times need to be less than 0.4 ms and to achieve these time scales, a new ignition concept of instantaneous fuel ignition is proposed. The same fabrication techniques mentioned in GGA fabrication are utilized in this work for fabricating conductive fuel microactuators. The same basic fuel ingredients used in GGAs are used in this research, but the fuel ingredients and compositions are modified to meet the requirements at hand.

2.2 Physical based Microactuators

In this work, we present a microjet-based approach to skin ablation that generates micron-scale holes localized to the stratum corneum to increase skin permeability to drug molecules by some order of magnitude. This approach involves using thermal and mechanical ablation concepts individually and as a combination to achieve superior results. By using thermo-mechanical microjets that are generated from the microactuator, we are able to contact the skin for just microseconds and in that way, effectively localize effects to the stratum corneum [51]. This thermo-mechanical ablation method is carried out by accelerating a microfluidic jet of vapor, and possibly liquid, from an array of microchambers with nozzles. These microactuators utilize the concept of electro-thermal ignition for micro-jet generation. An electro-thermal arc jet system consists of an anode and a cathode between which the propellant is placed. A microjet of the propellant is ejected when an arc is driven electrically across the propellant positioned between the two electrodes within the chamber. Formulations are water based and use FDA approved excipients. The microactuator device is characterized in terms of duration and thrusts delivered by the jet for various propellants.

Thermo-mechanical based ablation focuses on exposing skin's surface directly to the released jet. Hence, both temperature and velocity of the jet contributes towards creating micro-pores in skin. Thermal based ablation focuses on exposing skin surface to the jet indirectly using a masking system that helps in isolating the thermal and mechanical effects of the jet. The mask allows for using only the temperature of the jet for treating skin. For both concepts, the achieved permeability of skin is measured and compared to a control. The treated skin surface is studied using skin histology

experiments.

2.2.1 Transdermal Drug Delivery

From the beginning of drug delivery research, constant efforts are being made to find ways to enhance drug absorption into the body to improve efficiency of treatment and to reduce the toxicities associated with therapy. Common sites of drug administration include the eye, skin, nasal cavity, mouth, intestines and other parenteral routes such as intravenous, intramuscular, intraperitoneal and subcutaneous [52]. Each site or route of application presents biological barriers to the delivery of drugs. These barriers function in a physical, chemical, biological or combinatorial fashion [52, 53] depending on the specific mode and site of application of a given drug delivery system. In general, biological barriers are site specific and depend on the histological organization of the specific site.

Among the different biological barriers, the potential of using skin as a drug delivery path has attracted significant interest in the recent years. Even though skin is viewed as an impermeable barrier that offers protection against the entry of foreign agents into the body, intact skin can be used as a port for topical or continuous and systematic drug delivery. For topical drug delivery, skin is the prime target site for medication and for systematic drug delivery, skin is just used as a route of administration for delivery of drug via transdermal patches. The main advantage of using transdermal patches is that the drug can directly be entered into the body undistorted without having to pass through the body's various defense systems. It also circumvents other issues like enzymatic degradation, poor intestinal absorption and first-pass liver effects associated with oral drug delivery and the pain and inconvenience associated with intravenous

injections.

Transdermal drug delivery also readily lends itself to sustained or modulated delivery from a passive or active patch, in contrast to conventional methods that deliver a large, discrete bolus. However, transdermal drug delivery has its own limitations mainly because, the stratum corneum layer of skin, which is responsible for skin's impermeability, is well known for its function as a protective barrier [54]. It prevents the diffusion of potentially toxic chemicals from the external environment into the body as well as the loss of physiologically essential substances from the body. Generally, the stratum corneum layer is only permeable to small and lipophilic molecules limiting transdermal delivery to a small group of drugs that share a narrow set of common characteristics. Successful transdermal drugs so far, are low molecular weight (< 500 Da), have an octanol-water partition coefficient much greater than one, require low doses and cause little or no skin irritation. Thus, in order to expand the range of molecules that could be delivered via transdermal delivery, several enhancement techniques are developed. These enhancement techniques not only reduce the resistance of skin to drug delivery, but they also control the reversibility and safety associated with drug delivery. Several enhancement techniques are looked at in detail and reported in [15, 55].

2.2.1.1 Skin Anatomy

As mentioned in Section 2.2.1, as skin's main barrier properties arise because of its physical structure, we look at the detailed skin's anatomy in this section. For drug delivery through skin via transdermal patches, the extent of delivery is limited by the dense tissue and the size of drug molecules. The enhancement techniques developed for transdermal drug delivery often make the delivery process independent of the size of the

drug molecule. Nevertheless, skin's barrier properties still pose a challenge; less from a chemical perspective, but instead from a mechanical perspective. This section details the overview of skin anatomy, its mechanical and thermal properties that are relevant for drug delivery enhancement.

The skin is the largest organ of the human body. It forms a continuous external surface of the body which varies in thickness, color and presence of glands at different regions. Despite these variations, all types of skin have the same basic structure. It is composed of an outer epidermis, an inner dermis and an underlying subdermal tissue. The epidermis comprises of several physiologically active epidermal tissues and the physiologically inactive stratum corneum [52]. The epidermis is approximately 50-150 μm thick and consists largely of constantly renewing, outward moving cells called keratinocytes in the physically active tissue. Other cell types in the epidermis include melanocytes, Merkel cells and Langerhans cells. The entire epidermis is avascular and is supported by the underlying dermis. The outermost layer of the epidermis is the stratum corneum, a 10-20 μm thick layer of densely packed, dead, flattened, and metabolically inactive, cornified cells. As most of the epidermal mass is concentrated in the stratum corneum, it forms the principal barrier to the penetration of drugs [56]. This stratum corneum barrier layer is packed with hexagonal cells providing a large surface area with least mass. The intercellular spaces of stratum corneum are filled with multiple, broad lamellae whose lipids are composed of ceramides, cholesterol and free fatty acids in approximately equal proportions. The morphology of these lipids plays an important role in the barrier functions provided by the stratum corneum. A basement membrane separates the epidermis and dermis layers. The dermis represents the bulk of skin and is

composed of loose connective tissue and contains collagen and elastin fibers that provide tensile strength and elasticity to skin. This fibrous network is highly vascular and contains many sense receptors.

2.2.1.2 Mechanical Properties of Skin

Human skin is a non-homogeneous, anisotropic and a non-linear visco-elastic material which is subjected to a pre-stress in-vivo [57]. The mechanical and structural properties of skin vary significantly with age, skin type, from site to site and between individuals. Hence, it becomes extremely difficult to generalize the properties of skin. In most literature reports, while studying for mechanical properties of skin, the contribution of the epidermis layer is neglected. The biomechanical properties determined from testing whole skin are mainly due to dermis collagen [58]. However, the influence of epidermis on the overall mechanical properties of skin is reported in some literature like [59].

A common method for evaluating a material's physical properties under the application of a load is to measure stress as a function of strain. Stress is defined as the force per unit area upon which the force is acting. Strain is defined as the ratio of change in length induced by the stress to the original length. When the whole skin is considered, its mechanical response is considered to be nonlinear even though the elastin and collagen fibres are considered linearly elastic [58]. The nonlinearity in the stress-strain dependency of skin seems to arise from the non-uniformity of the structure and the collagen fibres in the dermis.

Collagen fibers are the major constituent of dermis layer of skin and form an irregular network of intervened fibers that run almost parallel to the skin surface [59]. Collagen is characterized by high tensile strength of 1.5-3.5 MPa, low extensibility and

high stiffness with a Young's modulus of approximately 0.1 GPa to 1 GPa in the linear region. Elastin fibers are the second main component of the dermis with a fiber width of 0.5-8 μm . These fibers are less stiff than collagen and show reversible strain of more than 100%. The mechanical properties of the stratum corneum layer are different from bulk skin's properties. These properties are reported to be highly influenced by the environmental conditions that they are exposed to such as relative humidity and temperature. Several groups investigated the effect of moisture on the tensile properties of stratum corneum. An overview of this data is given in [60]. Despite the difficulties in obtaining information on the mechanical behavior of skin, constant efforts are being made in this direction to obtain data both by experiments and modeling.

Several insertion and penetration studies in skin are reported in the literature. Davis [61] measured and predicted the force levels necessary to insert microneedles into the skin and correlated the obtained force with the geometry of the microneedle. The measurement of insertion force is made by a force-displacement testing station. Once prepared, a single microneedle is advanced to, began deflecting and finally punctures the skin on the hand of a human subject. The insertion event is identified by a sudden decrease in resistance of an electrical circuit formed in the skin between the microneedle and a counter electrode. During this movement, the force necessary to translate the needle is measured using a force transducer. The force required to press the needle against the skin increased with needle displacement, then showed a discontinuity upon insertion into the skin, and finally increased further when pressed deeper into the skin. It is observed that the insertion force into human skin varies linearly with the interfacial area of the needle and is independent of the needle wall thickness. The obtained force of insertion

ranged from 0.08 to 3.04 N, all of which could easily be applied by hand. By equating the applied work to insert the needle with the work needed to pierce the tissue, the puncture toughness necessary to penetrate skin is determined to be $G_p = 30.1 \pm 0.6 \text{ kJ/m}^2$.

Shergold and Fleck studied the formation of cracks in human skin [62, 63]. The penetration mechanism in skin is found to be dependant on the penetrator tip geometry. The penetration pressure needed for a flat-tipped geometry is found to be much larger than that of a sharp-tipped geometry of the same diameter. The penetration of the penetrator into a soft tissue indicated cracking of the tissue followed by reversible deformation when the penetrator is removed. Based on the direction in which cracking occurs, the crack formation mechanism is divided into two modes. When the crack is generated as a result of tensile stress perpendicular to the crack plane, it is called mode-1 crack. This tends to be the most commonly observed cracking mechanism. If it is generated as a result of shear stress acting parallel to the crack plane, it is called mode-2 crack. The fracture toughness measured for mode-1 crack is $1.7 \pm 0.6 \text{ kJ/m}^2$ and for mode-2 crack is $26.9 \pm 2.7 \text{ kJ/m}^2$.

The above data is significant for our research since it provides an understanding on the extent of forces needed in order to create conduits in skin. If we can deliver similar amount of forces in a rapid time scale by our physical enhancement technique, micro conduits can be created in skin with minimal discomfort to the patient and drug molecules can easily be delivered through skin via transdermal drug delivery techniques such as transdermal patches.

2.2.2 Skin Permeability Enhancement Techniques

The number of drugs that can be currently delivered by transdermal means is

highly limited by the strong barrier properties of stratum corneum layer of skin and the physico-chemical properties of drugs that make them impermeable to travel across this barrier layer of skin. The permeation enhancement techniques must be able to address this issue of facilitating the transport of drug across the skin into blood circulation to achieve a desired therapeutic effect. For transdermal delivery, the goal of enhancers is to maximize the flux through skin into the systematic circulation and simultaneously minimize the retention and metabolism of the drug in the skin in contrast to topical delivery which requires minimum flux and maximum retention within the skin [52]. Nevertheless, in both cases, drug must be able to penetrate across the stratum corneum layer of skin.

The methods of enhancing drug transport across the biological skin barrier can be broadly divided into physical and chemical means. Regardless of the means of enhancement used, the common goal of permeability enhancement is to reduce the threshold of biological barriers and the primary concern is the safety of the patient. Enhancers can increase drug diffusivity in the stratum corneum either by dissolving the skin lipids or by denaturing skin proteins [52]. With the enhancement of skin permeability, transdermal delivery of proteins, DNA, vaccines and several other conventional drugs which are submicron in size is made possible. The permeability enhancement techniques create pathways for drug delivery by three ways: polar, non polar and polar/non polar. The enhancers create a polar pathway by causing protein conformational change or solvent swelling. For a non polar pathway, the rigidity of the lipid structure is altered and the crystalline pathway is fluidized.

2.2.2.1 Chemical Approaches

A good penetration enhancer should facilitate the drug permeation across the skin in a predictable manner without disrupting skin barrier property irreversibly. It should reduce the diffusion barrier of stratum corneum layer without damaging the underlying viable cells [52]. Several solvents, surfactants and other compounds are tested in this regard to improve permeability of skin to drugs. Some of these chemical penetration enhancers including ethanol, propylene glycol, tween, oleic acid and azone are reported to enhance drug transport by altering the barrier properties of the stratum corneum [64]. However, to have a significant penetration enhancing effect, the amount of chemical that is needed might cause skin irritation and might become potentially toxic. The chemical enhancer should be pharmacologically inert, non toxic, non-irritating and must be compatible with most drugs to be used successfully. Although, chemical enhancers have limited skin enhancing capabilities, they can be combined with other enhancing techniques such as iontophoresis [15] to improve effectiveness. In most cases, these enhancers are used in combination with conventional transdermal patches.

2.2.2.2 Physical Approaches

2.2.2.2.1 Electrical based Approaches

Iontophoresis: Iontophoresis [15] refers to the process of delivery of charged ions and drug molecules across the skin by means of an electric field. It uses a mild electric current to increase the migration of drug molecules through skin. Drug migration process begins when two electrodes are placed on skin and a small voltage is supplied to the electrodes. The drug molecule begins to migrate across the skin and will be absorbed by the capillaries systematically. Depending on the polarity on the electrode, similarly charged ions can be introduced into the skin. By adjusting the current, the drug delivery

process and dosage can be tailored to meet the needs of individual patients. Iontophoresis is most suitable for the delivery of water soluble drugs because of electro-osmosis. Both charged and uncharged species can be delivered using this phenomenon. This technique is particularly suitable for the delivery of peptides and small proteins. The flux of small molecules below 1000u is typically 20-50 mg/day whereas molecules above 5000u generally has a flux of less than 1mg/day [65]. However, this drug delivery mechanism depends on several factors such as current density, the duration of application, drug concentration and the pH of the solution. The transport of the drug is generally increased with an increase in current applied and the concentration of the drug up to a certain level. Iontophoresis is however, not suitable for the delivery of large molecular weight drugs with MW > 10 kDa and water insoluble drugs. It is also not suitable for the delivery of peptides with an isoelectric point within the pH range of skin [15].

Electroporation: Electroporation [15] is another electrical enhancement technique that involves the application of high voltage electric pulses of very short durations to enhance skin permeability and making it reversibly permeable to drug molecules. Electroporation can be used to deliver large molecules such as peptides, polysaccharides and genes across the skin in a controllable manner. The rate of transport is controlled by the voltage used, duration, rate and number of pulses applied. However, electroporation requires very high voltages for effective drug delivery and the safety of the process becomes an issue. It also affects the morphology of skin and creates tiny pores in the stratum corneum transiently.

Sonophoresis: Sonophoresis or Phonophoresis [15] uses acoustic energy to make skin

permeable using ultrasonic waves. When sound with frequency beyond 20 kHz is applied to the skin, the skin structure is affected or convection is induced resulting in thermal, chemical or mechanical alterations in skin that drives the drug across the skin. A contact media like a gel is used to transmit ultrasound energy to the skin. Ultrasonic energy can permeabilize skin through its heating, radiation pressure, cavitation and acoustic effects. Low frequency sonophoresis is proved to interact with the superficial skin tissue and increase transdermal transport by orders of magnitude. The effectiveness of low-frequency ultrasound to enhance drug transport can further be increased by the addition of a surfactant. Administration of many different drugs such as insulin, heparin and vaccine has been demonstrated to be feasible with low frequency sonophoresis. Water soluble permeants, as well as several fairly large macromolecules have been reported to be successfully delivered by the acoustic energy generated by the ultrasound.

The above mentioned chemical and physical enhancement techniques disrupt the stratum corneum layer of skin on a nanometer scale. However, they have had limited clinical impact. This is, in large part, because the improvement obtained in transdermal transport is still not sufficient for many drugs under clinically acceptable conditions. Recent research in transdermal delivery suggests that the approach to disrupting skin on nanometer scale may be too mild. Micron-scale skin disruption should make skin much more permeable, yet still be safe and well tolerated by patients. Given that almost all conventional drugs, DNA and vaccines are submicron in size, creating holes of micro dimensions in the stratum corneum should permit delivery of a broad range of compounds. Yet, micron-scale disruption is unlikely to have significant safety or cosmetic concerns. The skin barrier is routinely breached during common experiences of

minor abrasion, shaving, dry skin and hypodermic injection, yet infection rarely occurs. This is because the skin is designed to prevent entry of pathogens, even in the presence of minor stratum corneum defects. This observation leads to the hypothesis that micron-scale disruption of stratum corneum can dramatically increase skin permeability to a broad variety of compounds without significant safety concerns. Prompted by this idea, a number of methods including thermal ablation [66], jet injection [67] and microneedles [68] have been developed to disrupt stratum corneum on the microscale.

2.2.2.2 Thermal based Approaches

Thermal ablation [66] of skin has been studied by a few investigators and has demonstrated some promise. The thermal ablation process involves the application of thermal energy to the skin. This thermal energy is generated either by using heating filaments or an array of electrodes that generate Joule heating by passing a short, high current electric pulse. This energy is supplied by means of resistive elements onto microscopic sites on skin. This approach involves rapid heating of the skin surface to thermally ablate micro-sized regions of stratum corneum. At each site, due to resistive heating, a micropore is created by flash vaporization of stratum corneum cells. A drug is then delivered through these pores by aligning a drug patch over these formed pores. These micropores can stay open for several days if the area is occluded but will seal off quickly once the patch is removed. If the thermal pulse to which the skin is exposed is short enough, then a steep thermal gradient across the stratum corneum can be obtained, so that deeper viable tissues are not heated. In this way, the ablation is targeted to the stratum corneum alone so that living cells and nerves found deeper in the skin are not affected. This concept of thermal microporation is used by a passport system developed

by Altea Therapeutics Corporation. It consists of a drug patch that is attached to an array of metallic filaments. The arrays are activated using an applicator to form aqueous channels in the outer layer of skin. Reported increase in drug permeability for a microporated skin is about 100-fold when compared to untreated skin [69].

2.2.2.2.3 Mechanical based Approaches

Jet Injectors: Jet injectors are hand held devices that deliver liquid medication or vaccine through a nozzle orifice in the form of a high pressure, high speed narrow stream that penetrates the skin [67]. Depending on the mechanical properties of the fluid stream, the drug can be delivered to different depths such as intradermal, subcutaneous or intramuscular tissue. The nozzle part of the jet injector device is held against the desired part of skin to be treated and the drug is released by using a trigger on the device. Jet injectors can be fabricated as multi-use devices or single use devices. Multi-use devices deliver the vaccine through the same fluid stream and nozzle for multiple doses. These devices allow for high work load and for the delivery of vaccine for up to 1000 subjects per hour. However, they suffer from issues like contamination by bodily fluids.

The single-use devices proved to be much safer than multi-use jet injectors as they use disposable cartridges of the vaccine. The drug fluid stream is delivered within a disposable vaccine cartridge and nozzle, with a new cartridge and nozzle for each patient, thus eliminating the risk of cross contamination between injections. Several single jet injectors such as Bioject, Injex, Lecrajet and J-Tip are commercially available. Bioject and Injex are used to deliver several drugs in a variety of healthcare settings. Lecrajet is designed for ergonomics and speed of delivery, with the capability to deliver more than 600 vaccine doses per hour.

Microneedles: Microneedles [68] is a promising technology that uses miniaturized needles to penetrate skin. This represents a newer technology that has received attention as a means to mechanically create conduits across the stratum corneum for minimally invasive delivery. Microneedles are fabricated as an array of pointed projections that can create micro pathways in skin for systematic delivery of drugs. Microneedles are fabricated with varying dimensions with the length of the needles ranging anywhere from 25 μm to 1000 μm . Shorter microneedles do not reach the nerve-rich regions of the deeper parts of skin and hence, the stimulus caused by microneedle insertion is weak and perceived as painless [70].

A number of studies focusing on the fabrication techniques, materials and geometry of microneedles are reported in the literature. Microneedles are generally batch fabricated using techniques borrowed from the microelectronics industry. This allows for fabrication of extremely small feature sizes with high precision and good reproducibility in a cost effective manner. Both solid and hollow microneedles are reported in the literature. These microneedles when used along with transdermal patches proved to increase skin permeability and offer all the desirable properties from a transdermal patch, i.e. continuous release, ease-of-use and painlessness. This not only allows for the administration of larger molecules across skin but also allows for achieving an efficient and patient-friendly drug administration system requiring minimal medical training or help from health care professionals. Several companies are currently working towards developing FDA approved microneedles for commercial drug delivery.

All of the above mentioned thermal and mechanical enhancement methods have demonstrated success in delivering drugs into the skin, but nonetheless have limitations.

Notably, the thermal methods require “long” heating times of many milliseconds that have caused lasting damage to the skin with cosmetic effects that remain visible for many days. Jet injection is notably unreliable in the hands of patients (as opposed to clinical personnel), cause pain and cause deep tissue damage in the form of bruising. Microneedles similarly cannot be localized to the stratum corneum, are invasive and penetrate much deeper into the skin. This provides motivation to assess the efficacy of microjet actuators as an alternative approach to the creation of small holes in the epidermis for drug delivery.

CHAPTER 3

FABRICATION PROCESS DEVELOPMENT

The combustion microactuators mentioned in the literature provide a basic concept for the fabrication of our conductive propellant based microjet actuators. The actuators mentioned in the literature are fabricated as a three layer configuration consisting of a chamber, a nozzle and an igniter. The individual components of the actuator are fabricated using conventional MEMS based fabrication techniques such as lithography and etching. The combustion chamber and nozzle are generally fabricated as two separate components in silicon or ceramic substrates and the igniter is patterned in a polysilicon deposited layer. The fuel that is housed in the combustion chamber is then ignited by resistive heating when sufficient electrical energy is supplied to the igniter. Though these actuators offer desired performance, they suffer from limited material selection and limited geometric complexity. For example, silicon, which is the predominantly used material in MEMS fabrication is brittle, has less impact resistance and tends to fracture along its $\langle 111 \rangle$ plane with little or no elongation. Also, as silicon has high thermal conductivity, it results in thermal losses from the actuator during the combustion process, thus resulting in poorer performance. These thermal losses become more prominent at small size scales because of the increased surface area to volume ratios. The performance of these actuators is also strongly dependent on the material and the dimensions of the igniter used.

Hence, in the fabrication of conductive fuel microactuators, fabrication techniques that address some of these issues are used. Microjet actuators that produce large forces in

extremely small time scales i.e., in the microseconds range, find applications such as in steering an axi-symmetric bluff body projectile for aerodynamic applications or in transdermal drug delivery where extremely short duration, high force jets can be used to pretreat skin and remove stratum corneum layer selectively for later delivery of high molecular weight drugs. Fabrication techniques that enable the fabrication of meso-scale sized devices are given importance in this research work. The mesoscopic size feature of the jet actuator offers a good compromise between larger conventional combustion systems and micro-scaled combustion systems and tends to satisfy several important functions where a premium is placed on mobility, compactness or specific point application. The meso-scale characteristic size feature of the device provides the benefits of high rates of heat and mass transfer, moderate surface to volume ratios which reduces thermal losses than the micro scale devices, and the opportunity to operate in various environments. Though these actuators are meso-scale in size, the internal mechanism of these devices still relies on much smaller, embedded micro structures for their functioning. Hence, these actuators offer rapid response, compact design and enable fabrication in large volumes resulting in substantial cost reduction for each device.

The materials that are chosen in the fabrication of jet actuators must possess high mechanical and thermal strengths so as to withstand high mechanical and thermal shocks that the device might experience during its application. For example, as mentioned in Section 5.1.6, during the launch of a flight vehicle, the device would experience high-g loads up to 10,000 g for tens of milliseconds. Hence, the materials that are used in actuator fabrication for this application should be able to withstand such high g-loads without any mechanical failure. Hence, the fabrication techniques used must allow the

use of robust materials such as high strength plastics and metals. As the solid propellant microactuators are one shot devices that lack restart ability, the fabrication techniques used must enable for batch fabrication of multiple actuators on same substrate to produce multiple jets from an array. The neighboring devices in an array should be isolated from each other to prevent any accidental misfires. This feature may call for low thermal conductive materials for making the chambers or for large gap between adjacent devices to prevent any coupled thermal effects or small gap between electrodes to obtain good performance at low power inputs. Finally, the fabrication techniques used must enable “vertical” fabrication to realize high aspect ratio features and must be able to offer geometrical accuracy at low cost in order to compare with macroscale device performance.

In order to address all these issues, fabrication techniques such as laser micromachining and adhesive lamination are used in the manufacture of our jet actuators. Laser micromachining is a low cost alternative to lithographic fabrication for patterning substrates to achieve high aspect ratio structures. Also, it offers design flexibility and the ability to work with wider variety of materials such as prefabricated alloys, polymers and ceramics. Lamination technology is often used in electronics packaging to protect silicon devices from harsh environments. Fabricating devices using laser micromachining and adhesive lamination techniques consolidates the fabrication and packaging steps, saving time and producing robust actuators that could be used in harsh environments and resulting in higher performance compared to existing actuators. Laser micromachining patterns layers of lamina, Section 3.2 and adhesive lamination bonds layers of patterned lamina together, Section 3.1. The following sections present the advantages and

limitations of each fabrication technique and their detailed use in the manufacture of microjet actuators.

3.1 Lamination

Microlamination is a process of forming a single block of material by combining individual webs of materials such as metals, polymers or ceramic materials in order to form a unified microsystem with required features. Microlamination is a good fabrication choice for several MEMS systems as in most cases, the use of a single web of material may not satisfy all the properties demanded. It is therefore of benefit to be able to combine properties of several and differing materials in order to achieve desired performance. The process of lamination starts by surface machining individual laminae with patterns containing the desired structures. The laminae are often thin sheets of base material having desirable mechanical and thermal properties that are important for the functioning of the final device. These individual laminae are then bonded together to form the final device. Three types of lamination techniques are commonly used for bonding the laminae together: adhesive lamination, diffusion lamination and fusion lamination [71]. In this work, we mainly concentrate on adhesive lamination technique for bonding different layers that make the microjet actuators.

3.1.1 Adhesive Lamination

Adhesive lamination is a technique that is compatible with a wide range of materials and requires an adhesive binder between layers to mechanically bind the individual laminae. Adhesive lamination is the preferred technique for our lamination purpose as it complements MEMS fabrication procedures without sacrificing typical attributes of MEMS devices such as batch fabrication, layered deposition and selective

material patterning. It also facilitates inter-bonding of materials such as polymers to metals at low cost and high volume. Adhesive bonding is also generally appropriate when there are large areas to join, when fatigue strength is a concern or when adhesives can provide increased manufacturing productivity. But, it also has many limitations. First, reduced feature sizes less than hundreds of microns, become increasingly difficult to obtain because of uneven adhesive overflow. Second, during the alignment of layers using alignment pins, the accurate alignment of features in different layers is limited by mechanical machining. Finally, adhesive lamination is constrained by commercial material availability. Most over-the-counter metal foils are limited to 12.5 μm thickness, and anything less than that has to be specially ordered which makes the fabrication process expensive.

In spite of these limitations, adhesive lamination based techniques are well suited for mesoscale device fabrication. Figure 3 shows the typical adhesive lamination process [35]. An adhesive is applied between two laminae placed under a press, and a force is applied to a movable platen of the press. The platen temperature ' T_h ', is set at or above the curing temperature of the adhesive. The adhesive curing rate depends on this temperature. A vacuum pump may be used to remove trapped air to ensure a void free, consistent adhesive layer. The adhesive used during lamination process should enable for even distribution of stresses over the whole area of contact. It should also minimize the stress concentrations at the edges of the laminated area. For the fabrication of jet actuators, a high bond strength and minimal overflow of the adhesive is desired. The quality of the adhesive joint is quantified by the bond strength at the adhesive interface. This bond strength determines the loading that can be applied to the adhesive joint.

External loads when applied to the joint generally produce non uniform stress distributions at the joint [72]. These local stress concentrations which may be many times the average stress are often unrealized, and may determine the actual force that the joint will sustain. Since, fracture initiates when and where local stress exceeds local strength, stress concentrations have a large influence on the breaking strength of a joint.

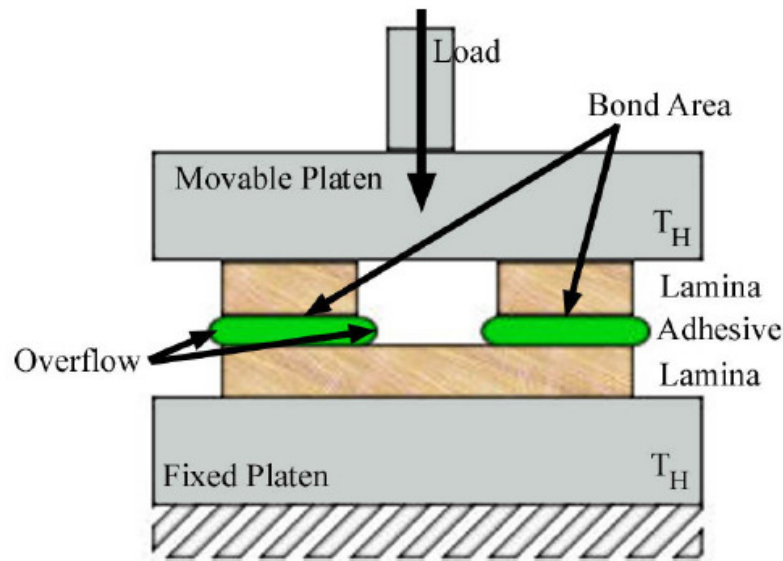


Figure 3: Features of adhesive lamination process

The strength of an adhesive bond is generally measured by a parameter called peel strength, ' ψ '. Peel strength is the average load per unit width of bond line required to separate bonded materials where the angle of separation is 180 degrees. A practical adhesive bond for jet actuators should be strong enough to withstand high combustion pressures and confine overflow of adhesive to acceptable regions of the device. In jet

actuators, the adhesive between individual laminae experiences perpendicular loading when generated gases increase pressure in the combustion chamber. This increased pressure creates forces on the unbounded sections of the laminae, perpendicular to the adhesive layer creating a bending moment due to the displacement of the pressure force and the adhesive bonding force. The maximum pressure that the material can withstand can be related to the size of the combustion chamber represented by length ' l_c ' and width ' w_c ' of the chamber and the peel strength ' ψ ' as [22]:

$$p_c(max) = \psi \frac{2(l_c + w_c)}{l_c w_c} \quad (7)$$

Also, in most cases after adhesion, as the adhered laminae will be stiffened by a clamp, high strength adhesives were chosen without noting adhesive stiffness. Practical square-profile combustion chambers tested range from 2 x 2 mm² to 6 x 6 mm². In these size ranges, the maximum allowable pressures based on peel strength data range were measured and reported by English [22] to be between 0.5 and 21 MPa for various adhesives. These tests demonstrate the feasibility of using lamination in conjunction with MEMS processing because thin layers of material may be laminated without damaging the mm-scale features of the device. Also, as will be seen in Section 5.1.2, the typical idealized pressures generated within a combustion chamber during combustion process falls in this range, further supporting the use of these materials in the fabrication of jet actuators.

3.1.1.1 Adhesive Selection

In the process of choosing the correct adhesive and developing an optimized bonding process, there are several critical decisions that need to be made. The adhesive

selection, for example, may influence the processing conditions that are required and the joint design that is necessary [73]. Therefore, the adhesive selection must be made by concurrently considering all of the parameters involved in the bonding process. Table 3 is a list of considerations that must be examined in order to make the appropriate adhesive choice for the application. All the factors listed are necessary when considering an adhesive.

The adhesive selection process begins with a general knowledge of the materials to be bonded. Generally, a major consideration in selecting an adhesive is the type of substrates that must be held together. This sometimes offers an indication of the nature of the surface to which the adhesive will bond. A general rule of selection of proper adhesive is to choose an adhesive that will wet the substrate [73]. Adhesive systems must be chemically compatible with the substrate or have a modulus similar to the modulus of the substrate being bonded [71, 72]. The substrate material should not inhibit the curing process of the adhesive and the adhesive should not adversely react with the substrate. When cured, the adhesive should have a modulus and thermal expansion coefficient similar to the substrate or else have toughness to accommodate stresses caused by thermal movements.

Along with the type and nature of the materials to be bonded, the surface preparation that they may require is also a major factor in determining which adhesive to use. Adhesives and substrates should also have similar chemical resistance properties. Physical properties such as surface energy and surface roughness are also important in achieving a strong bond. For good adhesion, the surface energy of the adhesive must be lower than that of the substrate. The increased surface area of roughened surfaces

enhances bonding for many materials, like glasses, ceramics and metals.

The polymer substrates tested in microjet actuators include mylar, acrylic and thermoset epoxy. An acrylic adhesive is used with acrylic substrate; a pressure sensitive adhesive is preapplied to mylar and the thermoset epoxy bonds to itself when heated. It was made sure that the individual adhesives used with the laminae did not exhibit adverse side effects. The peel strength values for the adhesives tested were obtained from the manufacturer's technical data sheet and this data is included in Table 4. Additional adhesive overflow data were reported by English in [22] and included here in Table 5.

Table 3: Considerations to be made while choosing appropriate adhesive [73]

Consideration	Importance
Properties of substrate	Adhesive must wet the substrate surface. It must have lower surface energy than the substrate. This can be achieved by either modifying the adhesive or subjecting the substrate to a surface treatment
Joint design and load	Most adhesives are better when the joint is designed so that they are under shear. Peel and cleavage stresses are notoriously harsh on adhesives. Toughness and flexibility are required when peel, impact or thermal shock forces will be present.
Service environments	Certain polymeric systems withstand certain environments better than others. However, multiple environments may provide unexpected problems. All adhesives should be tested in the service environment.
Properties of adhesive	Often the elastic modulus will give an indication of the adhesive's value in certain applications. Tough, flexible adhesives are better in peel, impact, thermal shock and when substrates of differing thermal expansion must be bonded. Brittle, rigid adhesives generally have better heat and chemical resistance, tensile strength and creep resistance.
Application methods	The availability of production resources must be considered. Such parameters will determine the best form (film, paste, etc.) required from the adhesive
Assembly needs and rate of cure	Many adhesives will require fixtures and jigs until the adhesive cures to a handling strength. The cost of such resources will often determine how much set or cure time can be acceptable. Some adhesives provide fast production.
Vendor selection	Reliability, price, willingness to meet demand and offer technical assistance, and training are all-important characteristics in selecting a vendor. It is likely that several vendors are available to supply the needed adhesive.
Testing	Standard tests are suitable for comparing the relative characteristics of different adhesives, but they do little in determining the performance or longevity of the joint in actual service. Prototype testing under selected environmental conditions is generally required to insure an efficient product.

Table 4: Lamination adhesives tested

Adhesive Manufacturer/Product	Adhesive Type	Viscosity [cps]	Peel strength Material [N/m]
3M/Super 77 [74]	Spray synthetic elastomer	200-5000	Aluminum 700-875
ISOLA/FR406 [75]	Prepeg epoxy	Fiberglass thermoset matrix	Flexural strength 503 MPa
Flexcon [76] Densil1078K	Silicone pressure sensitive adhesive	Prelaminated cured adhesive	Stainless steel 682
3M/DPS810 [77]	2 part acrylic epoxy	Part A: 95,000 to 100,000 Part B: 90000 to 95000	Etched Aluminum 4027
3M/DPS460 [78]	2 part epoxy	Part A: 150,000 to 275,000 Part B: 8000- 14000 to 14000	Etched Aluminum 8750-10500

Table 5: Adhesive overflow testing [22]

Adhesive brand name	Laminae	Adhesive thickness [μm]	Press force per bond area [kPa]	Press temperature [K]	Cure time [min]	Overflow [μm]
Super77	Acrylic	60	2780	294	30	130
Densil10	Mylar	10	2780	294	10	0
DP810NS	Acrylic	80	2780	338	20	350
DP460NS	Acrylic	110	2780	338	20	170

3.2 Laser Micromachining

This chapter details the use of high power lasers in the fabrication of microjet actuator devices. For the lamination process to have utility, a machining method which not only is capable of patterning structures within the laminae is needed, but also is versatile, easy to use, and should be capable of rapid machining of a wide range of materials. Though MEMS research to date, is widely dominated by lithography and etch based fabrication techniques, these techniques are highly restricted with the materials that can be used (notably silicon, silicon dioxide, silicon nitride and few metals), whereas, MEMS in general calls for much broader selection. Laser micromachining answers this issue by offering the ability to use much broader base materials, including polymers and other functional materials. It is also an alternate patterning technique to lithographic machining that is applied in MEMS field for the direct fabrication of devices. Some examples of laser based fabrication include laser micromachining of polymer masters for subsequent replication and laser assisted deposition and etching [79].

Unlike lithography based machining, laser machining is a direct write patterning tool, avoiding the costly and time consuming process of generating photolithographic masks. It is a one step alternative to chemical etching process which avoids over or under etching due to unoptimized exposure that is generally possible with wet etchants and offers selective material removal. Also, as no solvent chemicals are required with laser machining, it reduces waste handling costs and avoids environmental hazards associated with chemical etchants. Several MEMS devices such as hollow microneedles [68], microchannels [80] and stents [81] fabricated using this technique are reported in the literature.

Though laser micromachining for lamina patterning is a serial process, it offers following advantages over electrochemical machining when combined with lamination techniques [79].

- It allows for wide selection of materials to suit a particular application. Materials such as metal, polymer or ceramic with specific and tailored properties can be laminated together.
- Versatility in pattern design and aspect ratio. Specific laser machining design can be created on a computer and transferred to a numerically controlled laser in relatively few steps. High aspect ratio structures can easily be produced just by stacking more laminae.
- Quick progression from design to final device.
- Minimum feature size that could be made is well suited for mesoscopic devices. Feature sizes as small as 10 μm can be generated depending on laser and material parameters.
- Both small and large features can be produced using the same equipment.
- Little shape warpage during assembly and bonding.
- Full system integration into a single block of material can be achieved.

Laser micromachining which is defined as “the direct etching of solids by pulsed laser radiation” relies on the process of ablation. The lasing medium in a laser can be gas, solid, liquid, or in the case of semiconductor lasers - electrons. Gas and solid state lasers are practical for most industrial machining applications. Two types of lasers are used in our research work. A gas CO_2 laser is used to pattern polymers and plastics and a solid state IR laser is used for patterning metal layers. Laser properties such as wavelength,

spot size and power of these lasers are mentioned in Table 6. The laser patterning process starts when a laser beam is transmitted from the laser at a certain wavelength and energy through a lasing system onto the target material. The target material absorbs, transmits and reflects the incident radiation. The energy beam of the laser generally has a Gaussian profile with a peak energy density at the center of the profile. Hence, the laser removes material faster at the center of the beam than at the edges.

The absorption of laser energy at the surface of the solid results in the ablation of target material. The percentage of radiation absorbed by the target material is dependant on the materials absorptivity at the wavelength of the incident radiation. The choice of laser, its wavelength, power, and the choice of material i.e., its absorptivity and melting temperature determines the patterning rate for many processes. Selective patterning of materials is allowed by controlling these parameters. For example, by choosing the correct processing conditions for a metal-polymer substrate, metal layer can be patterned selectively without causing any damage to the underlying polymer layer. Also, as the laser beam produced from the laser is monochromatic, directional and coherent, laser ablation process is directional with the material ablated in the direction of the laser. This directional nature of laser machining eliminates severe problems in metal foil patterning.

Table 6: Laser machining equipment

Laser	Type	Wavelength [μm]	Power [W]	Spot size [μm]
Resonetics	Nd:YLF	1.047	15	40
New Hermes	CO ₂	10	30	150

3.2.1 Common Lasers Used in Industry

CO₂ laser: The CO₂ laser used in the manufacture of microjet actuators is the most common and inexpensive laser used in industry. A CO₂ laser uses a gas mixture of CO₂, N₂ and He. The CO₂ molecules constitute the active lasing medium, the N₂ gas serves as an energy transfer mechanism and the He atoms enhance the population inversion by depopulating the lower energy states. It offers a wide range of power output capabilities with high efficiency and long penetration depths. This machining is a thermal process where the beam performs its cutting and drilling functions by overloading the target surface thermally. The CO₂ laser shown in Figure 4 is used for current machining and has a peak power of 60 W and a wavelength of 10.6 μm which can easily be absorbed by materials like acrylic, mylar, FR406 and most polymers. It enables selective patterning of polymers in the presence of metal because metals are highly reflective at 10 μm wavelength. During machining process, the stage of CO₂ is fixed, and the laser position is computer controlled. The minimum resolution of the beam diameter of the CO₂ laser is 150 μm which fixes the minimum width of the machining parts to 200 μm . CO₂ laser offers two cutting modes: a vector cut mode and a raster cut mode. The vector cut mode allows for cutting through the material completely and the raster cut mode allows for partial depth ablation in some materials at 1200 dpi.

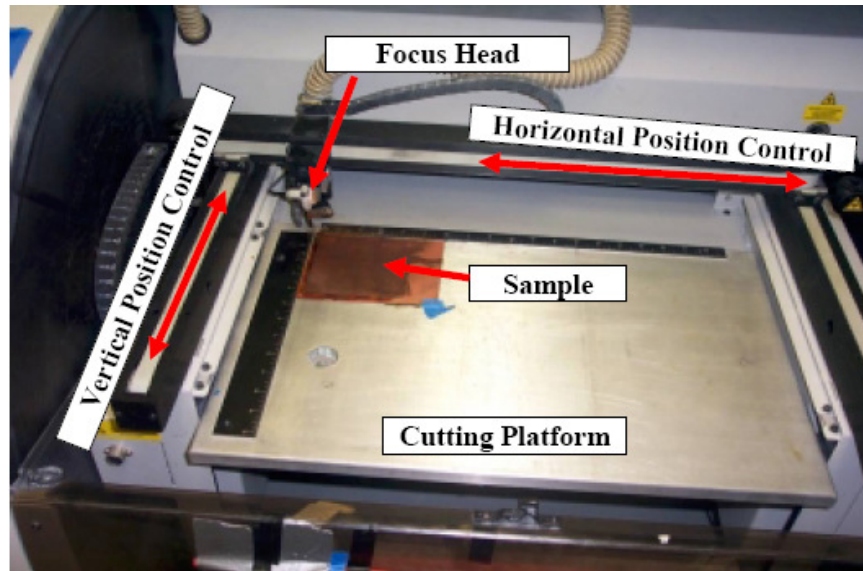


Figure 4: New Hermes 60 W CO₂ laser

Solid state laser: A solid state laser is constructed by doping a rare earth element or metallic element into a variety of host materials. The most common host materials are Y₃A₁₅O₁₂ (YAG), LiYF₄ (YLF) and amorphous glass. Nd:YAG and Nd:YLF lasers are the most commonly used solid state lasers in the machining industry. Nd:YAG lasers have a wavelength of 1.064 μm and Nd:YLF has a wavelength of 1.047 μm . A Nd:YLF laser with a peak power of 15 W and a wavelength of 1.047 μm is used for patterning electrode layers in microjet actuators. As this wavelength is readily absorbed by most metals, several metals can be considered for electrode patterning. This laser can pattern metal layers up to a thickness of 2 mm. The Nd:YLF laser wavelength is poorly absorbed by polymers because infrared radiation is transmitted through many polymers, and the energy density of the laser is too low to efficiently pattern polymers. Therefore, the Nd:YLF can be used to selectively pattern metal laminated to polymer substrates. The stage of the IR laser is computer controlled, and the beam size limits the minimum width

of the patterned metal to 100 μm . Figure 5 shows the computer controlled stage and the focus head of the IR laser that are used for patterning of metal layers.

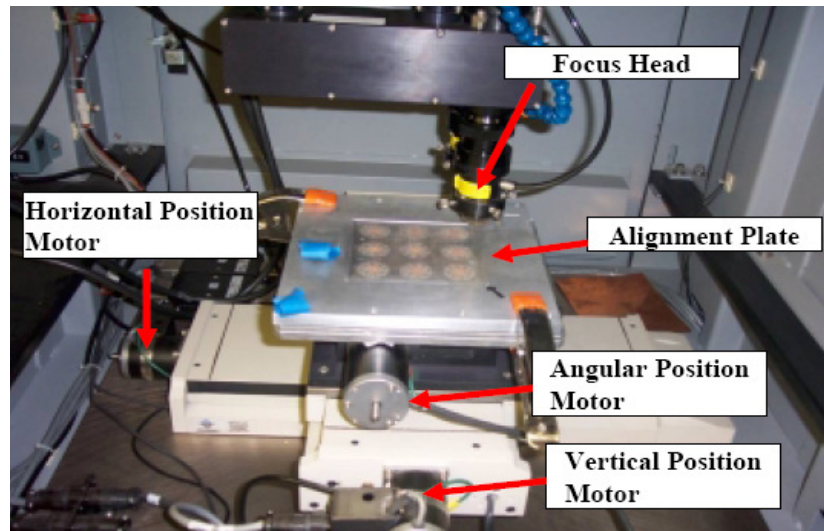


Figure 5: Resonetics 15 W Nd:YLF laser

3.3 Fabrication Sequence

Sections 3.1 and 3.2 reviewed approaches used in fabricating lamination based microjet actuators. First, individual actuators are developed and tested for their performance. Once individual actuators are optimized from a performance perspective, they are batch fabricated in arrays to meet the requirements and be applied towards the final application. Detailed fabrication sequence is depicted for two types of actuator arrays. These actuator arrays are broadly classified into two dimensional and three dimensional actuators. These actuator types mainly differ in terms of their electrode

design and fabrication. The fabrication sequence also describes the procedures and materials used to generate various parts of the actuator. In addition to these fabrication sequences, another fabrication sequence is presented in Appendix A. The actuators presented in Appendix A demonstrate fabrication of three dimensional microactuators by integrating laser micromachining techniques with photolithography and chemical wet etching techniques. This thesis just describes the fabrication sequence for such three dimensional devices and leaves their testing for future work.

3.3.1 Two-Dimensional Electrode based Radial Array Structures

The fabrication concept of the actuator is depicted in Figure 6. The actuator is fabricated as a five layer configuration: a chamber layer, in which the propellant is stored, two electrode layers placed on either side of the propellant and two backing layers placed on top and bottom of the electrode layers to seal the chambers and to provide the desired structural integrity. Laser micromachining is used to pattern these different layers and adhesive lamination is then used to bind all the layers together and form a unified device. For making the chamber and the backing layers, materials which are mechanically strong enough to withstand both the internal and external pressures the actuator experiences during its operation are desired. They must also have good thermal insulating properties in order to minimize any thermal losses to the chamber sidewalls during actuation. For this purpose, thermally insulating plastic materials with high mechanical strength are investigated. Similarly, the materials chosen for the electrode layers must possess good electrical conductivity in order to supply electrical energy to the conductive propellant without any losses. For this purpose, metals such as brass and titanium are investigated. The same fabrication concept is utilized for making both chemical based and physical

based actuators and the assembly works for both conductive propellants that could be ignited by the discharge of direct currents and for non-conductive propellants that could be ignited by arc-discharge across two closely spaced electrodes. Both individual and multiple actuators can be fabricated on the same substrate using this concept. The actuator design could also be easily modified to release the propellant jet either from the side or from the top of the actuator as desired by the application. For firing the actuators from the side, the nozzle is integrated into the chamber layer as shown in Figure 6 and for firing the actuators from the top, the nozzle is micromachined in the top electrode and backing layers.

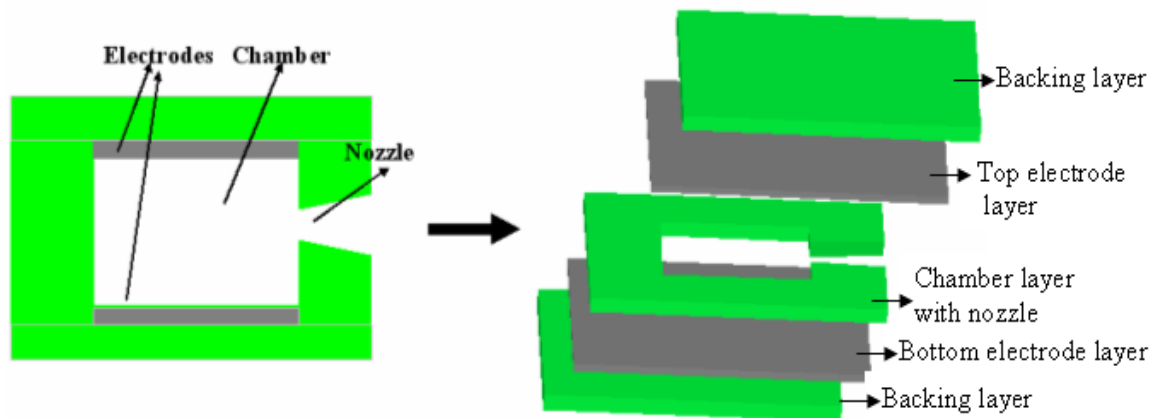


Figure 6: Fabrication concept of the microactuators

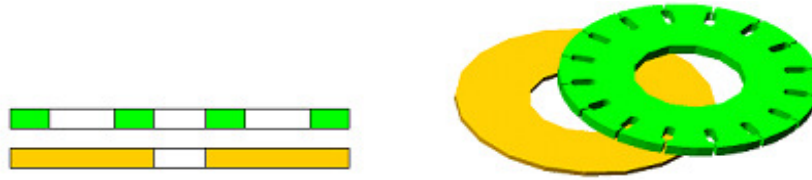
3.3.1.1 Chemical based Microactuators

Chemical microjet actuators are fabricated using laminated layers of plastics such

as mylar and acrylic and metal foils such as brass. Mylar and acrylic materials provide the mechanical strength and thermal insulation required from the chamber and backing layers during the actuation process and brass offers the desired electrical conductivity for the electrode layers. Figure 7 depicts the detailed fabrication sequence of making multiple actuators on a single substrate using laser micromachining and adhesive lamination techniques. Fabrication of multiple, one-shot devices enables the generation of multiple jets from the same structure. These actuators are fabricated so as to release jets in a radial direction from the disk. Radially firing multi-actuator disks are required for the application discussed in Section 5.1.6.

The fabrication procedure starts by laser patterning individual polymer films with a CO₂ laser to form base layers and chamber layers. The base layers are used to seal the chamber and provide mechanical strength to the structure. Individual chamber layers are stacked to form a hollow chamber and to achieve the desired height of the combustion chamber. For this purpose, either 250 μm thick individual mylar layers or 1.5 mm thick acrylic layers are used. The nozzle part is integrated into the chamber layer during laser patterning as shown in Step 1. The mylar layers are patterned with a 30 W laser at a speed of 50% and 4 passes. The thicker acrylic layers are patterned at a speed of 80% and 5 passes. Occasionally, refocusing of the laser needs to be done between passes. In Step 2, a 50 μm thick brass metal foil is laminated to the bottom and top backing substrates and patterned using a Nd:YLF laser to form the top and bottom electrodes and contact pads respectively. The laser parameters used for patterning brass electrode include 15 W laser power, 1047 nm wavelength, 2 mm/s speed and 2 passes. The lamination process is discussed in detail in Section 3.1. In Step 3, the combustion chamber layer is laminated

on to the bottom electrode. These chambers are then filled with conductive propellant in Step 4. Propellants with low viscosity are piped through a syringe to fill the chamber and solid conductive propellants are dispensed into the combustion chamber and mechanically pressed down using a spatula so that the propellant touches the electrodes uniformly. When possible, acetone is added to the dry solid propellant mixture to enhance the flow of the propellant into the chamber so that a uniform blob of propellant is formed. Excess propellant is then wiped from the chamber surface using a q-tip. Once the propellant is filled into all the chambers in the panel, it is allowed to dry in a dry box at 7% relative humidity at 21°C until the fuel cures. Finally, in Step 5 the top electrode layer is laminated to seal the combustion chamber. Figure 8 shows a panel of microactuators fabricated using this standard fabrication sequence. The picture shows actuators fabricated till Step 3 in Figure 7 before filling the chambers with propellant and their final sealing. Each panel fabricated consists of 9 disks with 8 or 16 actuators in each disk.



Step 1: Pattern 250 µm thick mylar layers with CO₂ laser.

Laser parameters: 30 W Power, 50% Speed, 4 Passes, refocus between passes



Step 2: Laminate Brass foil to backing layer. Align to IR-laser and pattern Brass foil with IR laser to form top and bottom electrodes.

Laser Parameters: 1047 nm, 15 W power, 2 mm/s, 2 passes



Step 3: Laminate chamber layer to the bottom electrode



Step 4: Fill chambers with fuel. Allow assembly to rest at 21° C, 7% RH until fuel cures. Clean top surface of assembly.



Step 5: Laminate top electrode attached top mylar backing layer to seal combustion chambers.

Legend: Mylar backing layer Electrode layer Chamber layer Solid propellant

Figure 7: Fabrication sequence of two-dimensional electrode based radial array microactuators

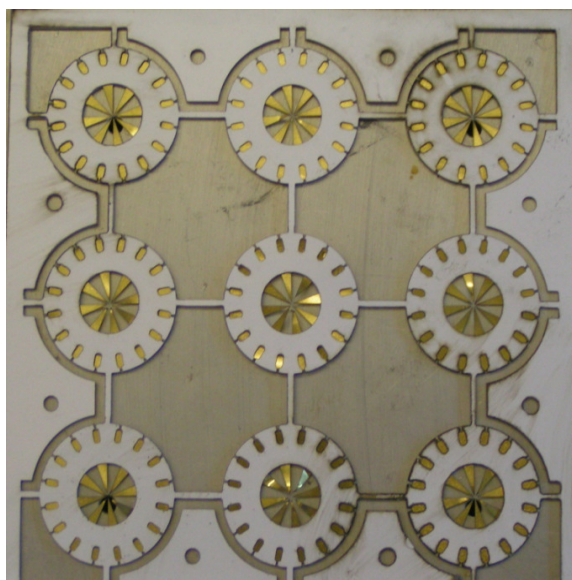


Figure 8: Array of chemical microactuators

3.3.1.2 Physical based Microactuators

For the purpose of demonstrating the use of physical microjet actuators for the application of transdermal drug delivery, two dimensional based electrode array structures mentioned in the above section are used. These radially firing actuators are fabricated using laser micromachining and lamination techniques. The actuator fabrication sequence is depicted in Figure 7. An array of actuators is fabricated using laminated layers of mylar, acrylic and metal foils such as brass or titanium. The fabrication procedure starts by laser patterning individual polymer films with CO₂ laser to form backing and chamber layers. The backing layers are patterned from 1.5 mm thick acrylic sheets and the chamber layer is patterned in 250 μ m thick mylar sheet. The metal sheets used for patterning electrode layers are then laminated to the bottom and top backing layers and patterned using an IR laser. Different materials such as brass, nickel and titanium with varying thicknesses in the range of 25-50 μ m are tested as electrode

materials. These materials are chosen based on the fact that they can easily be laser machined, obtained at low cost and are robust enough to withstand high internal and external forces. The chamber layer is then laminated onto the bottom electrode and filled with desired propellant, typically an aqueous solution containing a drug model, salt and optional gelling agent. The length and area of the chamber sets the total volume of the device while the thickness of the chamber sets the distance between electrodes. In these devices, both nozzle and chamber are patterned in the same substrate. The nozzle is positioned in such a way that the released jet fires radially from the actuator. Microactuator array is then sealed using the top electrode and backing layer. Figure 9 shows a panel of microactuators fabricated using this fabrication technique. Each panel consists of about 16 disks with two actuator devices in each disk. The propellant used in these microactuators is varied to study the effect of released jet on the permeability achieved in skin.

As physical microjet actuators mainly rely on the concept of arc generation, the distance between electrodes plays an important role in controlling the amount of input energy needed for pressure generation. The optimum gap between electrodes is chosen so as to minimize the energy required for arc generation by as much as possible. Based on this, the distance between electrodes is fixed at 250 μm and the chamber volume is varied from 1-8 μL of drug solution, respectively. The nozzle diameter is varied between 50 and 400 μm in order to vary jet velocity.

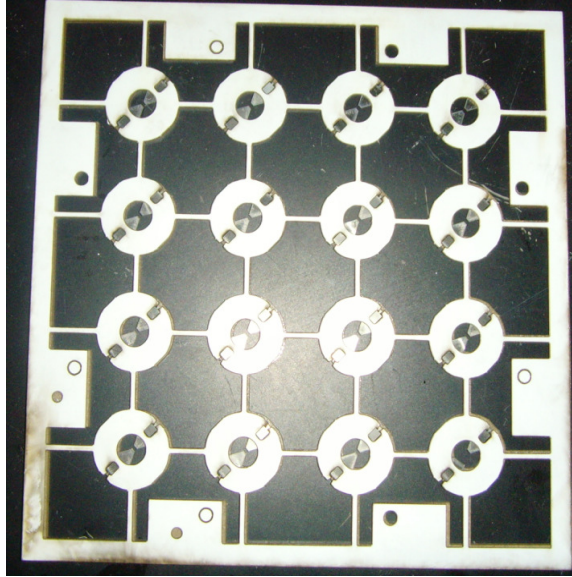


Figure 9: Array of physical microactuators

3.3.2 Three-Dimensional Electrode based Radial Array Structures

As will be shown in Chapter 5, in the conductive fuel based microactuators, the distance between electrodes plays an important role in optimizing the device electrical resistance and the input power consumed for device operation. In the above mentioned two dimensional microactuators, the distance between electrodes is fixed by the chamber layer thickness. Hence in most cases, the minimum electrode distance is dependant on the thickness of the commercially produced thin polymer films. When a 250 μm thick mylar layer is used as chamber layer, the distance between electrodes is 250 μm and when 2.5 mm thick acrylic layer is used as chamber layer, the electrode distance is 2.5 mm. In order to make the distance between electrodes independent of the chamber layer thickness, three dimensional electrode array devices have been developed. For this purpose, each electrode is fabricated as a multi-fingered structure and the gap between

fingers can easily be varied by controlling the laser parameters. The fabrication sequence for such a three dimensional microactuator array is depicted in Figure 10. Based on the laser machining limitations, the minimum distance between electrode fingers is limited to 70 μm and the maximum thickness of the electrodes to 125 μm . Using this technique chambers with volume range of 1-5 mm^3 are fabricated. The fuel is packed into the space between electrode fingers. To further increase fuel volume, additional chamber layer is attached on top of the electrode layer as shown in Figure 10. This thesis just describes the development of such three dimensional microactuators and leaves their testing for future work.

This concludes the description of the techniques used to fabricate microjet actuators. The fabrication procedures presented in this chapter offer MEMS based approaches to produce millimeter scale jet actuator devices that are robust enough to be used in harsh environments. Lamination based fabrication technique when combined with laser micromachining technique allows for batch fabrication of large number of jet actuators at low cost. Finally, through selective material selection for the chamber and the electrodes layers, reliable and rapid ignition of the propellant can be achieved. The microjets released from the lamination based actuators offer a simple solution to generate large, rapid forces that could potentially be applied towards various applications that require rapid response from the jets.

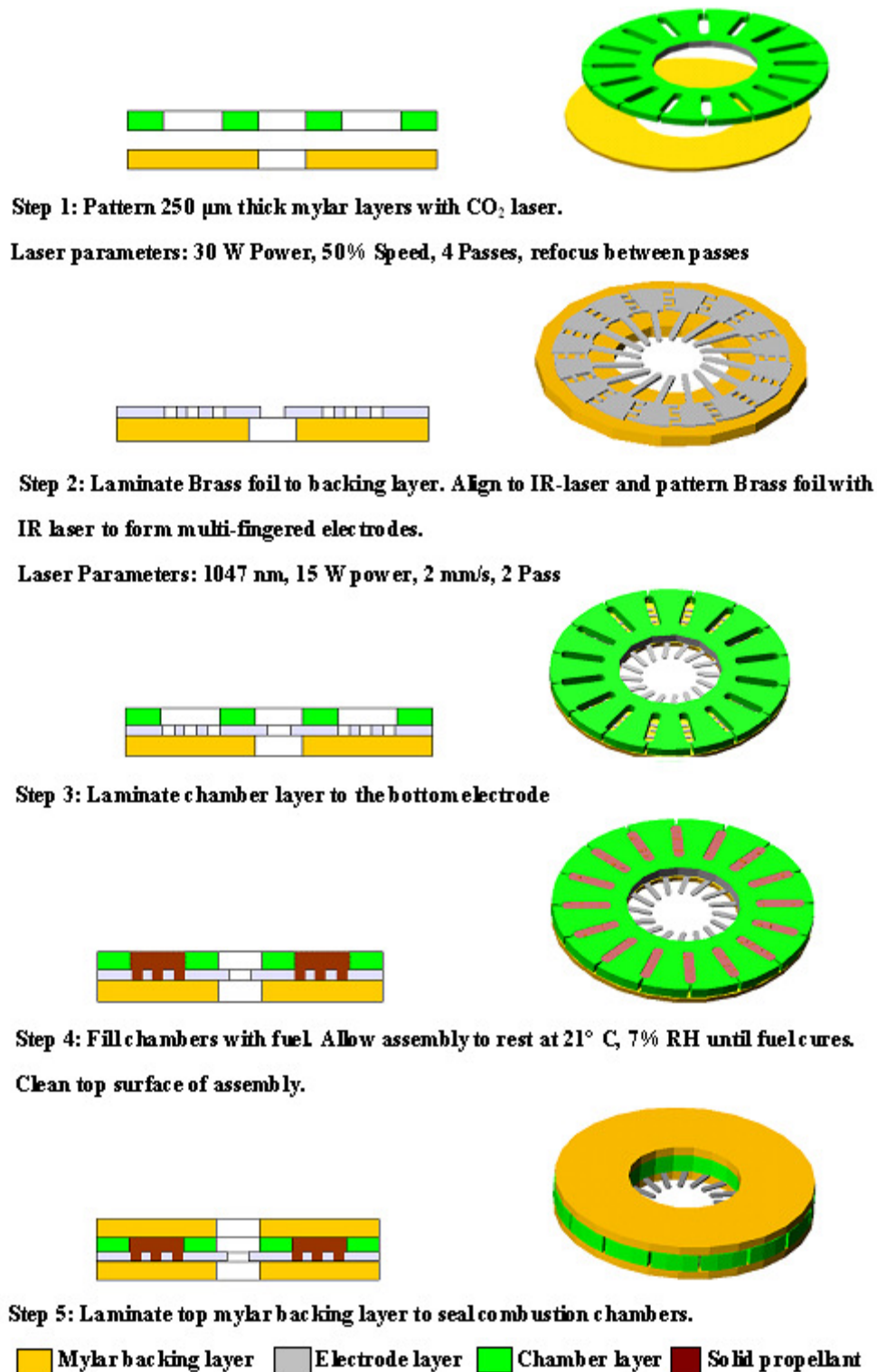


Figure 10: Fabrication sequence of three-dimensional electrode based radial array microactuators

CHAPTER 4

TEST METHODS

4.1 Chemical based Microactuators

This chapter provides detailed information on the testing methods and apparatus used to characterize electrically powered, lamination based microjet actuators. Chemical based microactuators are fabricated as discussed in Section 3.3.1.1 and integrated with conductive solid propellant. Detailed information on the development of conductive energetic propellants is discussed in this chapter. The developed conductive propellant is then tested for its electrical conductivity to ensure repeatability of the ignition process. The electrical circuit developed for the ignition of the conductive propellant is characterized for the required ignition power and ignition energy. The conductive propellant based microactuator is then tested for the amount of gas generated during the combustion process. Finally, the performance delivered by the actuator is measured using a force measuring setup and an impulse measuring ballistic pendulum setup.

4.1.1 Propellant Processing

As stated in the literature review, energetic solid propellant selection is very important to the performance of a microjet actuator. Solid based fuels, though they offer less performance in traditional applications than liquid fuels, are easier to handle and require only simple fuel systems where both the oxidizer and the fuel components of the propellant can be mixed and stored together until the time of ignition. Solid propellants are broadly classified into homogeneous, heterogeneous and composite propellants. Among these, composite propellants are best suited for use in microactuators as they

offer a wide range of specific impulse and burn rates which can easily be achieved by tailoring the energetics of each individual fuel component. However, composite propellants require time consuming powder processing to ensure good and repeatable performance. On small scales, this general limitation of composite propellants can be taken to our advantage as it provides us with an option of processing the fuel in lab allowing for finer control of propellant properties.

Several composite propellant ingredients including oxidizing agents, fuel components, polymeric binders and conductive dopants are surveyed in our research for their feasibility to be used in microjet actuators and these ingredients are reported in Table 7. Among these, the most important component in a composite propellant is the oxidizer as it provides the necessary oxygen that is required for the combustion reaction. The oxidizing agents surveyed in this research include ammonium perchlorate, potassium perchlorate and potassium chlorate. Another integral component of composite propellants is the fuel component. The fuel ingredients surveyed include potassium ferricyanide and antimony trisulfide. The binder components surveyed are nitrocellulose, glycidyl azide polymer and acetone. The conductive dopants tested include carbon black and graphite powder.

All the propellant ingredients used in the microactuator development are generally bought in 2-5 lb quantities from chemical suppliers. Among these, the oxidizing agents, nitrocellulose binder and potassium ferricyanide are obtained from Firefox Enterprises. The typical particle size range of the obtained oxidizing agents is in 90-400 μm range. Nano size carbon black and micro size graphite powders are obtained from Asbury chemicals. The reported particle size of carbon black is 29 nm and graphite is 5-10 μm .

Both carbon black and graphite were reported to be conductive by the supplier with an electrical resistivity of 0.34 Ω -cm and 0.08 Ω -cm respectively. GAP is obtained from Mach 1, Inc as a diluted mixture of 40% by volume polymer and 60% by volume of ethyl acetate. While using GAP during experiments, the ethyl acetate in the solution is allowed to evaporate before use.

Table 7: List of ingredients for composite conductive propellants

Type	Typical Wt%	Chemical Name
Oxidizer	0-70	Ammonium Perchlorate
		Potassium Perchlorate
		Potassium Chlorate
Binder	0-15	Glycidyl Azide Polymer
		Nitrocellulose
		Acetone
Fuel	0-30	Potassium Ferricyanide
		Antimony Trisulfide
Conductive dopants	2-20	Graphite
		Carbon Black

The literature review section provided some possible energetic propellant formulations using these fuel ingredients. Based on this information, solid propellant formulations that offer good performance at small size scales are developed in our lab and described in this section. The performance reported for these fuels in the literature is based on large scale applications. However, the same performance is not expected to be

achieved from small scale fuel systems. This is because the small scale fuel systems suffer from higher thermal losses when compared to large scale systems as they expose a greater percentage of released hot gases to the low temperature side walls. The side walls have detrimental effects on the combustion reaction. First, low temperature walls remove heat from the product gas, reducing the ability of the gases to produce a high temperature jet. Next, reactants that contact the side walls lose momentum and have less chance to collide with other reactants thus reducing the chance of reaction propagation. In addition, at small size scales, the surface area to volume ratio of the combustor chamber increases, resulting in higher thermal losses associated with close chamber side walls.

While preparing the conductive energetic propellants on small scales, proper methods for mixing and processing of conductive solid propellants are surveyed. As small quantities of propellant mixtures are prepared in multiple batches during testing, it is extremely important to minimize any batch to batch variations in order to achieve uniform performance. This means that the following variables in the propellant mixture should be well controlled [27]:

- Compositions of each fuel component
- Conductive additives
- Particle size of ingredients
- Loading method and pressure
- Mix homogeneity
- Moisture or humidity during mixing and loading
- Propellant surface contact with electrode material

Of these items, the composition of the oxidizer, fuel and other components is

generally maintained by carefully weighing each component to maintain uniformity in the ratio of ingredients. A digital scale (Mettler AE200 digital balance) with precision of 0.1 mg is used to measure propellant ingredients. The particle size of the propellant grain affects the burn rate, where propellants with finer particles typically burn faster than propellants with larger grain sizes [27]. Hence, to control particle size, a ball mill and sieve are used to grind and sort the powders. Good loading method and high loading pressures maximize the final packing density of solid propellant in the combustion chamber and this in turn increases the burn rate of propellant. The mix homogeneity of the propellant mixture affects how consistently the conductivity of the propellant can be reproduced and how consistently the propellant burns throughout the propellant volume. Solvents are used to reduce the viscosity of the fuels to improve wetting and mobility of ingredients. Finally, moisture content in the fuel can adversely affect the performance of solid propellant. Humidity can introduce inert water into the propellant and combustion energy is wasted in heating this inert material, reducing the performance of the propellant. Hence, the moisture content in the fuel is controlled through the use of oven drying and dessicants.

Selection of the right propellant for microactuator development is also affected by the following factors. First, laboratory equipment needs to be available to allow safe handling and storage of the propellant ingredients. Second, the propellant ingredients must readily be available. Third, large scale performance data demonstrated a wide range of fuels that could be used in microjet actuators to obtain the desired range of specific impulse and burn rate values. Other selection criteria like shock sensitivity are neglected in some cases in order to increase specific impulse or burn rate. The powder processing

techniques developed for conductive solid propellant processing are based on industrial processes presented in Section 2.1.2. The individual solid propellant ingredients used in chemical microjet actuators are stored as received in sealed plastic bags. Before being used, small quantities of individual materials are removed from the shipping container, ground, sorted and then stored in one of the two desiccant dryers with relative humidity < 8%. The purpose of storing the ingredients in a desiccant is not to remove all the moisture, but to maintain consistent moisture content from batch to batch. Two desiccant jars are used, one for oxidizer and one for fuel components. Figure 11 shows all the processing steps used during solid propellant processing. Steps 2 and 3 in Figure 11 show grinding and sorting of individual propellant ingredients. A ball mill is used in Step 2 for grinding because a micropulverizer is not available. The nylon ball mill is charged with 3/8" diameter cylindrical alumina pellets, and then filled with 176 g of oxidizer. The mill is operated at 120 rpm to create a consistent cascading action of the alumina pellets within the ball mill. An automatic sieve shaker is used in Step 3 to speed the sorting action within the sieves. The 3" sieves are of the following sizes: 500 μm , 212 μm , 90 μm , 53 μm and 27 μm . Potassium perchlorate, ammonium perchlorate, and potassium ferricyanide are ground and sorted using these techniques. Each ingredient requires its own ball mill and set of sieves to prevent cross contamination. Potassium chlorate is used as received because it is sensitive to shock and accidental ignition.

Steps 4 and 5 in the solid propellant preparation process are drying and mixing respectively. To force moisture removal from hygroscopic powders, a vacuum oven as shown in Figure 11 is used. A vacuum bake is conducted below the powder decomposition temperature and held until the moisture content is satisfactorily removed.

During this step, the mass of the propellant before and after baking is recorded to determine the amount of moisture removed. This drying step is performed at 473°K for 4 hours. When the powders are dried and sorted, they are ready for mixing. When mixing propellants, Step 5, the following procedures are used. First, powders are weighed separately in 20 mL beakers using a Mettler AE200 digital balance. Then, a binding agent is added to the oxidant and stirred until uniform. Individual additives are then added and stirred using a stirring rod until the mixture is uniform. With most binders, plasticizers or solvents are added to reduce the working viscosity of the mixture and improve the solids loading in the binder. Adding acetone or nitrocellulose lacquer is an example of this.

Conductive chemical propellants thus made are directly cast from mixture into the combustion chamber by hand pressing into the combustion chambers. Solvents such as acetone are added not only to reduce the propellant viscosity and increase handling safety, but it also ensures forming uniform and good contact of propellant with the electrodes. The solvent allows the propellant to flow easily when being filled in the chamber. The solvent evaporates after casting leaving the propellant mixture in the combustion chamber. Reducing the viscosity of the mixture with solvents eliminates voids in the propellant. The cast propellant is allowed to cure for 12 hours at room temperature and 7% relative humidity. Once cured, excess propellant is wiped from the arrays to prepare the surface for lamination of the top electrode layer. Once cured and bonded, an array of jet actuators are assembled and are ready for testing.

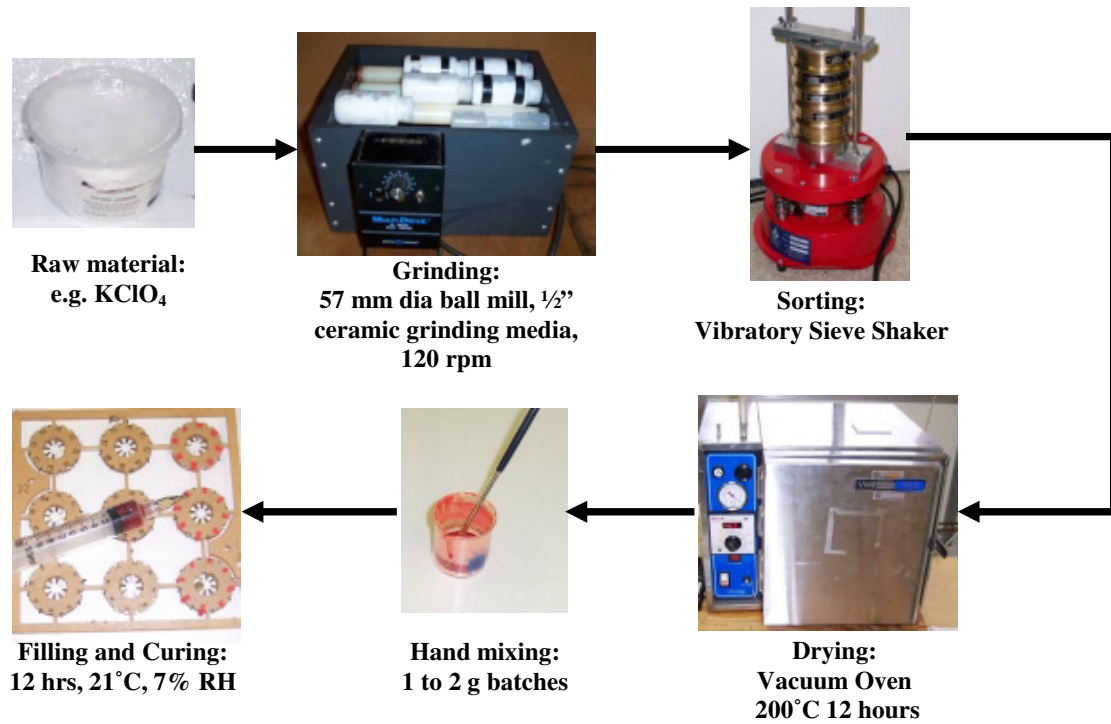


Figure 11: Propellant powder process flowchart

The first step in testing the conductive fuel microactuators is to look for the conductivity of the propellant. Several conductive solid propellant mixtures used for this purpose are reported in Table 8. Among these mixtures, not all the mixtures were proved to be conductive enough to be ignited using electrode discharge of currents. Hence, only a few of these mixtures are finalized to be integrated into the microactuators. For each of these finalized fuel mixtures, several weight ratios of each fuel component are tested to determine the optimum composition of the fuel for good conductivity, minimum ignition requirements and high burn rate. These fuel mixtures and their optimum compositions are reported in Table 9. The optimum composition of each fuel mixture is used for the final characterization of the microjet actuators.

Table 8: Propellant mixtures prepared in lab and tested for fuel conductivity

Mix No	Oxidizer	Binder	Fuel	Additives	Conductive additive powder
1	NH ₄ ClO ₄	GAP	-		Graphite
2	NH ₄ ClO ₄	GAP	-		Carbon/Graphite
3	NH ₄ ClO ₄	GAP	-		Carbon
4	-	GAP	-		Carbon
5	-	GAP	-		Carbon/Graphite
6	-	GAP	-		Graphite
7	KClO ₃	-	Sb ₂ S ₃	Acetone	Carbon black
8	KClO ₄	Nitrocellulose	K ₃ [Fe(CN) ₆]	Acetone	Carbon black
9	KClO ₄	Nitrocellulose	K ₃ [Fe(CN) ₆]	Acetone	Carbon/Graphite

Table 9: Sample weight ratios for the finalized solid propellant formulations

Mix No	Oxidizer	Wt Ratio	Binder	Wt Ratio	Fuel	Wt Ratio	Conductive additive	Wt Ratio
1	KClO ₃	6	-	-	Sb ₂ S ₃	1	Carbon	0.5
2	KClO ₄	3	Nitrocellulose	0.75	K ₃ [Fe(CN) ₆]	1	Carbon	0.5
3	-	-	GAP	0.8	-	-	Carbon	0.2
4	NH ₄ ClO ₄	1	GAP	1	-	-	Carbon	0.2

Among the finalized propellant formulations mentioned in Table 9, Mix 1 is a pyrotechnic noise making propellant known to detonate at atmospheric pressures and ignite easily with electrical ignition. Because mixtures of potassium chlorate and sulfur fuel are susceptible to accidental detonation, the potassium chlorate is used as received.

Mix 1 is prepared as follows:

1. Combine 1 g KClO_3 to some acetone
2. Stir to coat KClO_3
3. Add 0.17 g Sb_2S_3
4. Add 0.08 g of nano size carbon black powder.
5. Stir ingredients by adding small amount of acetone to ease mixing with a stirring rod
6. Fill actuators immediately by pressing the mixture into the chamber
7. Let the mixture dry in the chamber for 12 hours before sealing the chambers with the top electrode and top backing layers

Mix 2 is obtained from the literature and is reported to have very fast burn rates, but no stoichiometry was reported. The ratio of potassium ferricyanide and binder is varied in the mixture to achieve the desired performance. The mixture used for final testing is prepared as follows:

1. Combine 1 g KClO_4 to 0.25 g of Nitrocellulose lacquer
2. Stir to coat KClO_4
3. Add 0.33 g of $\text{K}_3[\text{Fe}(\text{CN})_6]$
4. Add 0.16 g of carbon black
5. Stir ingredients by adding small amounts of acetone to ease mixing

6. Fill actuators immediately
7. Let the mixture dry in the chamber for 12 hours before sealing the chambers

Mix 3 is conductive glycidyl azide polymer (GAP) mixture. Because GAP is reported in literature as an energetic binder, no other fuel or binder is added to it. GAP propellant is mixed with carbon black and then filled into the combustion chambers. The final propellant, Mix 4, is comparable to propellants cited in the development of the micropylors and smartdust. This propellant is chosen for comparison to existing microthruster technology.

Mix 4 is prepared as follows:

1. Combine 1 g NH_4ClO_4 to 1 g GAP
2. Add 0.2 g carbon black
3. Fill chambers immediately

4.1.2 Fuel Conductivity Measuring Setup

For conductivity measurements, chambers as shown in Figure 12 are filled with the conductive propellant to be tested. Electrodes are inserted on either side of the chamber and the resistance of the fuel is measured using a multimeter. The resistivity of the conductive propellant is calculated using Ohm's law as:

$$\rho = RA/L \quad (8)$$

Where 'A' is the area of the combustion chamber and 'L' is the distance between electrodes. The conductivity of propellant is then calculated by:

$$\sigma = 1/\rho \quad (9)$$

Several fuel compositions mentioned in Table 8 were tested for conductivity by

varying the composition of the fuel ingredients and conductive dopants.

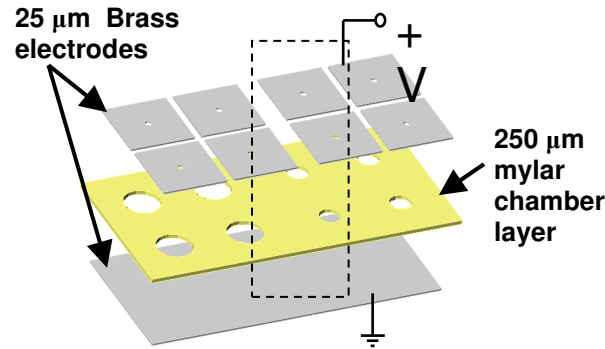


Figure 12: Microchamber used for conductivity measurements

4.1.3 Gas Generation Measuring Setup

In order to measure the amount of gas released from the microjet actuator during combustion event, a gas generation setup is utilized. The quantity of gas released during actuation is measured in terms of number of moles or volume of the released gas. The measuring setup consists of a closed and sealed vessel that measures pressure at constant volume. In general, the pressure inside a closed chamber is dependant on the volume of the chamber, mass of propellant, temperature and the rate of combustion [82]. But, when the released gases are allowed to cool for sufficient period of time, the effect of temperature and rate of combustion can be neglected.

The apparatus used for measuring the amount of gas released is shown in Figure 13. The apparatus consists of a cylindrical closed sealed vessel and a diaphragm-style

pressure transducer. The vessel is made from stainless steel and can be divided into three parts for easy installation of the actuator inside the vessel. The pressure transducer is attached to the top part of the vessel using standard tube fittings and electrical feed throughs are provided at the bottom part of the vessel. The microactuator is placed within the vessel and the electrodes are connected to the electrical setup using electrical feed through connections. These feed through connections allow for the initiation of the propellant actuation. Once the actuator is placed within the vessel, the top and bottom parts of the vessel are sealed using a copper gasket, a butyl rubber gasket and six 5/16", grade 8 hex bolts to make the chamber air tight. The volume of this closed vessel is 23 cm³. The sensitivity of the measurement can further be increased by decreasing the free volume available within the closed vessel. This is done by inserting an aluminum insert within the vessel. The volume occupied by this aluminum insert is 12 cm³, thus reducing the overall free volume available for the gases released to 11 cm³. The mass of the fuel consumed during actuation is measured by measuring the weight of the actuator before and after the actuation process. The pressure within the chamber is recorded before, during and after the combustion process. The amount of gas produced is calculated based on an ideal gas equation of state:

$$\Delta N = (N_t - N_o) = N_o \left(\frac{P_t}{P_o} - 1 \right) \quad (10)$$

The moles of gas produced are determined by obtaining the pressure difference within the vessel. The volume of gases released is then calculated by converting the moles of gas released during combustion using:

$$V_p = \frac{\Delta N R_u T_o}{P_o} \quad (11)$$

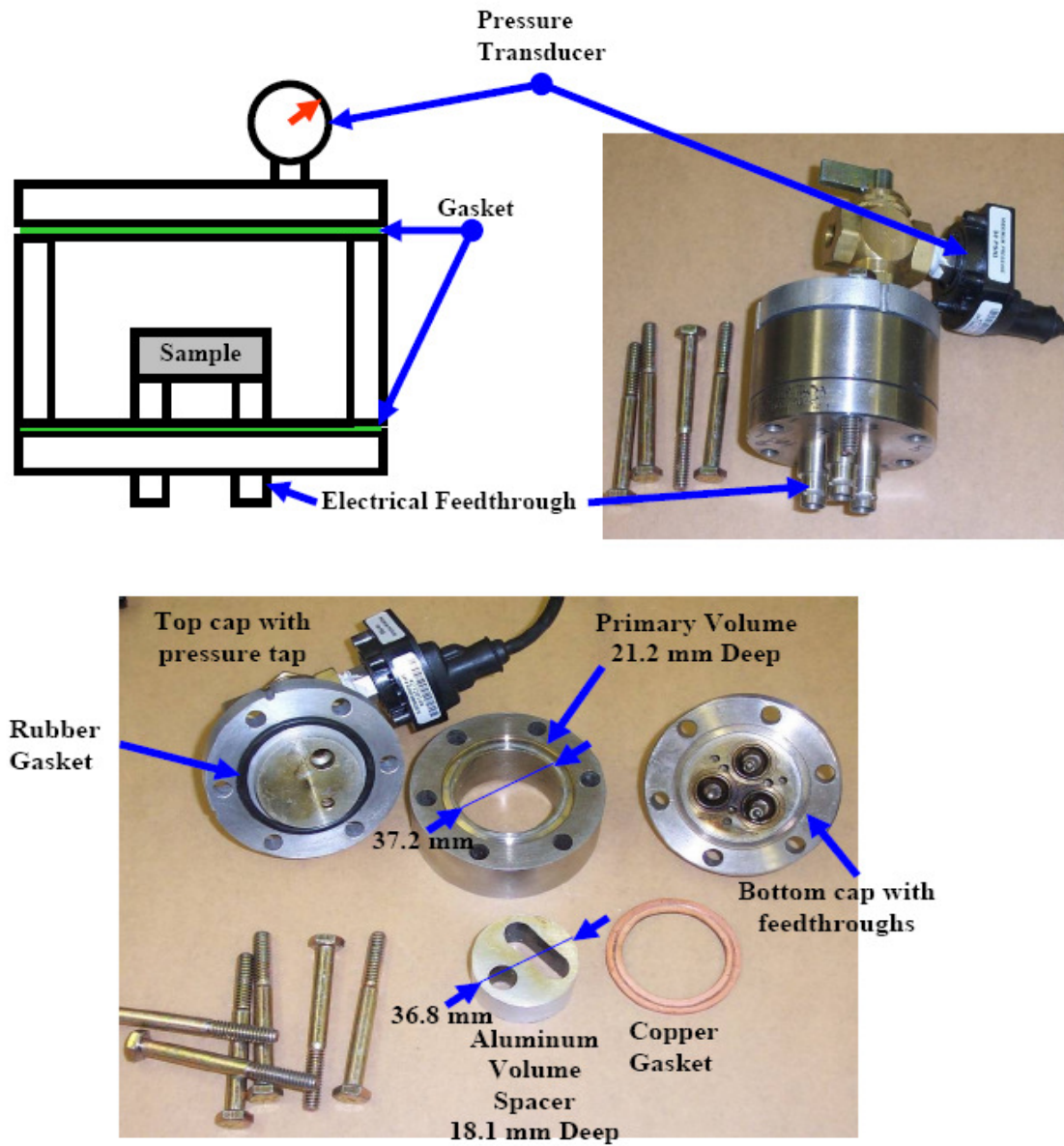


Figure 13: Pressure bomb used for measuring amount of gas released

4.1.3.1 Pressure Sensor Calibration

The pressure transducer used during the testing procedure is an omega PX180-O30GV3 stainless steel diaphragm transducer. The sensor has the capacity to measure from 0 to 2 atm gauge pressure, with an output range of 0 to 100 mV and rated accuracy of 0.3%. The sensor is initially calibrated using compressed air. The sensor scale is measured to be 0.021 atm/mV and the results of the calibration are shown in Figure 14. The pressure data is then recorded by connecting the transducer to a 12 bit data acquisition box for an input range of 1 V. Hence, the voltage resolution is 0.49 mV and the pressure resolution is 0.99 kPa. These measurements are made for single combustion chambers and the chamber pressures are recorded after the gases are cooled completely. As the thermal mass of the vessel is large, the gases released have cooled within hundreds of milliseconds. The recorded chamber pressures are then converted into volumes of gas at 298°K and 1 atm using ideal law.

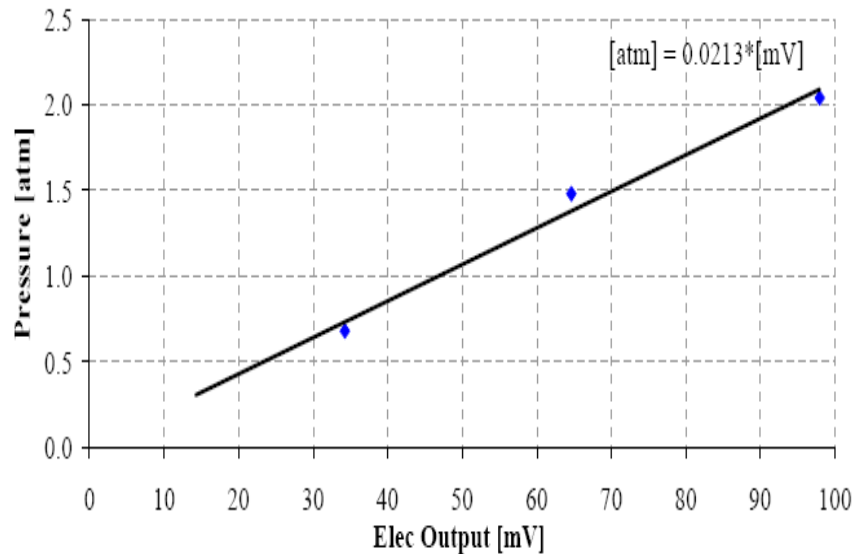


Figure 14: Pressure bomb calibration [22]

4.1.4 Force and Burn Time Measuring Setup

Much of the measuring setup is described in [22], and the treatment that follows is taken in large part from that reference. The burn rate characteristics of conductive fuel microjet actuators include impulse delivered, thrusts generated, ignition delay time and impulse durations. These parameters are important in determining the actuator performance as they are critical in maintaining the control authority of the actuator arrays when implemented in an application. Total impulse acts as a yardstick in measuring the total effect of the released jet from the actuator and is defined as the time integral of thrust delivered over the burn duration. Burn duration must be controlled to set an actuator pulse frequency, e.g., for a spinning projectile. Ignition delay time, defined as the time taken from the application of input energy to the fuel to the beginning of combustion process must be well controlled so that the combustor fires in a control direction, making actuator reproducibility an important manufacturing constraint.

A force stand is a classic testing method used to determine the burn characteristics of large scale actuators. A fixed force sensing setup is used to measure the burn characteristics of the actuator for a given fuel composition, device geometry and nozzle design. Unlike large scale actuators where the magnitude of thrust generated is much greater than the sensitivity of the measuring system, microactuators suffer from extremely fast rise times and short burn times which lead to large vibrations of the force measuring system. These system vibrations make it extremely difficult to differentiate the actual force released from the actuator from the additional forces sensed by the sensor due to the vibrations imparted from the system. Hence, measuring burn characteristics of the microactuators is not as straight forward as measuring the burn characteristics of large

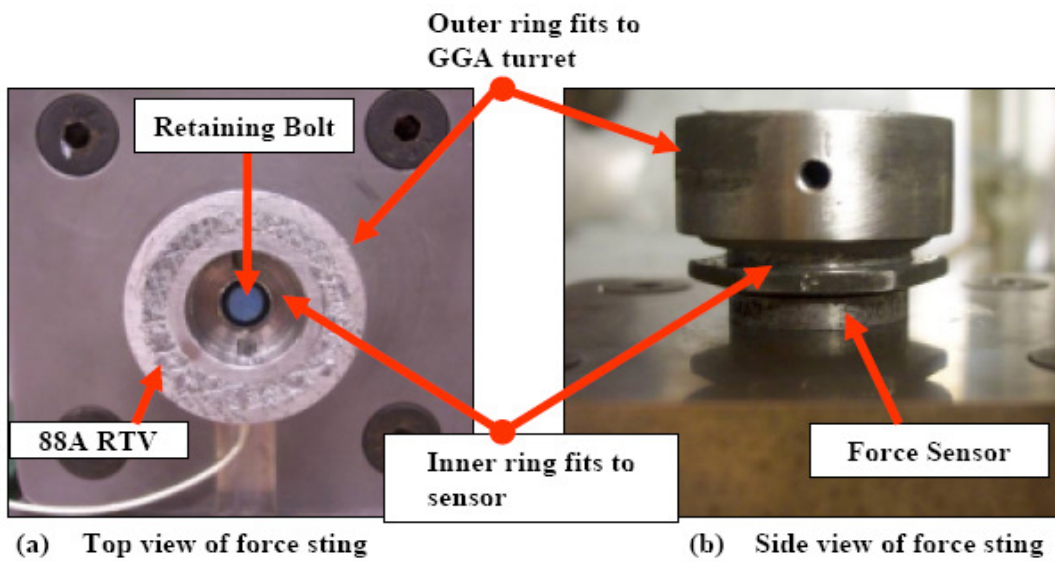
scale actuators.

The force sensing setup that is needed for measuring burn characteristics of a small scale actuator must be able to reduce the effect of external vibrations without greatly sacrificing the time resolution of the system. This is achieved by reducing the overall mass of the force sensor setup and by using damping materials. The force sensing setup as shown in Figure 15 includes a piezoelectric ring type force sensor securely mounted to a small and heavy metal block which in turn is mounted on a uniform leveled table with a solid heavy platform on top to reduce damping. An adapter connects the actuator mounting assembly to the force sensor assembly. This adapter is provided with a damper to reduce vibrations in the sensor.

The sensor used for measuring burn characteristics is a ring type piezoelectric force sensor with a model # 9144A21 obtained from Kistler Instruments Corp. The sensor contains two quartz elements sensitive to shear force in one direction. The force to be measured is transmitted by stiction to the quartz elements and these produce an electrical charge directly proportional to the force applied. The force sensor is connected to a charge amplifier using a bnc connector so as to convert the charge signal obtained from the sensor into a proportional voltage that could be acquired later. The charge amplifier used along with the Kistler sensor is a Kistler model # 5010. This amplifier is a versatile, line powered, dual mode amplifier that works either in a charge mode or a voltage mode. In charge mode, this unit converts the input charge signal such as a Kistler sensor signal into proportional controlled voltage. The long time constant mode on the amplifier permits measurement of short duration static and quasi-static events. The scale and the sensitivity settings are designed to provide a direct readout in volts per mechanical unit to

be measured, thus eliminating mathematical manipulations. The sting and the base plate surrounding the sensor are held together by a 5/8" grade 8 bolt with a preload tightening torque of 23 Nm. A rotating turret assembly is machined to hold and properly align the actuator arrays during testing. The turret is connected to the sting and held in place using two #6 cap screws. The actuator is fired radially through slits in the turret and the force released is transferred to the sensor.

Figure 16 is a flow chart of the force data acquisition system. The force sensor senses the force released and produces an electric charge proportional to the force. A charge amplifier is used to convert this electric charge to proportional voltage. The signal from the charge amplifier is fed into a data acquisition system, stored and recorded on a computer as force vs. time. The voltage equivalent signal from the charge amplifier is fed to a National Instruments BNC 2090 junction box and then to a 12-bit data acquisition box from National Instruments MIO-16E. This data is recorded on an AMD650 desktop PC using labview software. Figure 17 shows a sample result of the acquired force data and burn characteristics are determined from this data. The thin vibrating line represents actual data acquired from force sensor using data acquisition system. A 20-point moving window average is plotted along with the actual force data. This force data is then integrated to obtain the calculated impulse of the actuator.



(c) Turret styles

(left to right) Wide Angle Exhaust, Projectile, Stacked Actuators

Figure 15: Force sensor setup

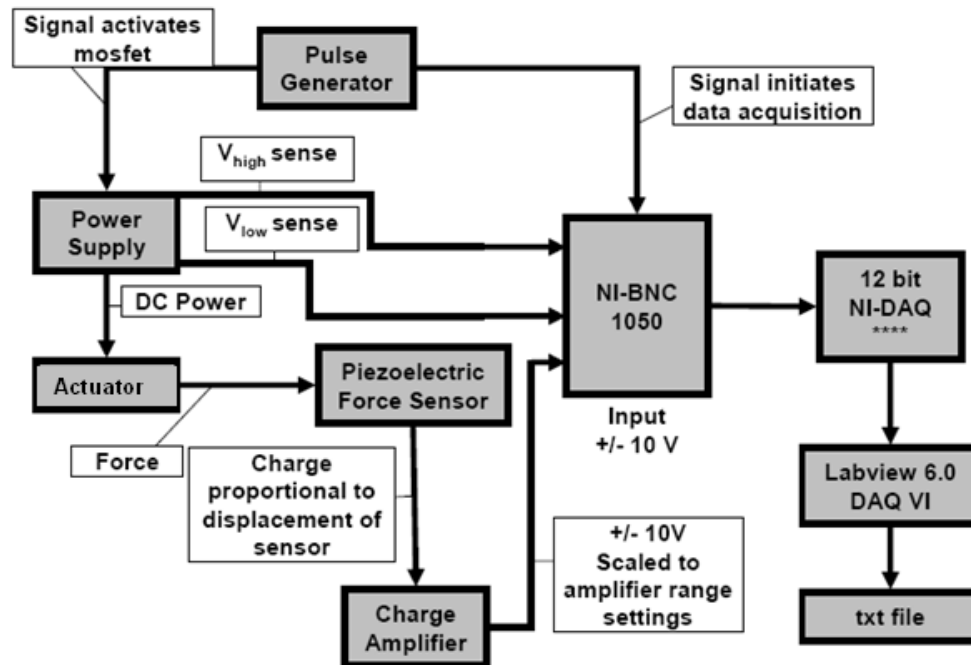


Figure 16: Force sensor data acquisition

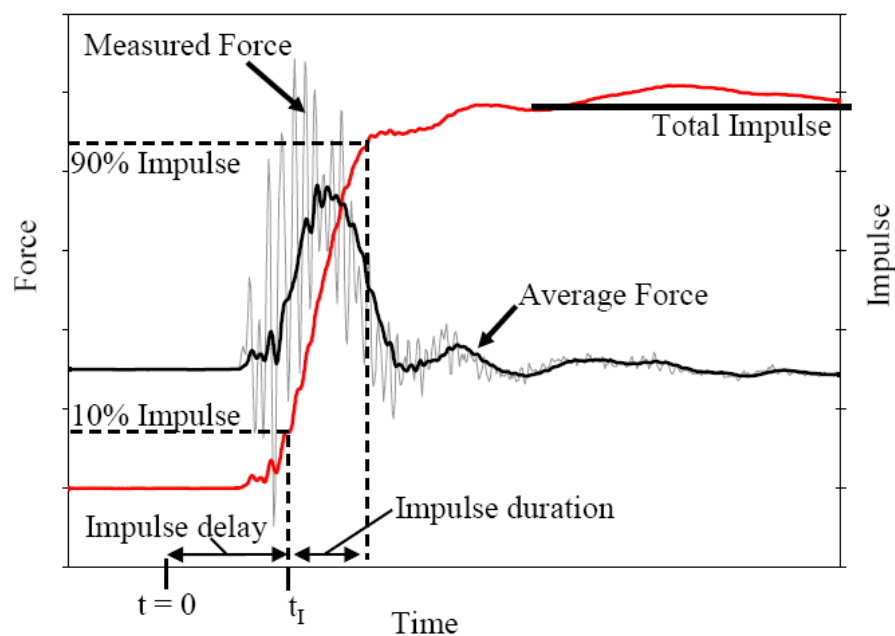


Figure 17: Force sensor output result

4.1.4.1 Force Sensor Calibration

Before using the force sensor for determining the burn characteristics, it needs to be calibrated. This is done using static weights. The sensing setup consist an inner rod, an outer ring and a urethane damper. The sensor is secured along the inner rod using a grade 8, 5.8” bolt and the actuator mounting assembly is attached to the outer ring. A 200 gm weight is hung from the sensor in the positive force direction. Using this weight the sensor sensitivity is adjusted to measure the corresponding 2 N force. A series of dynamic calibration measurements were made to measure the burn times to less than 2 ms and minimize the errors in calculating impulse values while using a damper. These measurements help in comparing calculated impulses from a known input impulse. The input impulse is supplied by dropping a ball of known weight onto the actuator mounting assembly from a fixed distance and recording the force using the force sensor. The measurements were repeated for three different weights of 0.1 g, 1 g, and 7.5 g being dropped from a distance of 27 mm. The force recorded is integrated to obtain impulse generated. In order to reduce high frequency vibrations that occur due to metal to metal collision, a thin layer of clay is pressed to the impact zone of the mounting assembly. Addition of this clay layer is critical because any elastic collisions between the ball and the mounting assembly would make the impulse calculated to be higher than the actual impulse. This layer of clay not only helps in causing an inelastic collision between the ball and the mounting assembly but it effectively reduces the rebound velocity of the ball to zero.

The momentum at impact is obtained from:

$$\vec{L} = m\sqrt{2g\Delta z} \quad (12)$$

This is equal to the impulse at impact by:

$$I = \Delta (m\vec{v}) \quad (13)$$

Figure 18 shows results obtained from calibration tests for three different balls of mass 0.1, 1 and 7.5 g each dropped from a distance of 27 mm onto the sensor. The momentum at impact is calculated using Equation 12 to be 0.0727, 0.7275 and 5.556 mNs respectively. The actual impulse calculated from the sensor is 0.08, 0.81 and 5.71 mNs respectively. With an error percentage of 10%, 11.4% and 2.8%, these results show a good agreement between theoretical and measured impulses. The small variation between the measured and input impulses can still be explained by several factors such as a numerical integration error or due to a slight elastic collision between the dropped ball and the mounting setup. Nevertheless, this experiment confirms that the actuator impulse measured using a force sensor is reasonable.

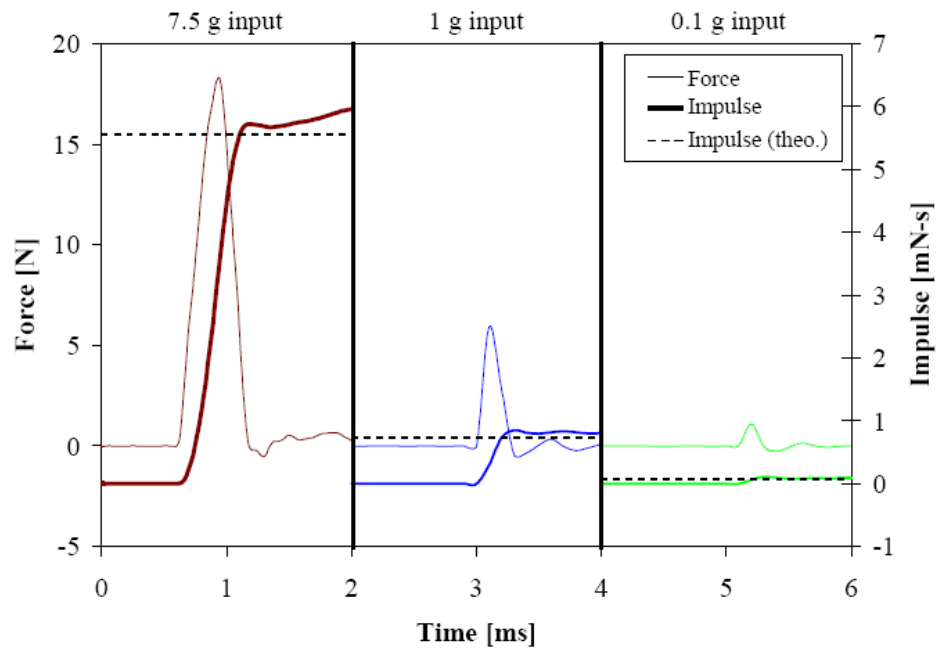


Figure 18: Force sensor impulse calibration

4.1.5 Impulse Measuring Setup

In order to measure the impulse generated from microjet actuators, the above mentioned force sensing setup is used. However, this measuring setup suffers from the disadvantage of obtaining impulse from time resolution of the force profile, which is subjected to errors because of external vibrations caused by the system. Several other impulse measuring setups such as pendulum style force measuring system are reported in the literature [43, 44]. This approach is ideal for measuring impulse delivered from small scale actuators as it is highly sensitive to extremely small impulse variations without any vibration errors. For our testing purposes we developed a ballistic pendulum setup and compared the impulse obtained from these measurements to the impulse obtained from the force sensing measurements. This comparison helps in optimizing the actuator performance as this setup is more sensitive for measuring low impulse delivered by the actuators than the force sensor setup.

A ballistic pendulum is a classic method for determining the velocity of a projectile. A typical ballistic pendulum consists of a mass attached to one end of a pivot arm, with the arm and mass free to rotate, as shown in Figure 19. In a perfectly inelastic collision, a bullet is fired into the stationary pendulum, which captures the bullet and absorbs its energy. This accelerates the mass, generating kinetic energy. The stationary pendulum now moves with a new velocity just after collision. Because of this collision, the center of gravity of the pendulum and the ball is raised from the initial equilibrium position of the pendulum to a height above that position. As the height increases, a potential energy due to gravity builds up. As the property of conservation of energy requires that the total energy of the system be conserved, the velocity comes to zero at

some maximum elevation change. The potential energy of the mass at the maximum elevation change is equal to the maximum velocity at the bottom of the pendulum arc, so elevation change can be related to the momentum of the pendulum. As the momentum and the total impulse are equal, the total impulse applied to the mass is calculated based on the vertical displacement of the mass. The detailed calculations for obtaining the total impulse are shown in this section.

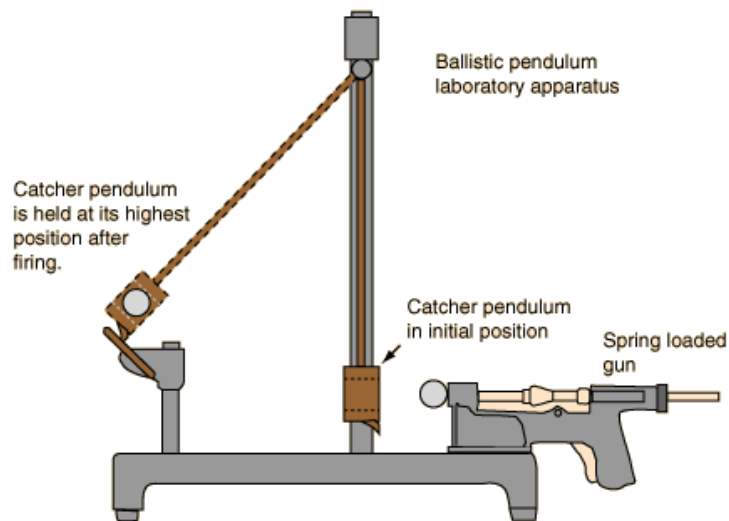


Figure 19: A typical ballistic pendulum setup [83]

The ballistic pendulum setup that is used for measuring impulse from microjet actuator is shown in Figure 20(c). Two 32 AWG copper wires (0.2032 mm) are used to form a 43.4 cm pendulum arm. The individual wires are tightened around nylon bolts that are used to adjust the length of each wire, setting the total length of the pendulum wire. The nylon bolts are fixed at 53 cm apart, so that the length of each support wire is 50.8

cm. The pendulum mass is suspended inside an enclosure to reduce the effects of airflow in the room on the movement of the mass and the position of the vibrometer is adjusted so as to focus on the center of the pendulum mass. The mass that is used to form the pendulum was stereo-lithographed using epoxy in the shape of a sphere with inputs to provide electrical connections to the actuator as shown in Figure 20(b). Two #2-56 threaded cap screws are used to create mechanical contact between the electrodes and the pendulum wires. An additional cap screw is used to clamp the actuator firmly to the epoxy ball. A single actuator as shown in Figure 20(a) is used for testing in the ballistic pendulum. This single actuator represents each actuator in the array used during the final application.

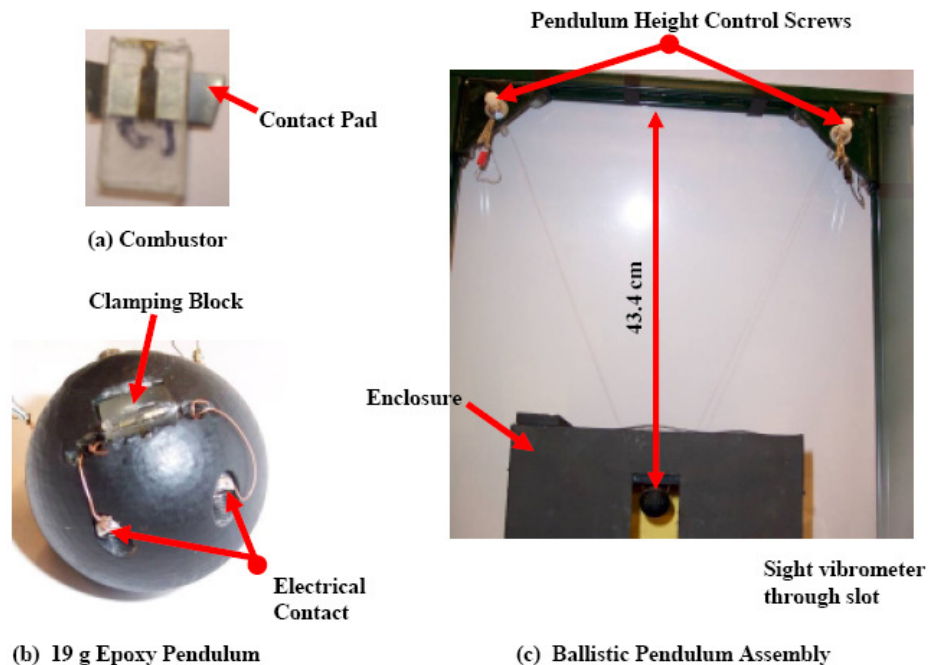


Figure 20: Pendulum experimental apparatus

The data acquisition system used for impulse measurements is shown in Figure 21, and is described in detail in the next several sections. The data acquisition setup consists of a pulse generator, a power circuit, a data acquisition board, a desktop PC with labview software and a vibrometer. A pulse generator is used to supply a square, 5 V DC pulse to a mosfet in the power circuit. A high voltage is supplied to the pendulum wires from the high voltage power supply using the power circuit. This power circuit conducts current through the pendulum wires to the actuator embedded within the mass at the end of the pendulum. The conductivity of the fuel placed between the electrodes initiates the actuation process because of joule heating. Once the actuator fires, the reaction force from the actuator swings the pendulum arm. The length of pendulum arm when initially at rest is 43.4 cm. After actuation, the pendulum arm swings and the maximum vertical displacement, Δz at time $t = \Delta t$, is measured. A laser vibrometer, which is a Polytec OFV 3001 Vibrometer Controller with OFV303 Sensor Head, is used to measure the horizontal position of the mass. A +/- 10V signal is conducted through a National Instruments BNC 2090 junction box to a National Instruments DAQ MIO-16E data acquisition board from where the data is recorded on a AMD650 desktop PC using labview software. The data record included the pulse signal, the voltage across the combustor and pendulum wires, the voltage across the mosfet in the power circuit, and the displacement signal from the laser vibrometer. Figure 22 shows sample data gathered from the ballistic pendulum for conductive propellant filled actuator.

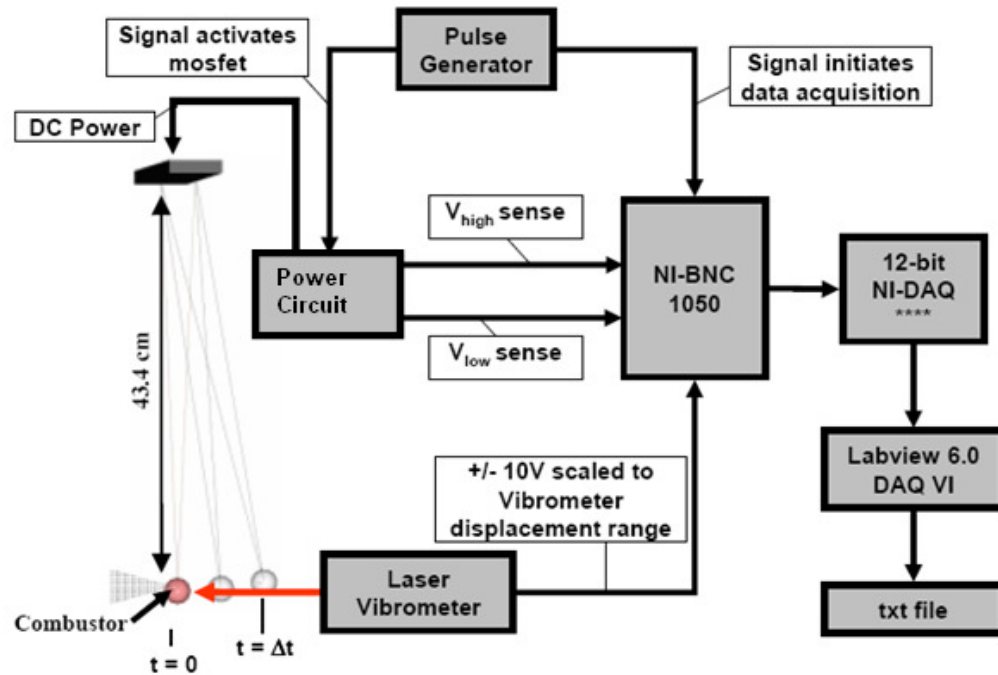


Figure 21: Pendulum measurement flowchart

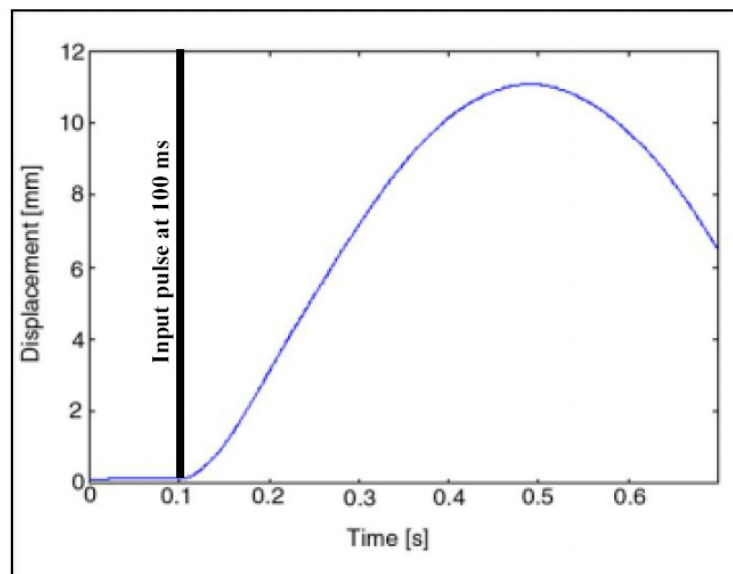


Figure 22: Vibrometer output from pendulum setup

4.1.5.1 Impulse Calculations

The impulse generated by the actuator is measured using the signal obtained from the laser vibrometer. The laser vibrometer measures the horizontal position of the swinging mass as an equivalent voltage signal. As the pendulum arm is pivoted, the angle, Φ , formed by the pendulum arm with the vertical at the fixed end can be obtained from the horizontal displacement, Δx , and the length of the pendulum, L_{pen} , as:

$$\tan(\Phi) = \frac{\Delta x}{L_{pen}} \quad (14)$$

The horizontal position measured from the vibrometer is typically less than 20 mm. Hence, for small angles, $\Phi = \tan(\Phi)$ and the vertical displacement of the mass is calculated to be:

$$\Delta z = L_{pen} (1 - \cos(\Delta x)) \quad (15)$$

Because of this displacement of the pendulum ball, the center of gravity of the pendulum and the ball is raised from its initial equilibrium position to a height above that position. As the height increases, a potential energy due to gravity builds up. As the property of conservation of energy requires that the total energy of the system be conserved, the velocity comes to zero at some maximum elevation change. The potential energy of the mass at the maximum elevation change is equal to the maximum velocity at the bottom of the pendulum arc, so elevation change can be related to the momentum of the pendulum by:

$$mv = m\sqrt{2g\Delta z} \quad (16)$$

This net change in momentum of the pendulum is equal to the impulse applied to the

pendulum. Substituting Newton's law into the definition of impulse yields:

$$I = \int_{t1}^{t2} F \cdot dt = \int_{t1}^{t2} \frac{d}{dt} (mv) dt \quad (17)$$

The specific impulse is then obtained based on the total impulse measured by the ballistic pendulum. The mass of the fuel burnt is measured by weighing the actuator before and after the combustion process using a microbalance. The specific impulse is then obtained by dividing the total impulse with the mass of the fuel burnt using the equation:

$$I_{sp} = \frac{I}{\Delta(mg)} \quad (18)$$

4.1.6 Ignition Electronics Setup

The process of electro-thermal ignition of conductive solid propellant is a series of complex processes. It starts by the production of electrical energy from an ignition source. When sufficient electrical energy is supplied from the ignition source to the conductive propellant as shown in Figure 23, the temperature of the propellant increases until its decomposition temperature is reached. In this figure, for time $t < 0$, no current flows through the conductive fuel as the switch between power supply and actuator is open. At $t = 0$, the switch is closed, resulting in an electrical path between the power supply and conductive fuel. The ideal electrical characteristics for such a system will be as shown in Figure 24. As constant voltage is supplied from the power supply, the voltage across the actuator remains constant. With the supply of electrical current, the temperature of the fuel increases with time. As the fuel resistance is dependent on temperature, the conductivity of the fuel decreases with time resulting in a decrease in

flow of current through the propellant. Once the fuel reaches its decomposition temperature, it ignites at time ' t_{ignition} ', releasing combustion gases. After time ' t_{ignition} ', as no more conductive fuel is present in the actuator, the circuit breaks and the current at the actuator finally drops to zero. Ignition power, which is defined as the power consumed in actuator ignition is a characteristic of the electrical circuit that varies with time between the onset of application of ignition energy and the onset of ignition itself as shown in Figure 24.

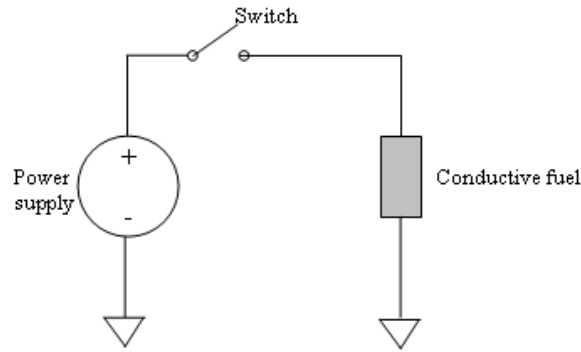


Figure 23: Ignition source schematic

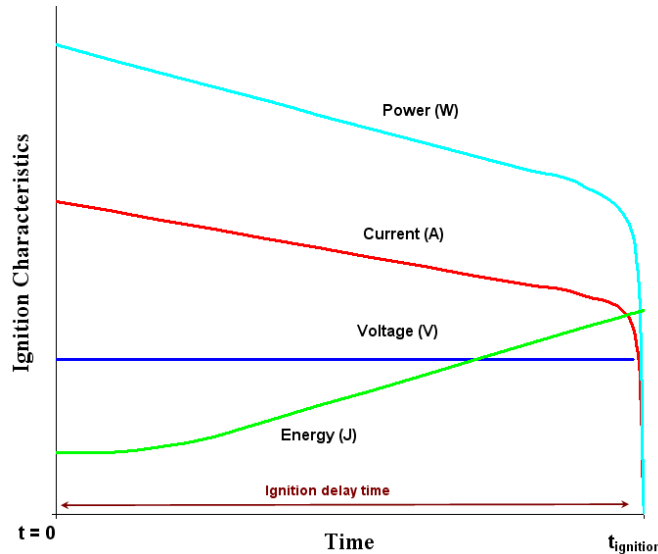


Figure 24: Ideal ignition characteristics expected for conductive fuel actuator

However, the above mentioned electrical characteristics are expected for an ideal case, where all the energy supplied from the power supply is supplied to the actuator without any losses. In reality, there are several losses associated with the components used in the electrical circuit. For example, when a capacitor alone is used to supply electrical energy to the actuator, a constant voltage cannot be supplied to the actuator, instead, the voltage gradually drops as the capacitor is discharged and the fuel resistance is increased. If the capacitor is allowed to recharge after ignition, the voltage sharply rises back to the original value. At the onset of ignition, the current falls sharply as shown in Figure 25 since the vaporizing fuel no longer provides a conductive path.

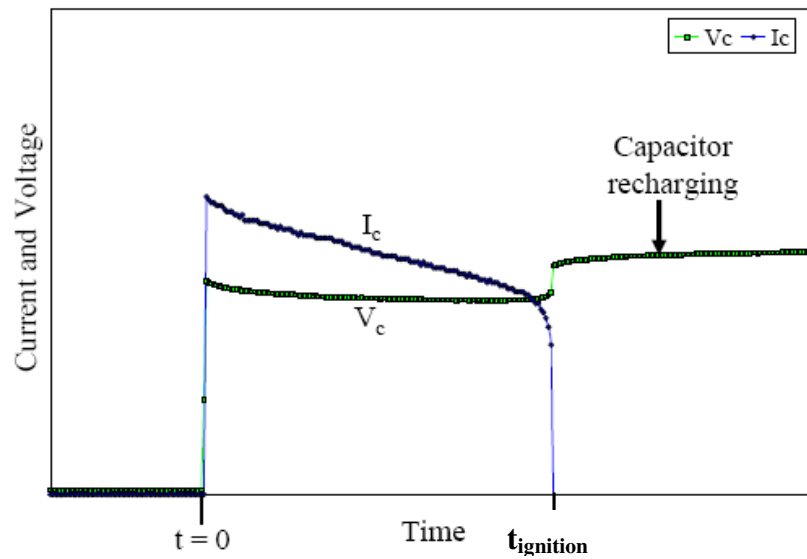


Figure 25: Typical voltage and current data obtained with a capacitor as ignition source

Repeatable power output and secure electrical connections are extremely significant while choosing the supply electronics. It helps in minimizing the ignition delay time variations that might be attributable to electronics, thus enabling precise time control of actuator initiation. Also, the faster the supply of electrical energy from the ignition source, the lesser would be the delay time of ignition. In addition, for all the components used in the power circuit, portable alternatives should be available so that the power circuit can be replicated in a portable form without any significant losses to be integrated into a portable application.

For the purpose of testing these microactuators, two circuits are developed. The first power circuit is developed for lab scale testing purposes and it makes use of larger electrical components available. This circuit is used during the characterization of the microactuators in our laboratory. Hence, this is discussed in detail in this section. The second circuit developed is a portable alternative to the first, so that it can be integrated with the actuators for portable applications. It supplies the same power ratings as the first but utilizes smaller electrical components. Though we have characterized the portable circuit, as it is not used during lab scale testing, it is not detailed in this section but instead discussed in Appendix B.

4.1.6.1 Equipment and Setup

The lab scale testing power supply presented in Figure 26 is used to heat the conductive propellant placed between two electrodes via joule heating using capacitive discharge. The main components of the circuit include a high voltage DC power supply, a capacitor, a mosfet and a pulse generator. Other minor components include a toggle switch, a push button, a mosfet driver and voltage dividers. A capacitor with ratings of

560 μF capacitance and 250 V maximum voltage is connected in parallel with a high voltage power supply with a maximum operating voltage of 1200 V (Kiethley Instruments). The capacitor is used to store the required electrical energy and later supplement it to the actuator via pulse delivery through a mosfet switch. An external pulse generator is used to activate the mosfet. The power mosfet (International Rectifier IRG4P254) has maximum ratings of 250 V and 55 A. As the required gate voltage for this mosfet is high, it is used along with a compatible mosfet driver so as to reduce the requirements for the gate voltage drive signal to 5 V. A toggle switch is used in the circuit to connect and disconnect the power supply when required in order to charge the capacitor. Three 23 k Ω resistors placed in parallel are connected in series with the high voltage power supply so as to make the capacitor the load of choice during the discharge of voltage. Two voltage divider circuits are placed on either side of the actuator to measure the voltage drop across the combustor and across the mosfet. A voltage divider is obtained by connecting two resistors in parallel. The voltage drop obtained across the mosfet is used to calculate current through the mosfet according to the technical data sheet supplied from the manufacturer. The obtained voltage is recorded using a 12-bit, data acquisition board (National Instruments DAQ MIO-16E) with a junction box (National Instruments BNC-2090). Labview software is used to record voltage and current data on an AMD650 Desktop PC. The sensing signal is sampled at 120 kHz to maximize sampling of the force sensor. The maximum input voltage to the data acquisition board is $\pm 10\text{V}$. Once the ignition process is over, the high voltage power supply is disconnected and any remaining energy in the capacitor is discharged using a push button. Figure 27 shows the actual power circuit setup used during testing.

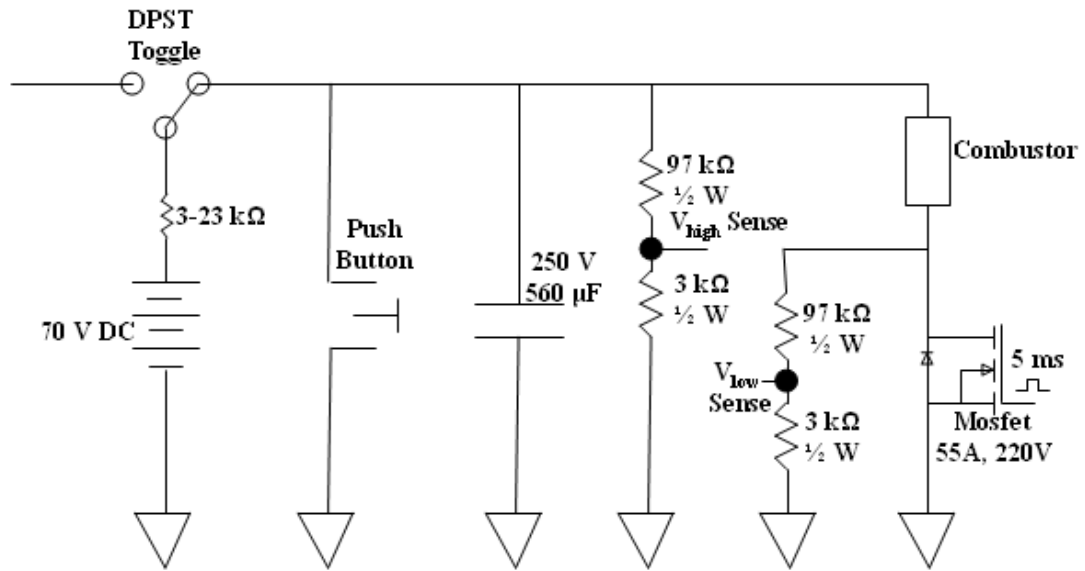


Figure 26: Power supply schematic used for testing

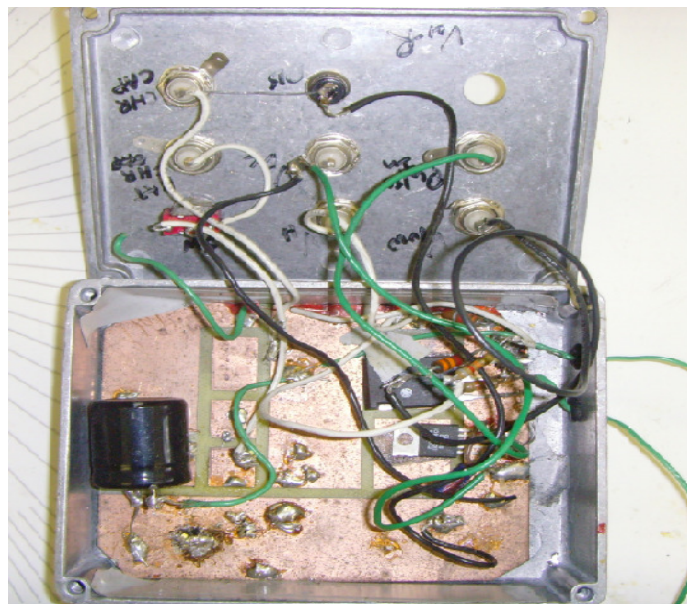


Figure 27: Power supply used during testing

From the voltage data obtained from this sensing setup, ignition characteristics such as ignition power and ignition energy are calculated as follows:

Ignition Power: The ignition power is calculated based on the recorded voltages from the high voltage divider and the mosfet voltage divider see Figure 26. Both voltage dividers scaled the actual voltage so that it could be captured on the data acquisition system described in Section 4.1.6.1. According to the manufacturer's technical data sheet, the drain current, I_c , could be related to mosfet's drain-to-source voltage for each gate voltage. Based on this information, the drain current is calculated accordingly using voltage values measured at the mosfet. The proportionality constant between the drain current and the mosfet voltage is obtained to be 9 when a gate voltage of 7.5 V is used. The pulse power ' W_c ', then is simply the current times the voltage, where the uncertainty increases as the voltage across the fuel decreases. To summarize:

$$\Delta V_c = (V_{high} - V_{low}) \quad (19)$$

$$I_c = 9 V_{low} \quad (20)$$

$$W_c = \Delta V_c * I_c \quad (21)$$

Ignition Time: Reviewing Figure 26, the combustor is placed on the high voltage side of the power mosfet. When the mosfet is activated, the mosfet drain voltage is pulled near ground, allowing current to flow through the actuator and mosfet. As mentioned previously, the current flowing through the fuel causes joule heating of the conductive fuel. At an appropriate temperature, the actuator then ignites, breaking the circuit. The ignition event is marked by a drop in current through the mosfet. The optimum pulse width for the ignition process is chosen based on this ignition time, so that the ignition happens within the duration of the applied pulse.

Ignition Energy: The ignition energy is calculated by numerical integration (trapezoid rule) of the discretely calculated electrical power. The sampling rate of the data acquisition board was 120 kHz. The ignition energy is calculated until the time ignition is observed. Figure 28 shows the result trend of the power and ignition energy for a standard combustion event. The electrical power dissipated in the conductive fuel dropped as the capacitor is discharged. Numerical integration of power was performed by the following approximation:

$$E_i = \frac{1}{2} (W_i + W_{i-1}) (t_i - t_{i-1}) + E_{i-1} \quad (22)$$

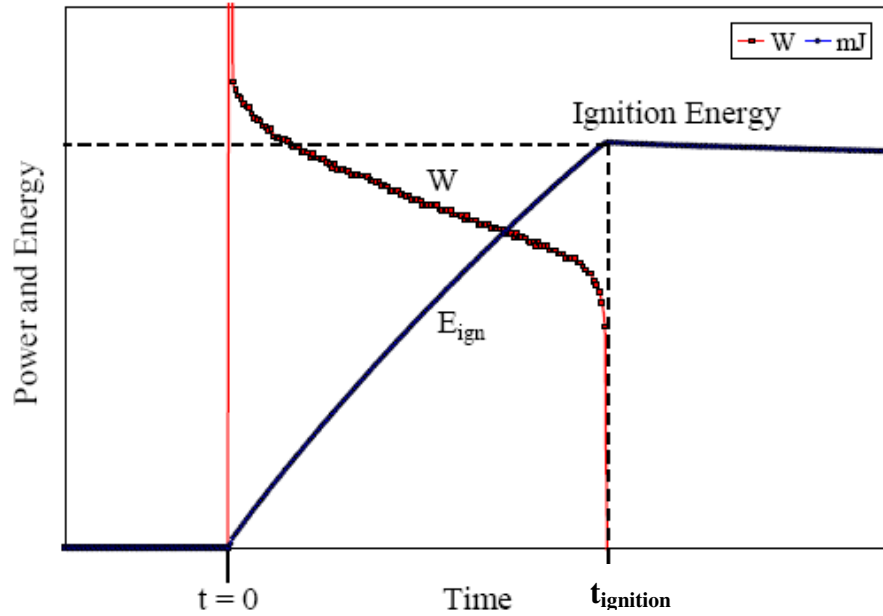


Figure 28: Typical electrical power and energy data obtained

4.1.6.2 Actuator Electrical Packaging Issues

The electrical interface between the ignition electronics and the microjet actuator must be carefully considered. In order to transfer electrical energy from the electrodes to the propellant, the electrode material chosen should have good electrical and thermal conductive properties. The use of ideal electrode materials is not always practical if they are difficult to connect to control electronics. The cost savings of batch fabrication will be lost if excessive time and money are required to establish electrical connections. As mentioned earlier, one of the limitations of lamination technology is the increased difficulty in establishing electrical connections to control electronics.

Hence, we focused on proposing a solution to this limitation where good electrical contacts could be achieved by soldering on to the electrode material or by using conductive epoxy to join the control electronics with the electrode material. For these reasons, brass material is chosen as the choice for electrode material. Brass is an alloy of copper and zinc with a melting point of about 930°C and a density of 8400 kg/m³. It has an electrical resistivity of $20 \times 10^{-9} \Omega\text{m}$ and can easily be soldered onto printed wiring boards without significant surface preparation. Figure 29 shows a jet actuator array that utilizes soldering technique to connect brass electrode to external wiring for electrical connections. Laser patterned solder tabs were made in the electrode array and buswires are passed through these tabs patterned on each electrode. These tabs effectively make the actuator a surface mount device. The buswires can then easily be passed through a printed wiring board and soldered to contact points on the printed wiring board. Also, the buswire can be passed through multiple arrays, allowing the arrays to be stacked during the final application. Alternately, conductive epoxy could be used to join brass to external

wiring. Conductive epoxy connects the buswires to the electrode tabs patterned in brass. Conductive epoxy connections easily facilitate stacks of actuators, but are somewhat expensive.

The contact resistance of soldering joint is much less than the conductive epoxy joint. However, care must be taken while soldering as the fuel gets heated because of the heat transferred from the electrode material to the fuel. This might lead to accidental misfiring of the actuators causing a safety issue. This issue could be eliminated by using conductive epoxy. Though the conductive epoxy connections have some contact resistance associated with it, as this resistance is much smaller than the resistance of the propellant, conductive epoxy connections can be feasible in our laminated microactuator systems.

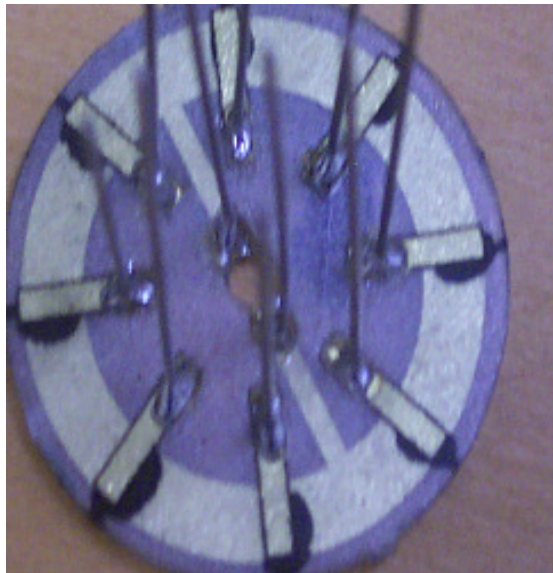


Figure 29: Microactuator array with connection wires attached using soldering technique

This chapter provided the detailed information on conductive propellant processing and several testing methods and apparatus used during the characterization of chemical based microactuators. A force sensing setup is used to measure the thrusts delivered by the microactuators and a ballistic pendulum setup is used to measure the impulse delivered by the actuators. Finally, an ignition electronics setup is presented in Section 4.1.6 to supply the required electrical energy to the conductive propellant. The ignition circuit is characterized to obtain the ignition power and energy required by the actuators to sustain combustion.

4.2 Physical based Microactuators

The physical based microactuators operate on the principle of electro-thermal arc generation. The actuator consists of a microchamber filled with liquid propellant placed between two electrodes. When sufficient electrical energy is supplied to these closely spaced electrodes, an arc is discharged between electrodes building up temperature and pressure within the system. This causes a phase change of the propellant within the chamber and the high pressured propellant exits the chamber in the form of a fluidic jet, through a nozzle. The released jet is characterized for thrusts delivered and its duration using a force sensing setup and ignition electronics setup. Finally, the released jet is used to create micro conduits in skin by placing skin in the path of the jet. The treated skin is then tested for its permeability using permeability testing setup and histology examination setup.

4.2.1 Force and Burn Time Measuring Setup

For characterizing the microjets for released thrust and durations, the same force sensing setup described in Section 4.1.4 is used. This setup consists of a piezoelectric

ring type force sensor securely mounted and calibrated. The obtained signal from the force sensor is converted to proportional charge or voltage using a charge amplifier. This electric signal is then fed into a data acquisition system, stored and recorded on a computer as force vs. time. Figure 30 shows a sample result of the acquired force vs. time data from a physical jet actuator and the released jet characteristics are determined from this data.

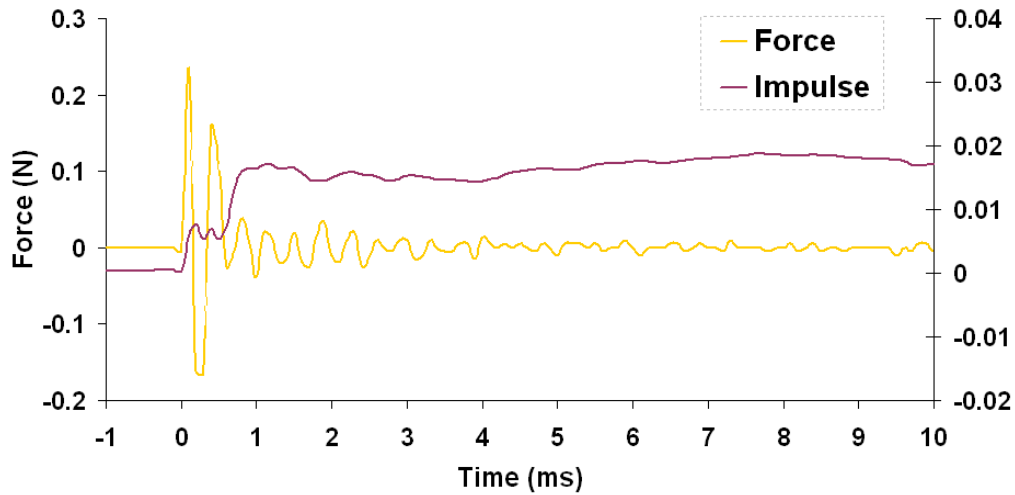


Figure 30: Force and Impulse obtained from physical microjet actuators

4.2.2 Ignition Electronics Setup

The ignition electronics circuit used to supply the necessary electric current to the microactuator is discussed in Section 4.1.6. Repeatable power output is required from the supply electronics to obtain good reproducibility in microjet generation both in terms of

force delivered and the duration of the released jet. The power supply presented in Figure 26 is used to heat the propellant placed between two electrodes via arc generation using capacitive discharge. Ignition power, time and energy are calculated according to equations mentioned in Section 4.1.6.

4.2.3 Permeability Testing Setup

For performing skin characterization experiments, heat stripped human epidermis is used to verify the creation of micro pores when exposed to microjets. First, heat stripped human epidermis is prepared for transdermal permeability and histology experiments. For this purpose, sections of human skin are obtained from autopsy (Emory University of Medicine Body Donor Program, Atlanta, GA) and plastic surgery procedures. The skin is stored at -80°C (FZU-13; Thermotron Industries, Holland, MI) until use. Both whole skin and just the epidermis layers are used for testing purposes. Before separating the epidermis from the dermis using a heat stripping technique, the skin is removed from the freezer and allowed to thaw completely for 3-4 hours.

A heat stripping method is used to separate the epidermis from dermis [84]. Once the skin is thawed, fat is removed from the dermis by scraping it with a scalpel handle (AliMed Inc., Dedham, MA). The skin is then submerged in a 60°C water bath for 2 minutes. After removing the skin from the water bath, it is gently dried with paper wipes (Kimwipes EX-L; Kimberly-Clark Corp., Roswell, GA). The epidermis is then slowly and gently peeled off the dermis using the curved edge of a spatula. The epidermis will spread out on the water surface with the viable epidermis side down due to the hydrophilic nature of the viable epidermis [85].

To expose the skin barrier to the released jet, the skin sample is held against the

mask using a q-tip. Once the skin is exposed, the skin layer is removed and is prepared for permeability testing. A blue hydrophobic dye (Trypan blue solution (0.4 %), Sigma Chemical Corp.) is applied on the epidermis. After 10 minutes the blue dye is removed and the stratum corneum is patted dry with a wipe. The under side of epidermis is viewed by light microscopy (Olympus SZX12; Melville, NY) to determine if the dye goes across the skin.

4.2.3.1 Quantitative Drug Permeability Measuring Setup

Once the epidermis is pierced by thermo-mechanical ablation, pieces of exposed epidermis are loaded into Franz diffusion chambers to measure permeability. Franz diffusion is a standard model used to measure the delivery rate of drug through membrane in transdermal drug delivery research [86]. A Franz diffusion chamber (Vertical diffusion cell – Franz cell; PermeGear, Hellertown, PA) is shown in Figure 31. The upper compartment is the donor compartment and it contains a solution of drug molecules to be delivered across the epidermis into the receptor compartment below. Both the compartments are greased to prevent leakage when the chamber is assembled.

The epidermis is exposed to the jet before hydrating because the Young's modulus of stratum corneum depends on hydration [87]. The epidermis is placed on ten layers of tissue paper or on top of dermis. Pieces of epidermis and support mesh (300 μm polypropylene woven screen cloth; Small Parts, Inc) are loaded into the diffusion chambers and both compartments are then filled with phosphate buffer saline (PBA; Sigma Chemical Corp.). The donor compartments are sealed and then the loaded chambers are stored for 2 hours at 32 °C to hydrate the skin. These chambers are placed on the multi-water-immersible stirrer in a 32°C water bath (Immersible multi-stirrer, Cole

Parmer; Vernon Hills, Illinois). The donor compartment is in contact with the stratum corneum side of the skin. The lower compartment is the receptor compartment and it contains 5 ml of well-stirred phosphate buffered saline. It is in contact with the underside of the viable epidermis. Calcein is used for model drug. The PBS solution in the donor compartment is replaced with a calcein solution with 1 mM concentration. We assume that steady state of concentration in a receptor compartment achieves within an hour. After 3 hours, a portion of the receptor solution is sampled. Calcein intensity in receptor is analyzed using a spectrofluorometer (QM-1; Photon Technology International, South Brunswick, NJ) and calcein concentration is interpreted from a calibration curve made by the prepared drug solution with the known value of the concentration. The epidermis is removed and placed on a glass slide. The size of holes the micro jets make is then inspected under a fluorescent microscope (IX-7, Olympus) to calculate flow flux of mode through epidermis. Other drug analog molecules such as sulforhodamine were also tested for permeability. Sulforhodamine B (Molecular Probes, Eugene, OR) is used as a low molecular weight drug analog and Texas red BSA (Molecular Probes, Eugene, OR) is used as a high molecular weight drug analog. The concentrations of sulforhodamine B and Texas red BSA in the donor solution are 1 mM and 0.01 mM respectively.

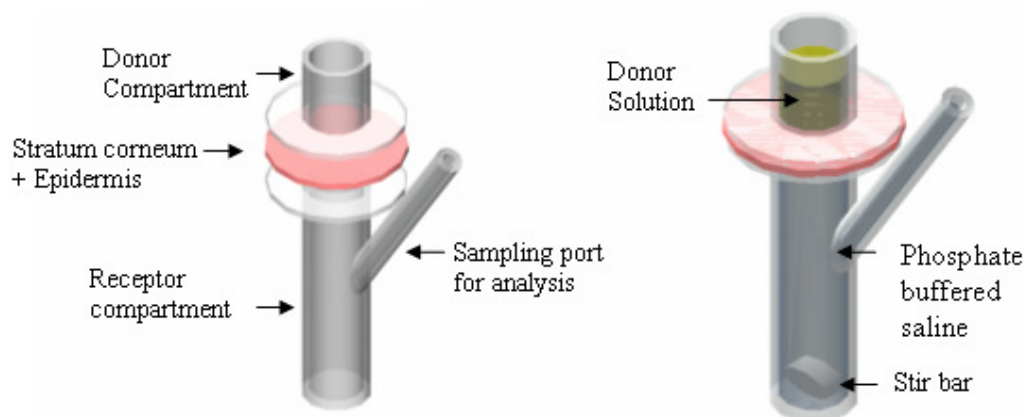


Figure 31: Quantitative skin permeability measuring equipment

4.2.4 Histological Skin Examination

Histology is the study of the microscopic anatomy of cells and tissues. It is performed for examining the exposed skin tissue under a light microscope to visualize the drug diffusion through the pores created by the micro thermal ablation system. For our histological examination, full thickness porcine cadaver skin without subcutaneous fat layer and human epidermis skin are chosen. After the skin is exposed to the microjets with approval from the Georgia Tech IACUC, the skin is placed in the Franz cell and exposed to the drug from the donor solution until the drug diffuses through the micropores developed. After the determined application time: 1, 6 and 12 hours, skin samples were prepared for histology by placing them in a cryomold, immersed in O.C.T compound (Tissue-Tek, Sakura Finetechnical, Tokyo, Japan) and freezing them using liquid nitrogen. Thin tissue sections of about 20 μm thick were prepared using a cryostat (Cryo-Star HM 560 MV, Microm, Walldorf, Germany) maintained at -23°C . Each cryo-

sectioned sample is H&E stained. H&E staining is the most common staining method in histology. This staining method involves the application of a basic dye hematoxylin, which colors basophilic structures with blue-purple hue and alcohol based acidic eosin Y, which colors eosinophilic structures bright pink. Hematoxylin staining when paired with eosin stains cytoplasm and collagen fibres pink and stains the nucleus blue. Stained samples were then collected on microscope slides (Micro-frost VWR) and later analyzed by microscopy (E600 Microscope/Image system, Nikon, Kawasaki, Japan).

CHAPTER 5

RESULTS

5.1 Chemical based Microactuators

As stated in Chapter 3, the design of microjet actuators is constrained by fabrication limitations imposed by the chosen processes. The equipment and materials used for the manufacture of the actuators limited the physical geometries that could be producible, and tests were performed to determine the range of these limitations. The laser micromachining techniques used to pattern different layers of the actuator limited the size features of each individual component of the actuator. The laser patterning of mylar sheets demonstrated line widths of 200 μm as the minimum feature size allowable by laser patterning for chamber and nozzle layers. The laser patterning of electrode material limits the maximum thickness of the electrodes to 125 μm and minimum widths to 150 μm . For electrode thicknesses of 50 μm and widths of 150 μm or greater, laser patterning of brass electrodes demonstrated fabrication yields as high as 99%. Also, commercial material availability determined the minimum thickness of each layer, thereby affecting the overall size of the microactuator chambers. These fabrication limitations are summarized and listed below:

1. Minimum combustor feature size: 200 μm
2. Minimum chamber thickness: 250 μm
3. Maximum electrode thickness: 125 μm
4. Minimum electrode width: 150 μm
5. Minimum gap between electrodes: 250 μm

6. Maximum gap between electrodes: 2.5 mm

Based on these constraints, the microactuators are designed to have chamber volumes in the 1-25 mm³ range. These actuators are then integrated with conductive solid propellants and tested for their performance. Several propellant mixtures mentioned in Table 8 are tested for fuel conductivity and ignition requirements. For each fuel mixture, its conductivity is measured and its ignition requirements are reported. The performance of the propellant integrated microactuators is then predicted using modeling and the results obtained from modeling are used to optimize the design of the microactuator. The fabricated microactuators are then tested to achieve large total impulse and short jet durations. The effects of chamber volume, nozzle dimensions, propellant mixture composition and input electrical energy on the performance of the actuator are reported. Finally, the feasibility of utilizing these microactuator arrays for maneuvering the path of a small projectile is discussed.

5.1.1 Fuel Conductivity Results

In order to validate and demonstrate the concept of rapid ignition of chemical propellants by Joule heating, the nonconductive solid propellant must be made conductive. This is achieved by adding micro or nano size conductive dopant particles to the nonconductive fuel mixtures. The conductivity of this prepared propellant mixture plays a significant role in designing the power supply and in achieving the optimum system performance. This impact of fuel conductivity on designing the power supply and in achieving the optimum performance is discussed in detail later in Section 5.1.3. Propellant formulations of various compositions are prepared for conductivity

measurements and are listed in Table 8 under Section 4.1.1. The conductivity of these mixtures is then measured using the test setup described in Section 4.1.2.

Table 10 summarizes the results obtained from conductivity measurements for various fuel compositions. The fuel compositions are mentioned as weight ratios. For example, in Table 10 Fuel 1 consists of 1 part by weight of NH_4ClO_4 , 1 part by weight of GAP, and 0.5 part by weight of carbon black. Initial attempts to make propellant conductive are performed with GAP based fuels. Micro size graphite particles are added to GAP and ammonium perchlorate in varying proportions as described in Section 4.1.1 and the conductivity of the mixture is measured. When graphite with a weight ratio of 0.5 (i.e., the ratio of weight of graphite to weight of main fuel component) is added to the mixture, GAP fuel became conductive with a conductivity of $1\text{e-}4 \text{ } \Omega^{-1}\text{cm}^{-1}$. When the amount of graphite in the mixture is doubled i.e. when it is increased to a weight ratio of 1, the conductivity of the mixture increased further to $3\text{e-}4 \text{ } \Omega^{-1}\text{cm}^{-1}$. These preliminary results indicated that polymeric, energetic fuels can infact be made conductive by adding solid conductive dopant particles. However, these mixtures are still not sufficiently conductive to be ignited with low input electrical energies. Any further attempts to make the fuels conductive by increasing the amount of graphite particles in the mixture reduced the energetic nature of the propellant and increased the difficulties associated with fuel processibility.

Next, attempts were made to replace 20% by weight of graphite in the same propellant mixture with nano size carbon black particles. The nano size carbon black is reported to be less conductive than the graphite particles by the supplier. However, the low density of nano size carbon black helps in increasing the number of dopant particles

that could be added in the same fuel volume for the same mass. With the addition of carbon black, the conductivity for the mixture increased by about 100 times when compared to the conductive mixtures containing just graphite. The conductivity for this mixture is measured to be $0.02 \Omega^{-1}\text{cm}^{-1}$. This increase in conductivity could be explained by the fact that the nano size carbon particles occupy the small spaces between the larger particles, thus acting as bridges and forming a good conductive path between the larger graphite particles. With further testing, we realized that the energetic propellants could be made conductive by adding just the nano size carbon black particles. Hence, during the testing of all other solid propellants, nano size carbon black was used as the conductive media. Potassium perchlorate based fuels and chlorate based fuels are tested with carbon black in different proportions to measure the fuel conductivity. For perchlorate based fuel, when the binder weight ratio is fixed at 0.75, the conductivity of the propellant increased from $0.17 \Omega^{-1}\text{cm}^{-1}$ to $0.55 \Omega^{-1}\text{cm}^{-1}$ with an increase in carbon black weight ratio from 0.5 to 1. A decrease in binder composition from 0.75 to 0.25 did not seem to significantly change the conductivity of the fuel mixture. For this fuel mixture a conductivity of $0.12 \Omega^{-1}\text{cm}^{-1}$ is measured. Similar testing was repeated for chlorate based fuels with carbon black as the conductive media. When the weight ratio of carbon black in this mixture increased from 0.5 to 1, the conductivity of the fuel increased from $0.1 \Omega^{-1}\text{cm}^{-1}$ to $0.25 \Omega^{-1}\text{cm}^{-1}$.

Based on the above results from conductivity measurements, among the different dopants, nano size carbon black is finalized to be used as the conductive media for all further testing. Adding carbon black as conductive dopant not only helped in achieving the desired conductivity for the fuel mixture at low weight ratios, but it also did not

drastically affect the energetic nature of the propellant. To study the effect of varying the amount of conductive dopant in the fuel mixture on fuel conductivity, potassium perchlorate based fuels and chlorate based fuels are made conductive by adding different ratios of carbon black and the conductivity of the mixtures is measured. The variation of fuel conductivity with the amount of carbon black in the mixture for perchlorate and chlorate based fuels is reported in Figures 32 and 33 respectively. For both of these measurements, the volume of fuel used was 15 mm^3 and the electrode spacing was 1.5 mm. As the amount of carbon black in the fuel increased, the conductivity of the fuel increased until a percolation limit is reached. However, the trend obtained for the conductivity dependency on amount of conductive dopant is different for potassium perchlorate based fuels and chlorate based fuels. This might be because of the different consistency of the fuel mixtures because of variation in the binder component added to both the fuels. For perchlorate based fuels, a rubbery nitrocellulose was added to the mixture and for chlorate based fuels, acetone was added as the binder. Depending on the consistency and energetic nature of the fuel, it is observed that addition of 2-20% and 0.5-2% by weight of carbon black to perchlorate based fuels and chlorate based fuels respectively made the fuels conductive enough to cause ignition without sacrificing their performance. The amount of conductive dopant needed for the ignition of chlorate based fuel is significantly less when compared to perchlorate based fuels because the potassium chlorate-antimony trisulfide fuel mixture has a much lower decomposition temperature than the potassium perchlorate-potassium ferricyanide based fuel.

For several of these fuel mixtures, the variation of fuel resistance with the physical dimensions of the propellant mixture is further investigated. The effect of

varying the fuel area and thickness on its resistance are studied. The dependency of fuel resistance on chamber area is measured for three conductive GAP based fuel compositions and compared in Figure 34. For all the three compositions, it was observed that with an increase in the area of the chamber, the resistance of the conductive propellant decreased following Ohm's law. When the area of the fuel is kept constant, the resistance of the fuel mixture decreased with an increase in weight ratio of graphite from 0.5 to 1. When some of this graphite is replaced by nano size carbon black particles the resistance decreased further. Next, attempts were made to study the effect of fuel thickness on resistance of the fuel. The fuel thickness is varied by varying the distance between the electrodes. These results are reported in Figure 35. For the same fuel composition, the conductive fuel obeys Ohm's law and its resistance decreased with an increase in area of the chamber and a decrease in fuel thickness or gap between the electrodes.

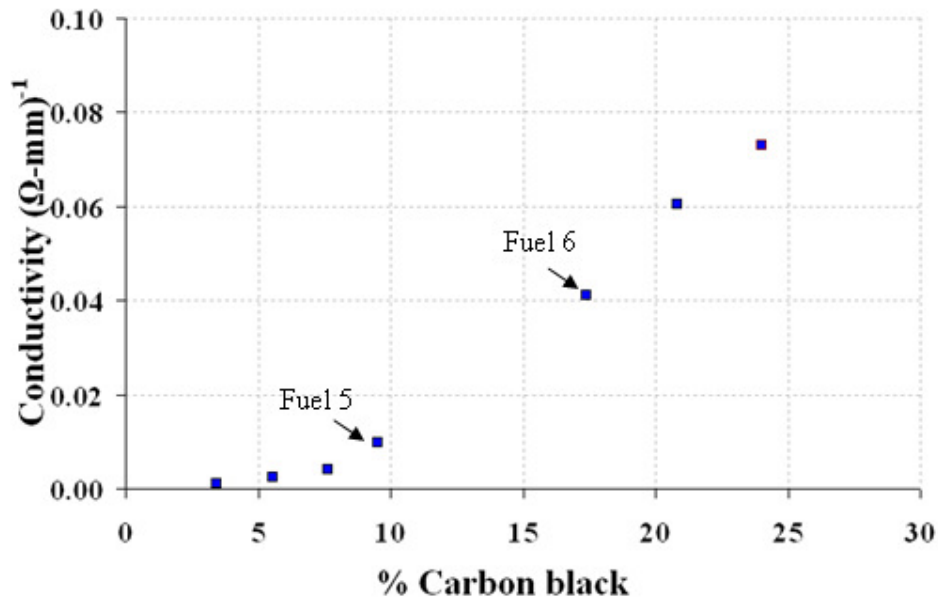
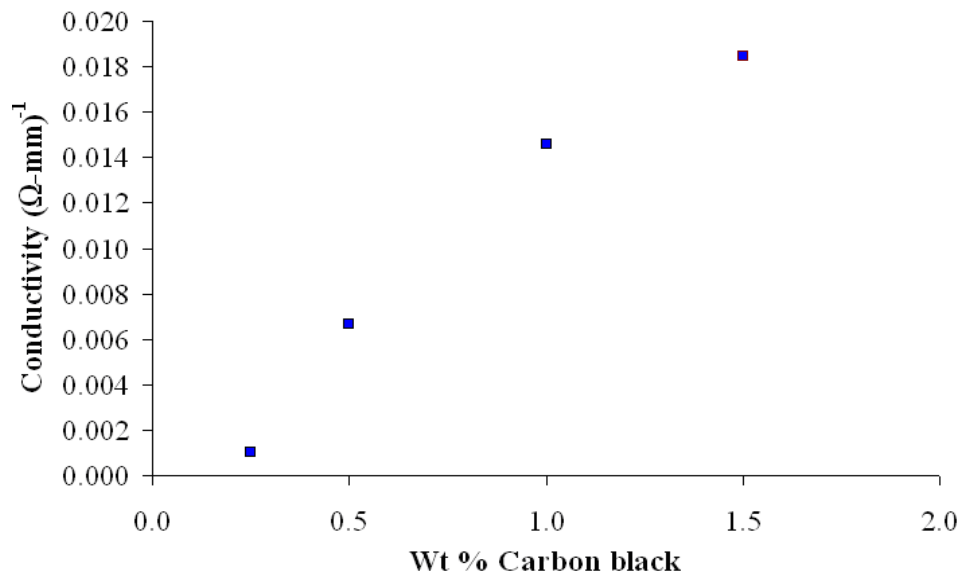


Figure 32: Variation of potassium perchlorate based fuel conductivity with the amount of conductive material

Table 10: Conductivity data for several composite propellant mixtures tested in lab

Fuel component In wt ratio	Fuel 1	Fuel 2	Fuel 3	Fuel 4	Fuel 5	Fuel 6	Fuel 7	Fuel 8	Fuel 9
KClO ₃								6	6
KClO ₄					3	3	3		
NH ₄ ClO ₄	1	1		1					
Sb ₂ S ₃								1	1
K ₃ [Fe(CN) ₆]					1	1	1		
Nitrocellulose					0.75	0.75	0.25		
GAP	1	1	1	1					
Carbon black			0.2	0.2	0.5	1	0.5	0.5	1
Graphite	0.5	1	0.8	0.8					
Conductivity ($\Omega^{-1} \text{ cm}^{-1}$)	$1e^{-4}$	$3e^{-4}$	0.03	0.02	0.17	0.55	0.12	0.1	0.25

**Figure 33:** Variation of potassium chlorate based fuel conductivity with the amount of conductive material

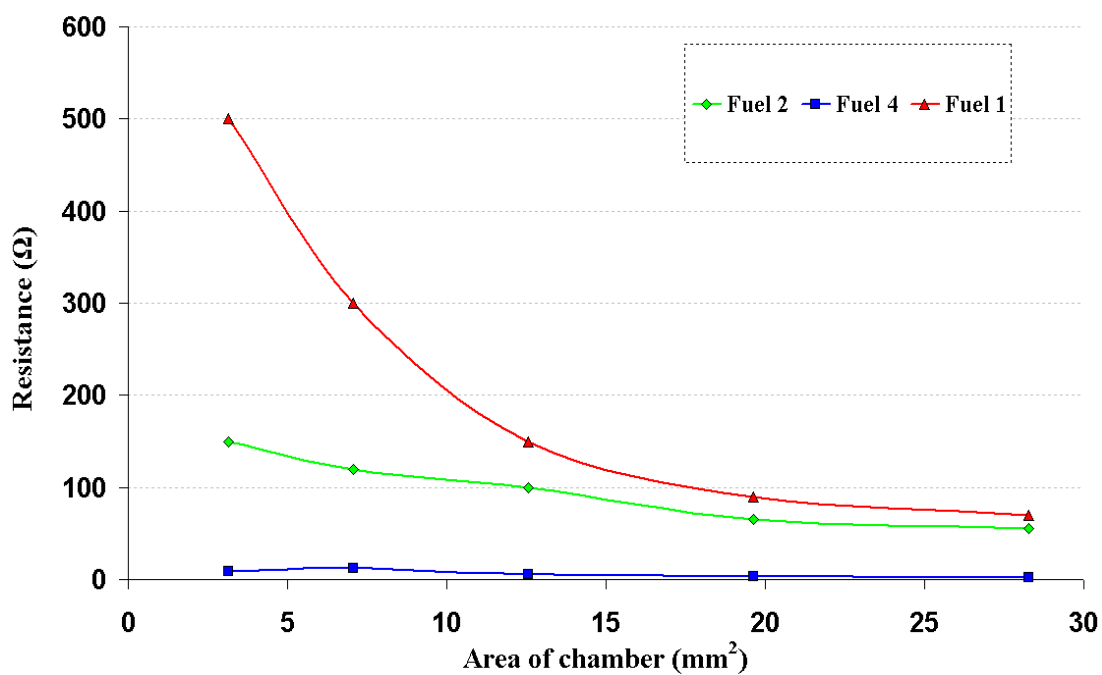


Figure 34: Variation of fuel resistance with conductive dopant and area of the fuel mixture

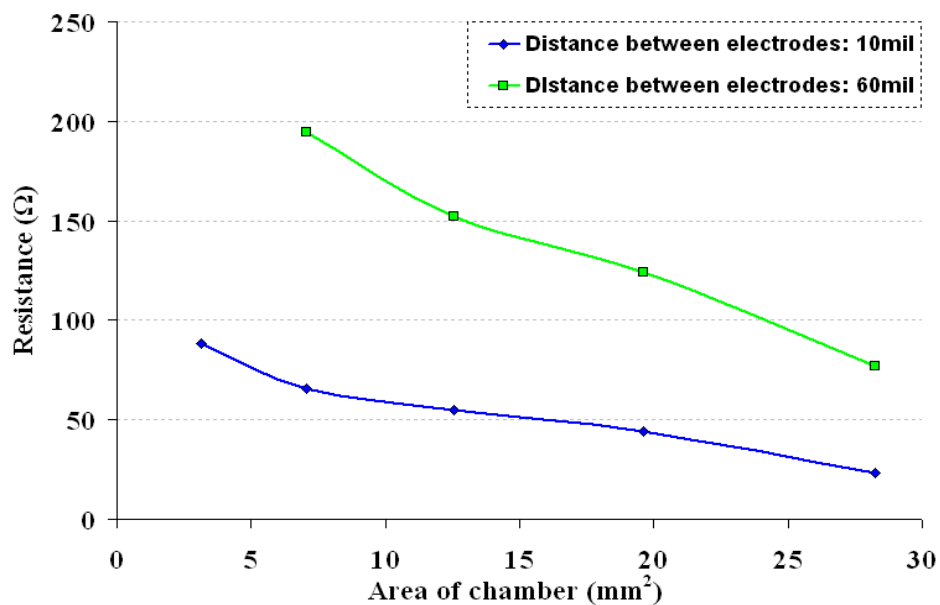


Figure 35: Variation of fuel resistance with gap between electrodes and area of the combustion chamber for Fuel 2

5.1.2 Actuator Modeling and Design

This section discusses the predicted behavior of combustion based microactuators based on simulations. The results obtained from simulations can not only be used to study the behavior of individual microactuators but they can also be used as a guideline while fabricating the microactuators to predict their performance dependency on several input parameters. An exhaust nozzle model similar to large scale chemical rockets is developed to study the behavior of impulse and discharge times delivered by microactuators with various input parameters. However, unlike large scale actuators, additional assumptions need to be made to account for the small size of the microactuators. In addition to this combustion model, an ignition model based on electro-thermal interactions between the electrodes and conductive propellant is developed to study the behavior of delay times of ignition. The solutions from the ignition and combustion models provide the resulted design criteria for the development of optimized microjet actuators.

5.1.2.1 Ignition Delay Time Simulations

Ignition delay time is defined as the time between the initial, transient period when a stimulus such as current, is applied to the propellant and the time when the combustion process actually begins. This time must be minimized to reduce the overall duration of the released jets. The delay times associated with conductive propellant ignition are predicted using electro-thermal interactions between the electrodes and the conductive dopant particles using COMSOL software. COMSOL is a multiphysics software that allows for combining various interaction modes by defining coupled PDE's so as to define the system at hand accurately. To define our system, we used a predefined multiphysics joule heating application mode which combines a conductive media DC

application and heat transfer by conduction application modes to study the electrical and thermal behavior of the conductive propellant. Using these two modes, a fully interactive system of two coupled PDE's with two different variables: ' V ' for electric potential and ' T ' for temperature are defined.

The conductive material heats up when an electric current passes through it due to electrical resistance. The potential distribution in the conductive media occurs almost instantly, but because unsteady heat transfer is a transient phenomenon, the full multiphysics model uses a transient analysis. In the heat transfer mode, resistive heating appears as a heat source. There is also a coupled effect working in the opposite direction: the material's electrical resistance varies with temperature, increasing as the material heats up. In the conductive media DC application mode, the electric potential ' V ' is the solution variable. The generated resistive heat ' Q ' is proportional to the square of the magnitude of the electric current density ' J ':

$$Q \propto |J|^2 \quad (23)$$

Current density, in turn is proportional to the electric field, which equals to the negative of the gradient of the potential ' V '. The coefficient of proportionality is the electrical resistivity $\rho = \frac{1}{\sigma}$, which is also the reciprocal of the temperature dependant electrical conductivity $\sigma = \sigma(T)$. Combining these facts gives the fully coupled relation:

$$Q = \frac{1}{\sigma} |J|^2 = \sigma |\nabla V|^2 \quad (24)$$

The resistive heating source term is defined as ' Q_{dc} ' in heat transfer application mode when using the joule heating predefined multiphysics coupling. The electrical conductivity is also a temperature dependant variable. Over a range of temperatures, the

electrical conductivity is a function of temperature according to:

$$\sigma = \frac{1}{\rho_0 (1 + \alpha(T - T_0))} \quad (25)$$

Where ‘ T ’ is the dependant variable for temperature from the heat transfer application mode. The values for ρ_0 (resistivity at reference temperature), α (temperature coefficient), and T_0 (reference temperature) are assigned to match our modeling situation. The resistivity of the fuel mixture was obtained from experiments. For predicting the behavior of ignition delay time with fuel dimensions, one particular resistivity value based on the carbon black composition is used during experiments. For studying these effects, a resistivity value of 0.022 Ωm for Fuel 6 is used. For studying the conductive dopant composition effects, the resistivity of the fuel mixture is varied according to the values obtained from experiments for three fuel mixtures (Fuel 5, 6 and 7). The temperature coefficient value is obtained to be $-5.6 \times 10^{-4} / \text{K}$ for carbon black from the literature. To combine the heat transfer effects, the following heat transfer equation is solved along with the conduction application mode.

$$\rho C_p \frac{\partial T}{\partial t} - \nabla(k \nabla T) = Q \quad (26)$$

The parameters of this equation are the density ‘ ρ ’, heat capacity ‘ C_p ’, thermal conductivity ‘ k ’, the temperature ‘ T ’, and an externally generated heat source ‘ Q ’ term.

Modeling using COMSOL software consists of the following major steps:

1. Defining the application modes.
2. Defining options and settings for the model.
3. Defining the geometry of the system.
4. Setting the physics for the system.

5. Generating a mesh.
6. Computing for the solution.
7. Post processing and visualization.

For applying the appropriate boundary conditions, a voltage of 70 V is supplied to one boundary of the supply electrode and the other electrode is kept at ground. The initial potential distribution across the conductive fuel and electrodes is written as a function of position. A distributed electrical resistance is applied across the electrodes and the propellant. Similarly initial and boundary thermal conditions are defined for both electrodes and the propellant. All the boundaries are initially kept at room temperature. The model is simulated using the default courser mesh in COMSOL for a time frame of 1 ms with a time interval of 0.01 ms and absolute tolerance of 0.001. The coarser mesh utilized for our simulations has a maximum scaling size factor of 5 with an element growth rate of 2. The obtained variation of temperature with time and position across the fuel between electrodes is presented in Figure 36. The fuel temperature increased with an increase in time for which the electrical energy is supplied to the propellant. However, from the simulation result we observed a sharp rise and drop in temperature at the edges of the conductive propellant. This effect could either be real effect in the system because of unusual variations in voltage distribution across the propellant or it could be a visual effect due to the mesh size variation across the system during the simulation. If it is due to the voltage distribution this effect needs to be further investigated. Otherwise, it could be safely ignored. In order to check this, we observed the voltage distribution within the system. Figure 37 shows this distribution across the length of the propellant between electrodes. We did not observe any unusual variations in the voltage distribution. Hence,

it was concluded that these peak effects can safely be ignored.

The ignition time delays are then determined by measuring the time it takes for the propellant system to reach the decomposition temperature of energetic propellant. The decomposition temperature of the KClO_4 mixture is obtained from the literature [88] where Massey studied the effects of heating a KClO_4 mixture with a Nichrome igniter. The above modeling is repeated for all the chamber geometries used in experiments with a fuel resistivity of $0.022 \text{ } \Omega\text{m}$. Both the gap between electrodes and the area of the chamber is varied to study the effect of these parameters on ignition delay times. Also the input DC voltage supplied to the electrodes is varied to study its effect on delay times. The time taken to reach the decomposition temperature is noted for each individual simulation and all are plotted together in Figure 38. The volume of the chamber and the electrodes distance are varied in simulations by replicating the exact length and width of the electrodes and the conductive propellant as per experiments. A voltage of 70 V is supplied for these simulations. In general, it was observed that the ignition delay times decreased with a decrease in the electrodes distance and an increase in fuel volumes. As the distance between electrodes increased from 1.5 mm to 2.0 mm, the ignition delay times increased from 0.68 ms to 1.16 ms for an input voltage of 70 V and a combustion chamber volume of 15 mm^3 . As the distance between electrodes is further increased to 2.5 mm, the delay time increased further to 2.54 ms. When the distance between the electrodes is fixed, the obtained ignition delay times decreased with an increase in chamber volume.

Ignition delay time variation is then plotted for different input voltages supplied. It was observed that as the input voltage supplied to the electrodes increased, the ignition

delay time reduced. From Figure 39, it can be seen that as the voltage increased from 60 V to 100 V, the delay times reduced from 0.6 ms to 0.2 ms. These results suggest that by controlling the input variables and the physical dimensions of the actuator, conductive solid propellant microactuators can easily be altered to meet the requirements for several applications. Next, efforts were made to study the effect of fuel conductivity on the delay times. For this purpose, three fuel resistivities were chosen based on the conductivities of Fuel 5, 6 and 7 and the distance between electrodes is fixed at 1.375 mm. The resistivities of each of these fuel compositions and the ignition delay times obtained for each case are reported in Table 11. It was observed that with in increase in fuel resistivity, the ignition delay times increased.

The obtained ignition delay time dependency on fuel dimensions, resistivity and the input voltage supplied can further be explained by analyzing the electrical circuit associated with conductive fuel ignition. To predict the ignition behavior of the microactuator and to estimate the dependency of energy consumed by the conductive propellant on fuel resistance and Thevenin resistance of the power circuit, we consider a simple circuit as shown in Figure 40. When a voltage of ' V_t ' is supplied from the power circuit having a Thevenin resistance of ' R_{th} ' to a microactuator having a fuel resistance ' R_f ', the current flow ' i_f ' through the propellant can be calculated using the equation:

$$i_f = \frac{V_t}{R_{th} + R_f} \quad (27)$$

Then, voltage across the actuator is its resistance times the current flow.

$$V_f = i_f R_f = \frac{V_t R_f}{R_{th} + R_f} \quad (28)$$

The amount of power consumed is calculated using:

$$P = i_f^2 R_f = \left(\frac{V_t}{R_{th} + R_f} \right)^2 R_f \quad (29)$$

The amount of energy consumed by the actuator is then calculated according to:

$$E = Pt = \frac{V_t^2 R_f}{(R_{th} + R_f)^2} t \quad (30)$$

From this equation, the dependency of energy consumed on fuel resistance can be predicted. The energy consumed by the actuator is zero when the fuel resistance is zero and it gradually increases until the fuel resistance becomes equal to the Thevenin resistance of the circuit. If the fuel resistance is increased further, the energy consumed decreases. If the resistance of the fuel is significantly larger than the Thevenin resistance of the circuit, then the energy consumed can be approximated to:

$$E \approx \frac{V_t^2}{R_f} t \quad (31)$$

The energy consumed by the actuator is directly proportional to the square of the voltage supplied and inversely proportional to the fuel resistance. As we increase the fuel thickness or decrease the fuel area, the resistance of the fuel increases according to Ohm's law. With an increase in fuel resistance, the energy consumed by the actuator decreases. Hence, it takes longer to consume the required amount of energy to start the ignition process. As the voltage supplied from the power supply increases, the amount of energy consumed by the conductive propellant increases resulting in a decrease in the delay time.

The dependency of ignition delay time on voltage can also be explained by looking at the heat generated because of resistive heating. The heat generated ' Q ' because

of resistive heating is proportional to the square of the magnitude of electric density ' J ', which in turn is proportional to the negative gradient of the potential ' V '. Combining these facts give the following relation between the heat generated and the voltage across the actuator:

$$Q = \frac{1}{\sigma} |J|^2 = \sigma |\nabla V|^2 \quad (32)$$

As the voltage drop across the propellant increases, the heat generated within the system increases resulting in a reduction in the ignition delay times.

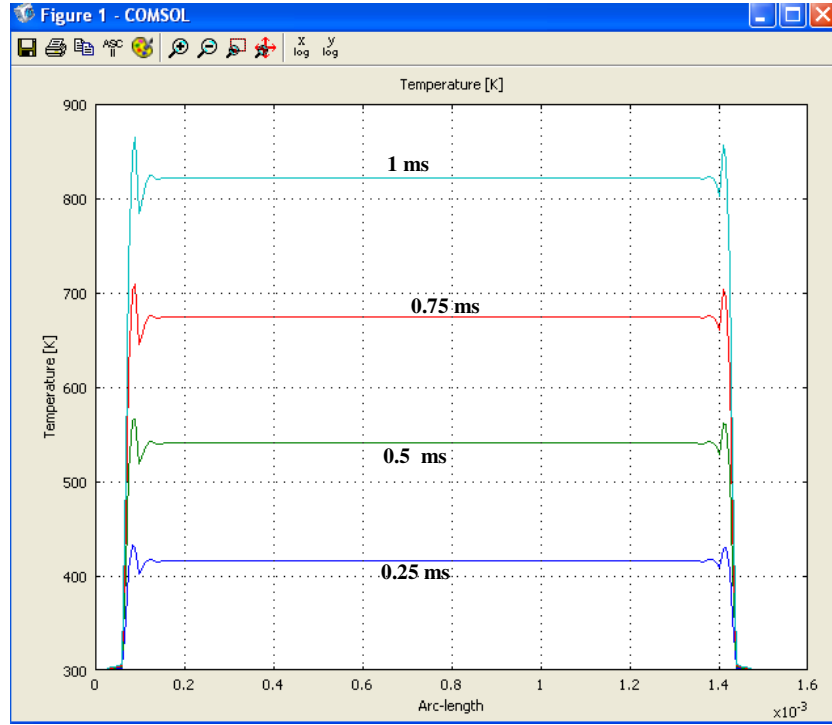


Figure 36: Estimation of temperature variation with time across the gap between electrodes

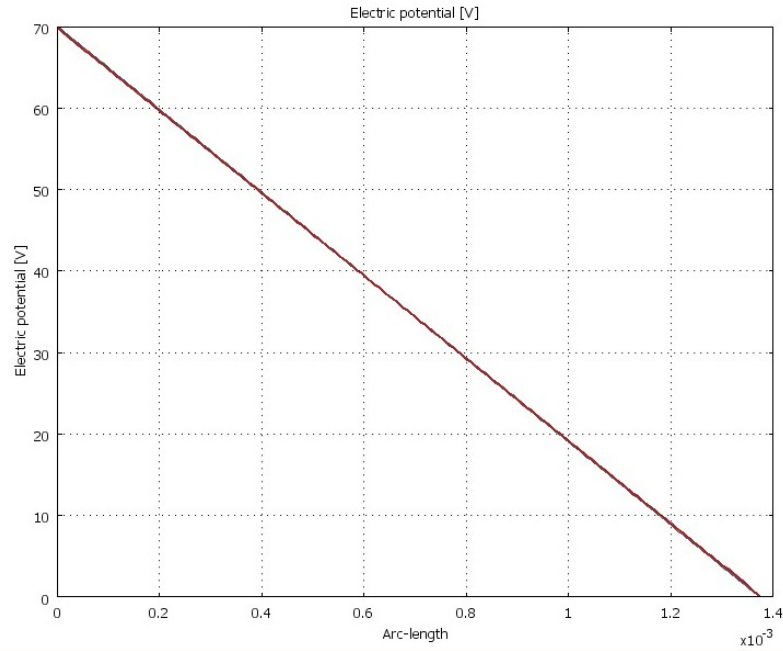


Figure 37: Voltage distribution across the conductive propellant placed between electrodes

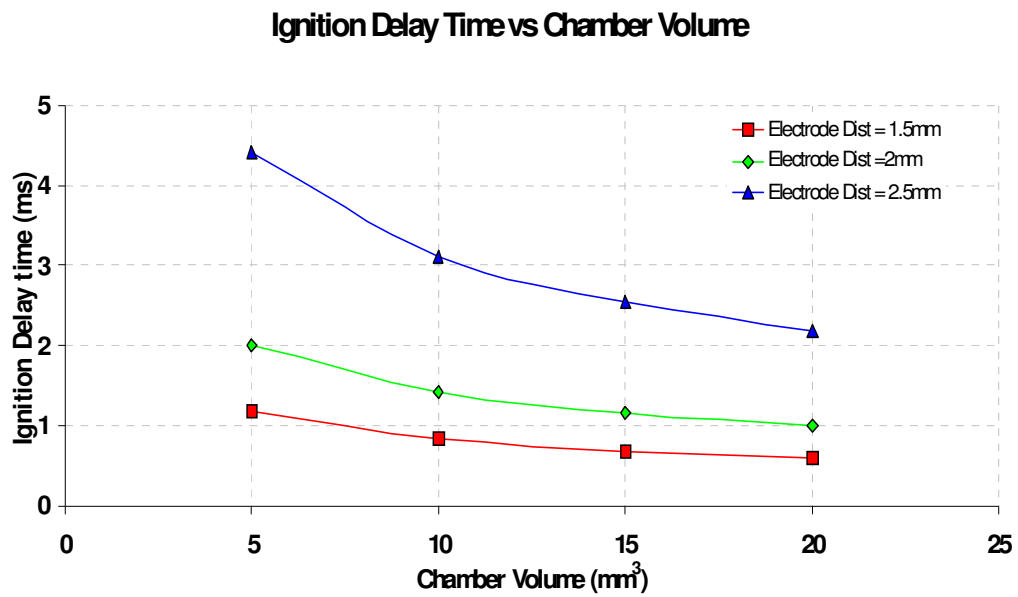


Figure 38: Predicted variation of ignition delay time with chamber volume and gap between electrodes

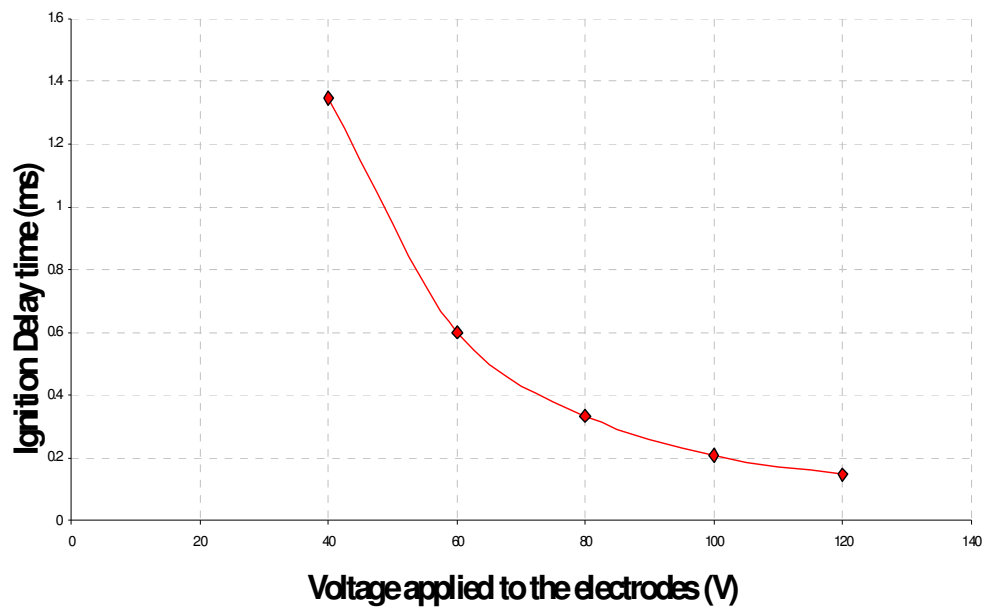


Figure 39: Predicted variation of ignition delay time with voltage applied across the electrodes

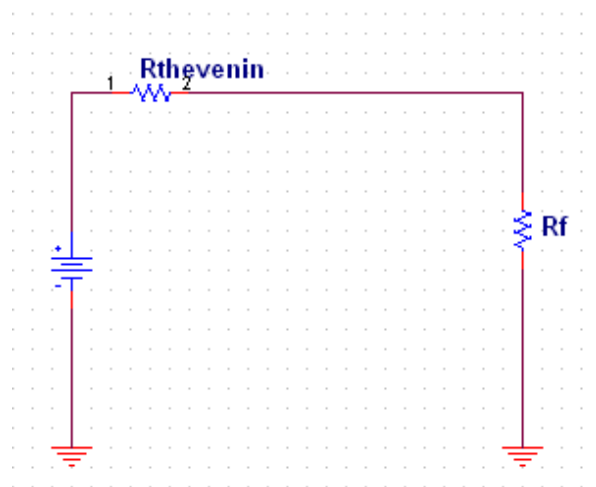


Figure 40: Simple electrical circuit with Thevenin resistance

Table 11: Predicted ignition delay times for three fuel compositions prepared in lab

Fuel type	Fuel Resistivity (Ωm)	Ignition delay time (ms)
Fuel 6	0.0182	0.8
Fuel 5	0.0588	1.9
Fuel 7	0.0833	3.1

5.1.2.2 Impulse and Discharge Time Simulations

Once the ignition process begins, the conductive propellant grains act as large, short duration heat sources throughout the propellant. Further, the ignition process occurs at multiple locations at the same time, thus making the combustion process very fast. Under these conditions, a model is developed with the assumption that the combustion and gas generation occurs on a short time scale in comparison to the time the released gases take to travel through the length of the nozzle. Hence, a nozzle-vented pressurized tank model is used for measuring the discharge time and impulse delivered by the released jet of gases. In this model, the reaction is assumed to be completed within the residence time of fuel in the chamber and the exhaust products are assumed well-mixed. The assumptions made in the development of this model are:

1. Ideal gas $PV = nRT$ (33)

2. Adiabatic, isentropic compressible flow through nozzle

$$P_1 \rho_1^{-\gamma} = P_2 \rho_2^{-\gamma} \quad (34)$$

3. Constant values of specific heat

4. Negligible expansion and frictional losses in the nozzle
5. Choked flow at the nozzle throat at some critical pressure
6. Negligible nozzle erosion

The modeling is done as two parts: First, the simple flow of the combustion gases from the pressurized tank is studied and then, a detailed study of flow of gases through a divergent nozzle is performed. The schematic of this gas expansion behavior is shown in Figure 41.

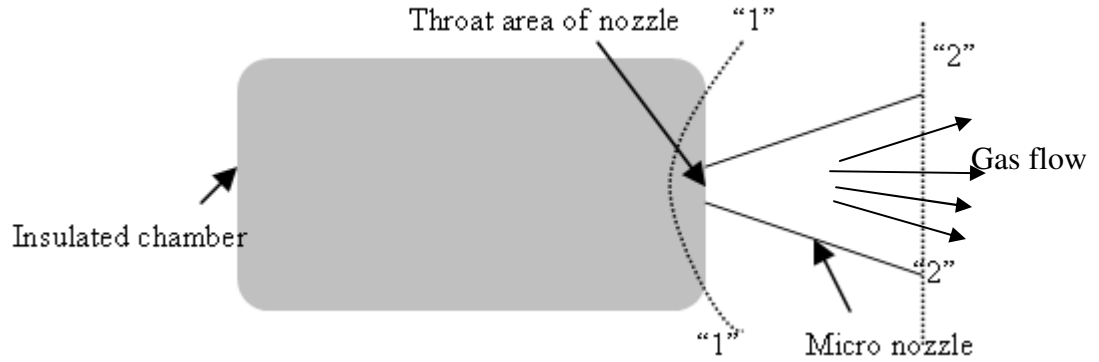


Figure 41: Schematic of flow of gases from a combustion chamber and a diverging nozzle

As the flow of released gases from the chamber is assumed to be frictionless and adiabatic, the flow behavior of gases can be described by an isentropic, reversible and unsteady state mechanical energy balance. This means that the entropy change is zero.

The total enthalpy ' h_0 ' is defined by [89]: $h_0 = h + v^2 / 2$ (35)

For relatively small openings, this unsteady flow behavior can be approximated to a quasi-steady state behavior and the system can be described using Bernoulli equation:

$$\frac{1}{2} v_2^2 + \int_1^2 \frac{1}{\rho} dP = 0 \quad (36)$$

The conservation of energy for an isentropic flow process between any sections 1 and 2 shows that the decrease in enthalpy has to be equal to the increase in the kinetic energy:

$$h_1 - h_2 = \frac{1}{2}(v_2^2 - v_1^2) = c_p(T_1 - T_2) \quad (37)$$

For ideal gases, the enthalpy is equal to the product of the specific heat and the absolute temperature. The principle of conservation of matter in a steady-flow process is expressed by equating the mass flow \dot{m} at any section x to the flow at section y :

$$d(vA/V) = 0 \quad (38)$$

When integrated, this gives a constant mass flow at any cross section x and y [89].

$$\dot{m} = \dot{m}_x = \dot{m}_y = A_x v_x V_x = A_y v_y V_y \quad (39)$$

For an isentropic flow process, the following equations hold between any points x and y :

$$T_x/T_y = (p_x/p_y)^{\gamma-1/\gamma} = (V_y/V_x)^{\gamma-1} \quad \text{where } \gamma = c_p/c_v \quad (40)$$

The nozzle is considered as a diverging section with its throat area at the side of the combustion chamber. The diverging section of the nozzle helps in expanding the combustion gases and accelerates the exhaust gases by increasing the exhaust velocity in supersonic flows and reducing the exhaust pressures to near atmospheric conditions. This allows for the conversion of internal energy of the gases into kinetic energy thus generating additional thrusts. The nozzle throat area, length and its divergence half angle determine the shape of the nozzle. All these parameters impact the gas expansion process into ambient air and as a result impact the exhaust thrust levels. The nozzle throat area A^* controls the discharge time of the released gases. The area of a two-dimensional nozzle as a function of its axial position is defined by the following equation:

$$A(x) = A^* + 2x d_c (\tan \phi), 0 \leq x \leq L \quad (41)$$

The flow of released gases through the nozzle throat is assumed to be compressible, ideal gas, adiabatic and to have a velocity of Mach 1 for a local nozzle temperature. Typically, the exhaust gases will reach sonic conditions at the throat of the nozzle, where speed of sound is given by:

$$a^* = \sqrt{\gamma RT} \quad (42)$$

Writing Equation 37 for the nozzle inlet and exit and combining with Equation 40 yields the exit velocity of gases [89]:

$$u_e^2 = \left(\frac{2\gamma}{\gamma-1} \right) \left(\frac{R_u T}{M} \right) \left[1 - \left(\frac{p_e}{p_c} \right)^{\frac{\gamma-1}{\gamma}} \right] \quad (43)$$

The flow of gases can be computed from the continuity equation, the isentropic relations and the nozzle gas velocity (Equations 39, 40 and 43) between any section in the nozzle and the chamber or nozzle inlet section as [89]:

$$\dot{m} = P_c A^* \left\{ \gamma \left(\frac{2}{\gamma+1} \right)^{\frac{\gamma+1}{\gamma-1}} \frac{M}{R_u T_c} \right\}^{\frac{1}{2}} \quad (44)$$

The thrust generated from the momentum transfer of gases along the nozzle length 'x' is then obtained from:

$$F = \dot{m} u_e + (P_x - P_a) A_x \quad (45)$$

The pressure ratio of the nozzle throat to the chamber is given by [89]:

$$\frac{P^*}{P_c} = \left(\frac{2}{\gamma+1} \right)^{\frac{\gamma}{\gamma-1}} \quad (46)$$

For a given mass flow rate, the local pressure versus cross-sectional area in the nozzle is given by the equation [89]:

$$A(x) = \frac{\dot{m}}{P_c} \left\{ \frac{2\gamma}{\gamma-1} \frac{M}{R_u T_c} \left(\frac{P(x)}{P_c} \right)^{\frac{2}{\gamma}} \left[1 - \left(\frac{P(x)}{P_c} \right)^{\frac{\gamma-1}{\gamma}} \right] \right\}^{\frac{-1}{2}} \quad (47)$$

The discharge time of released gases is then obtained by equating the discharge rate at the nozzle inlet from Equation 47 to the discharge rate from the chamber using the following equation and integrating for time:

$$\dot{m} = -V \frac{d\rho}{dt} \quad (48)$$

Setting Equation 44 equal to Equation 47 for mass flow rate yields the pressure profile vs. x , distance in the streamwise direction along the length of the nozzle. The normalized pressure ratio is then obtained by dividing the local pressure at the specific position in the nozzle with the combustion chamber pressure. The pressure ratio gives a measure of the expansion of the combustion products. With the pressure and area known at a streamwise position ' x ' along the nozzle, the thrust for a given nozzle geometry at some combustion temperature and pressure may be calculated for $x=L_{nozzle}$ according to Equation 45.

The above mentioned equations are solved using Matlab to obtain thrust and pressure ratios and the results obtained are reported here. The code used in Matlab is shown in Appendix C. An ideal nozzle expands combustion products to exhaust conditions. However in reality, a nozzle experiences frictional losses at the nozzle boundaries and releases gases by under-expansion or over-expansion to atmospheric pressure. Low divergence angled nozzles increase frictional losses and larger angles cause flow separation at the nozzle wall. The optimum divergence half angle for large scale rockets is reported to be between 12° and 17° [16]. Hence, in our simulations the effect of varying the nozzle divergence angle in this range for small scale nozzles is

studied. These results are reported in Figures 42 and 43. It is observed that varying the divergence half angle of the nozzle from 13° to 17° has little effect on varying the performance of the nozzle. Increasing the divergence half angle slightly reduced the local pressure ratio and increased the thrusts generated. The variation of local pressure ratios with divergence angle is slightly more pronounced at increased nozzle lengths. When the exit pressure of the released gases is equal to atmospheric pressure, the diverging part of the nozzle has a more profound effect for values of $A_e/A_t < 1.5$ and this effect is shown in Figure 44. This agrees with some of the results reported in the literature for micronozzles. This idealized analysis of the jet behavior with nozzle dimensions suggests that the nozzle angle is insignificant for the microactuator size scales.

The effect of varying the nozzle length on local pressure ratio and thrusts generated are presented in Figures 42, 43, 45 and 46. Choosing the right length of the nozzle is important in obtaining optimum thrust levels. If the nozzle is made too short, the gas flow cannot expand fully and the steady state cannot be reached. In general, increasing the nozzle length expands the combustion gases and increases their exit velocity thereby, resulting in increased thrusts. However, with an increase in length, the thrust and pressure ratio become less sensitive to nozzle length because less internal energy is available to be converted into kinetic energy. This behavior is confirmed from our modeling where increasing the nozzle lengths increased the thrusts delivered and decreased the local pressure ratio. For small nozzles i.e. $L_{nozzle} < 0.5$ mm, varying nozzle length has more profound effect on thrust than varying the divergence angle. In Figure 42, increasing nozzle length from 1 mm to 2 mm for a 15° nozzle increased the thrusts generated by 5%. Decreasing the length from 1 mm to 0.5 mm for a 15° nozzle decreased

the thrusts generated by 5.5%. Increasing the nozzle length from 1 mm to 2 mm for a 15° nozzle reduced the local pressure ratio by 50% from 0.050 to 0.025. Decreasing the nozzle length from 1 mm to 0.5 mm increased the local pressure ratio by 92% from 0.050 to 0.095.

The effect of nozzle throat area on local pressure ratio and thrusts delivered are presented in Figures 44, 45 and 46. Varying throat area of the nozzle has a more profound effect on varying the performance than varying nozzle length. The combustion temperature for this simulation is assumed to be 1800°K and the chamber pressure is assumed to be 50 MPa. Figure 45 shows the effect of varying the nozzle throat area across the length of the nozzle on delivered thrusts. For a nozzle length of 0.5 mm, as the throat area is increased from 1 mm² to 1.5 mm², the thrusts delivered increased by 42% from 57 N to 81 N. For a constant throat area of 1 mm², as the nozzle length is increased from 0.5 mm to 1 mm, the thrusts delivered increased by 9% from 57 N to 62 N. Figure 46 shows the effect of varying the nozzle throat area across the length of the nozzle on pressure ratio. For a nozzle length of 0.5 mm, as the throat area is increased from 1 mm² to 1.5 mm², the pressure ratio delivered increased by 22% from 0.18 to 0.22. For a constant throat area of 1 mm², as the nozzle length is increased from 0.5 mm to 1 mm, pressure ratio decreased by 39% from 0.18 to 0.11. For constant combustion chamber pressures and temperatures, the thrust can be magnified by increasing the throat area. Equation 45 shows how thrust delivered increases with increasing mass flow rate, and with increasing local pressure, $P(x)$, at the nozzle exit area, A_x .

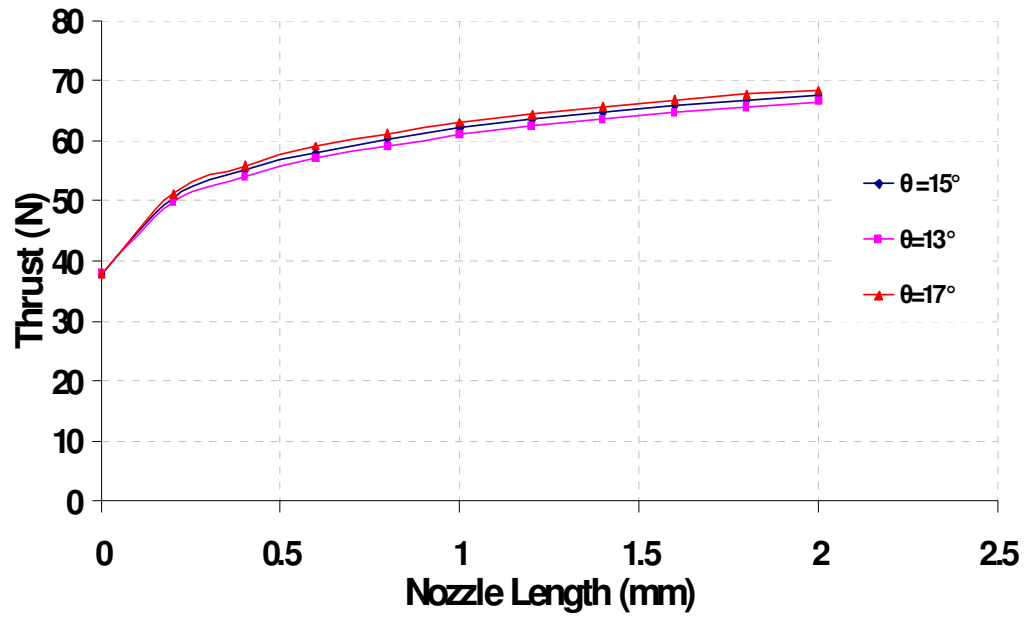


Figure 42: Predicted effect of nozzle length and divergence angle on released thrust

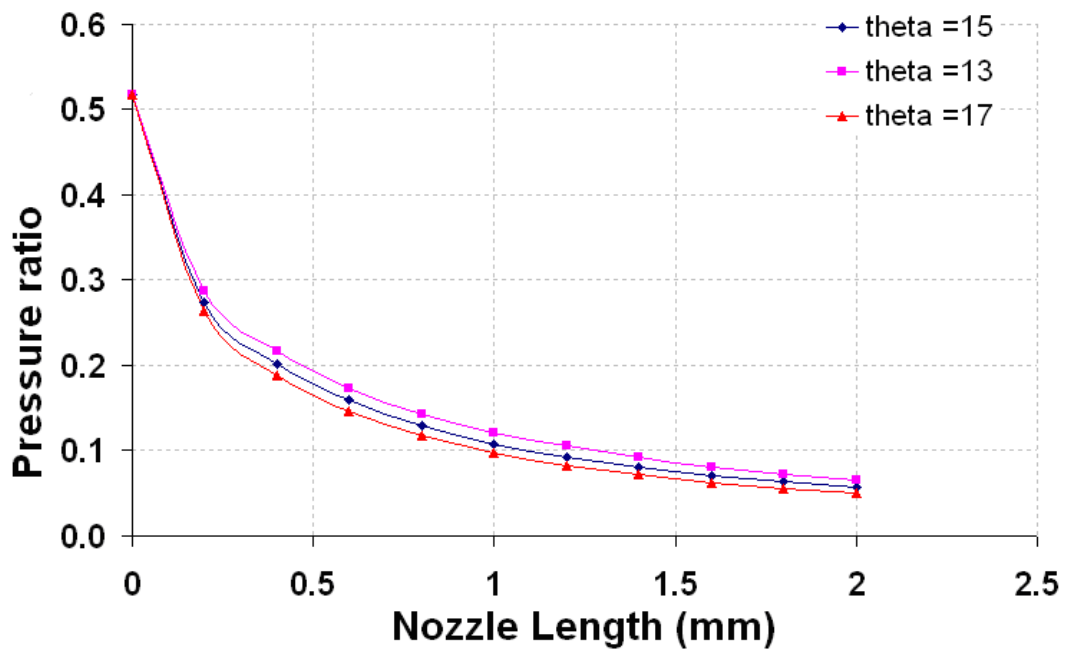


Figure 43: Predicted effect of nozzle length and divergence angle on pressure ratio

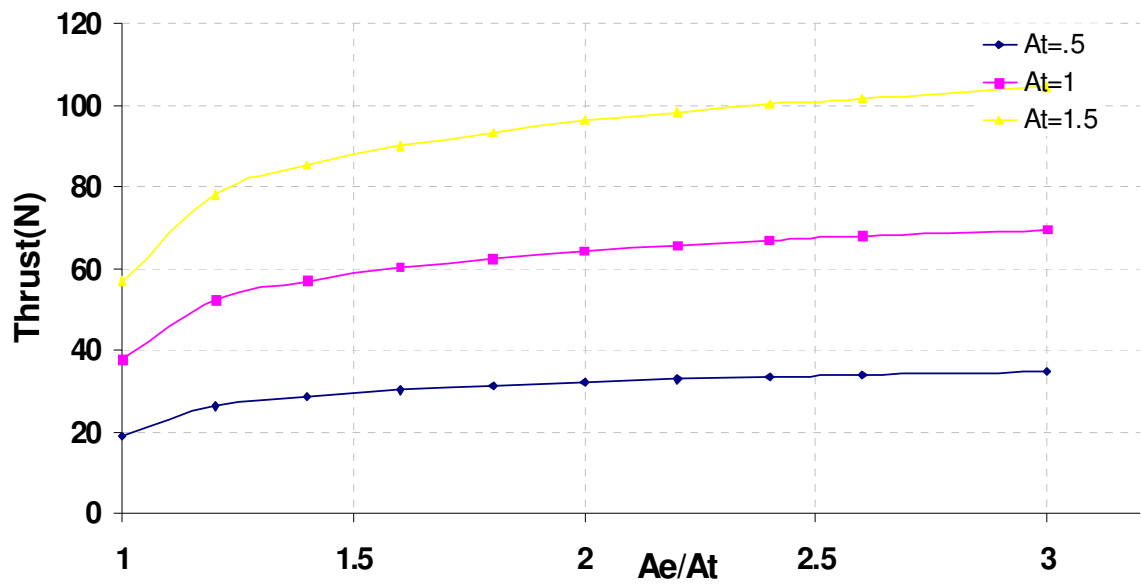


Figure 44: Predicted effect of nozzle entrance and exit dimensions on released thrust

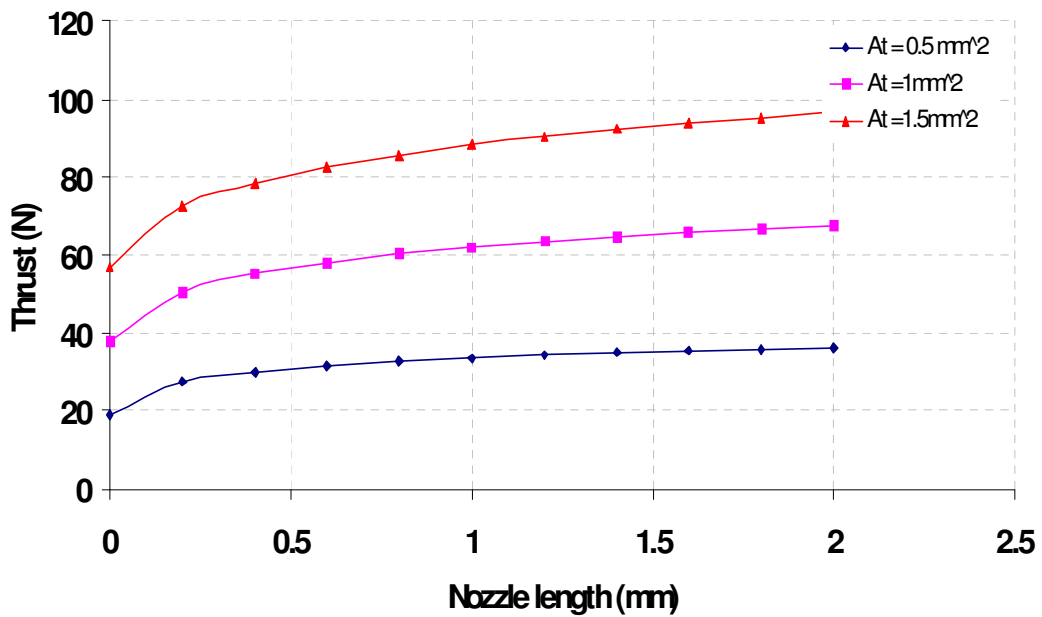


Figure 45: Predicted effect of nozzle throat area and length on released thrust

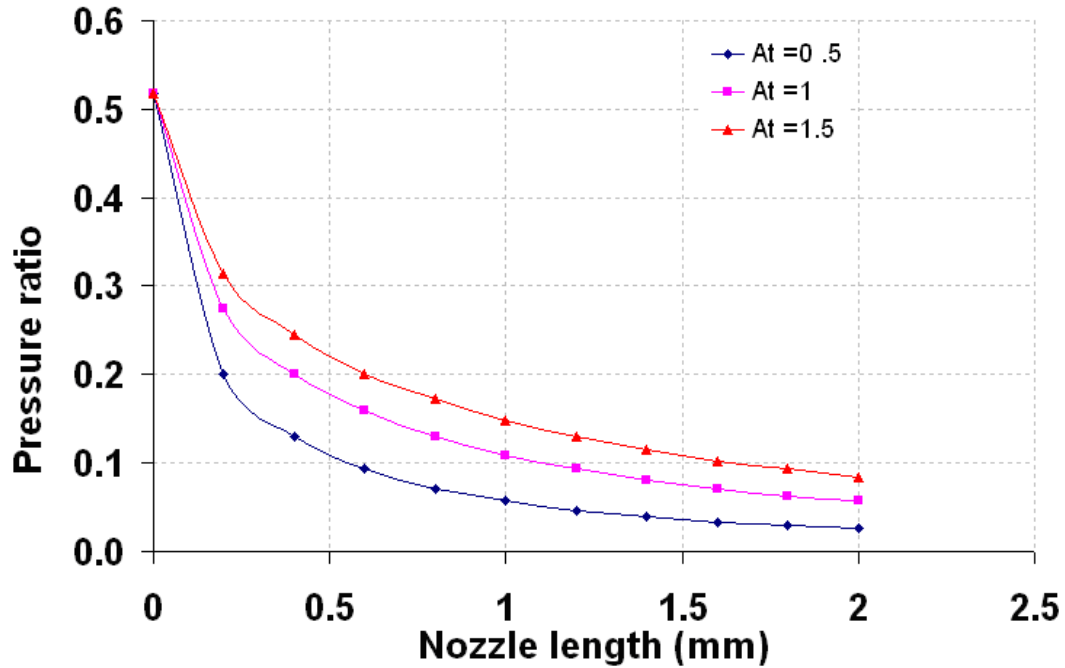


Figure 46: Predicted effect of nozzle throat area and length on pressure ratio

Figures 47 and 48 show the dependency obtained for the discharge time of released gases on nozzle throat area and chamber volume. The discharge time decreased with an increase in throat area of the nozzle and increased with an increase in chamber volume. Increasing the throat area from 0.1 mm^2 to 0.5 mm^2 for a 15 mm^3 volume chamber decreased the discharge time from 3.4 ms to 0.4 ms. Similarly, for the same throat area of the nozzle, the effect of varying the chamber volume on discharge time is shown in Figure 48. The discharge time of gases could be reduced by reducing the chamber volume. From these results, it was observed that increasing the throat area of the nozzle from 0.1 mm^2 to 0.5 mm^2 has larger effect on reducing the discharge time when compared to decreasing the chamber volume. This behavior can be explained by the fact

that as the throat area of the nozzle increases, the amount of released gases that can flow at the same time from the combustion chamber increases. So, for the same amount of gas generated, it takes less time to release all the generated gases.

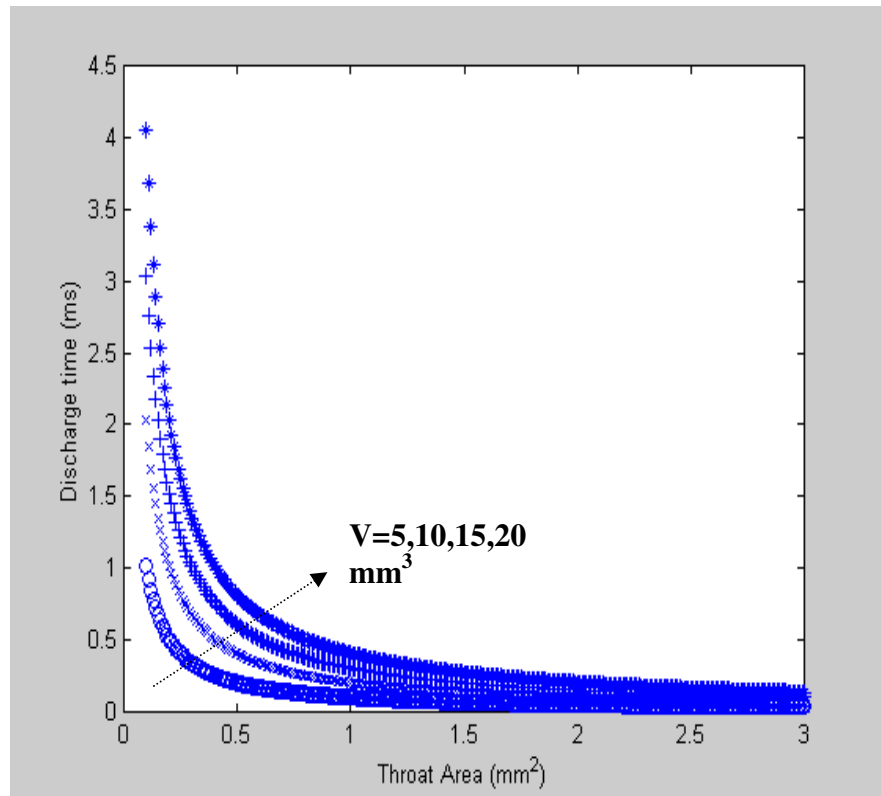


Figure 47: Predicted effect of nozzle throat area on discharge time

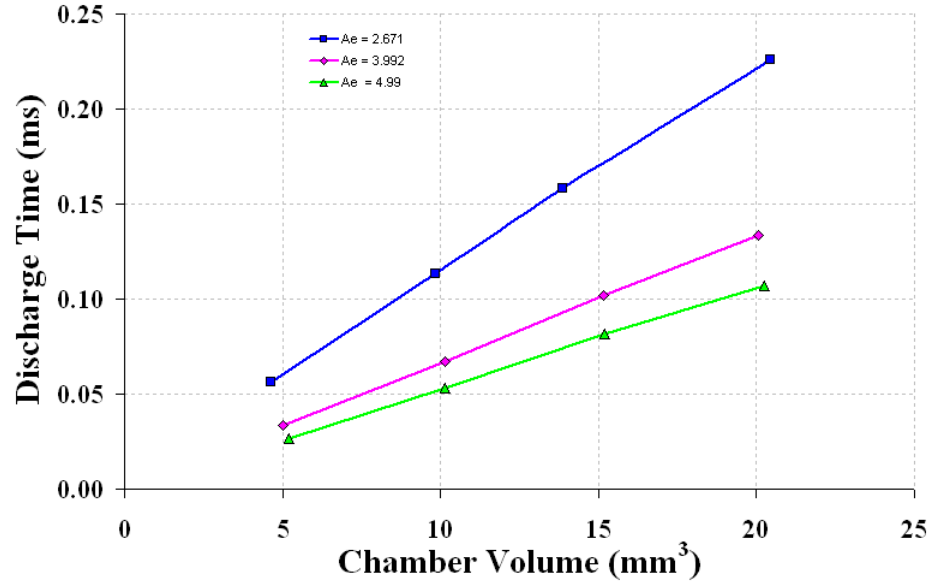


Figure 48: Predicted effect of chamber volume on discharge time

The impulse delivered by the microactuator is then obtained by integrating the thrusts delivered over discharge time according to the following equation:

$$I = \int F dt \quad (49)$$

Figures 49 and 50 show the predicted variation of impulse with the combustion chamber volume and pressure respectively. With an increase in chamber volume and pressure, the impulse delivered by the jet increases.

The specific impulse, which is an intrinsic measure of the efficiency of the propellant and propulsion system, can then be obtained by dividing the total impulse with the weight of propellant burnt according to equation:

$$I_{sp} = \frac{I_{tot}}{\rho_p V_c g} \quad (50)$$

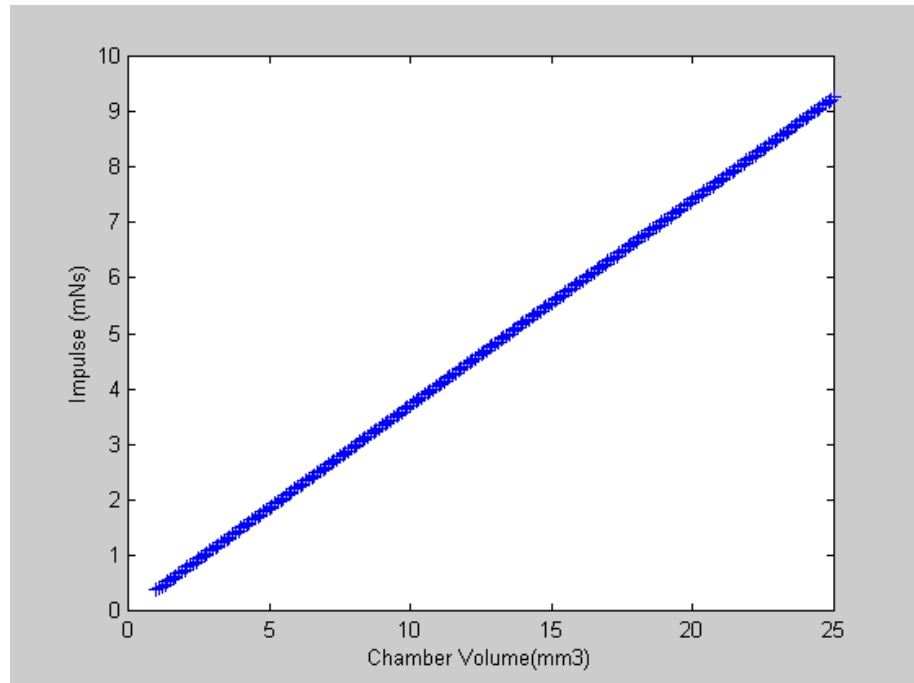


Figure 49: Predicted variation of impulse delivered with chamber volume

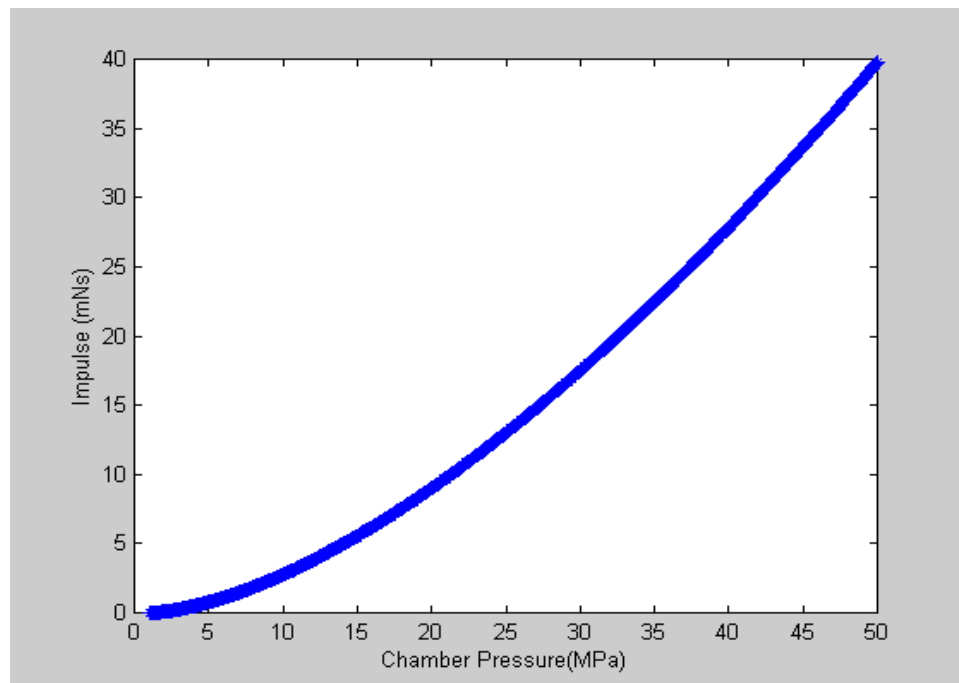


Figure 50: Predicted variation of impulse delivered with chamber pressure

5.1.2.2.1 Nozzle Design

The above analysis shows the predicted behavior of a microactuator with an ideal nozzle. The results obtained from modeling suggest that the nozzle throat area should be maximized to reduce the discharge times and to increase the thrusts delivered. As the throat area of the nozzle is increased, the exhaust rate of released gases increases thereby reducing the discharge time for the same volume of gases. However, Figure 47 shows that increasing the nozzle throat area beyond an optimum value does not improve the performance much. Further, for a chosen nozzle area, propellants with small burn rate constants may not meet the performance requirements for both duration and total impulse. In addition, assumption of an ideal nozzle neglects any frictional losses from the nozzle side walls. In reality, the heat losses from the nozzle are more pronounced and the gaseous stream loses momentum due to its interaction with the nozzle side walls. First, low-temperature walls remove heat from the product gas, reducing the ability of the gas to do useful work. Next, reactants that contact the side walls lose momentum and have less chance to collide with other reactants. This reduces the overall conversion rate of the reactants to products. Increased surface-to-volume ratios of the microactuators will increase the rate of these two effects and reduce their performance compared to an idealized prediction.

Hence, during the fabrication of the nozzle for our experiments, the nozzle design will require some iteration to obtain optimum results. The optimum nozzle length is chosen based on both good performance from modeling results and based on the structural integrity that is needed during the operation of the actuator. The size constraints of our actuator system limits the length that the nozzle can have to 2 mm. Area of the

nozzle is limited by the area and thickness of the chamber. For our experiments, the largest possible throat area is chosen so that best performance could be achieved from them based on ideal compressible flow concepts presented.

5.1.2.2.2 Combustion Chamber Design

The design of a combustion chamber is completely based on the performance parameters desired for an application. Choosing the right design for the combustion chamber depends on several of these design criteria: the solid propellant used, the volume of the combustion chamber and the area of the nozzle throat. All these factors affect the overall performance of the actuator. The combustion and nozzle theories discussed in Section 5.1.2.2 predict idealized effects of these design parameters on the total performance of the actuator. However, these theories do not take into account the thermal losses that might be resulting because of heat transfer to side walls and by convection. This section explains the design changes made in the actual design of the actuators to meet the performance goals set by a specific application. The choice of a solid propellant strongly affects the performance that can be delivered by the microactuators. Propellants with low combustion temperatures help in minimizing the ignition delay times associated with combustion. Fast burning propellants allow for use of larger nozzles, which helps in reducing frictional losses in the nozzle. However, fast burning propellants also over pressurize the combustion chamber, causing delamination of chamber layers and unwanted leakage. This would require careful choice of robust materials that could withstand high pressures in fabricating the chambers. Choosing a more energetic propellant or by increasing the solid propellant density will increase the energy density of the fuel within the same volume chamber, thereby increasing the total available impulse

for a given volume. The performance of the propellants is generally compared using the quantity, specific impulse. Specific impulse is defined as the amount of impulse produced per unit weight of the propellant. Hence, while choosing a propellant for our chemical jet actuators, several factors such as its energetics and density needs to be taken into account. Reported values for I_{sp} of solid based propellants in large scale rockets is between 150 and 250 s. Reported values for small scale solid propellants is around 15 s. This decrease in the specific impulse values is attributed to the increased inefficiencies and thermal losses associated with small scale combustors. It was reported in the literature [22], that the convective heat losses from the chamber sidewalls do not have a significant effect on the total impulse delivered by the jet. However, any inefficiencies in various stages of combustion reduce the impulse that can be delivered by the jet, and the effect of such inefficiencies become more prominent as the size scale of the actuators is reduced because of larger available surface to volume ratios.

The volume of the combustion chamber controls the discharge time and impulse delivered by the released gases. Our modeling results show that the discharge time and the impulse delivered increases with an increase in chamber volume. Hence, an optimum chamber volume must be chosen so as to increase the total impulse delivered by the jet and at the same time minimize the duration of the jet. As the required impulse increases, the volume of the chamber can be increased for the same propellant to achieve more impulse. By varying the chamber volume, the distance between the electrodes changes, thus, affecting the conductivity of fuel. The delay times associated with the actuator ignition are highly dependant on the distance between electrodes. Hence, choosing the optimum dimensions for the chambers is an iterative process. If the volume of the

chambers is increased by increasing the thickness of the chambers, it ultimately decreases the conductivity of the fuel thereby needing more input energy to achieve the same impulse and delay time values. Once data is recorded from the first design, variables such as electrode distance and chamber volume are altered to achieve a set impulse level. Then the electrode distance and nozzle parameters are optimized to achieve the desired ignition delay times and durations. Our modeling results also help by acting as an optimization and predictive tool in studying how these various design parameters interact and affect the final performance of the released jet.

5.1.3 Ignition Power Supply Characterization

The electrical characteristics of the power circuit used during the ignition of conductive propellant play a significant role in controlling the performance of the microactuator. The bench scale testing circuit used during the testing of microactuators is mentioned in Section 4.1.6. This circuit must be characterized for the input ignition energy which is defined as the minimum energy required from the power circuit by the conductive propellant to cause ignition and also for the energy consumed by the propellant during combustion process. The electrical control system variables include the material of conductive dopants, composition of dopants, the dimensions of the chambers, the distance between electrodes and the input power characteristics.

Figures 51 and 52 show the typical voltage, current and energy data consumed by the conductive fuel during ignition process. Voltage data is obtained by directly measuring the voltage across the actuator electrodes using a voltage divider circuit. The current data is obtained by measuring the voltage across the mosfet and from mosfet characterization as discussed in Section 4.1.6.1. The energy consumed during ignition is

then calculated according to Equation 22. Testing for power characterization using capacitive discharge of direct currents showed that both input voltage and capacitance of the discharge capacitor play a significant role in controlling the ignition process. From experiments, it was observed that carbon black based conductive fuels required at least 37 V and a discharge capacitor capacitance of 100 μF to start the ignition process. As the input voltage and discharge capacitor capacitance is decreased, the delay times associated with the ignition process increased. Even though the fuel ignited at 37 V, to minimize ignition delay time jitter and to obtain reproducibility in the results, a voltage of 70 V is supplied from a 560 μF capacitor during all the characterization experiments. These electrical parameters correspond to an input energy of 1.4 J. For a constant input energy supplied, the ignition energy consumed during ignition process increased as the conductivity of solid fuel increased. The reason for this behavior is explained in detail in Section 5.1.2.1.

Figure 51 shows the typical voltage and current data obtained across the actuator electrodes during ignition process. For this graph, the input voltage supplied to the actuator from the discharge capacitor is 70 V DC. Two electrodes are placed on either side of the conductive fuel at a distance of 1.5 mm and the electrodes are patterned in 50 μm thick brass sheet. For 70 V DC supplied, the initial voltage in the fuel started at 70 V and fell to 63 V in 1.56 ms. It should be noted that the voltage did not drop from 70 V all the way to 0 V, but instead it dropped to just 63 V. This small drop in voltage is enough for the ignition of conductive fuel. During the ignition process, the resistance across the fuel is not constant but is a function of temperature within the chamber. Once ignition begins and the temperature within the chamber reaches the decomposition temperature of

the fuel, combustion occurs. The current dropped from 2.18 A to 1.58 A in 1.56 ms. The obtained current and voltage data are then used to estimate the amount of energy consumed. Figure 52 shows the typical graph for the amount of energy consumed during the ignition process. Though an input energy of 1.4 J is supplied from the power circuit, the actual energy consumed by the conductive fuel is about 0.23 J.

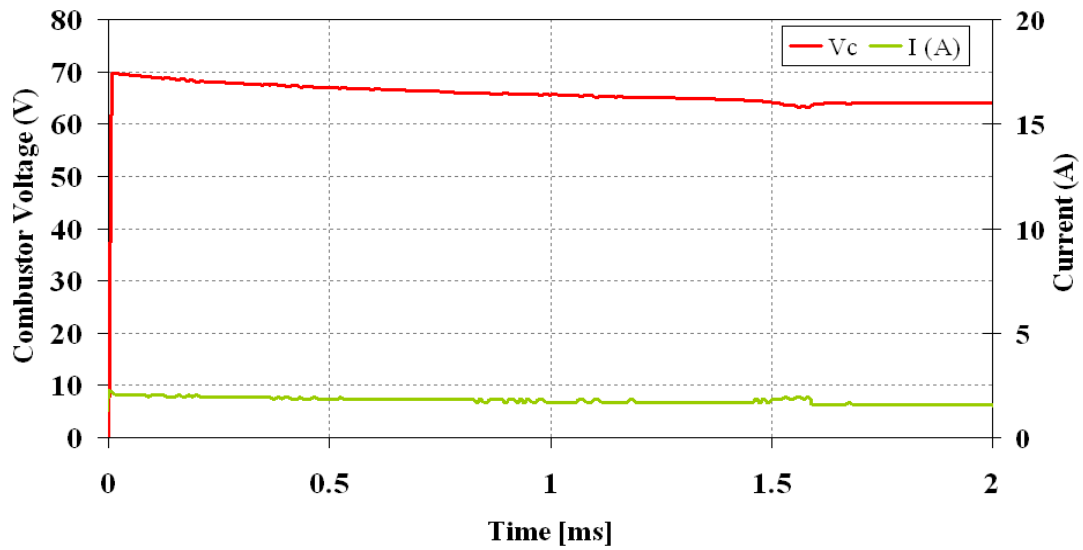


Figure 51: Voltage and current data obtained during ignition process

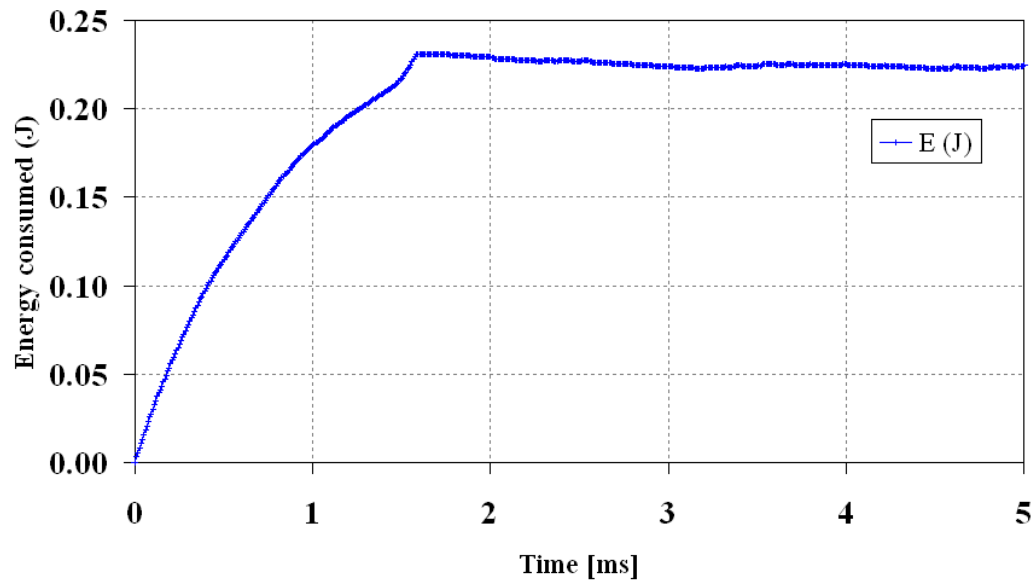


Figure 52: Energy consumed from the electrical setup during ignition process

As explained in Section 5.1.2.1, the energy consumed by the microactuator is dependant on fuel conductivity. To study this dependency, the amount of conductive dopant in the fuel is varied and the results are presented for two fuels. As the amount of conductive dopant in the fuel increased, the conductivity of the propellant increased and the energy consumed by the actuator increased. Figures 53 and 54 show this dependency for perchlorate and chlorate based fuels respectively. The average value and the standard deviation for each data point are obtained from 8 trials. As the resistance of the conductive fuel is significantly larger than the Thevenin resistance of the electrical circuit used for ignition, the energy consumed by the propellant increased with a decrease in fuel resistance or an increase in fuel conductivity according to Equation 31.

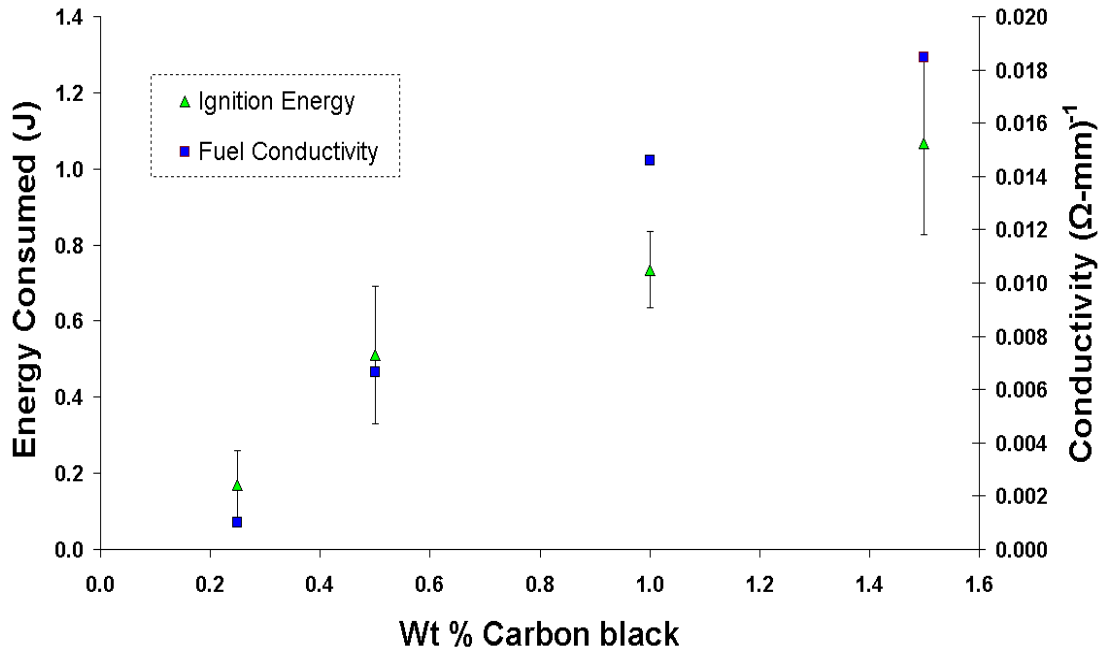


Figure 53: Dependency of energy consumed and fuel conductivity on the amount of conductive material for potassium chlorate based fuel

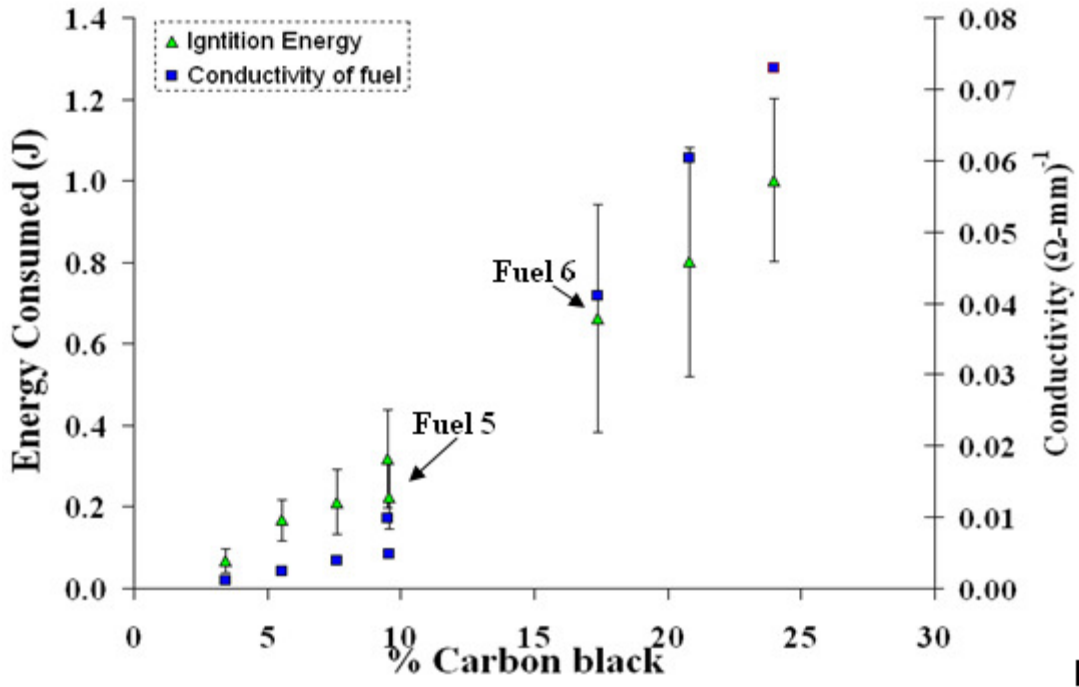


Figure 54: Dependency of energy consumed and fuel conductivity on the amount of conductive material for potassium perchlorate based fuel

Efforts are then made to study the effect of input electrical energy on ignition delay times. Figure 55 shows the dependency of ignition delay times on the energy input from the capacitor for two fuel compositions. Two different perchlorate based fuels are tested for this purpose. These fuels mainly differ in the amount of binder component added to the fuel. For all the results presented in this section, the same experiments are repeated for multiple actuators to obtain the average value and standard deviation for the obtained result. For testing for ignition delay times, 8 actuators are tested for each case and the error bar is calculated based on the standard deviation of the obtained values from the average. It is observed that the ignition delay time decreased with an increase in the input energy from the power supply. The effect of chamber geometry and the distance

between electrodes on ignition delay times is then studied for potassium perchlorate and potassium chlorate based fuels. For this purpose, one specific composition is considered for each fuel. The compositions of the perchlorate based fuel and chlorate based fuel considered for this testing are:

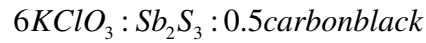
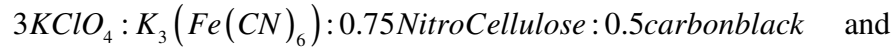


Figure 56 shows the dependency of ignition delay time of conductive perchlorate based fuel on chamber volume for three different electrode distances. In general, ignition delay time decreased with an increase in chamber volume and with a decrease in electrodes distance. For a constant volume of 15 mm^3 , as the distance between electrodes is decreased from 2.5 mm to 1.5 mm, the delay times decreased by 74% from 2.9 ms to 0.75 ms. This dependency can be explained by the concept described in Section 5.1.2.1. The results obtained from these experiments are then compared to the results obtained from modeling done using COMSOL multiphysics software. The distance between electrodes, chamber volume and the input voltage are varied in simulations to match the experimental conditions. Figure 57 shows this comparison of delay time variation with chamber volume for a constant electrode distance of 1.5 mm and an input voltage of 70 V from experiments and modeling for perchlorate based fuels. In this graph, the squares show the experimental values obtained and the triangle values are the results obtained from COMSOL modeling. During experiments, 12 actuators are tested for each case to determine the average delay times and the error bar associated with it. An empirical equation is then made to fit the experimental results and the result is plotted as a solid line. Figures 58 and 59 show the comparison of delay time variation with chamber

volume for perchlorate based fuels when the distance between electrodes is 2 and 2.5 mm respectively. All these results show a good comparison between results obtained from experiments and from modeling.

The same experiments are then repeated for potassium chlorate based fuels and the delay time dependency on chamber volume is reported in Figure 60. For this plot, the distance between electrodes is fixed at 1.5 mm and a voltage of 70 V is supplied from a 560 μF capacitor. For each fuel volume, 8 trials were performed to obtain the average delay time and its standard deviation. As expected the ignition times decreased with an increase in chamber volume. The maximum volume of the chamber used for this testing is 15 mm^3 . Above this volume, the actuator layers broke off during combustion because of the buildup of high pressures within the actuator. As the chamber volume increased from 5 mm^3 to 15 mm^3 , the ignition delay times decreased by 42% from 1.08 ms to 0.62 ms.

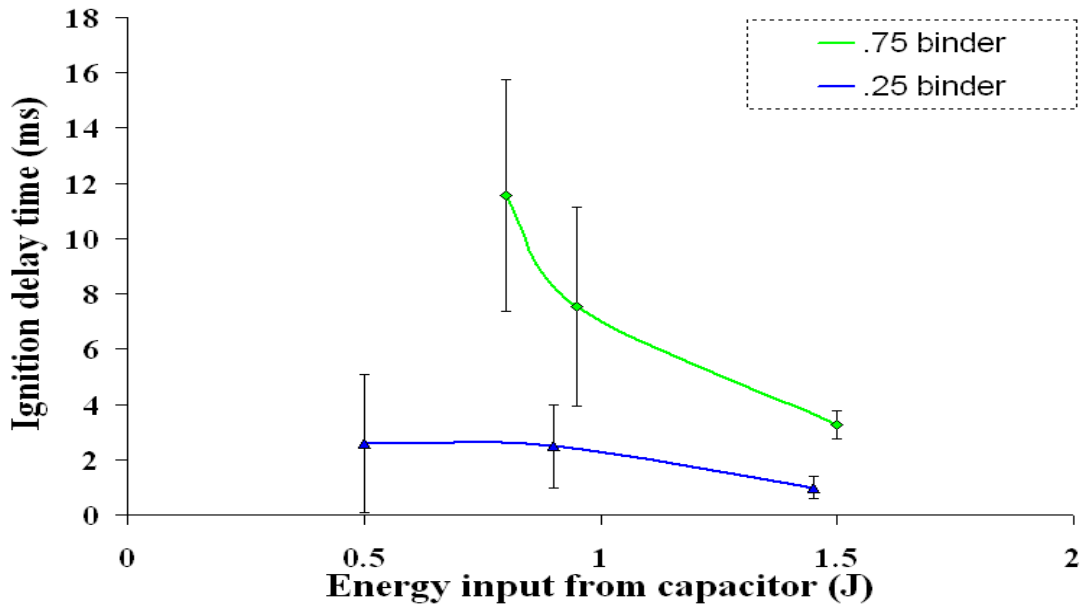


Figure 55: Variation of ignition delay time with input electrical energy for Fuel 5 and Fuel 7

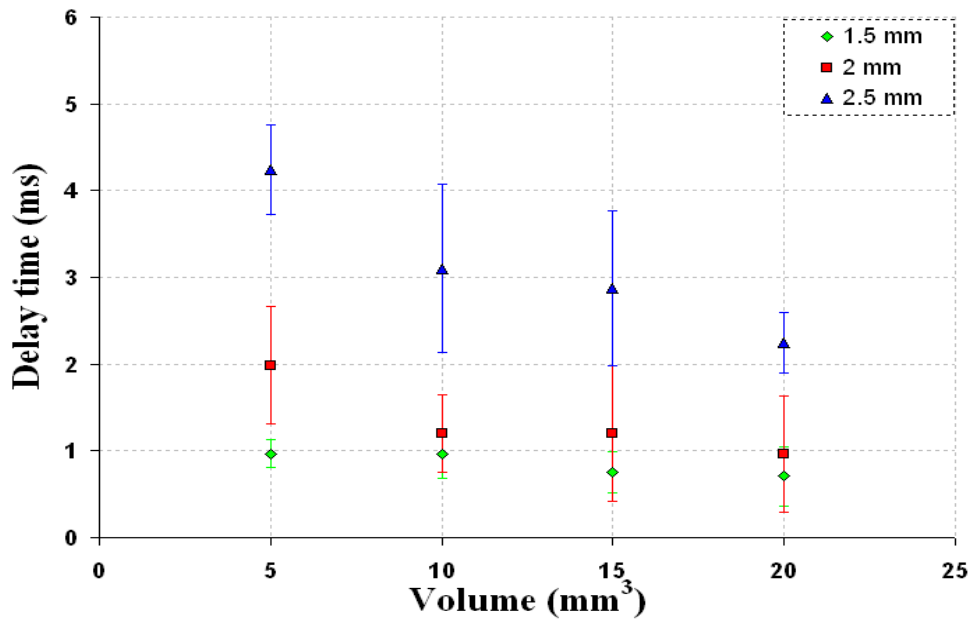


Figure 56: Dependency of ignition delay times for Fuel 5 on chamber volume and gap between electrodes

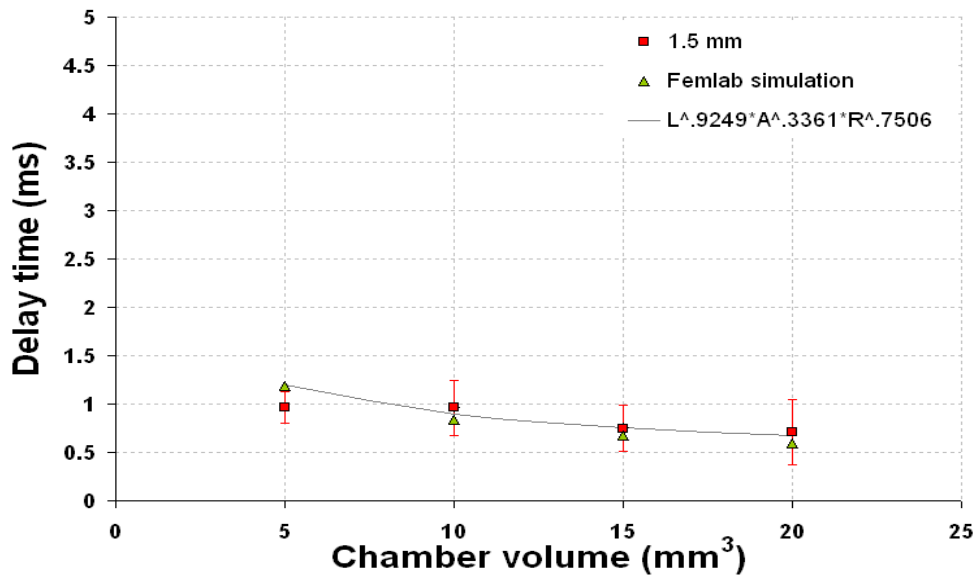


Figure 57: Dependency of ignition delay time on chamber volume for Fuel 5 when the distance between electrodes is 1.5 mm

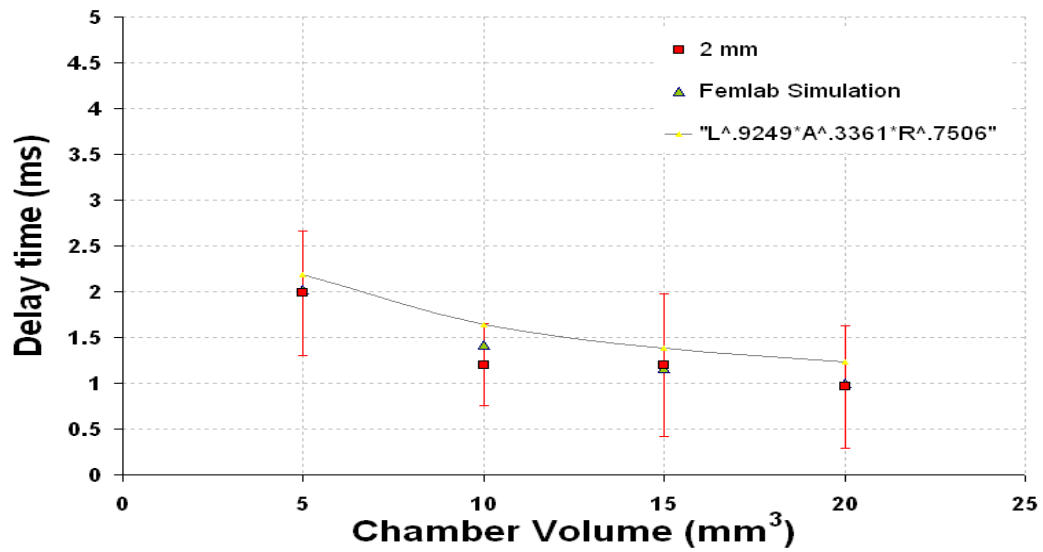


Figure 58: Dependency of ignition delay time on chamber volume for Fuel 5 when the distance between electrodes is 2 mm

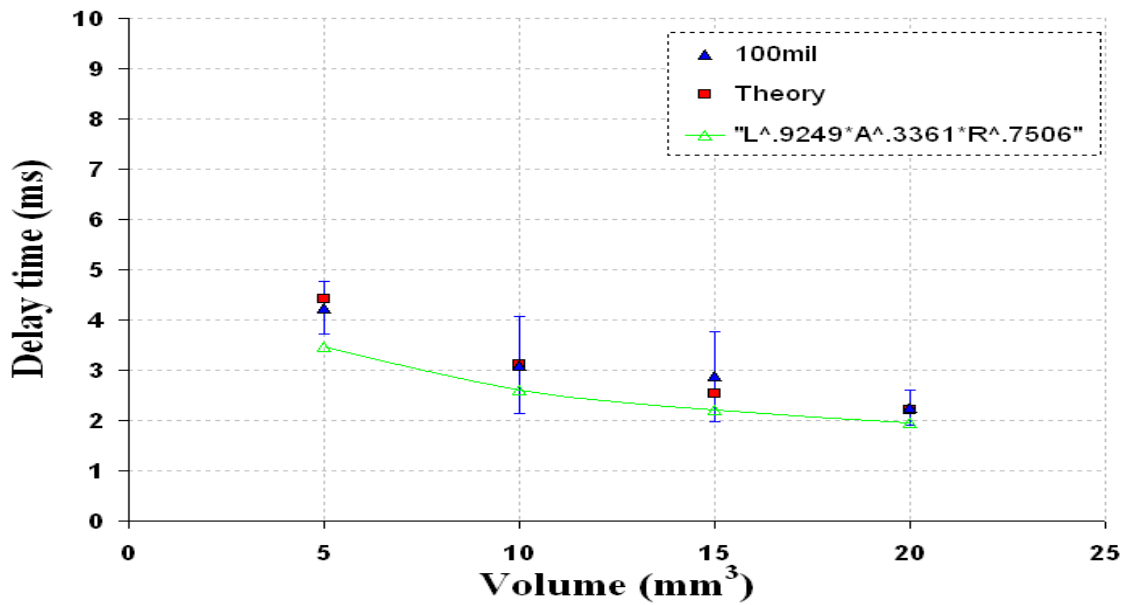


Figure 59: Dependency of ignition delay time on chamber volume for Fuel 5 when the distance between electrodes is 2.5 mm

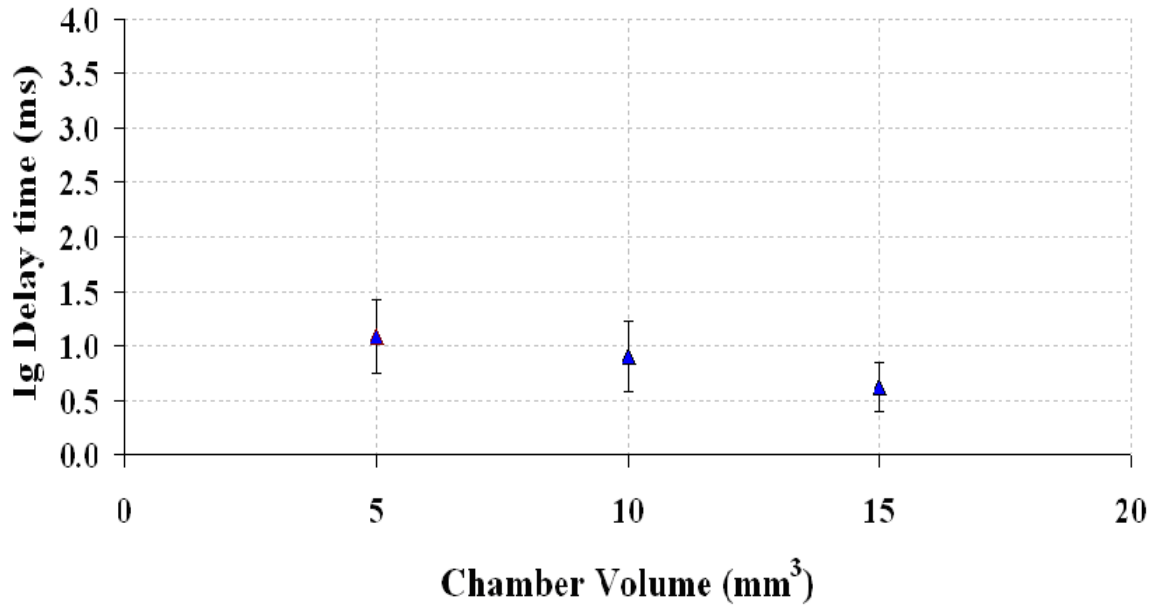


Figure 60: Dependency of ignition delay time on chamber volume for Fuel 8 when the distance between electrodes is 1.5 mm

5.1.4 Actuator Performance

5.1.4.1 Propellant Geometry and Composition Effects

The type of propellant and propellant composition used in microactuator plays a significant role in achieving the desired range of performance from the actuator. Also, as we deal with an array of such batch fabricated microactuators and try to achieve the same performance from each actuator, the consistency in propellant loading from device to device plays a significant role in minimizing the performance variations from one actuator to the other. Many solid fuels with varying propellant compositions are tested and among these, the optimum composition of oxidizer, fuel and conductive dopant components are finalized for each fuel type. The optimum composition of each fuel is

defined as the one which delivers maximum impulse from the fuel in least amount of time with good reproducibility. Three types of propellants are tested in this research work.

- GAP and ammonium perchlorate based fuels
- Potassium perchlorate (KClO_4) based fuels
- Potassium chlorate (KClO_3) based fuels

The type of propellant and the oxidizer-fuel ratio in each propellant affects the propellant density which in turn affects the loading density of propellant into the combustion chamber. This dependency of loading densities on fuel mixture ratio were reported in [22] for nonconductive composite propellants and it was demonstrated that GAP and composite propellants were in fact suited for integration into chemical jet actuator fabrication process. The loading density of the propellant is measured by dividing the mass of propellant burnt by the volume occupied by the propellant. In order to minimize the inconsistencies while preparing the propellant mixtures, all the components of the propellant are weighed using a micro balance with 0.01 mg resolution. The weight measurement of each component of the propellant should be accurate so that there is minimum deviation between different batches of propellant. Also, in order to minimize any variations during fuel filling process, acetone is added to the fuel mixture as described in Section 4.1.1 so as to facilitate easy mixing and for uniform casting of fuel into chambers.

The performance of the microactuators is measured in terms of specific impulse, impulse delivered and burn durations. Specific impulse offers a good measure for the energetics of the propellant and gives a good comparison between different fuels. It is an

intrinsic property of a propellant that is independent of the fuel volume. Specific impulse is calculated as the total impulse measured divided by the weight of propellant burned. Specific impulse is calculated for each fuel composition by measuring the total impulse delivered using a force stand as described in Section 4.1.4 or using a ballistic pendulum setup described in Section 4.1.5. The specific impulse values obtained from an optimum composition for each fuel type are reported in Table 12. Among all the fuels tested, chlorate based fuels offered the maximum specific impulse and GAP based fuels offered the least amount of specific impulse.

Efforts are then made to study the effect of adding conductive dopants to the fuel mixture on its performance. For this purpose, the specific impulse obtained from perchlorate based fuels between its conductive mixture and nonconductive mixture are compared. For nonconductive propellants, the performance results were presented in the literature [22] and these results are used here for comparison purposes. We compared the specific impulse of conductive perchlorate based propellant with nonconductive perchlorate based propellant and the results are reported in Figure 61. For nonconductive propellants, it was reported that the specific impulse delivered by the fuel can be varied by varying the amount of binder added to the fuel. The specific impulse for non conductive perchlorate based fuels range from 13 to 44.3 s with a standard deviation ranging from 15% to 33% of the mean value depending on the amount of binder in the fuel. In general, specific impulse delivered by the nonconductive propellant decreased with an increase in binder concentration. As can be seen from Figure 61, with the addition of conductive dopants, the specific impulse obtained from the propellant is still in a comparable range to that of the nonconductive propellant. The specific impulse

obtained from the conductive propellant is in the range of 25 to 40 s and it increased when the volume increased from 5 to 10 mm³ and decreased when the volume increased further from 10 to 20 mm³. These results agree with the trend obtained for nonconductive propellant mixtures. For the same volume of the fuel, the conductive fuel offered less impulse and burned faster. This decrease in impulse delivered could be explained by the fact that the actual energetics of the propellant is reduced when conductive dopant particles are added to the fuel occupying same volume. The faster burn times are expected for conductive propellants because of the ignition of the entire fuel at the same time. The experimentally obtained specific impulse of perchlorate based fuel is then compared to the result obtained from theory according to Equation 50. To estimate the theoretically obtained specific impulse, a combustion chamber temperature of 1800°K and pressure of 20 MPa are used. Figure 62 compares the experimental values with theoretical results for different chamber volumes. The experimentally obtained specific impulse values falls in an acceptable range with the theoretically obtained results.

Table 12: Specific impulse delivered by several propellant formulations

Propellant Formulation (Wt Ratio)	I_{sp} (s)
GAP : CB (1:1)	15
NH ₄ ClO ₄ : GAP:CB (1:1:0.2)	21
KClO ₄ :K ₃ [Fe(CN) ₆] : Nitrocellulose: CB (3:1:0.75:0.5)	36
KClO ₃ : Sb ₂ S ₃ : CB (8:1:0.5)	55

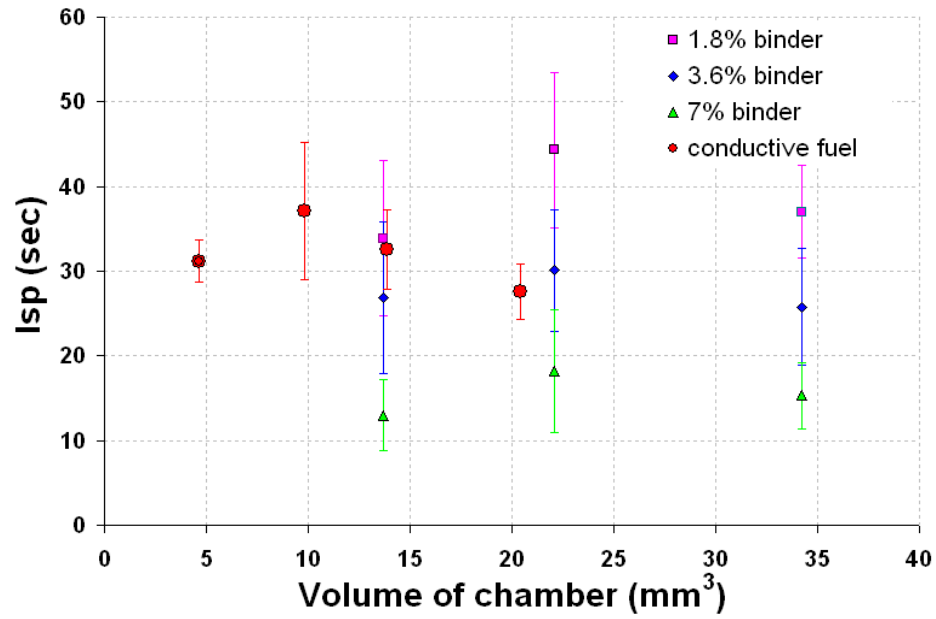


Figure 61: Comparison of specific impulse delivered by conductive and nonconductive potassium perchlorate based fuels

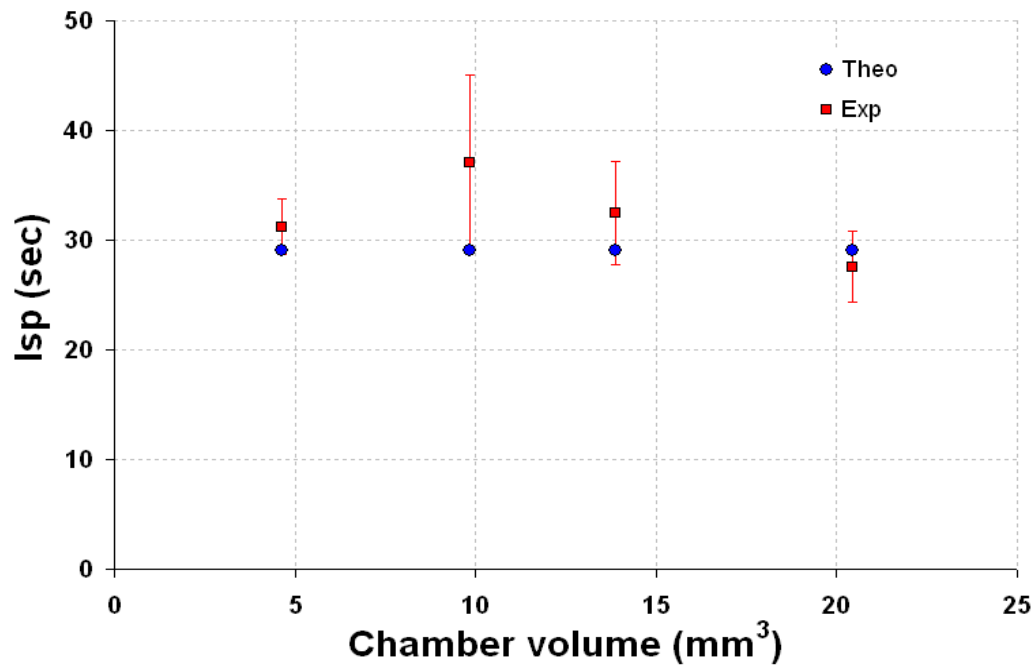


Figure 62: Comparison of experimentally obtained specific impulse values with theoretically obtained values for several combustion chamber volumes

The effect of fuel composition on actuator performance is then studied. In changing the fuel composition the percentage of oxidizer, binder and conductive dopants are varied independently to observe the effect of each component on the total impulse delivered from the microactuators. First, perchlorate based fuels are tested for this purpose. The variation of total impulse delivered from conductive perchlorate based propellant with the amount of conductive dopant in the fuel is shown in Figure 63. For this testing, the volume of the chambers and the distance between electrodes is kept constant at 15 mm^3 and 1.5 mm respectively and for each case 8 trials were performed. A voltage of 70 V is supplied from a $560 \text{ }\mu\text{F}$ capacitor. As the amount of carbon black in the fuel increased, the total impulse delivered by the actuator decreased. The impulse delivered by the conductive propellant decreased by 54% from 11 mNs to 5 mNs as the amount of conductive material in the fuel increased from 5% to 15% by weight. This decrease in delivered impulse can be explained by the fact that with an increase in the amount of conductive material, the actual chemical energetics of the fuel within the same volume decreases. Also, with more dopant material, the actual stoichiometry of the mixture is varied affecting the total combustion energy available from the fuel.

The effect of varying the binder composition on the performance of conductive propellant is then studied for perchlorate based fuels. The percentage of nitrocellulose binder is varied in the fuel mixture as $3\text{KClO}_4 : \text{K}_3(\text{Fe}(\text{CN})_6) : x\text{NClaque} : 0.5\text{CB}$. Changing the binder composition affects the available combustion energy in the propellant by changing the stoichiometry of the fuel mixture. The variation of impulse delivered with binder composition is shown in Figure 64. For a chamber volume of 15 mm^3 , the impulse delivered by perchlorate based fuel in the absence of binder is

approximately 5 mNs. When 5% nitrocellulose binder is added to the propellant, the impulse delivered by the fuel increased to around 12 mNs. When the binder composition is increased further, the impulse delivered by the fuel decreased. When 15% binder is added to the fuel, the impulse delivered decreased to about 8 mNs. These results suggest that perchlorate based fuels offer a maximum impulse when the binder concentration in the fuel is between 0 to 15%. Hence, an optimum composition of 5% nitrocellulose binder is added to perchlorate based fuels during all our further testing.

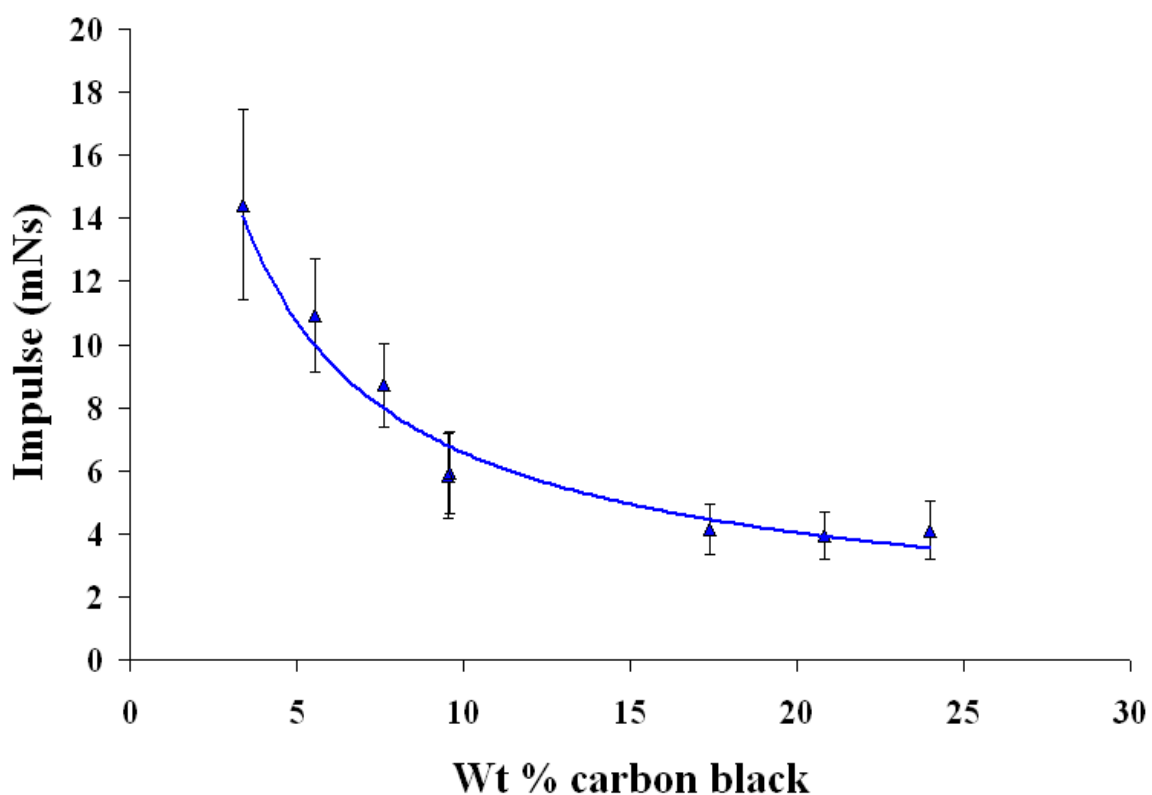


Figure 63: Variation of total impulse delivered with the amount of conductive material present in potassium perchlorate based fuel

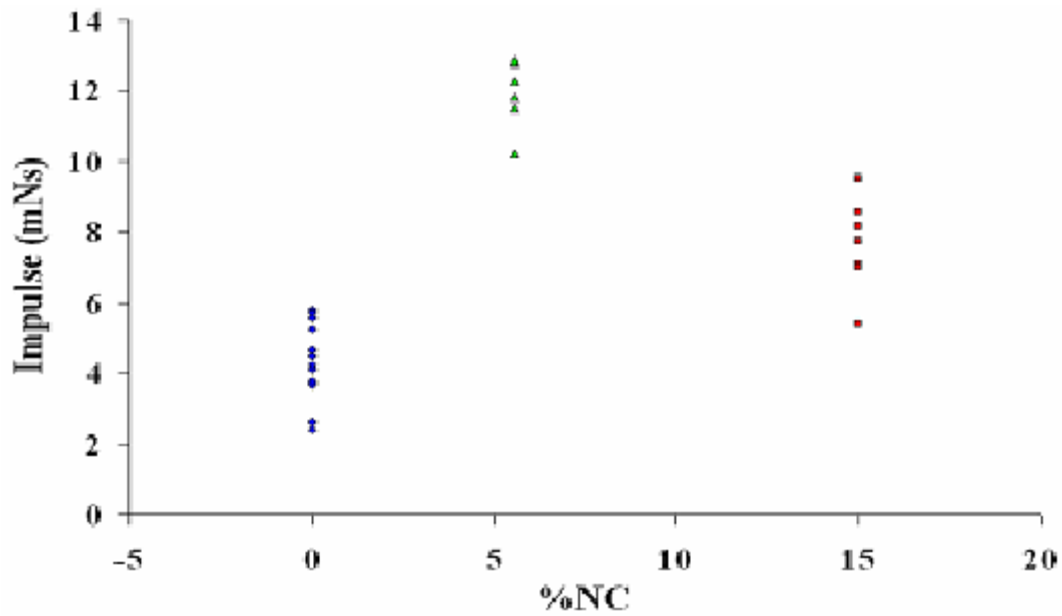


Figure 64: Experimental dependency of total impulse delivered with binder concentration for potassium perchlorate based fuels

The effect of varying the geometry of the chamber on impulse delivered is presented in Figure 65. The geometry of the chamber is varied in terms of chamber volume and the distance between electrodes. For all compositions and electrode distances, the impulse delivered by conductive perchlorate based propellant increased with an increase in chamber volume. At small volumes, the reduced impulse could be explained by the fact that the total combustion energy available is small at small size scales and also the thermal losses from the combustion chamber walls become more prominent. For perchlorate based fuels, when the electrode distance is fixed at 1.5 mm, the impulse delivered by the fuel reduced from an average value of 5.8 mNs to 1.9 mNs when the chamber volume is reduced from 15 mm³ to 5 mm³. The average value of impulse is obtained from 8 trials for each geometry. The variation of impulse with the gap between electrodes is also studied and compared in Figure 65.

The experimental results obtained are then compared to the theoretical results obtained from nozzle theory in Section 5.1.2.2 and plotted in Figure 66. In this figure, the squares represent the experimental values obtained and the solid line represents the theoretical data obtained for the same chamber volumes. For a chamber volume of 15 mm³, the average impulse delivered from 8 trials during experiments is 5.74 mNs with a standard deviation of 0.9 and the theoretical impulse delivered is 5.55 mNs. This shows a good comparison between the experimentally and theoretically obtained impulse values for conductive perchlorate fuel filled microactuators.

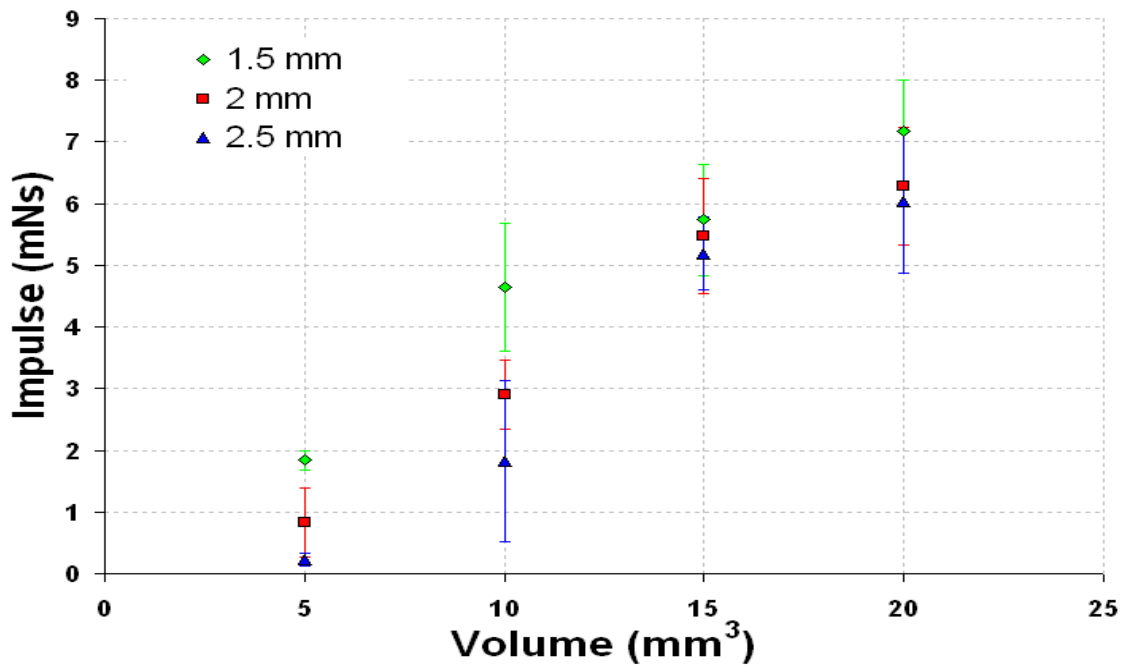


Figure 65: Experimental dependency of total impulse delivered with chamber volume for potassium perchlorate based fuels

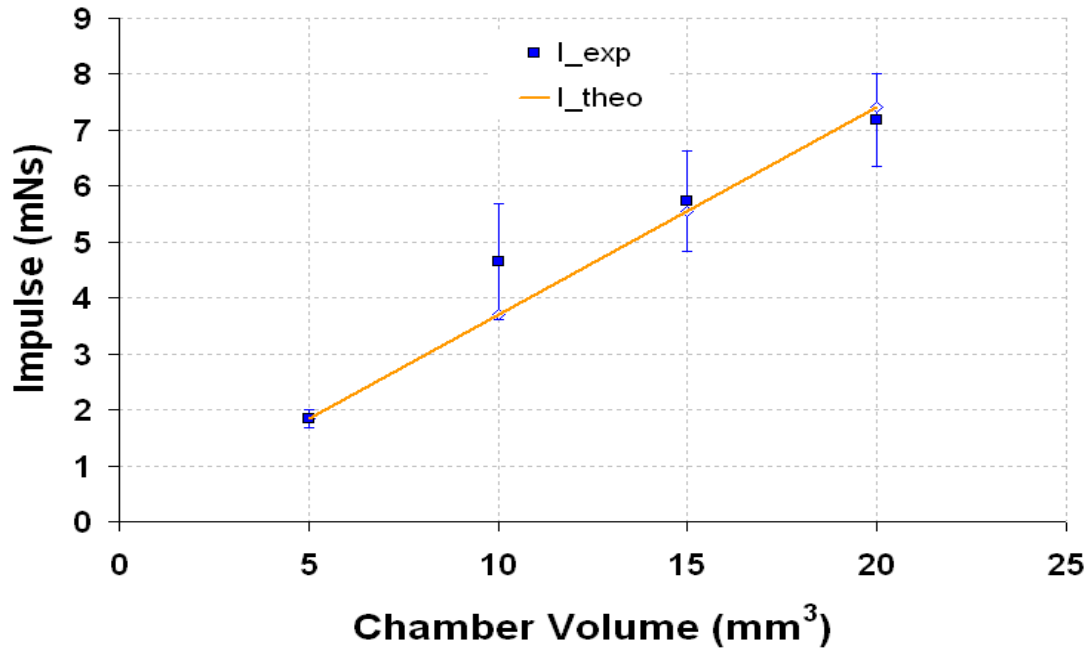


Figure 66: Comparison of experimental and theoretically obtained total impulse for potassium perchlorate based fuels

The same experiments are then repeated for chlorate based fuels. The effect of varying the composition of conductive material in the fuel is presented in Figures 67 and 68. For these experiments a voltage of 70 V is supplied. Figure 67 shows the effect of varying the composition of conductive dopant on the impulse delivered by the propellant. For each composition, 6 trials were performed to determine the average and standard deviation of the impulse. Similar to perchlorate based fuels, the impulse delivered by the propellant decreased with an increase in dopant composition. The effect of varying the chamber volume on the impulse delivered by chlorate based fuel is then studied. For this purpose, two fuel compositions are tested and the results from 6 trials for each case are presented in Figure 68. As the volume of the propellant increased, the impulse delivered by the propellant increased suggesting that the chamber volume can easily be scaled to meet the specific application requirements.

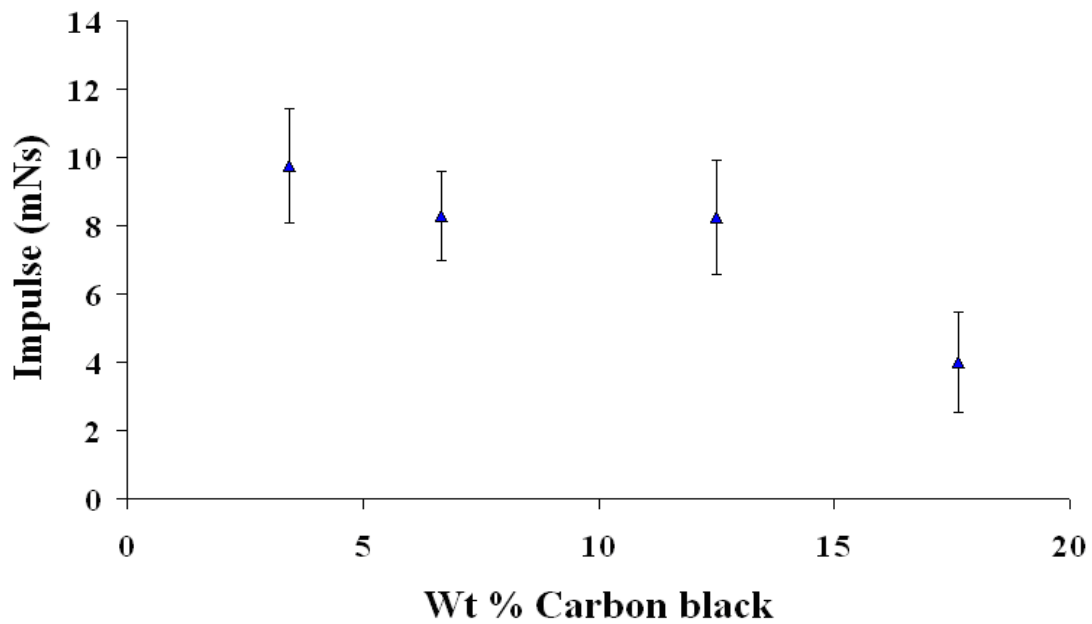


Figure 67: Variation of total impulse delivered with fuel composition for potassium chlorate based fuels

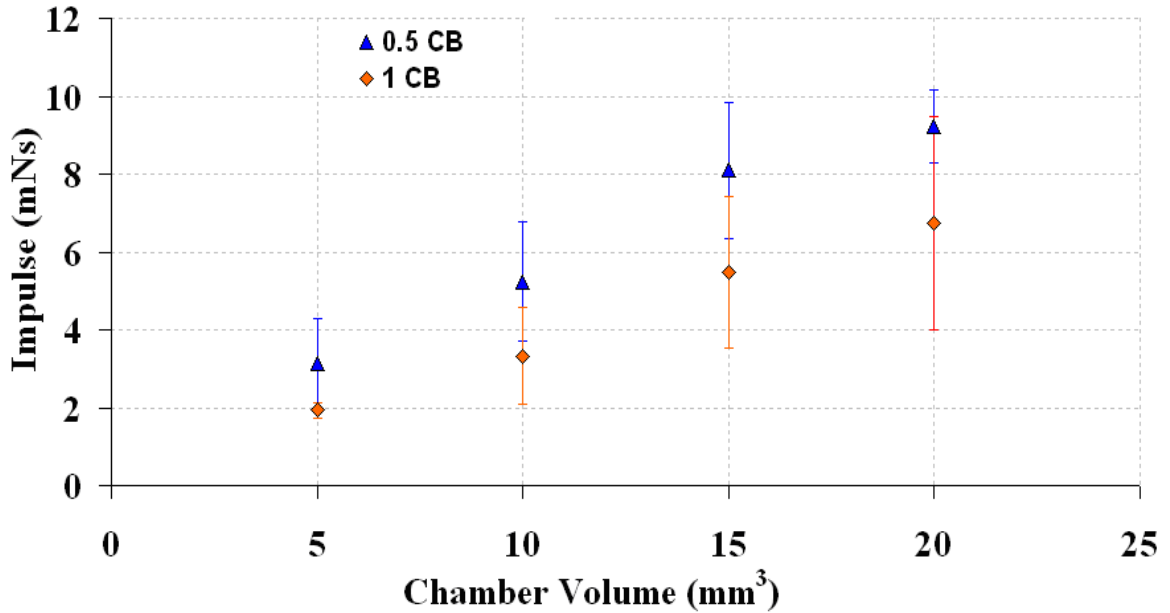


Figure 68: Experimental dependency of total impulse delivered with chamber volume for potassium chlorate based fuels

5.1.4.2 Nozzle Geometry Effects

The nozzle component in a microactuator plays an important role in controlling the duration of the released jet from the actuator. The nozzle part of the actuator not only helps to direct the jet of exhaust gases in a desired direction so as to generate directional forces, but it also helps in increasing the burn rate of solid propellants by restricting the gas flow from the combustion chamber. Restricting the gas flow results in an increase in chamber pressure thereby, resulting in faster combustion. Optimum nozzle design also helps in expanding and accelerating the released gases, increasing the total impulse delivered by the microactuator. Hence, nozzle design is studied to observe the effect of nozzle physical dimensions on impulse duration of the released jet. The nozzle parameters used during actuator performance testing are determined based on the results that are obtained from modeling of nozzle theory described in Section 5.1.2.2. The final nozzle design is optimized to generate large forces in extremely short durations.

The effect of nozzle throat area on the duration of the jet is observed and reported for perchlorate based conductive fuels. Figure 69 shows the effect of nozzle throat area on the discharge time of perchlorate based fuels for different volume chambers. Each experiment is repeated with 8 microactuators to obtain an average duration and standard deviation from the average. The experimentally obtained durations are then compared with the results obtained from simulations. In this figure, the squares and diamonds represent the experimentally obtained values for two different throat areas (A_t) and solid lines represent the result obtained from modeling. As the throat area of the nozzle is increased, the discharge time of released gases decreased for a constant volume of fuel. This trend could be explained by the fact that, as the throat area of the nozzle is

increased, more amounts of released gases can flow through it at the same time and so, require less amount of time to release equal amount of gases than nozzles with small throat areas.

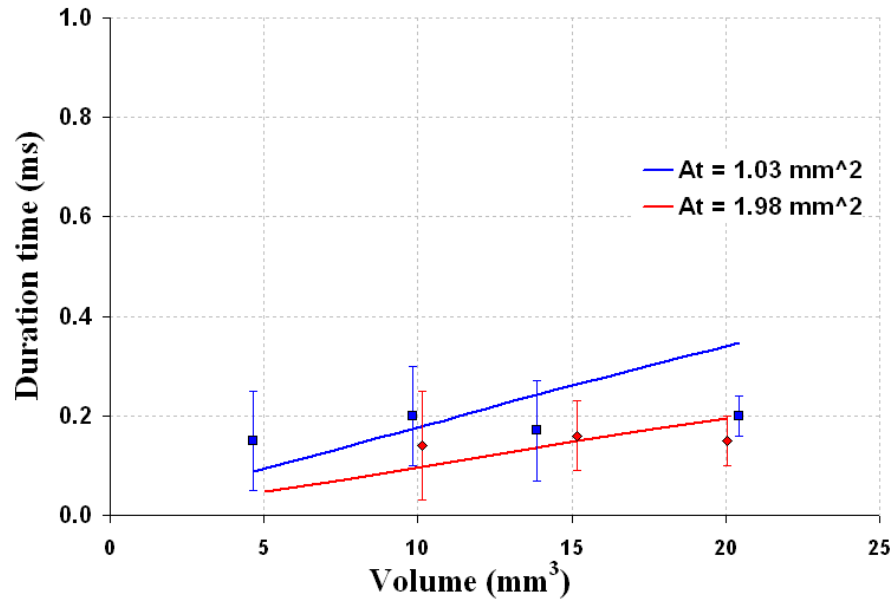


Figure 69: Effect of nozzle throat area on discharge times for perchlorate based fuels

Efforts are then made to see if the actuator chamber dimensions or electrodes distance has any effect on the duration of the released jet. Ideally, for the same fuel composition and volume, the distance between electrodes should not have any affect on duration as we are assuming that once ignition begins, duration of the released jet is a function of amount of gas produced and the nozzle dimensions. As can be seen from Figure 70, no specific trend is observed for the variation of durations with the distance between electrodes. This confirms our concept of rapid combustion of fuel and it also confirms our hypothesis that the only times associated with combustion is the amount of time it takes for the released gases to travel through the length of the nozzle.

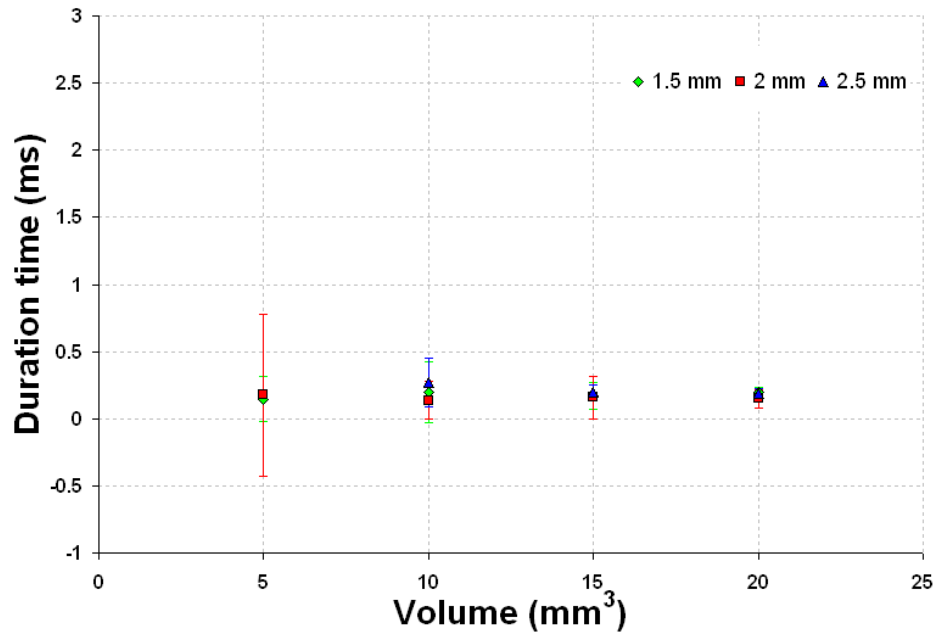


Figure 70: Effect of gap between electrodes on discharge times of the jet

Finally, a high speed video camera is used to record the combustion event and capture the released jet from the microactuator. When the combustion event is captured at 100,000 frames per second, it was observed that combustion of the conductive propellant happened in one time frame. Figures 71 shows a high speed image of the released jet for perchlorate based fuel with aluminum additives and Figure 72 shows a high speed image of the released jet from GAP based fuels with carbon black additives.

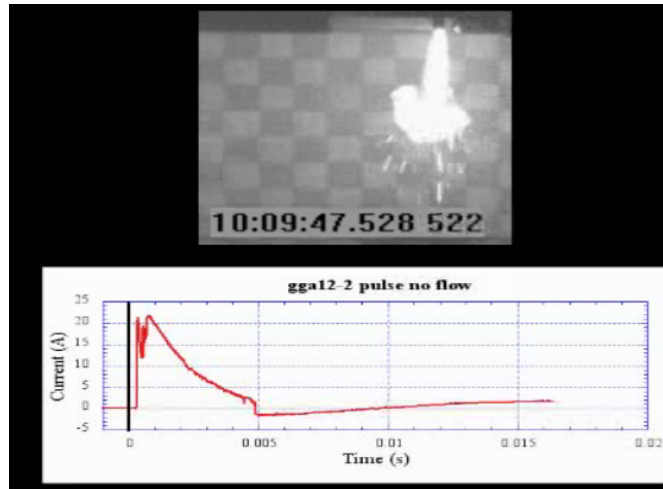


Figure 71: High speed video capture of perchlorate - aluminum fuel jet

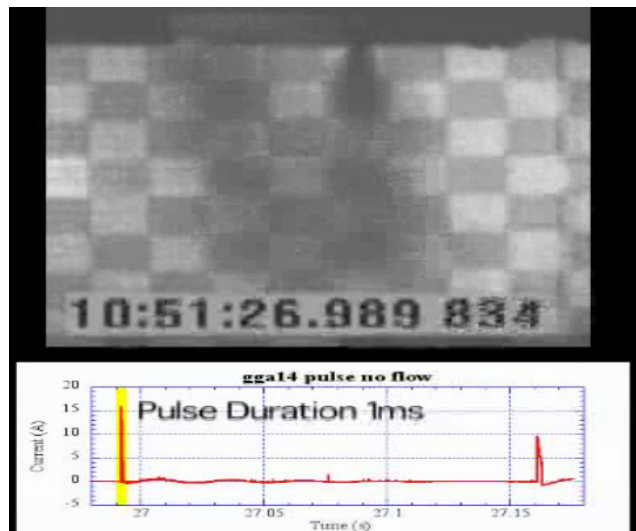


Figure 72: High speed video capture of GAP - carbon black jet

5.1.4.3 Solid Propellant Gas Generation

The amount of gas generated from the microactuator is measured in terms of volume of gas released per unit volume of propellant (V_{gas}/V_{fuel}). This performance

parameter is chosen because it enables us to compare between different fuels and fuel compositions. The amount of gas generated from the microactuator is measured for the following two conductive fuel mixtures:

- GAP based fuel (Fuel 3)
- Potassium perchlorate and potassium ferricyanide based fuel (Fuel 5)

The amount of gas released for these fuel mixtures is measured using the equipment and setup described in Section 4.1.3. A pressure vessel is used to record the change in pressures associated with the gas release. During measurement, the product gases are permitted to cool to room temperature before the final average pressure is recorded using a pressure transducer so that water vapor in the product gas stream is condensed before the pressure is recorded. Figure 73 shows the typical pressure curve obtained from the pressure transducer. The pressure data obtained from pressure transducer is converted to absolute pressure and then converted to moles of gas released according to Equation 10 by assuming an ideal gas behavior of the released gases. The moles of gas produced from the fuel is converted into volume of gas using ideal gas law at a temperature of 273°K and pressure of 1 atm. This volume is then divided by the actuator fuel volume to yield the amount of gas released per unit volume of solid propellant. Propellant volume is obtained by dividing the weight of propellant consumed during combustion with its density. In order to measure the weight of propellant consumed, the weight of the actuator before and after combustion is measured using a microbalance. Though we have tested many fuel compositions for each propellant, during characterization of the amount of gas generated, we selected a specific composition that generated high impulse and short duration jets. Table 13 shows the compositions of each

propellant tested and the amount of gas released for each formulation. The volume of gas released for perchlorate based fuels and GAP based fuels are measured as a function of fuel volume and presented in Figures 74 and 75 respectively. For perchlorate based fuels, as the chamber volume increased, the amount of gas generated from the propellant increased. As GAP was reported in literature as a gas generating propellant, the actuator volumes tested for GAP mixtures are smaller than the volumes used for perchlorate based fuels. Even in small volumes, the amount of gas generated from GAP based fuels is higher when compared to perchlorate based fuels. However, as the testing of GAP based fuels is performed with just two fuel volumes, the dependency of gas released with fuel volume could not be concluded.

The ratio of V_{gas}/V_{fuel} obtained for GAP based propellants and potassium perchlorate based propellants are then plotted in Figure 76 as a function of chamber volume. For perchlorate based fuels, the volume of gas released per volume of fuel is measured to be between 100 and 200. The fuel volumes tested for this purpose range from 5- 20 mm³. For GAP based fuels, the volume of gas released per volume of fuel, V_{gas}/V_{fuel} , is measured to be between 250 and 450. The microactuators filled with GAP formulations have a volume of 5 -10 mm³.

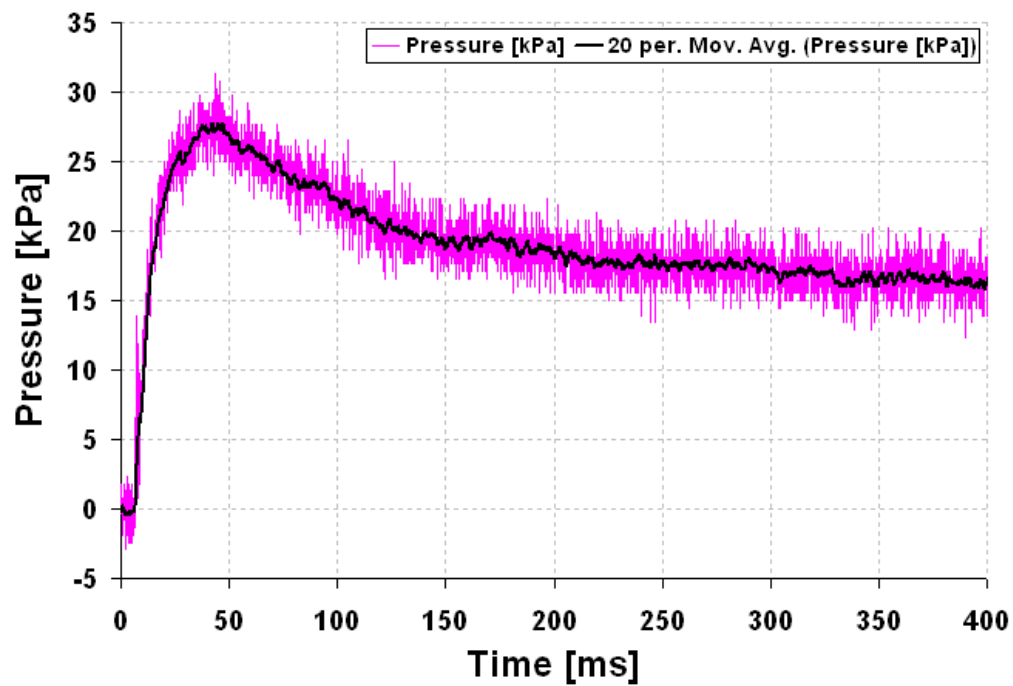


Figure 73: Pressure signal received from pressure transducer

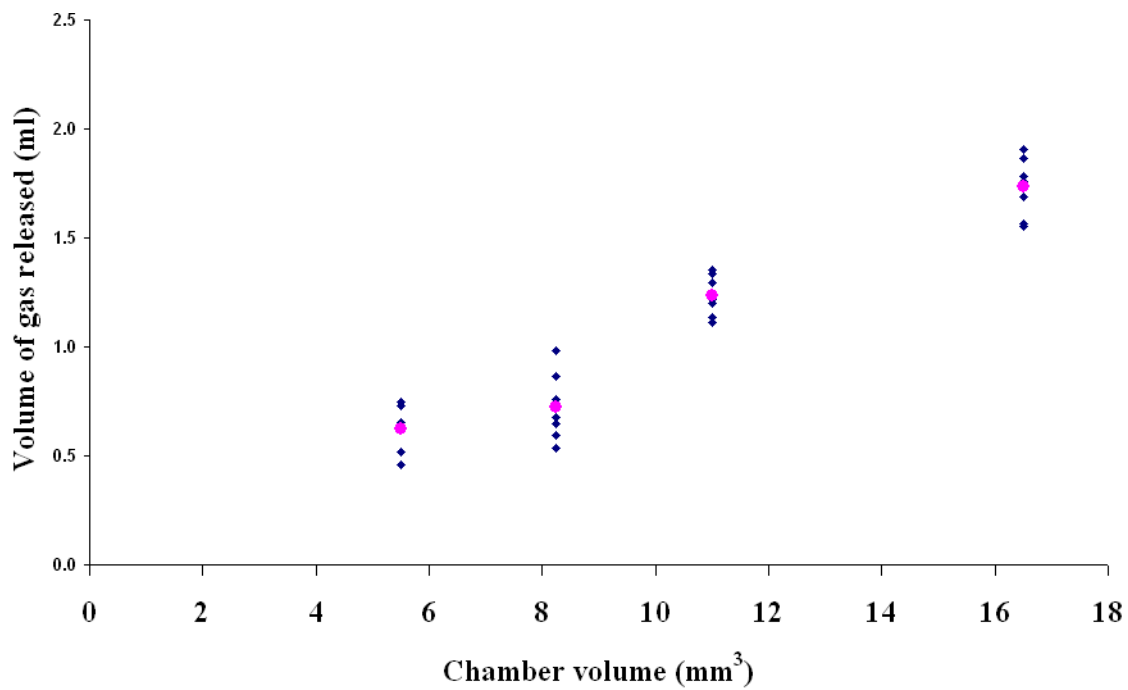


Figure 74: Amount of gas released for Fuel 5 as a function of fuel volume

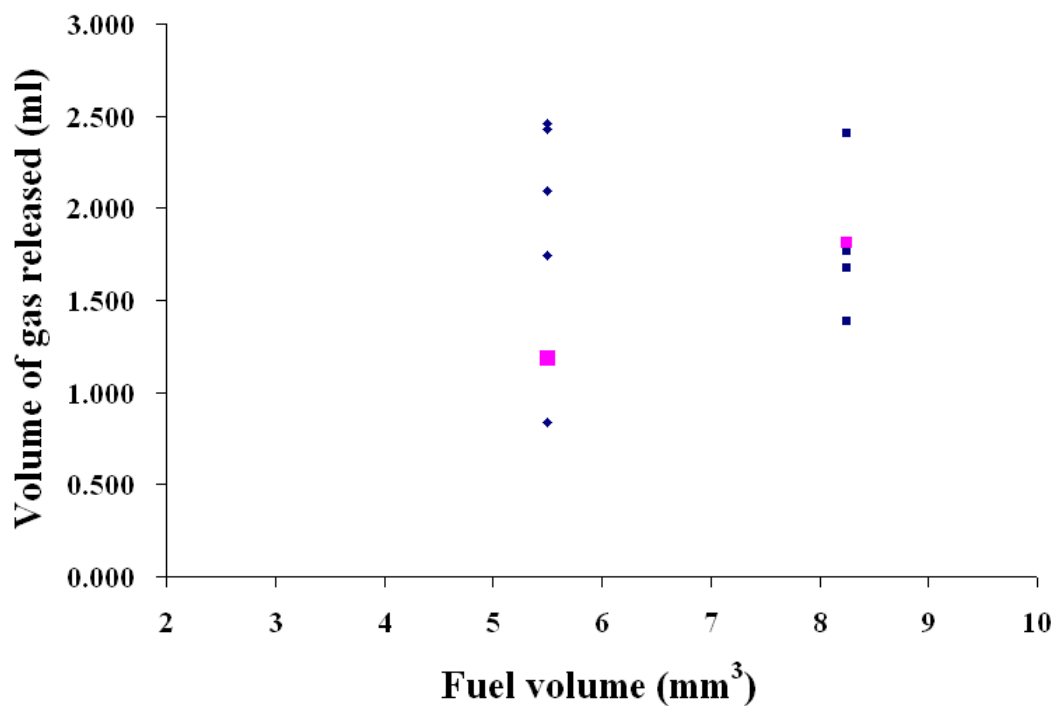


Figure 75: Amount of gas released for Fuel 3 as a function of fuel volume

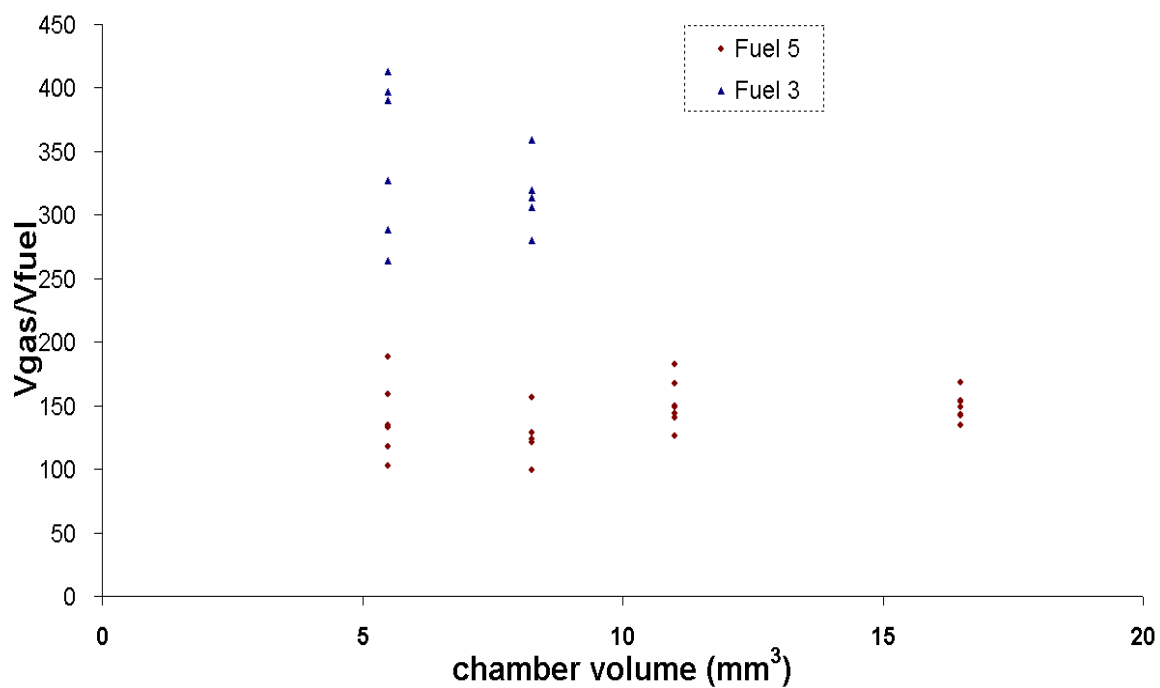
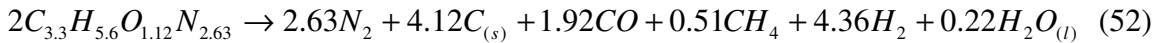
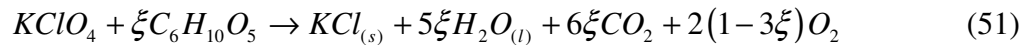


Figure 76: Comparison of gas generation results for GAP based propellant (Fuel 3) and potassium perchlorate based propellant (Fuel 5)

Table 13: Amount of gas generated for Perchlorate and GAP based fuels

Propellant formulation	Experimental Gas produced [cc _{air} /cc _f]	Exp/Theoretical Gas produced
3:1:0.75:0.5 KClO ₄ :K ₃ [Fe(CN) ₆]:Nitrocellulose:CB	137	0.25
1:0.2 GAP:CB	314	0.15

Efforts were then made to compare the experimentally obtained fuel volumes with the theoretically estimated results. For estimating the theoretical amount of gas released for perchlorate based fuels, the chemical reaction between potassium perchlorate and cellulose is considered. Equation 51 represents the theoretical reaction of potassium perchlorate and cellulose for cellulose mole fractions, ‘ ξ ’ between 0 and 1/3 [22]. Cellulose is used as an analog to the nitrocellulose that we used as the binder component. For room temperature product gases, the theoretical amount of gas produced from this reaction is 2 moles per mole of potassium perchlorate. Based on this ratio, the amount of gas generated theoretically from the same volume of fuel used in experiments is measured. Similarly, Equation 52 represents the theoretical decomposition of GAP. GAP decomposition produces 4.7 moles of gas per mole of fuel.



The experimental amount of gas released for perchlorate based fuels is measured to be 20-27% of the theoretically estimated gas production. Similarly, for GAP based fuels the experimental amount of gas released is 20-24% of the theoretically estimated gas production. These results were reported in Table 13. The decrease in experimental to

theoretical released gas for conductive perchlorate and GAP based fuels can be explained by the fact that the conductive material in the fuel is not accounted for in theoretical estimations. Because of these additive dopants, the actual volume of the energetic propellant is less than the estimated value used during theoretical calculations. At small volumes, additional heat losses because of quenching effects also could have contributed for reduced conversion of reactants to product gases. The amount of gas generated from conductive perchlorate based fuel is then compared to the amount obtained from nonconductive fuel as reported in [22]. For nonconductive perchlorate based fuels, the amount of gas released was reported to be 31-37% of the theoretically estimated gas production [22]. In spite of reduced conversion of GAP fuel into gaseous moles, GAP based fuels generated more amount of gases than the perchlorate based fuels. For the same chamber volumes, GAP based fuels released almost double the amount of gas when compared to perchlorate based fuels. These experiments demonstrate that GAP is a superior gas generating propellant than potassium perchlorate based propellants and hence, would be a good choice to be used in the microactuators when the actuators are intended to be used for applications like air bag deployment.

5.1.5 Microactuator Feasibility for Projectile Maneuvering

As the performance required from the microactuators varies from application to application, knowing the exact requirements of a specific application is critical in checking the feasibility of using microactuators towards that application. One such application that we are interested in is to maneuver the path of a 25 mm gun launched projectile using chemical microactuators. This section discusses the specific requirements that are needed from microactuators for this application and whether the developed

microactuators meet those requirements.

5.1.5.1 Application Requirements

For using microactuators for projectile maneuvering, the physical dimensions of the projectile and its spin rate control the overall performance desired from the actuator. In this thesis, we focus on a 25 mm diameter cylindrical projectile operating at a spin rate of 600 Hz. In order to maneuver its path, multiple actuators need to be fabricated on a single substrate as an array so as to release chemical jets radially from the body of the projectile. Also, for this purpose, all the control actuators and the control electronics need to be housed within the projectile. As the projectile has a cylindrical shape, an axis of revolution is defined along the length of the cylinder. The goal of using this test vehicle is to demonstrate a divert greater than the dispersion of uncontrolled rounds. For example, a 10% diversion pattern for the projectile requires at least 1 meter of lateral divert for 100 meters of flight. The total flight time for 100 meters was calculated based on the projectile spin rate to be 0.14 seconds. Volumetric constraints of the projectile limit the overall size of the actuators that can be housed within the projectile. The following list summarizes the limitations imposed on the actuators to facilitate integration into the flight vehicle [22]:

- Launch shock of the vehicle: 10,000 g
- Target divert: 1 m lateral divert per 100 m of flight
- Projectile spin rate: 600 Hz
- Control period: 0.14 s

The spin rate and control period of the test vehicle determines the timing constraints needed from the released jets. A spin rate of 600 Hz means that the projectile

makes one revolution every 1.67 ms. If the projectile is divided axisymmetrically into four quadrants, the impulse delivery of each individual actuator is limited to 0.416 ms. Hence, in order to deliver impulse in the desired direction, the time scale for each actuator needs to be controlled to within +/- 0.208 ms to ensure that the actuator releases jets in the appropriate direction.

Flight stability requires the use of multiple low impulse jets rather than a single large impulse jet. Making an array of multiple actuators also requires additional material to separate the combustion chambers and to provide contact pads for electronics. This limits the total number of actuators that can be made on a single array and controls the number of actuators to be fired per revolution. An arbitrary 10% dispersion in unguided projectiles determines the impulse goals for individual actuators. A simplified estimate of the divert is made by neglecting the aerodynamic and gyroscopic effects of the projectile. This estimate assumed that the discrete impulse bit causes a discrete change in momentum. Specifically, the y-velocity increased by an amount of total impulse divided by the projectile mass whenever an actuator is fired. The set of equations for the x and y positions at discrete time 'i' are:

$$\begin{aligned} V_{y,i} &= V_{y,i-1} + \frac{I_{actuator}}{m_{projectile}} \\ X_i &= X_{i-1} + V_x \Delta t \\ Y_i &= Y_{i-1} + V_{y,i-1} \Delta t \end{aligned} \quad (53), (54) \text{ and } (55)$$

If the mass of the projectile is assumed to be 150 grams and if there are a total of 32 actuators, the solution to this system for impulses of 1, 2.07, 5.45 and 10 mNs is plotted in Figure 77. The minimum calculated impulse to achieve a divert of 1 m within 100 m is calculated to be 5.55 mNs. The following list summarizes the estimated

performance requirements for the actuators based on above calculations:

1. Maximum volume of each actuator: 25 mm^3
2. Minimum actuator impulse: 5.55 mNs
3. Maximum duration of the jet: 0.416 ms
4. Maximum ignition delay variation: $\pm 0.208 \text{ ms}$

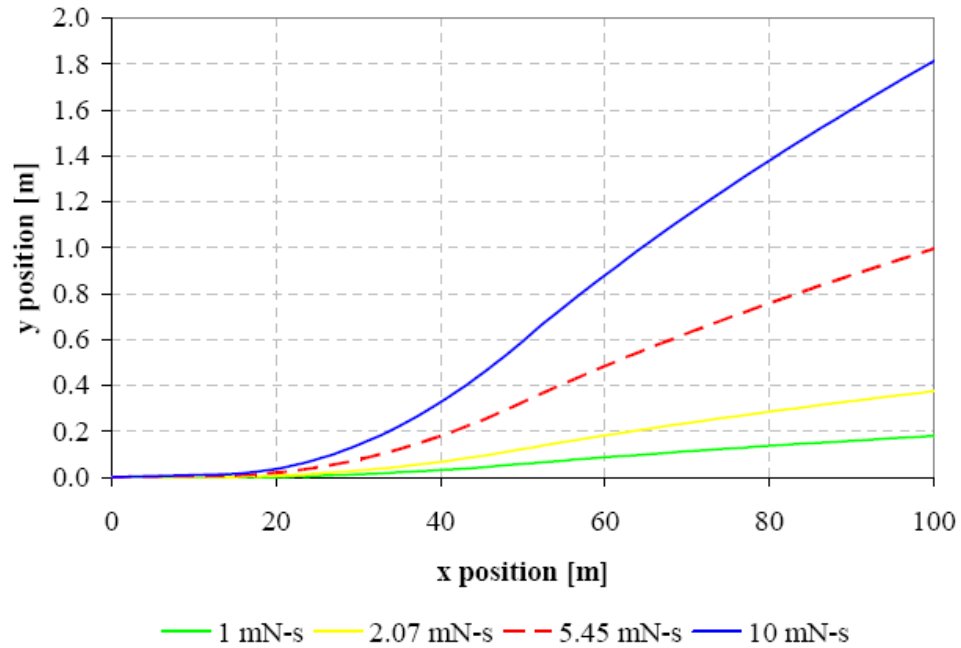


Figure 77: Impulse based displacement of 150 g projectile with x-velocity of 70 m/s and 32 actuator impulse bits in the y-direction

5.1.5.2 Actuator Performance

The above section details the requirements that are needed from the microactuator for the application of maneuvering the path of a 25 mm projectile. Chemical based microactuators that utilize perchlorate based and chlorate based conductive fuels are tested for this purpose. The impulse and the durations delivered by the microactuators are measured for both perchlorate based and chlorate based conductive fuels for varying

amounts of binder and fuel compositions. For testing perchlorate based conductive fuels, a chamber volume of 15 mm^3 is chosen. The distance between electrodes is fixed at 1.5 mm and an input voltage of 70 V is supplied from a $560 \text{ }\mu\text{F}$ capacitor and a high voltage power supply. Figures 78 and 79 show the performance results in terms of Impulse delivered vs. Duration for perchlorate based fuels with differing amounts of binder and conductive dopants. When the binder weight ratio in the fuel is fixed at 0.25, the performance of the actuators decreased with an increase in amount of conductive material in the fuel as shown in Figure 78. For a fuel with 3.4% by weight of carbon black, an average impulse of 14.44 mNs is delivered by the actuator in a burn time average of 0.12 ms with a standard deviation of 0.1 ms. As the amount of conductive material increased from 3.4% to 5.5% by weight, the average impulse delivered decreased to 10.91 mNs and the average duration increased to 0.18 ms with a standard deviation of 0.07 ms. With further increase in conductive material to 9% by weight, the impulse delivered by the jet dropped to 5.94 mNs and the average duration increased to 0.3 ms with a standard deviation of 0.1 ms. Next, the amount of binder material in the perchlorate fuel is increased and its effect on impulse and duration of the jet is studied. For the same amount of conductive material in the fuel, when the binder composition is increased, the impulse delivered by the jet did not change much. However, the durations have almost doubled. When the weight % of carbon black is 9%, the average duration time for 0.25 ratio of binder is 0.3 ms with a standard deviation of 0.1 ms. When the binder composition is changed to 0.75 ratio, the average duration obtained is 0.57 ms with a standard deviation of 0.13 ms. The impulse delivered by the actuator decreased with an increase in the amount of conductive material in the fuel. The performance delivered by perchlorate

based fuel with 0.25 wt ratio of nitrocellulose binder and 3.4% by weight of conductive material meets the performance requirements to be used in a 25 mm projectile maneuvering application.

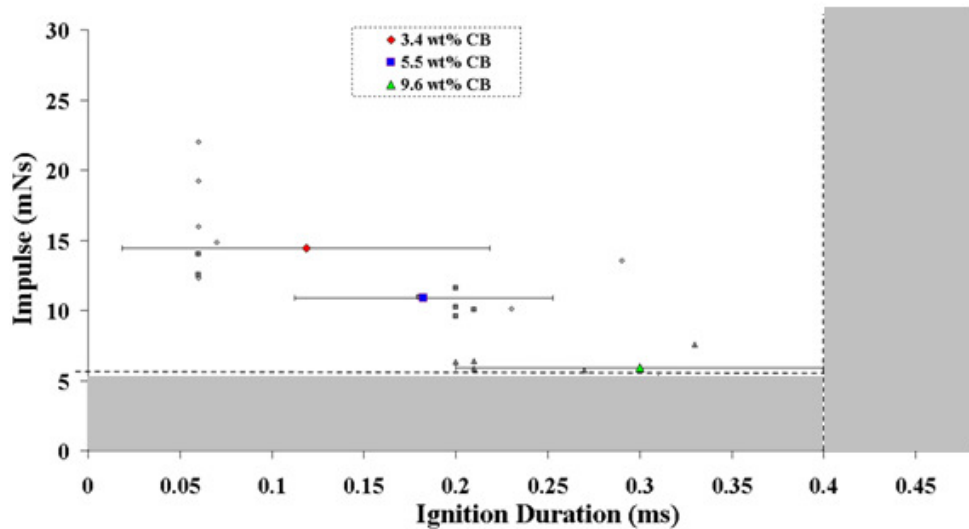


Figure 78: Actuator performance: 15 mm³ combustion chamber with perchlorate based fuel with 0.25 x by weight of binder composition and varying conductive material composition

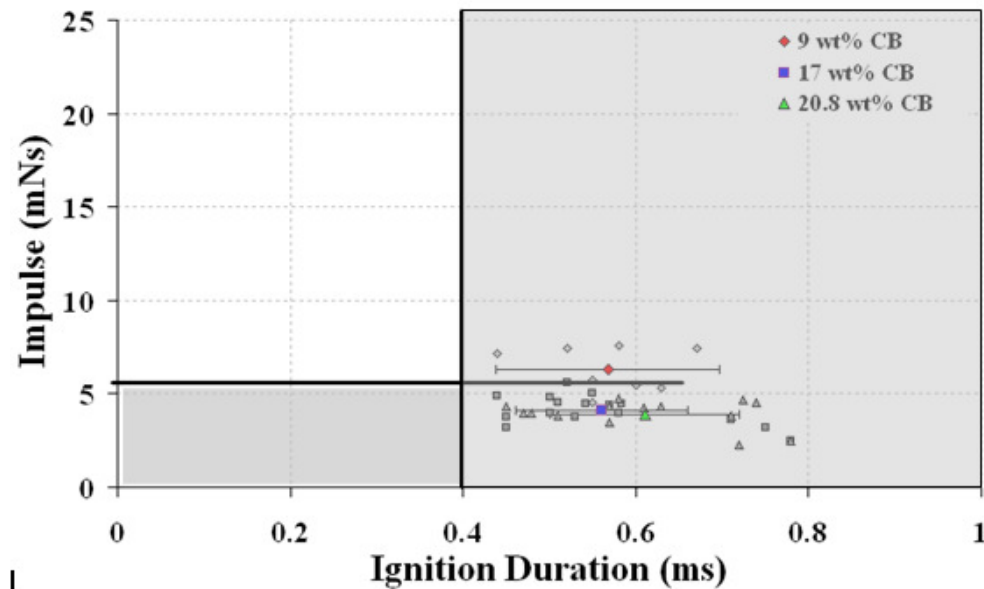


Figure 79: Actuator performance: 15 mm³ combustion chamber with perchlorate based fuel with 0.75 x by weight of binder composition and varying conductive material composition

The same experiments are then repeated for chlorate based fuels to check for its feasibility to be used in the final application. The fuel composition used for this testing purpose is $6KClO_3 : Sb_2S_3 : xCB$. As the amount of carbon black in the fuel increased, the impulse delivered by the microactuator decreased and the duration increased. Three fuel compositions were tested for this purpose and the results are shown in Figure 80. When a carbon black fuel ratio of 3.4% by weight is used along with nonconductive chlorate based fuel, an impulse of 9.77 mNs is delivered in a duration of 0.18 ms with a standard deviation of 0.04 ms. When the carbon black composition is increased to 6.7% by weight, the impulse released decreased to 8.29 mNs and the average duration of the jet increased to 0.2 ms with a standard deviation of 0.06 ms. The performance delivered by chlorate based fuel with 9% by weight of conductive material meets the performance requirements to be used in a 25 mm projectile maneuvering application. The above results show that the performance obtained from the microactuators can easily be altered by changing the fuel composition, actuator geometry and input energy parameters to meet the requirements for many applications.

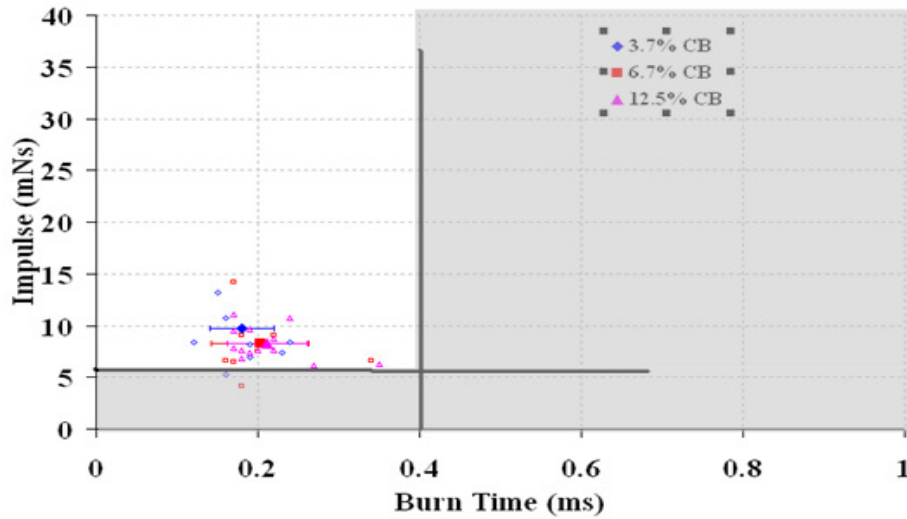


Figure 80: Actuator performance: 15 mm³ combustion chamber with chlorate based fuels with varying compositions

5.2 Physical based Microactuators

This section presents the results obtained from the characterization of physical jet microactuators that operate on the principle of arc-generation. When sufficient electrical energy is supplied to a physical propellant (as opposed to chemical) placed between two closely spaced electrodes in a microchamber, an arc is generated within the system causing a rise in the temperature and pressure of the system. This rise in temperature and pressure causes a phase change of the propellant resulting in the high pressured propellant to exit the chamber in the form a fluidic jet through a nozzle. The microactuators are characterized for the required electrical energy, force generated and duration. Finally, the released jets are used to perform skin ablation experiments and the extent of skin permeation achieved is measured.

5.2.1 Actuator Characterization

The microactuators which are fabricated using laser micromachining and lamination techniques as described in Section 3.3.1.2 are characterized for device performance. The equipment and materials used for the manufacture of the actuators limited the physical geometries that are possible and these limitations are summarized in Section 5.1. As the concept of arc-generation relies strongly on the distance between electrodes and the input power supplied, the actuation process is optimized to minimize these parameters. The smaller the gap between electrodes, the smaller is the required input electrical energy for arc-generation. As the minimum distance possible between the electrodes using the above fabrication techniques is 250 μm , this distance is used while characterizing the actuators for the input power requirements. Finally, the actuators should be able to deliver consistent performance to be used in a final application. The type of propellant used and the geometry of the microactuator both contribute significantly towards achieving consistent performance from the actuator.

For testing the microactuators, a power circuit as discussed in Section 4.1.6 is used to supply electrical energy to the electrodes. The power circuit is characterized to study the required electrical input characteristics to create an arc when the distance between the electrodes is fixed at 250 μm . Figure 81 shows the typical voltage, current and energy consumed by the actuator during arc-discharge process. Voltage data is obtained by measuring the voltage across the actuator electrodes using a voltage divider circuit. The current data is then obtained by measuring the voltage across the mosfet and from mosfet characterization as discussed in Section 4.1.6.1. The energy consumed during the arc generation process is then calculated according to Equation 22. It was observed that a voltage of at least 147 V is needed from a 560 μF capacitor to generate an

arc across two electrodes placed 250 μm apart. From Figure 81, it can be seen that the input voltage immediately drops from about 140V to 95 V within less than 0.1 ms suggesting that the arc-generation process is extremely rapid. This small drop in voltage is enough for the generation of an arc across 250 μm spaced electrodes.

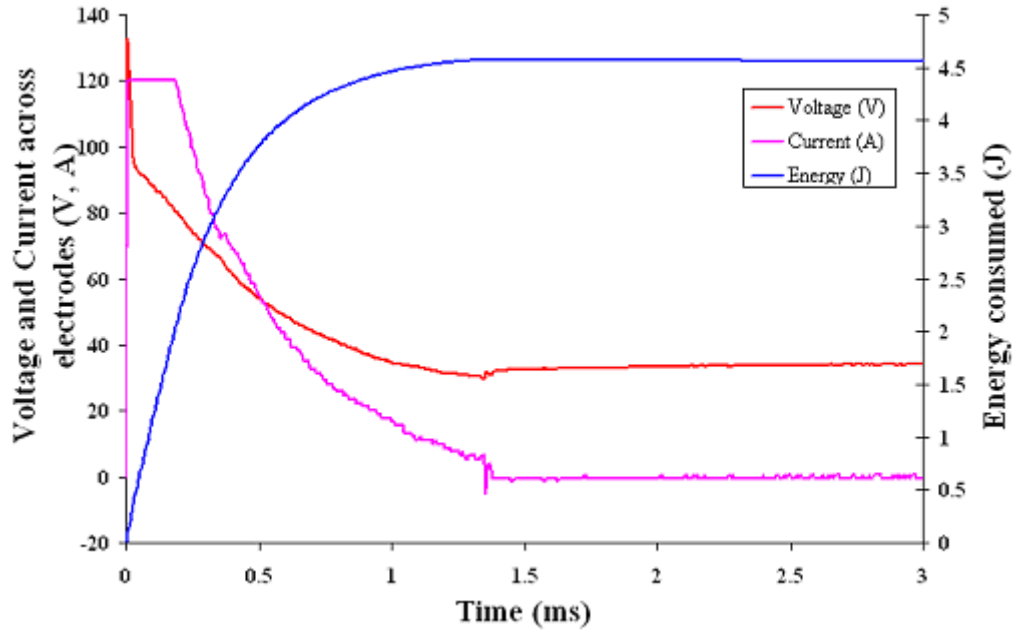


Figure 81: Power characteristics consumed from the power supply during the arc generation process

5.2.1.1 Mechanical Characterization

Once the input power requirements are known, the physical microactuators are characterized for duration and force for several physical propellants using the test setup discussed in Section 4.1.4. Figure 82 shows the average forces delivered by different propellants occupying a chamber volume of 1 mm^3 when the distance between electrodes is fixed at 250 μm and a voltage of 147 V is supplied to the electrodes from a 560 μF

capacitor. In order to compare the forces delivered by several propellants, a control is prepared by using an empty chamber filled with air. The average force delivered for the control is about 0.34 N. The chambers are then filled with solutions of deionized water, ethanol mixed with salt solution in different proportions, and salt solutions. The average force delivered when the chambers are filled with deionized water is 0.84 N with a standard deviation of ± 0.32 N. Salt water based ethanol formulations are then prepared in several compositions to study the effect of adding salt to the solution. Because ethanol is a volatile solvent that would evaporate quickly during storage, it is mixed with 1-4% hydroxyl-propyl-methyl cellulose (HPMC), which served as a thickening or gelling agent. Ethanol gel with increased concentration of salt solution showed an increase in delivered forces. When the salt concentration in ethanol solution is 0.1%, the generated forces increased to 1.19 N with a standard deviation of ± 0.08 N. When the salt concentration is increased further to 0.3%, the forces delivered increased to 1.5 ± 0.27 N. When 100% salt solution is used, the force generated increased to 2.4 N with a standard deviation of ± 0.37 N. This increase in generated force magnitude with addition of salt to the solution can be explained by the increase in conductivity of the propellant solution with addition of salt. Table 14 summarizes the different formulations tested and the forces obtained.

Table 14: Amount of forces generated by several propellants

Formulation	Average Force (N)	Standard deviation
Air	0.34	
Deionized water	0.84	0.32
10% water, 90% ethanol, 0.1% NaCl, 2% HPMC	1.19	0.08
30% water, 70% ethanol, 1.5% NaCl, 2% HPMC	1.5	0.27
Salt solution	2.4	0.37

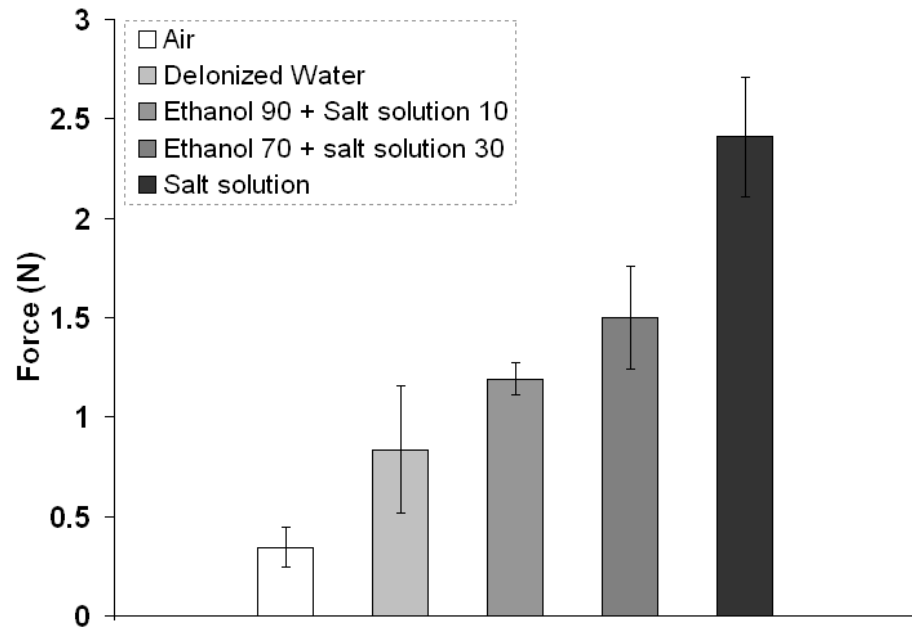


Figure 82: Force data obtained for several propellants occupying a chamber volume of 1 mm³

The duration of the jet is then measured from the force data and also by imaging the released jet using high-speed microscopic photography. Figure 83 shows an image of the jet emitted from the microdevice upon activation. Both these measurements indicated that the arcing and microjet ejection occurred on a time scale of 100 μ s.

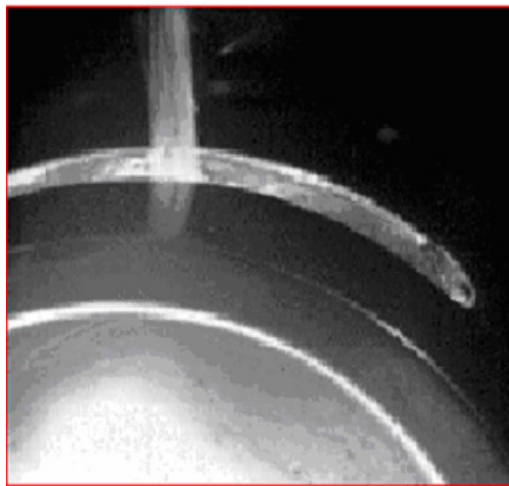


Figure 83: High speed imaging of released jet from physical microactuator

From the previous testing, as we saw an increase in the generated force with the addition of salt particles, we hypothesized that adding conductive particles to the propellant might increase the conductivity of the propellant and hence, might result in reducing the input power required to generate the arc and increase the force delivered. Hence, the effect of adding solid micro particles to the propellant is studied by adding nano size gold particles. As expected, ethanol gel with gold particles showed higher forces and the force generated increased with an increase in gold particle concentration. The force generated by this jet is observed to be in the range of 2-10 N depending on the composition used. This increase in generated forces could be attributed to the microsize

particles which act as projectiles jetting out from the microdevice.

5.2.1.2 Thermal Characterization

In order to characterize the thermal ablation of skin, knowing the temperature of the released jet is critical. Hence, efforts are made to estimate the maximum temperature which the propellant can reach within the chamber based on the input electrical energy supplied to the propellant. From the voltage and current characteristics measured during the ignition process, the total input energy required to cause arc ablation is estimated. For these calculations, water is used as the propellant medium. If all the electrical energy supplied to the electrodes is used to heat the water medium, the rise in temperature of water can be calculated by considering the specific heat of water, heat of vaporization of water into steam and the specific heat of steam according to Equation 56. Based on these calculations, the maximum temperature that water propellant can reach within the microchamber is estimated to be 1095°C. The detailed calculations for obtaining the temperature are shown below:

$$E = (mC_p \Delta t)_{water} + m\Delta H_{vaporization} + (mC_p \Delta t)_{steam} \quad (56)$$

Specific heat of water: 4.186 J/g°C

Specific heat of steam at 1 bar and 100 °C: 2.04 J/g°C

Heat of vaporization of water ($\Delta H_{vaporization}$): 2255 kJ/kg

$$m = \rho * V = 10^{-3} \text{ g}$$

The amount of energy consumed = 4.6 J

$$\Rightarrow 4.6 = (10^{-3})(4.186)(100-25) + (10^{-3})(2.04)(T-100) + 10^{-3}(2255)$$

$$\Rightarrow T \approx 1095 \text{ °C}$$

5.2.2 Skin Characterization

The characterized microactuator is then used to study its feasibility for use in improving skin's permeability for later delivery of drugs. In order to increase skin's permeability, the stratum corneum layer of skin must be selectively removed without causing any damage to the underlying layers of skin. The skin is exposed to the jet released from the microactuator both directly and indirectly to study the effects of thermal and mechanical effects of jet on skin ablation.

5.2.2.1 Thermo-Mechanical Exposure of Skin

To study the thermo-mechanical effects of jet on skin, the microactuator is activated by placing it in contact with human or porcine cadaver skin. Figure 84 shows one such skin surface which is exposed to an ethanol microjet. The exposed skin is then imaged and its permeability to a drug analog molecule is studied. For initial experiments, shaved porcine cadaver skin is used for exposure. The skin is held in the path of the jet using a q-tip as the skin might move because of the force from the released jet. Figure 85 shows the same exposed skin that is stained with trypan blue using a protocol mentioned in Section 4.2.3 at a magnification of 90x. The small area in skin which is exposed to the jet becomes blue which is a representative of an increase in permeability to the drug.



Figure 84: Microscopic image of skin surface exposed to an ethanol microjet

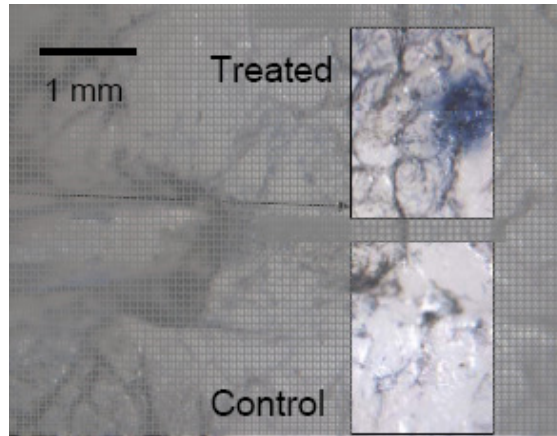


Figure 85: Microscopic image of trypan blue stained skin surface exposed to the jet

The treated area is then histologically examined by cryo-sectioning and H&E staining according to the protocol described in Section 4.2.4. From Figure 86 it can be seen that the stratum corneum layer of the skin is completely removed in the exposed area with some damage to the underlying epidermis layer. When an ethanol propellant containing gold microparticles is used as a jet, confocal imaging of the affected skin after cryo-sectioning showed penetration of gold particles into stratum corneum layer fully as shown in Figure 87. These histology results showed promising results with minimal damage to the skin tissue when compared to the damage caused by long term thermal treatment. However, when the skin is directly exposed to the thermo-mechanical jet from the actuator, the ablation effects were not just limited to the stratum corneum layer. Histological examination of skin showed that the underlying viable epidermis layer was partially ablated too.

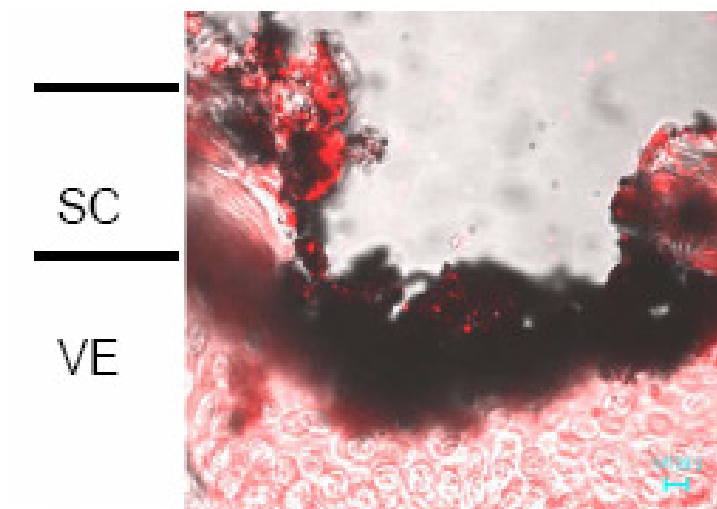


Figure 86: Histologically examined skin surface exposed to an ethanol jet

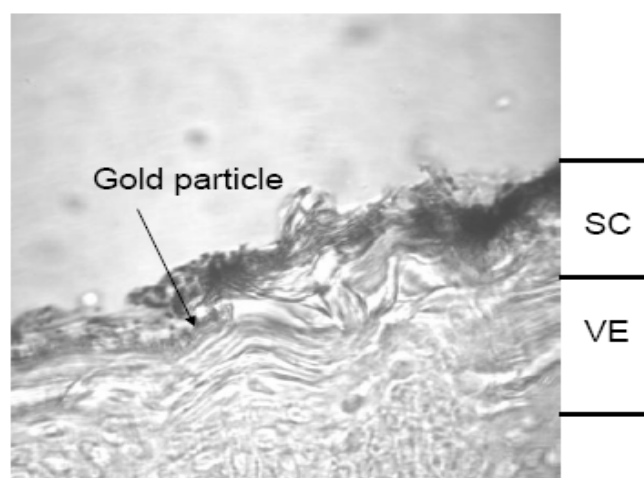


Figure 87: Histologically examined skin surface exposed to an ethanol jet containing gold nano particles

From the previous testings we saw that when the skin is directly exposed to the jet released from the actuator, the size of ablation site is significantly large and the effects of ablation were observed at much deeper thickness in skin than the thickness of stratum

corneum layer. To minimize the size of the ablation site and to obtain localized effects, further testing is done with the skin being exposed to the jet through a mask consisting of circular holes as shown in Figure 88. For initial localized testing, a PDMS mask is used to control the size of the skin ablation and effectively guide the removal of stratum corneum in a highly localized manner. Corresponding to a 100 x 100 μm size mask, the holes generated in the skin measured approximately 100 μm in size. The size of these ablation sites could be changed by simply changing the size of the masking holes in the microdevice. Histological examination of exposed skin through a mask showed highly selective removal of stratum corneum as shown in Figure 89. Figure 89(a) shows as enface image of ablated skin at three adjacent locations. Figure 89(b) shows a histological cross section of skin ablation at two adjacent sites from a different skin sample. Figure 89(c) shows a further magnified view of one of these ablation sites. Figure 89(d) shows a still greater magnification of the edge of an ablation site from another skin sample. These representative images showed highly localized ablation that completely removed the stratum corneum which is critically important for increasing skin permeability, but does not appear to damage the viable epidermis.

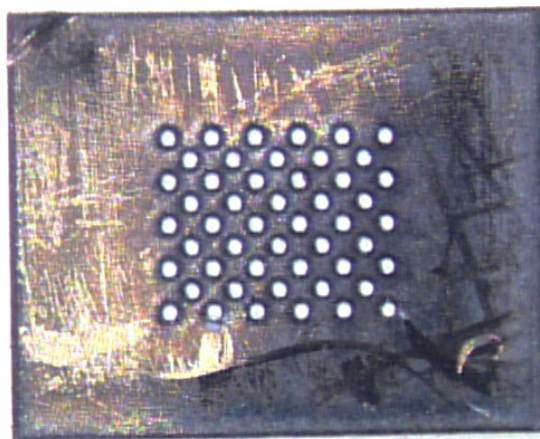
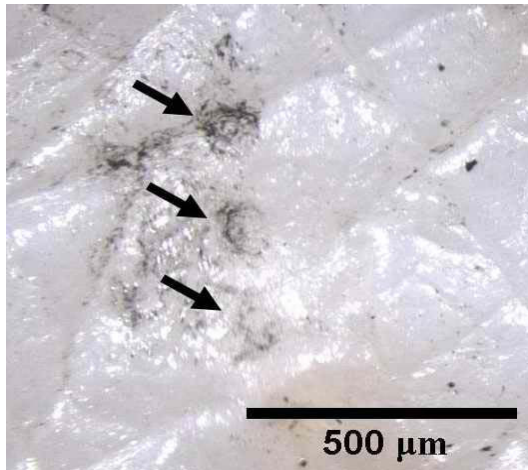
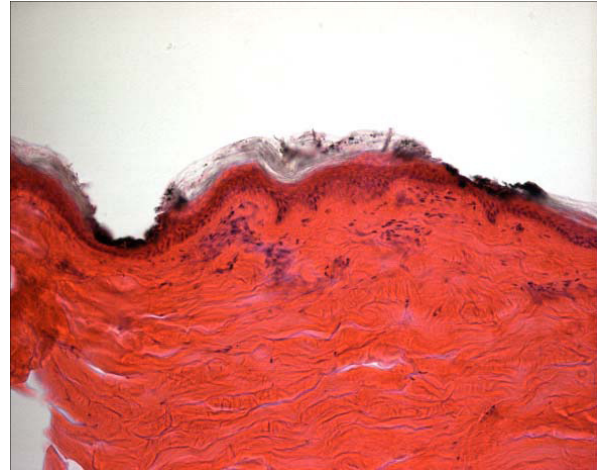


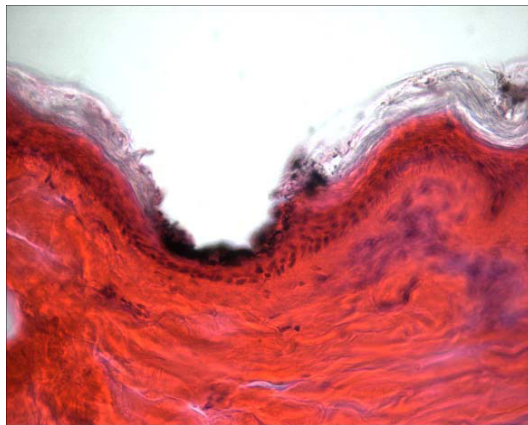
Figure 88: Patterned mask used for localizing the effects of thermo-mechanical jet exposure on skin



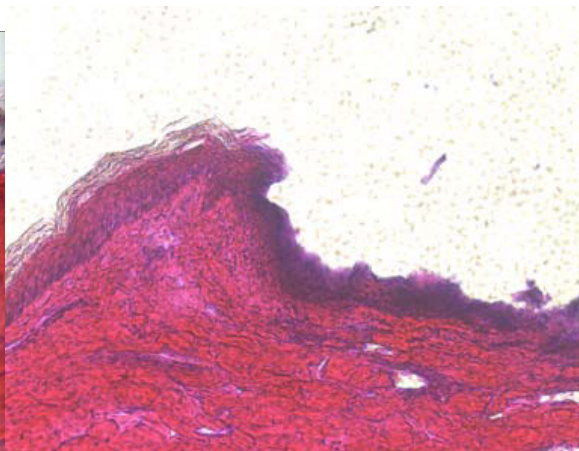
(a)



(b)



(c)



(d)

Figure 89: Histological examination of locally exposed porcine skin

From the above histology results, it can be seen that the stratum corneum layer of skin is efficiently removed. This observed efficient removal should increase skin permeability to drug molecules. Hence, permeability measurements of exposed skin to a drug analog molecule are performed as described in Section 4.2.3. Figure 90 shows permeability measurements made for delivery of calcein across treated human cadaver skin. For untreated skin, this permeability is just 10^{-5} cm/h, because calcein is a relatively large (623 Da), hydrophilic compound. After arc ablation of the skin with water, the permeability increased by 1000 fold to a value of 10^{-2} cm/h. This large increase in skin permeability is highly significant for drug delivery applications. Arc ablation with ethanol-saline formulation also increased skin permeability, but to a lesser extent. Arc ablation with an empty (i.e., air-filled) micro-chamber also increased skin permeability, but only by a factor of 10. Arc ablation with water ejected from the microchamber was probably more effective because it more efficiently transferred heat (and momentum) to the tissue as compared to air.

Additional formulations of propellants were tested and skin permeability is compared. As shown in Figure 91, the use of (i) ethanol with gold microparticles, (ii) ethanol-saline with salt microparticles, (iii) ethanol with gold microparticles placed on the skin surface and (iv) ethanol-saline (without microparticles) all increased skin permeability by 100-1000 fold. We hypothesized that such microparticles could be important because they (i) could increase the conductivity of the microjet formulation and/or (ii) could act as projectiles jetted at the skin. However, statistical testing showed no significant difference between these four formulations, given the large error bars. Comparing the data in Figure 91 with the data in Figure 90 suggests that the exact

formulation of the jet may not be critical to increasing skin permeability; such that water, ethanol and ethanol-saline all dramatically increased skin permeability. Moreover, the presence of gold or salt microparticles did not have a significant effect. Efforts were then made to correlate the permeability data to the force generated by the microjets. Figure 92 shows the data obtained for the reaction force of the microjet plotted against the increase in skin permeability for a series of experiments carried out using a saline solution as the propellant.

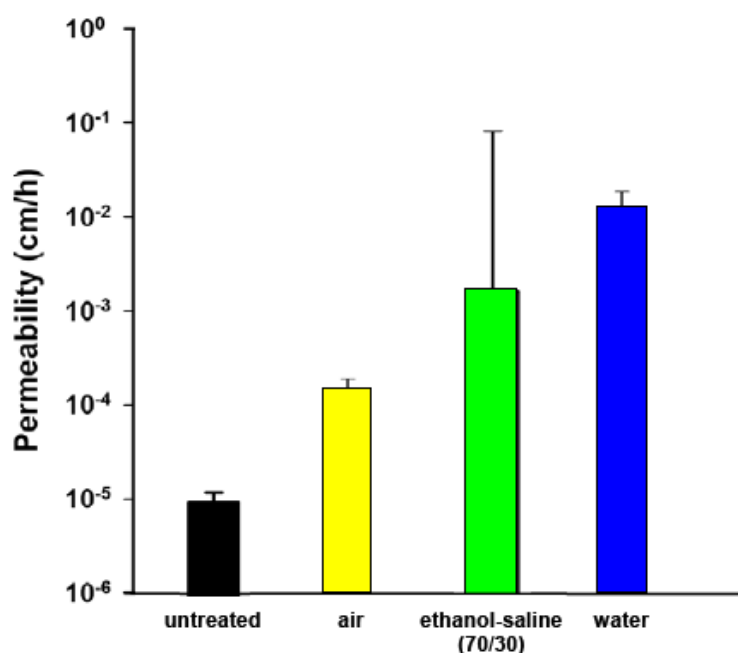


Figure 90: Permeability results obtained in jet exposed human cadaver skin for several propellants

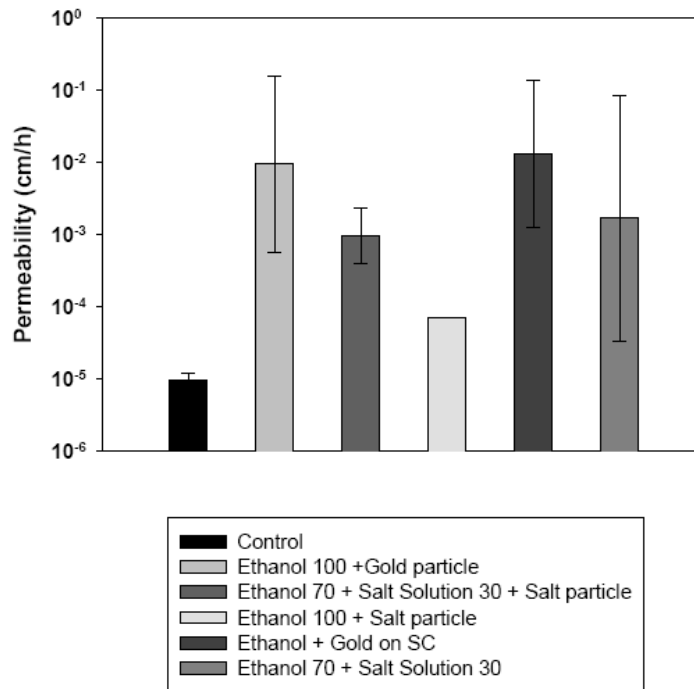


Figure 91: Permeability results obtained in jet exposed human cadaver skin for several propellants containing solid microparticles

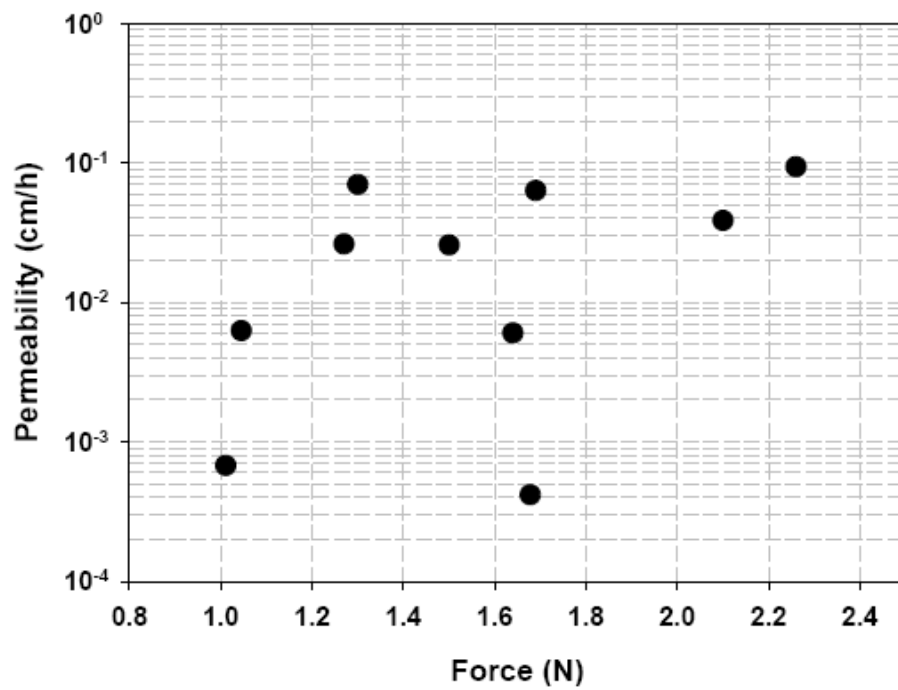


Figure 92: Dependency of permeability obtained with reaction force obtained from the jet

5.2.2.2 Thermal Exposure of Skin

From the previous results, it was shown that a thermo-mechanical jet successfully creates micron size pores in the stratum corneum layer of skin and increases the skin's permeability with minimal damage to the underlying skin tissue. But, from the previous results, it is not clear how much of this increase in skin's permeability is due to thermal effects or due to the mechanical effects of the jet. Hence, in this section, efforts were made to isolate the thermal and mechanical effects of the jet and study the effect of thermal jet on exposed skin surface. For this purpose, the temperature of the released jet needs to be measured. A temperature indicator, liquid crystal paper is used to measure the temperature of the jet. However, if the thermal indicator paper is placed in the direct path of the jet, it is damaged because of the mechanical force from the jet. Hence, the indicator paper is placed beneath a 25 μm thick titanium or tungsten mask. Using this approach, the temperature on the underside of the mask is measured to be at least 290°C. However, given the very short duration of the thermal pulse, there should be a steep temperature gradient across the mask. Hence, in order to estimate the temperature of the jet that impacts the top side of mask, thermal calculations based on transient analysis of heat conduction are performed across the mask using COMSOL modeling. From these simulations, the temperature of the released jet from the actuator is predicted to be at least 1000°C. As tungsten is more thermally conductive than titanium, in order to reduce the temperature gradient across the mask, a 25 μm thick tungsten mask is used for all further testing. Tungsten metal is not only strong enough to withstand any damage caused by the mechanical force of the jet but it is also highly thermally conductive so that the thermal losses associated with the masking layer are minimal.

5.2.2.2.1 Temperature Profile of Skin

Next, in order to estimate the depth to which the skin is ablated, the temperature across the skin surface is calculated using computer simulations and the results are presented in Figures 93, 94 and 95. This temperature estimation is important to study the extent of depths to which the skin is ablated. The simulations were performed for two cases: (a) when the skin is directly exposed to the jet and (b) when the skin is indirectly exposed to the jet using an external mask. For the first case, as we estimated that the jet temperature is around 1000°C , we used this temperature as the temperature at the surface of skin. The skin is modeled as a structure consisting of both epidermis and dermis layers and the physical properties for each layer are obtained from the literature and presented here in Table 15 [90]. The simulations were carried out using transient thermal analysis mode in COMSOL 3.3 and the resulted temperature gradient for different times of exposure and various skin depths were plotted in Figure 93. From this graph, it can be seen that the smaller the exposure time, the higher is the thermal gradient across the skin. As the jet exposure time is typically in 100-300 μs range, we are interested in looking at this time scale of exposure. When the skin is exposed to a surface temperature of 1000°C for 100 μs , it can be seen that the stratum corneum layer which is the top 20 μm reaches a very high temperature i.e about 600°K . The next layer of skin which is the viable epidermis is also affected at these time scales of exposure. From these simulations, we observed that when the skin is directly exposed to the jet even for a short time i.e less than 100 μs , it is very hard to limit the effects just to the stratum corneum. Hence, in order to limit these effects, we must reduce the temperature of exposure of skin. This temperature reduction can be achieved experimentally by an indirect exposure of skin

using an external mask. These indirect exposure temperature simulations are done for two cases. For the first case, we used a 25 μm thick titanium film as the external mask and the results are presented in Figure 94. When the temperature at the titanium top surface is fixed at 1273°K, the exposure times show that the skin needs to be exposed for at least 500 μs for the stratum corneum layer to ablate. When the time of exposure increased to 10 ms, the temperature rose to 796°K. If the skin is further exposed for a time of 100 ms, the temperature at 20 μm depth of skin is 1011°K. However, on the time scale of interest, i.e., 100 - 300 μs range, the skin is hardly affected. Hence, titanium is not a good choice for the metal mask because of the steep temperature gradient across the material. Further simulations are then performed to study the effects of using 25 μm thick tungsten film as an external mask. For this case, the temperature profile is presented in Figure 95. For the time scale of interest, i.e, 100 - 300 μs range, it can be seen that only the stratum corneum is exposed with minimal effects to the deeper layers of skin. So, in order to limit the ablation effects to just the stratum corneum layer which is about 20 μm thick, a 25 μm thick tungsten film can be used. If the time of exposure is increased from 100 μs to 1 ms, the temperature at 20 μm depth of stratum corneum increased from 309°K to 346°K. When the time of exposure increased to 10 ms, the temperature rose to 811°K at a skin depth of 20 μm . If the skin is further exposed for a time of 100 ms, the temperature at 20 μm depth of skin is 1054°K. These results give us an idea on what the exposure times need to be in order to selectively ablate the stratum corneum and they can also be used to optimize our testing by controlling propellant volumes, exposure times and the exposed jet temperature in order to control the pore size formed in skin.

Table 15: Properties of skin used in thermal simulations [90]

Property	Symbol	Units	Epidermis Values	Dermis Value
Specific Heat	Cp	J/Kg*°C	3580	3300
Thermal conductivity	k	W/m*°C	0.21	0.4
Initial surface temperature	T	°C	32	32
Density	ρ	Kg/m ³	1200	1200
Thickness	t	M	80e-6	2e-3

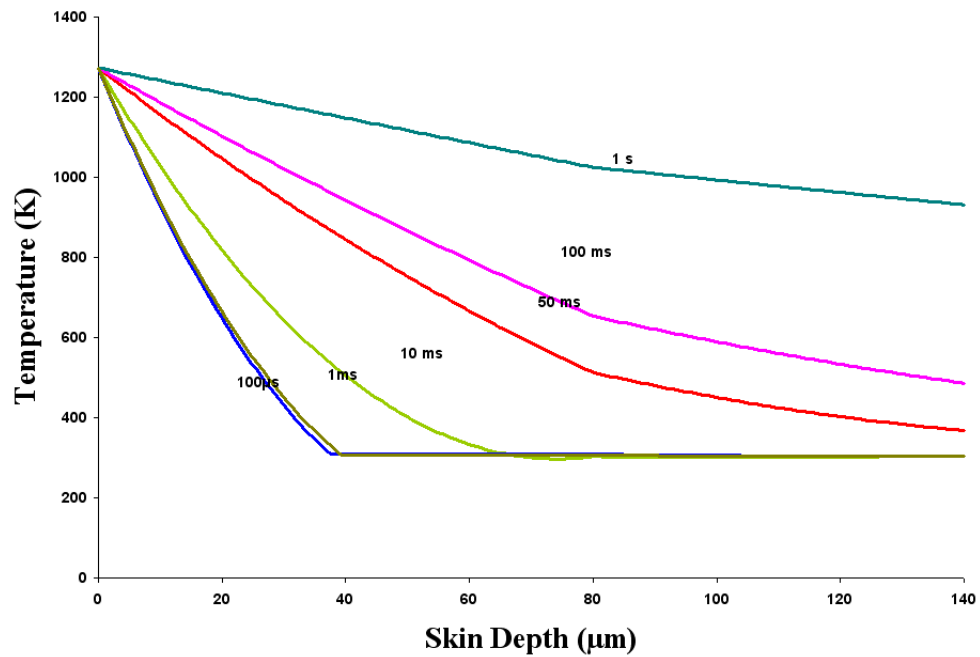


Figure 93: Temperature profile obtained in skin from simulations for a direct exposure to a thermo-mechanical jet

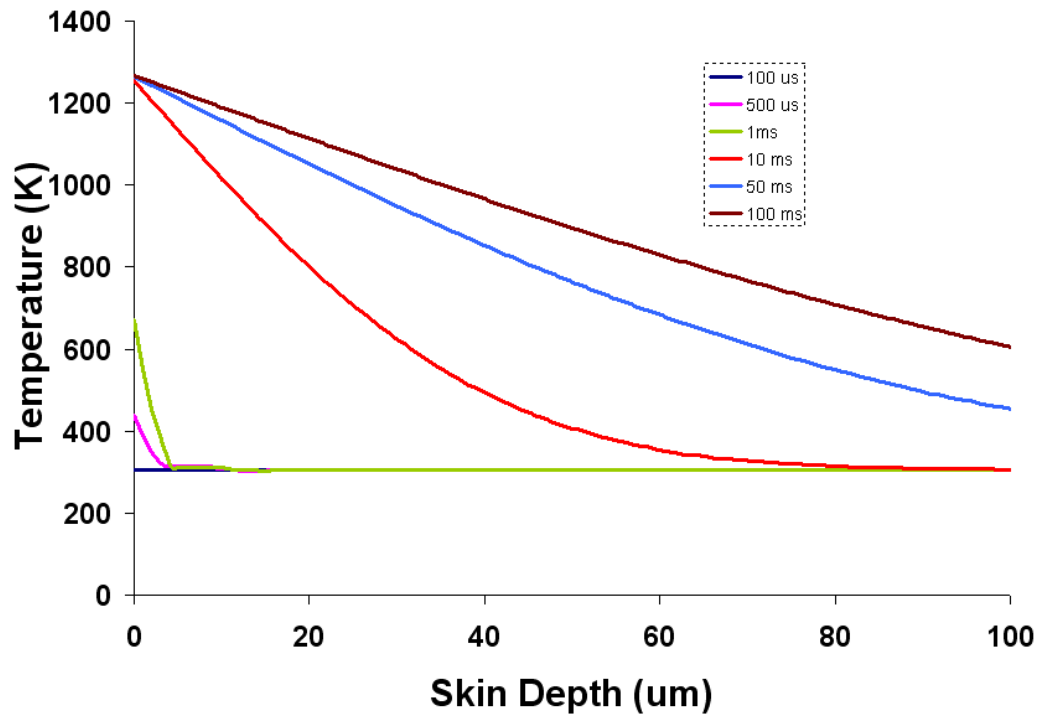


Figure 94: Temperature profile obtained in skin from simulations for an indirect exposure to a thermo-mechanical jet using a 25 μm thick titanium mask

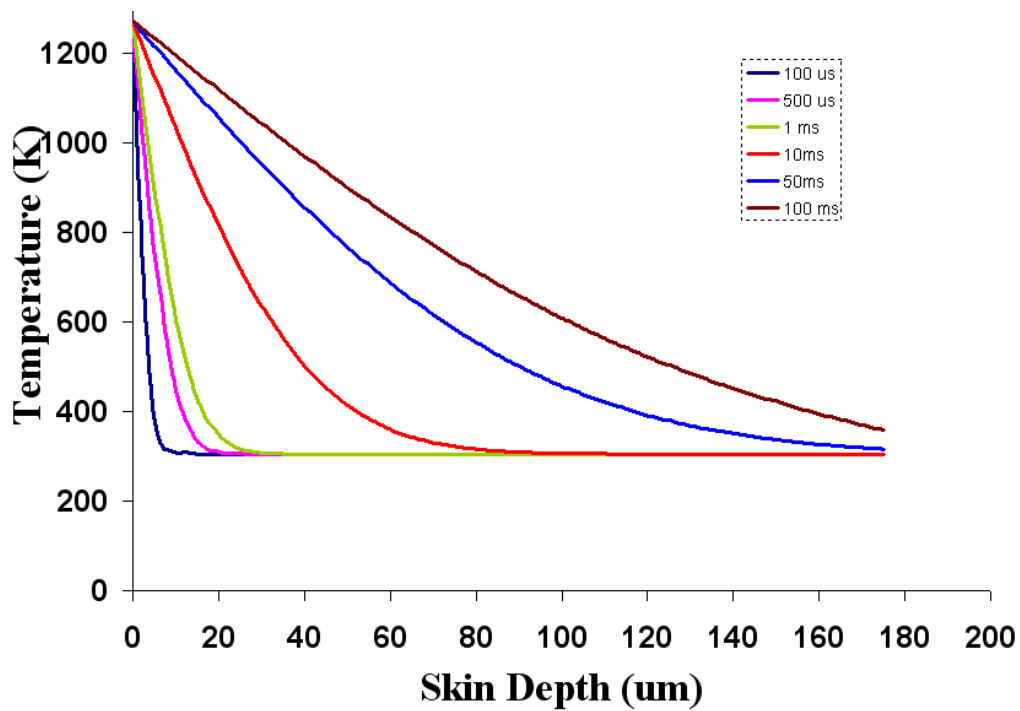


Figure 95: Temperature profile obtained in skin from simulations for an indirect exposure to a thermo-mechanical jet using a 25 μm thick tungsten mask

For studying the thermal effects, a solid mask is placed in the path of the jet in direct contact with the skin's surface. For this purpose, a 25 μm thick tungsten layer is used as the mask. Figure 96 shows porcine skin surface before and after the ablation process. Figure 96(a) shows the surface of untreated skin (control) and Figure 96(b) shows the same skin surface after it is thermally exposed.

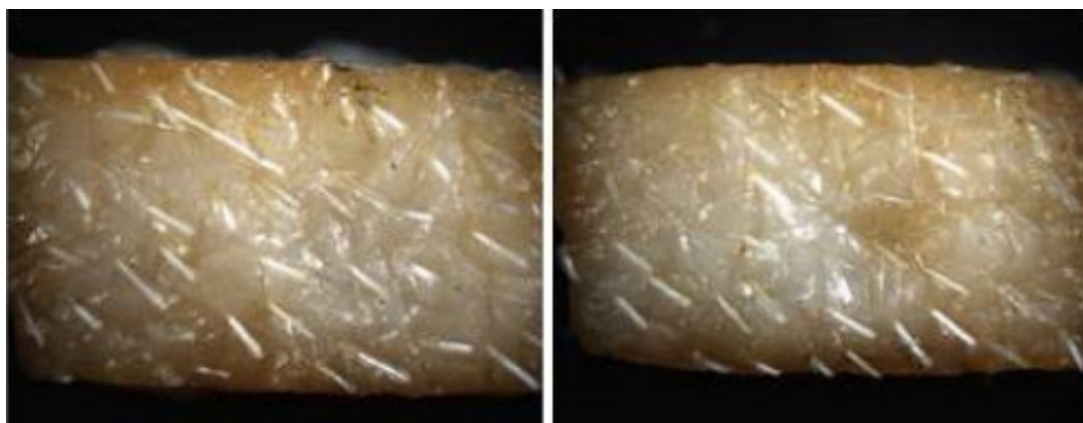


Figure 96: Picture of skin before and after exposure to a thermal jet

The exposed skin is then tested for its permeability to a model drug, sulforhodamine. Figure 97 shows the same skin sample after the delivery of sulforhodamine for 12 hours. Comparing to the control sample, the skin surface around the ablated site showed the radially decreasing intensity of purple staining by sulforhodamine, implying the diffusion of the drug into skin. The extent of this drug diffusion into the skin is then identified with the histological examination of the skin sample as shown in Figure 98.

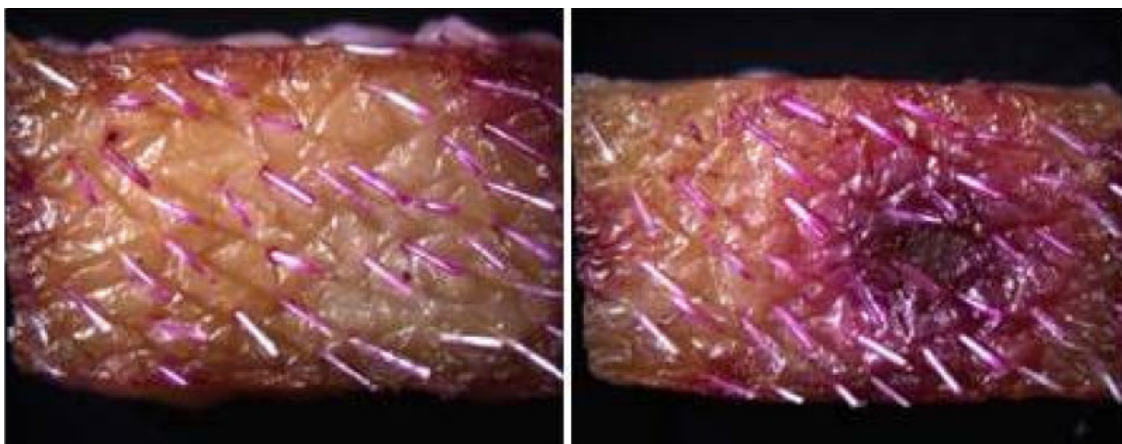


Figure 97: Skin shown in Figure 96 after treating with sulforhodamine drug to study its permeability

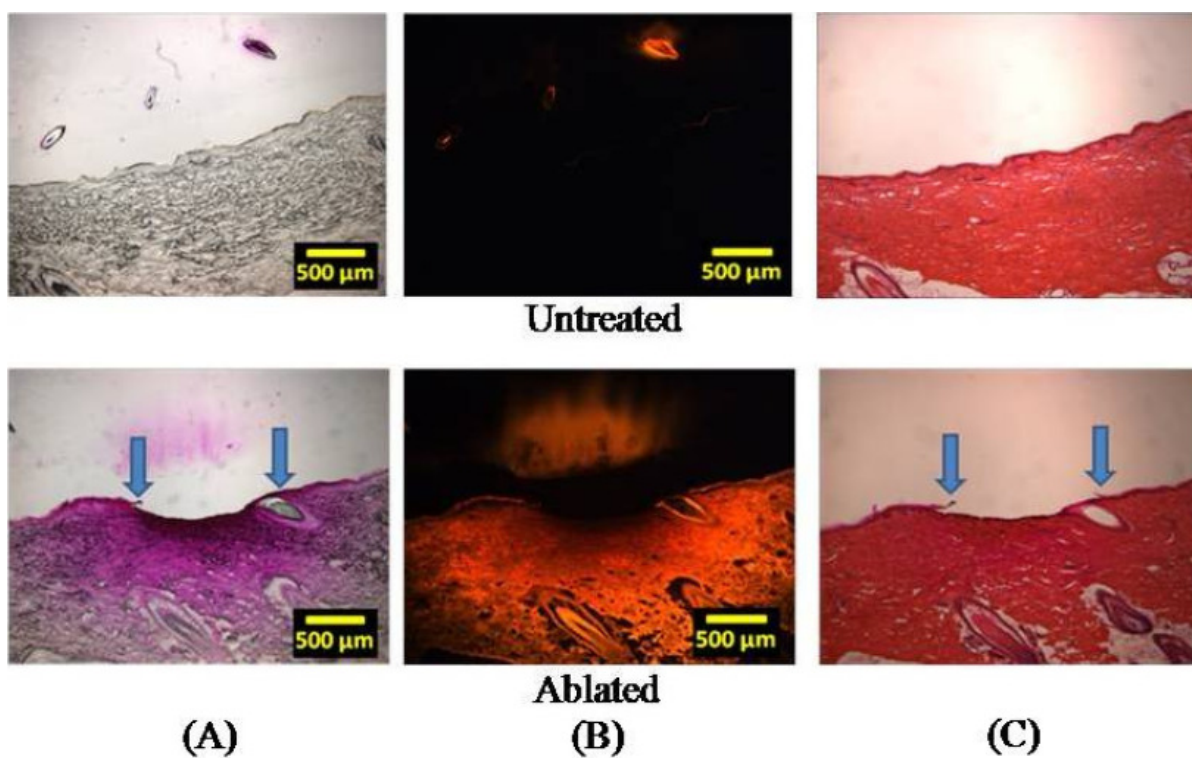


Figure 98: Histological examination of skin shown in Figure 97

While the histology of control sample showed no diffusion of hydrophilic sulforhodamine, the brightfield and fluorescent images of the ablated sample show a gradient in sulforhodamine delivery from the ablated top to the deeper tissue and fluorescence due to the diffused sulforhodamine, respectively. Figure 98 shows a cross section of the stained skin sample which had intact stratum corneum and which lost stratum corneum after thermal exposure, without damage to the underlying epidermis.

Next, efforts were made to localize the thermal effects to micro regions on skin. So, a double mask is placed in the path of the jet in contact with skin's surface. The mask is made of two layers, first of which is a solid layer made out of 25 μm thick tungsten sheet and the second layer is made out of 25 μm thick titanium layer consisting of an array 100 μm size circular holes as shown in Figure 88. The solid mask layer is used to eliminate the mechanical effects of the jet and the patterned mask with localized windows enables for controlled heat ablation. This localization of skin ablation can control the permeability rate of drug by controlling the area of exposed skin irrespective of jet's dimensions. Figure 99(a) shows an ablated skin sample that is subjected to localized thermal exposure. The ablated skin sample is treated with sulforhodamine for 12 hours to study the permeability to a drug analog. The same skin sample is then histologically examined to study the extent of permeability and the effective removal of stratum corneum as shown in Figure 99(b).

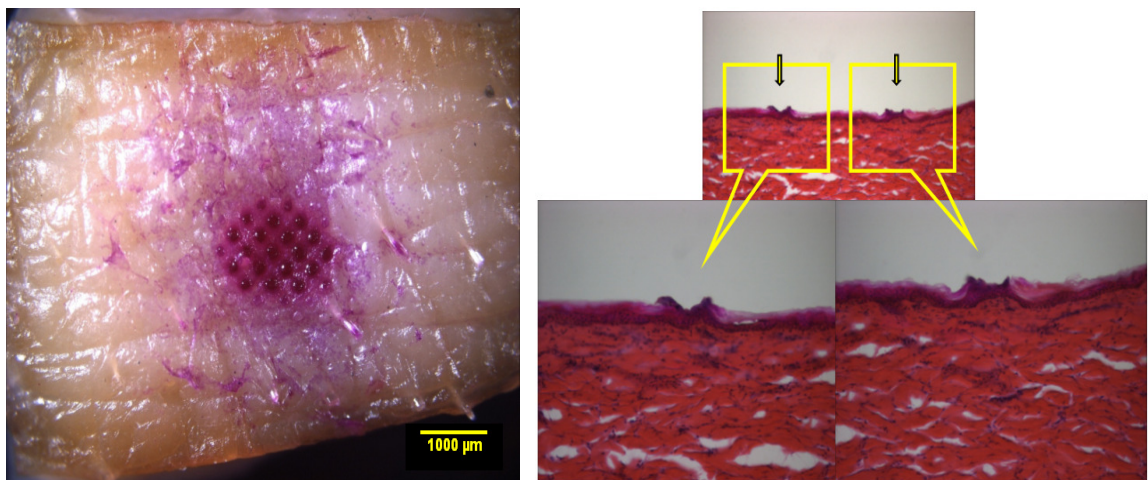


Figure 99: Locally ablated skin surface exposed to a thermal jet

This concludes the results section for the physical based microactuators. Physical based microactuators are successfully characterized and applied to improve skin's permeability. Both thermal and mechanical effects of the jet on skin were studied to determine the dominant effects. It was observed that the thermal effects of the jet alone are sufficient to create microconduits in skin without causing any permanent damage to the skin. The effected skin is characterized to study the thermal and mechanical effects of the jet exposure and the extent of drug permeability is measured.

CHAPTER 6

CONCLUSIONS

Throughout the course of this study, the development of the electrically powered chemical and physical microactuators was discussed. First, the concept of operation of the microactuator is mentioned and validated. Next, laser micromachining and lamination techniques were used to batch fabricate robust devices on a single substrate. Fabrication of actuators from robust materials improves MEMS reliability in harsh environment based applications. It also eliminates the need for additional packaging steps to ensure protection of the device from environment which significantly reduces the fabrication costs. Use of lamination fabrication while making microactuators demonstrates that material selection can be expanded to meet the specific conditions put forth by an application. For example, while making the chemical actuators, the materials utilized for fabricating the chambers should be able to withstand high chemical reaction temperatures, typically several thousand degree Celsius without compromising on the structural integrity. Materials such as acrylic, which melts at 130°C, can still be used for such as application provided the residence time and heat transfer from combustion to the chamber walls are minimized. While making physical actuators, the materials used for actuator fabrication should not react with the liquid propellants stored inside. Hence, materials with suitable chemical properties should be chosen. Lamination fabrication also allows for easy transition of the lab based fabrication techniques to more industrial based mass manufacturing techniques such as printed circuit board processing.

The microactuator development demonstrated tools and techniques to control the actuation process and generate rapid response from the microactuators. A power circuit that supplies the required input energy for the actuation process is developed and used for actuator characterization. During actuator characterization, the control parameters that are looked for are the ignition delay times, thrusts delivered, impulse delivered and impulse durations. The actuators were optimized to meet the requirements of a specific application. The chemical based microactuators were optimized to produce rapid jets that offer large forces in extremely short durations and their feasibility to be integrated into a 25 mm bluff body projectile to maneuver its path while spinning at 600 Hz is discussed. The physical based microactuators were optimized to produce low impulse, rapid jets to be used for selectively ablating the stratum corneum layer of skin to increase skin's permeability to high molecular weight drugs. Recommendations for future work for both the actuators are presented in this chapter.

6.1 Chemical Based Microactuators

The solid propellant microthrusters mentioned in the literature demonstrated that large fluidic forces can be achieved from millimeter scale batch fabricated combustion chambers. The forces achieved from these devices are much higher than any other fluidic microactuators. However, the time scale of generation of these forces is not given importance. This is because most of these microactuators were intended to be used for station keeping applications for kg-scale satellites where time control of the force output is not necessary. The gas generation actuators reported in the literature focused at this issue in greater detail and developed actuators that generated large forces in small time scales, typically in milliseconds. These actuators were successfully demonstrated for use

in maneuvering a 50 mm diameter projectile's path while rotating at a spin rate of 60 Hz. However, in these actuators, the solid propellant is ignited by supplying the required electrical input energy through a micromachined igniter and the delay times associated with transfer of energy from igniter to the propellant grain are significant and were compensated with the control electronics connected to the microactuator. The time scales achieved by these actuators are still not sufficient to be used for maneuvering a 25 mm projectile spinning at 600 Hz.

The work presented in this thesis is an extension to the GGA work, where we have tried to minimize the impulse durations further by proposing a concept of rapid and uniform ignition of the propellant. This rapid ignition is achieved by making the propellant conductive by adding micro or nano size conductive dopant particles to the propellant and igniting it by means of electrode discharge of direct currents. The actuator development process continued with alternate propellants, conductive dopants, power supply configuration and actuator geometry to shape the impulse curve as desired.

The development of conductive propellant microactuators satisfied several objectives. First, batch fabrication of microactuators utilizing laser micromachining and adhesive lamination techniques was demonstrated for mm-scale devices. Next, solid propellant selection criteria were established with focus on safety, performance and performance reliability. Efforts were then made to make the propellant conductive by adding conductive dopant particles such as nano size carbon black without sacrificing the performance of the propellant. Then, an electro-thermal model that describes the ignition of conductive fuel with electrode discharge was developed to predict the effect of process variation on the performance variation. This model determined the input power, the

distance between electrodes and fuel conductivity that are necessary to minimize the ignition delay times. It also explained how the energy consumed by the conductive propellant can be varied by varying the fuel resistance. Next, a combustion model used in large scale rocket design is adapted to microactuator system to predict the effect of actuator physical parameters on its performance variation. This model predicted the optimum chamber dimensions, nozzle dimensions and fuel energetics for use in microactuator assembly to generate rapid forces and short durations. Then, the actuators are fabricated and characterized. Characterization techniques to determine total impulse, impulse delays and burn time were presented. Microactuators that offer a range of impulse and burn times were demonstrated through appropriate propellant selection and actuator design. Timing control of impulse duration and ignition delays were also reported. The specific requirements for the application of maneuvering the path of a 25 mm projectile spinning at 600 Hz were then presented and the feasibility of achieving the desired performance from our conductive propellant based microactuators was discussed. However, the actuators were not implemented in a real time application. We recommend this for future work where microactuator arrays compatible to the application need to be fabricated and integrated into a test vehicle. Any improvements desired from the actuators can be made by improving the fabrication approaches and propellant loading techniques to ensure uniform and consistent behavior from the actuators. With respect to fabrication, structural failure of the actuators was observed when the chamber pressures were too high. Further research into materials and bonding techniques applicable for actuator fabrication could improve the structural integrity of the devices. With respect to propellant loading, currently, conductive propellants were pressed down into the

chambers by hand to achieve complete loading and good contact with the electrodes. The loading techniques could be improved further to ensure uniformity from device to device. A bulk loading process such as doctor-blading or prefabricated solid propellant pellets would ensure consistent mass loading of the propellant into combustion chambers. In this thesis, we have just focused on the application of projectile maneuvering. However, the developed chemical actuators could be used in several other applications such as in air bag deployment which requires rapid gas generation or in microspacecraft applications that require small but accurate forces from the actuators. With little optimization, our chemical actuators can easily be altered to meet the specific requirements at hand.

6.2 Physical Based Microactuators

The physical based microactuators discussed in this dissertation operate on the principle of arc generation across two closely spaced electrodes. Though ignition of the propellant by means of arc discharge is a fairly established concept, its implementation in large scale actuators is highly limited as the input power required to generate an arc in such systems would be extremely high and in most cases, practically unattainable. However, this concept could easily be adapted at small size scales because, then the input power required would be much smaller and can easily be supplied from a portable power circuit. When the propellant is placed in the path of the generated arc in a closed and thermally insulating chamber, the energy generated from the arc is transferred to the propellant and rises the temperature and pressure within the system. This causes a phase change of the propellant and the high pressured propellant exits the chamber through a nozzle in the form of a jet. This concept of arc generation and jet release from the physical microactuators was demonstrated and characterized for the input power

requirements, force delivered and duration of the jet. An array of multiple actuators were fabricated using laser micromachining and adhesive lamination techniques. The actuator development process is verified for several propellants and actuator geometry to achieve small and rapid jets from the actuator. The temperature rise within the chamber is estimated from temperature simulations.

The actuators were then applied for transdermal drug delivery application. Exposure of skin to the jet delivered from the microactuator can be classified as an enhancement technique that can be combined with a drug delivery system to increase the permeability of drugs through skin. Hence, skin's barrier properties were looked at in detail and the required mechanical forces from the jet to puncture skin were discussed. Some of the currently existing skin permeation enhancement techniques were discussed and their limitations were presented. The permeability achieved in skin when it is exposed to the released jet from the actuator was studied and compared to a control. For this purpose, the thermal and mechanical effects of the jet were isolated to study their effect on skin independently and as combined and the extent of skin permeation achieved was compared. The treated skin was then tested for the delivery of drug analog molecules to study the extent of permeation. The rise in temperature in exposed skin as a function of skin's depth was simulated for several exposure times to estimate the extent of damage in skin's surface. These temperature simulations give us an idea of the durations required from the microactuator to achieve the desired ablation in skin with minimal damage and inconvenience to the patient.

Most of the work done in this thesis on physical microactuators is focused at developing a concept, validating the concept and finally, implementing it for a specific

application. However, more work needs to be done with respect to the optimization of the microactuators. This work includes more research into the materials and fabrication techniques utilized for the fabrication of the microactuators. More FDA approved and compatible solutions need to be tested for their use in transdermal drug delivery application. Also, the physical based microactuators developed in this research work were fabricated as radially firing devices. However, the application of the actuators for transdermal drug delivery would be more feasible if the actuators deliver the jet from top like any conventional patch device. So, for future work, we recommend that the microactuators be fabricated in a more conventional patch like form and if possible, be integrated along with a drug delivering device, so as to develop a complete system that can not only increase skin's permeability but also allows for the delivery of the drug from the same system.

APPENDIX A

THREE DIMENSIONAL MICROACTUATORS BASED ON LITHOGRAPHY AND LASER MICROMACHINING

This section describes the fabrication sequence of three dimensional microactuators fabricated using lithography based and laser micromachining techniques. This fabrication technique utilizes the concept of geometrically dispersed multiple igniters within the volume of a microactuator to increase the response times of conductive propellants. Integrating laser micromachining and lithography techniques allows for reducing the feature size of the microactuator components without sacrificing the overall volume of the microactuators. A 10x10 array of igniters were formed in the form of high aspect ratio pillars that minimized resistance through the conductive fuel. Each pillar has a diameter of 100 μm and a height of 500 μm with center to center distance of 280 μm . As shown in Figure 100, pillar structure SU8 is patterned on a glass substrate. A uniform seed layer is then deposited. The seed layer is then patterned using laser micromachining to isolate the adjacent electrodes. For laser machining, an excimer laser is used. Addition metal is then electroplated on top of the isolated electrodes. SU8 structure is later separated from the glass substrate. Actuators fabricated using this technique is presented in Figure 101.

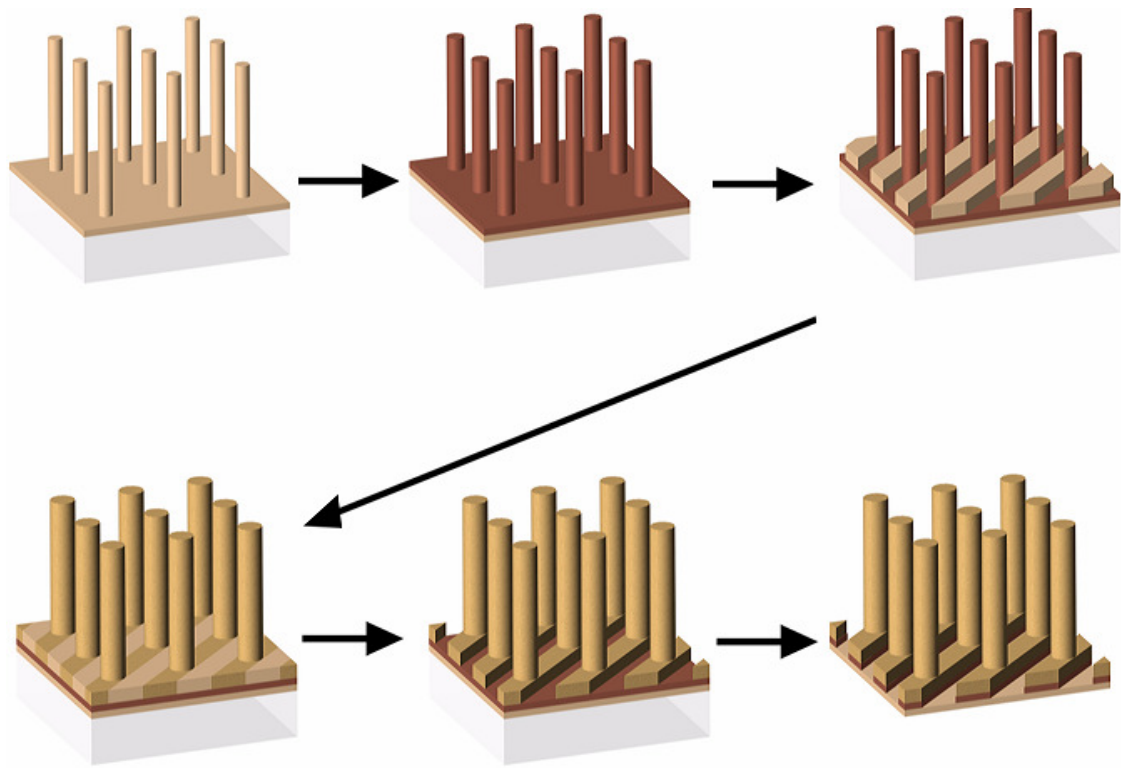


Figure 100: Multi pillared microactuator fabrication schematic

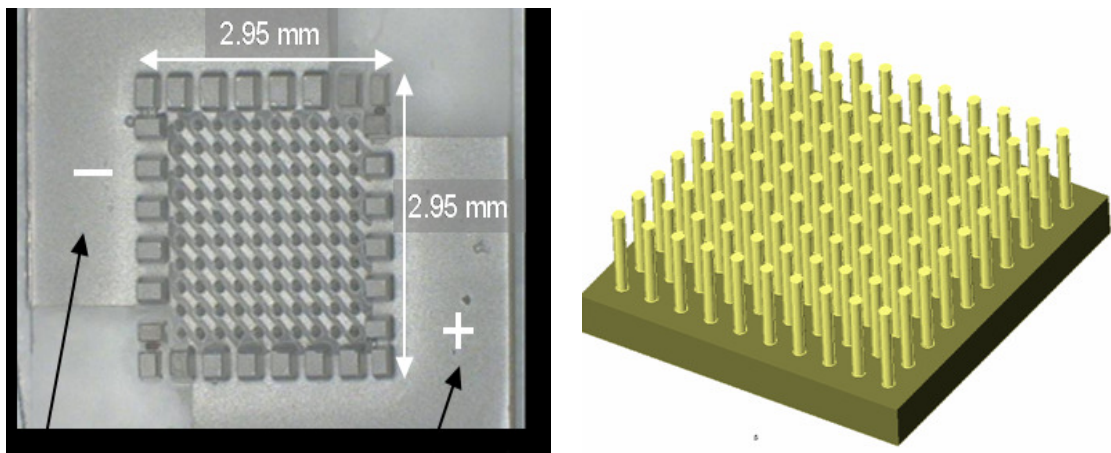


Figure 101: Multi pillared three dimensional structure

APPENDIX B

POWER CIRCUIT FOR PORTABLE APPLICATIONS

For adapting the microactuators for use in a final application, a portable circuit that can supply the desired power input must be developed. In the case of projectile maneuvering, all the control actuators and the control electronics should be fit into the body of the projectile. In this section, a portable boost converter power circuit that meets the physical requirements to be placed within a small projectile body is reported. The schematic of the developed portable power circuit is shown in Figure 102. This power supply can be used to heat the conductive propellant placed between two electrodes via joule heating using capacitive discharge. The main components of the circuit include batteries, a charging capacitor, an inductor, a discharge capacitor, a diode, a mosfet and a pulse generator. Other minor components include a switch, a mosfet driver and voltage dividers.

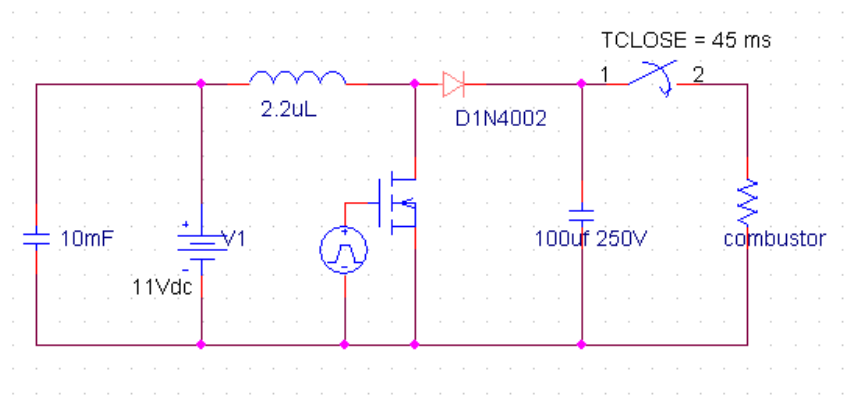


Figure 102: Portable power circuit schematic for use in a small scale projectile

A voltage of 11 V is supplied from a bank of charging capacitor and 3 rechargeable batteries each with a voltage of 4 V connected in series. The batteries and the capacitor act as power source replacing the high voltage power supply used in the bench scale circuitry for the purpose of supplying the required energy capacity. The capacitor is added in parallel with the battery supply so as to slow the discharge rate of the batteries and at the same time supply the pulse current. It has a capacitance of 10 mF. The batteries are still required to charge the capacitor at least once every few seconds. As the mosfet switch is turned on using the pulse generator, an inductor with an inductance of $2.2\ \mu\text{H}$ acts as a temporary storage element where energy is stored incrementally from the supply bank. As the required gate voltage for the mosfet is high, it is used along with a compatible mosfet driver so as to reduce the requirements for the gate voltage drive signal to 5 V. When the mosfet switch is turned off, this energy and additional energy from the input is transferred to the output capacitor with ratings of 100 μF capacitance and 250 V of maximum voltage by means of a diode switch where it is stored until the discharge time. This energy is then supplied to the actuator at the desired time using a power switch. Though this circuit is not tested in the final application, it is characterized in lab and also by using pspice modeling to determine the final voltage obtained from the circuit.

APPENDIX C

NUMERICAL SIMULATIONS BASED ON NOZZLE THEORY

The following code is written in Matlab to solve for the thrust, impulse and duration of the microactuators using combustion and nozzle theory. Exact syntax may have been changed to facilitate typesetting.

Nozzle Theory

```
At=1.0355e-6;

%for At =.1e-6:.01e-6:3e-6;

Ae = At*2;

%Ae = 4.99e-6;

%At =2.46975e-6;

%Ae = 4.99e-6;

k=1.46;

Mt =1; % Mach# at throat

Pe =1.013e5;

Rg = 8.314;

R = Rg*1000/29;

M=29;

Me=2.254;

%for vol = 1e-9:.1e-9:25e-9

vol =15e-9;

Tc=2100; % Chamber Temperature
```

```

for Pc0 = 1e6:.1e6:50e6

%Pc0 =15e6; % chamber pressure

Vc0 = R*Tc/Pc0; % Chamber Specific Volume

Pc = Pe*(1+(k-1)*(Me^2)/2)^(k/(k-1)); % nozzle entrance Pressure

Vc = R*Tc/Pc; %nozzle entrance specific volume

Tt = 2*Tc/(k+1); % Throat Temperature

ut= sqrt(2*k*R*Tc/(k+1)); % Throat Velocity

Pt = Pc*((2/(k+1))^(k/(k-1))) ;% Throat pressure

Vt = Vc*(((k+1)/2)^(1/(k-1))) ;% Throat Specific Volume

ue = sqrt(2*k*R*Tc*(1-(Pe/Pc)^((k-1)/k))/(k-1)); % exit Velocity

Ve = Vc*(Pc/Pe)^(1/k); % Exit Specific Volume

Te = Tc*((Pe/Pc)^((k-1)/k)); % Exit Temperature

mfr = Pc0*At*k*sqrt(((2/(k+1))^(k+1)/(k-1))/k/R/Tc))

force =mfr*ue

PR = Pe/Pc

const = sqrt(2*Pc*(k/(k-1))*(((Pe/Pc)^(2/k))-((Pe/Pc)^((k+1)/k))));

%for vol = 2e-9:.1e-9:20e-9

t = 1000*2*vol*(((1/Vc0)^(1/2))-((1/Vc)^(1/2)))/At/const

I = force*t*1e-3;

ImNs= I*1e3

Isp = I/(9.8*1300*vol)

%rate = 0.4* ((Pc0*1e-6)^0.5) %mm/ms/Mpa^n

```

```
plot(Pc0*1e-6,Isp, '*')  
  
xlabel('Chamber Pressure (MPa)')  
  
ylabel('Specific Impulse (s)')  
  
hold on  
  
end
```

REFERENCES

- [1] Helvajian, H., Microengineering for Aerospace Systems. Aerospace Press, El Segundo, CA and AIAA, Reston, VA, 1999.
- [2] Henning, A. K., "Microfluidic MEMS," IEEE Aerospace Conference, Aspen, Colorado, Mar 21-28, 1998.
- [3] Grosjean, C., Yang, X., and Yu-Chong Ti, "A practical thermopneumatic valve," Proc. 12th IEEE International Conference on MEMS, Florida, Jan 17-21, 1999.
- [4] Zengerle, R., et al., "A micro membrane pump with electrostatic actuation," Proc. IEEE MEMS Workshop, pp. 19-24, 1992.
- [5] Voldman, J., Gray, M. L., and Schmidt, M. A., "An integrated liquid mixer/valve," JMEMS, vol. 9, no. 3, pp. 295-302, 2000.
- [6] White, A., A review of some current research in MEMS with defense applications. Australia, DSTO-GD-0316: Aeronautical and Maritime Research Laboratory, February 2002.
- [7] Carlen, E. T., and Mastrangelo, C. H., "Paraffin actuated surface micromachined valves," Proc. 13th IEEE International Conference on MEMS, Japan, Jan 23-27, 2000.
- [8] Rich, C. A., and Wise, K. D., "An 8-bit microflow controller using pneumatically actuated microvalves," Proc. 12th IEEE International Conference on MEMS, Florida, Jan 17-21, 1999.
- [9] Man, P. F., Mastrangelo, C. H., Burns, M. A., and Burke, D. T., "Microfabricated capillary-driven stop valve and sample injector," Proc. 11th IEEE International Conference on MEMS, Germany, Jan 25-29, 1998.
- [10] Rossi, C., Esteve, D., and Mingues, C., "Pyrotechnic actuator: A new generation of si integrated actuator," Sensors and Actuators A, vol. 74, pp. 211-215, 1999.

- [11] Koeneman, P. B., Busch-Vishniac, I. J., and Wood, K. L., "Feasibility of Micro Power Supplies for MEMS," J. MicroElectroMechanical Sys., vol. 6, no. 4, pp. 355-362, 1997.
- [12] Davenas, A., "Development of modern solid propellants," Journal of Propulsion and Power, vol. 19, no. 6, pp. 1108-1128, 2003.
- [13] DiBiaso, H. H., English, B. A., and Allen, M. G., "Solid-phase conductive fuels for chemical microactuators" Sensors and Actuators A, vol. 111, pp. 260-266, 2004.
- [14] Zhao, Y., English, B. A., Choi, Y., DiBiaso, H., Guang, H., and Allen, M. G., "Polymeric microcombustors for solid-phase conductive fuels," 17th IEEE International Conference on MEMS, Maastricht, 2004.
- [15] Banga, A. K., "New technologies to allow transdermal delivery of therapeutic proteins and small water-soluble drugs," American J. Drug Delivery, vol. 4, no. 4, pp. 221-230, 2006.
- [16] Rossi, C., Do Conto, T., Esteve, D., and Larangot, B., "Design, fabrication and modeling of MEMS-based microthrusters for space application," Smart Materials and Structures, vol. 10, pp. 1156-1162, 2001.
- [17] Sutton, G. P., "History of liquid propellant rocket engines in the united states," Journal of Propulsion and Power, vol. 19, no. 6, pp. 978-1007, 2003.
- [18] Hunley, J. D., "The history of solid-propellant rocketry: What we do and do not know," AIAA Paper 99-2925, 1999.
- [19] English, B.A., Gadiraju, P., Rinehart, C. S., Glezer, A., and Allen, M. G., "Gas generator actuator arrays for flight control of spinning body projectiles," Proc. 19th IEEE International Conference on MEMS, Istanbul, Turkey, January 2006.
- [20] Micropropulsion, "<http://www.design.caltech.edu/micropropulsion/>," May 5, 2008.
- [21] Micropyros, "<http://www.laas.fr/micropyros/>," May 5, 2008.
- [22] English, B. A., "Laminated gas generator actuator arrays," Doctorate, Georgia Institute of Technology, 2006.

- [23] Turner, M. J. L., Rocket and Spacecraft Propulsion: Principals, Practice and New Developments. Chi Chester, UK: Praxis Publishing LTD, 2000.
- [24] Kubota, N., Propellants and Explosives: Thermochemical Aspects of Combustion. Weinheim, Germany: Wiley-VCH, 2002.
- [25] Accurate, "Smokeless powder double-base msds no. 1003.002," p. 6, 2006.
- [26] Brauer, K. O., Handbook of Pyrotechnics. New York: Chemical Publishing Co. Inc., 1974.
- [27] McLain, J. H., Pyrotechnics: From the Viewpoint of Solid State Chemistry. Philadelphia, PA: The Franklin Institute Press, 1980.
- [28] Kerr-McGee., The Chlorate Manual, 1st ed. Oklahoma City, OK: Kerr-McGee Chemical Corp, 1972.
- [29] Chase, M. W., et al., JANAF Thermochemical Tables, 3rd ed. Washington, D.C. or New York: American Chemical Society and American Institute of Physics for the National Bureau of Standards, vol. 1, 1986.
- [30] Sarner, S. F., Propellant Chemistry. New York: Reinhold Publishing Corporation, 1966.
- [31] Taylor, J., Solid Propellant and Exothermic Compositions. New York: Interscience Publishers, Inc., 1959.
- [32] www.sciencelab.com, "Potassium chlorate msds, cas 3811-04-9," p. 6, Dec 10, 2005.
- [33] Henkin, H., and McGill, R., "Thermal response of spherical explosives charges subjected to external heating," Industrial and Engineering Chemistry, vol. 44, p. 9, 1952.
- [34] Schumacher, J. C., Perchlorates: Their Properties, Manufacture, and Uses, ser. Monograph. New York: Reinhold Publishing Corporation, vol. 146, 1960.

- [35] James, R. W., Propellants and Explosives. Park Ridge, NJ: Noyes Data Corporation, 1974.
- [36] www.sciencelab.com, "Potassium perchlorate msds, cas 7778-74-7," p. 6, Dec 10, 2005.
- [37] Bircumshaw, L. L., and Newman, B. H., Proc. Roy. Soc. London, vol. A227, 1954.
- [38] Holzmann, R. T., Chemical Rockets. New York and London: Marcel Dekker., 1969.
- [39] www.sciencelab.com, "Ammonium perchlorate msds, cas 7790-98-9," p. 6, Dec 10, 2005.
- [40] M. S. Materials, "Gap-5527 3m™ gap polyol msds," p. 8, 2005.
- [41] NASA, "Solid propellant processing factors in rocket motor design," p. 75, 1971.
- [42] Hude, H., "Solid fuel development for gas-generating microactuators," Masters, Georgia Institute of Technology, 2003.
- [43] Zhang, K. L., Chou, S. K., and Ang, S. S., "Development of a solid propellant microthruster with chamber and nozzle etched on a wafer surface," Journal of Micromechanics and Microengineering, vol. 14, pp. 785-792, 2004.
- [44] SmartDust, "<http://www.bsac.eecs.berkeley.edu/archive/users/warneke-brett/smartdust/>," May 5, 2008.
- [45] Lewis, D. H., Janson, S. W., Cohen, R. B., and Antonsson, E. K., "Digital micropropulsion," Sensors and Actuators A, vol. 80, no. 2, pp. 143-154, 2000.
- [46] Rossi, C., Esteve, D., Temple-Boyer, P., and Delannoy, G., "Realization and characterization of micro pyrotechnic actuators and fem modeling of the combustion ignition," Sensors and Actuators A, vol. 70, pp. 141-147, 1998.
- [47] Rossi, C., Esteve, D., and Mingues, C., "Pyrotechnic actuator: a new generation of si integrated actuator," Sensors and Actuators A, vol. 74, pp. 211-215, 1999.

- [48] Rossi, C., Schied, E., and Esteve, D., "Theoretical and experimental study of silicon micromachined microheater and dielectric stacked membranes," *Sensors and Actuators A*, vol. 63, pp. 183-189, 1997.
- [49] Rossi, C., Rouhani, M. D., and Esteve, D., "Prediction of the performance of a si micromachined microthruster by computing subsonic gas flow inside the thruster," *Sensors and Actuators A*, vol. 87, pp. 96-104, 2000.
- [50] Orieux, S., Rossi, C., and Esteve, D., "Thrust stand for ground tests of solid propellant microthrusters," *Review of Scientific Instruments*, vol. 73, no. 7, pp. 2694-2698, 2002.
- [51] Gadiraju, P., Park, J. H., Lee, J. W., Prausnitz, M., and Allen, M. G., "Micro-ablation of skin by arc discharge jet ejection for transdermal drug delivery," *Proc. 14th International Conference on Solid-State Sensors, Actuators and Microsystems*, Lyon, France, June 10-14, 2007.
- [52] Hsieh, D. S., "Drug permeation enhancement: theory and applications," *Drugs and The Pharmaceutical Sciences*, vol. 62, 1994.
- [53] Chaubal, M. V., Overview of Polymeric Drug Delivery, "<http://www.engr.umbc.edu/~chaubal/review.html>," May 3, 2008.
- [54] Loftsson, T., and Olafsson, J. H., "Cyclodextrins: new drug delivery systems in dermatology," *Int. J. Dermatology*, vol. 37, pp. 241-246, 1998.
- [55] Banga, A. K., *Electrically Assisted Transdermal and Topical Drug Delivery*, 1998.
- [56] Ross, M. H., Pawlina, W., and Kaye, G. I., *Histology: A Text and Atlas*, 4th ed. Lippincott Williams & Wilkins, 2003.
- [57] Gibson, T. K., "On the anatomy and physiology of the skin i-iv," *J. Plast. Surg.*, vol. 31, 1978.
- [58] Payne, P. A., "Measurement of properties and function of skin," *Clin. Phys. Physiol. Meas.*, vol. 12, pp. 105-129, 1991.

- [59] Hendriks, F. M., Brokken, D., Oomens, C. W., Bader, D. L., and Baajjens, F. P., “The relative contributions of different skin layers to the mechanical behavior of human skin in vivo using suction experiments,” *Med. Eng. Phys.*, vol. 28, pp. 259-266, 2006.
- [60] Wu, K. S., Van Osdol, W. W., and Dauskardt, R. H., “Mechanical properties of human stratum corneum: Effects of temperature, hydration and chemical treatment,” *Biomaterials*, vol. 25, no. 5, pp. 785-795, 2006.
- [61] Davis, S. P., “Hollow microneedles for molecular transport across skin,” Doctorate, Georgia Institute of Technology, 2003.
- [62] Shergold, O. A., and Fleck, N. A., “Mechanics of the deep penetration of skin solid with application to the injection and wounding of skin,” *Proc. R. Soc. London. A*, vol. 460, pp. 3037-3058, 2004.
- [63] Shergold, O. A., and Fleck, N. A., “Experimental investigation into the deep penetration of soft solids by sharp and blunt punches, with application to the piercing of skin,” *J. Biomech. Eng.*, vol. 127, pp. 838-848, 2005.
- [64] Williams, A. C., and Barry, B. W., “Penetration enhancers,” *Adv. Drug. Deliv. Rev.*, vol. 56, no. 5, pp. 603-618, March 2004.
- [65] Naik, A., Kalia, Y. N., and Guy, R. H., “Transdermal drug delivery: Overcoming the skin’s barrier function,” *Pharm. Sci. Tech, Today.*, vol. 3, no. 9, pp. 318-326, September 2000.
- [66] Park, J. H., Park, J. -W., Yoon, Y. -K., Joung, Y., Choi, S, Lee, J., Allen, M. G., and Prausnitz, M. R., “Wireless thermal micro-ablation of skin for transdermal drug delivery,” *BMES conference*, Baltimore, MD, September 2005.
- [67] Baxter, J. R. S., and Mitragotri, S., “Investigations of needle-free jet injections,” *Proc. 26th Annual International Conference of IEEE EMBS*, San Francisco, USA, September 2004.
- [68] Henry, S., McAllister, D. V., Allen, M. G., and Prausnitz, M. R., “Microfabricated microneedles: A novel method to increase transdermal drug delivery,” *J. of Pharmaceutical Sci.*, vol. 87, pp. 922-925, 1998.

- [69] Passport patch, “<http://www.alteatherapeutics.com>,” July 3, 2007.
- [70] Kaushik, S., Hord, A. H., Denson, D. D., McAllister, D. V., Mitra, S., Allen, M. G., and Prausnitz, M. R., “Lack of pain associated with microfabricated microneedles,” *Anesth. Analg.*, vol. 95, pp. 502-504, 2001.
- [71] Adams, R. D., *Adhesive Bonding: Science, Technology, and Applications*. New York: CRC Press, 2005.
- [72] Library, P. D., *Handbook of Plastics Joining: A Practical Guide*. Norwich, NY: Plastics Design Library, 1997.
- [73] Petrie, E. M., *Handbook of Adhesives and Sealants*. 2nd Ed., McGraw Hill, 2007.
- [74] 3M, “Super 77 adhesive – bulk version,” p. 6, July 2004.
- [75] Isola, “Mechanical properties by isola grade,” p. 4, May 2002.
- [76] Flexcon, “Product construction sheet: Densil 10 78k,” p. 2, June 2005.
- [77] 3M, “Scotch-weld low-odor acrylic adhesives dp810, dp810ns,” p. 6, June 2004.
- [78] 3M, “Scotch-weld epoxy adhesives dp460 off-white, dp460ns,” p. 6, March 2004.
- [79] Paul, B. K., and Peterson, R. B., “Microlamination for microtechnology-based energy, chemical and biological systems,” *ASME Int. Mech. Eng. Cong and Expo*, vol. 39, pp. 45-52, Nov 15-20, 1999
- [80] Martin, P M., Matson, D. W, Bennett, W.D., and Hammerstrom, D J., “Fabrication of plastic microfluidic components,” *Proc. SPIE – Int. Soc. Opt. Eng. (USA)*, vol. 3515, pp. 172-176, 1998.
- [81] Kathuri. Y. P., “Laser microprocessing of stent for medical therapy,” *MHS’98. Proc. of Int. Symposium in Micromechatronics and Human Science*, pp. 111-114, 1998.
- [82] Suceska, M., *Test Methods for Explosives*. New York: Springer, 1995.

- [83] Typical Ballistic Pendulum, "<http://hyperphysics.phy-astr.gsu.edu/hbase/class/phscilab/balpen.html>," May 3, 2008.
- [84] Kligman, A. M., "Preparation of isolated sheets of human stratum corneum," *Archives of Dermatology*, vol. 88, no. 6, 1963.
- [85] Monteiro-Riviere, N.A., *Comparative Anatomy, Physiology, and Biochemistry of Mammalian Skin*, In *Dermal and Ocular Toxicology*. Boca Raton, FL, CRC press, 1991.
- [86] Bronaugh, R. L., "Methods for in vitro percutaneous absorption studies II. Animal models for human skin," *Toxicol. Appl. Pharmacol.* vol. 62, pp. 481-488, 1982.
- [87] Van Duzee, B. F., "The fluence of water content, chemical treatment and temperature on the rheological properties of stratum corneum," *J. Invest. Dermatol.* vol. 71, no. 2, pp. 40-44, 1978.
- [88] Massey, J. M. J., *A Heat Transfer Model Study of the Hot Wire Initiator*. Springfield, VA22161: National Technical Information Service, 1964.
- [89] Sutton, G. P., *Rocket Propulsion Elements*. 6th ed. Wiley Interscience Publication, 1992.
- [90] Jiang, S. C., Ma, N., Li, H. J., and Zhang, X. X., "Effects of thermal properties and geometrical dimensions on skin burn injuries," *BURNS*, vol. 28, pp. 713-717, 2002.

VITA

PRIYA D. GADIRAJU

Priya Gadiraju received her Bachelor's degree in Chemical Engineering from Osmania University, India in 2001 and a Master's degree from University of Illinois, Chicago in 2003. Upon graduation, she joined Georgia Institute of Technology to seek a Doctorate degree in Chemical Engineering and a Master's degree in Electrical Engineering. During this time, she has worked on several projects in the area of Micro Electro Mechanical Systems (MEMS). She has accepted an offer to join Intel Corporation as a Senior Process Engineer after the completion of her Doctorate.